Designing Colloidal Open Crystals & Empty Liquids

Andreas Neophytou

a thesis submitted to the
University of Birmingham
for the degree of
doctor of philosophy

School of Chemistry
College of Engineering and Physical Sciences
University of Birmingham

July 19, 2023

UNIVERSITY OF
BIRMINGHAM

University of Birmingham Research Archive

e-theses repository

This unpublished thesis/dissertation is copyright of the author and/or third parties. The intellectual property rights of the author or third parties in respect of this work are as defined by The Copyright Designs and Patents Act 1988 or as modified by any successor legislation.

Any use made of information contained in this thesis/dissertation must be in accordance with that legislation and must be properly acknowledged. Further distribution or reproduction in any format is prohibited without the permission of the copyright holder.

ABSTRACT

Because their shape and interactions can be readily controlled, colloidal particles are particularly well suited to act as building blocks for the bottom-up fabrication of complex three-dimensional structures. The self-assembly of sub-micrometre colloidal particles has long been recognised as a promising approach to fabricate photonic materials that operate at visible wavelengths. Cubic diamond-structured colloidal photonic crystals are particularly sought after for their applications in visible light management because of their ability to support a complete photonic band gap at low refractive-index contrasts; however, their realisation *via* self-assembly pathways has proved to be a long-standing challenge.

In this context, this thesis presents a body of computational studies that devise self-assembly routes for designer triblock patchy colloidal rods and tetrahedral patchy particles to yield colloidal diamond crystals by encoding ring selection rules to circumvent kinetic traps. We show that the photonic band gap of the resulting crystals assembled from the triblock patchy rods is robust to stacking faults, thus circumventing the requirement of polymorph selection in a scalable fabrication method. Additionally, using patterning symmetry concepts, we present a bottom-up route to an enantiomorphic pair of single gyroid crystals comprising colloidal spheres, and demonstrate their assembly from rationally designed patchy spheres. We show that the single colloidal gyroid, and its inverse structure, supports a wide complete photonic band gap in addition to exhibiting rich chiroptical properties, making them attractive chiral photonic crystals.

Colloids, traditionally seen as "big atoms" and more recently with the development of the concept of "colloidal molecules", are also perfectly suited to act as model systems for atomic and molecular systems, and provide a window through which we can glean new insight into a number of fundamental problems in condensed matter physics. One such problem is the liquid-liquid phase transition – hypothesised to underpin the anomalous thermodynamic properties of water. We rationally design a colloidal analogue of water using triblock patchy particles, showcasing that this model displays the well-known water thermodynamic anomalies, as well as a liquid-liquid critical point. Using this model, we reveal that the liquid-liquid phase transition of tetrahedral networks can be described as a topological transition between an unentangled low-density liquid and an entangled high-density liquid, the latter containing an ensemble of topologically complex motifs. We show that this topological distinction between the low-density and high-density liquids also holds for molecular water in connection with the liquid-liquid phase transition.

ACKNOWLEDGEMENTS

Firstly, I would like to convey my deepest thanks to my Ph.D. supervisor Dr Dwaipayan Chakrabarti, without whom this thesis would not have been possible. I feel truly fortunate to have been a student of his, not only due to his guidance over the scientific research which this thesis contains, but also as a mentor in various aspects of life. I am particularly grateful for the innumerable hours he has given to discuss whatever random thought has occurred to me, and for teaching me how to ask the right questions and tell a story – for teaching me how to be a scientist. In particular, I will miss the Friday afternoons which were dedicated to philosophical discussions and reflection – someday I will achieve enlightenment and make it to the Himalayas.

Next I would like to also thank Professor Francesco Sciortino, whom I visited in Rome and in many ways has become my second Ph.D. supervisor. Again, much of this thesis would not have been possible without Francesco, who has introduced me to the world of phase transitions and critical phenomena (and of course water!) during my short stays with him. His kindness and willingness to teach (and in some instances learn) made working with him a truly enjoyable experience. I would also like to thank everyone in Rome for making my stay there an enjoyable experience, and one full of coffee and pizza.

I must also extend my sincere gratitude to Professor Vinothan Manoharan and his research group who hosted me in his lab during 2022 and for making me feel truly a part of the Manoharan group. In particular, I would like to thank Jessica Sun for teaching me how to do experiments with colloids, LaNell Williams for teaching me about viruses (and being a friend!), Tim Chiang for indoctrinating me into the cult of bouldering and willing to discuss science over coffee at any point, and Caroline Martin and Audrey von Raesfeld for making time in the lab an enjoyable experience. A special thanks must also go to Ahmed Sherif for saving me from being homeless in the second half of my stay in Boston. The whole group of 115 Franklin Street have my undying gratitude for making my stay in Boston an experience I will never forget.

I would like to thank Helen Abbott and Chris Avins for making my time at Birmingham as a Ph.D. student an enjoyable one, Wesley Flavell for being who he is and for working with me on the colloidal gyroid work (it's been a pleasure!) and teaching me how to use Blender.

I would also like to thank my parents Ellen and Phytos, and grandparents Stavroulla and Antonis, for their constant encouragement and support throughout my many years of study.

Finally, I would like to thank the Institute of Advanced Studies at the University of Birmingham, the Turing Scheme, and Royal Society International Exchanges IES\R3\183166 for their support and funding.

PUBLICATIONS

The work presented in the thesis chapters have so far led to the following publications:

- **Neophytou, A.**, Manoharan, V.N. and Chakrabarti, D., 2021. Self-assembly of patchy colloidal rods into photonic crystals robust to stacking faults. *ACS Nano*, **15**, 2668-2678.

- **Neophytou, A.**, Chakrabarti, D. and Sciortino, F., 2021. Facile self-assembly of colloidal diamond from tetrahedral patchy particles via ring selection. *Proc. Natl. Acad. Sci. U.S.A.*, **118**, e2109776118.

- **Neophytou, A.**, Chakrabarti, D. and Sciortino, F., 2022. Topological nature of the liquid–liquid phase transition in tetrahedral liquids. *Nat. Phys.*, **18**, 1248-1253.

- **Neophytou, A.** and Chakrabarti, D., 2022. Self-assembly of colloidal open crystals: programmed to yield. In *Frontiers of Nanoscience*, **21**, 111-128.

- Flavell, W., **Neophytou, A.**, Demetriadou, A., Albrecht, T. and Chakrabarti, D., 2023. Programmed Self-Assembly of Colloidal Single Gyroid for Chiral Photonic Crystals. *Adv. Mater.*, **Accepted Author Manuscript 2211197**

Other works to which the author has contributed as a doctoral student include:

- Rao, A.B., Shaw, J., **Neophytou, A.**, Morphew, D., Sciortino, F., Johnston, R.L. and Chakrabarti, D., 2020. Leveraging hierarchical self-assembly pathways for realizing colloidal photonic crystals. *ACS Nano*, **14**, 5348-5359.

- Xiao, M., Stephenson, A.B., **Neophytou, A.**, Hwang, V., Chakrabarti, D. and Manoharan, V.N., 2021. Investigating the trade-off between color saturation and angle-independence in photonic glasses. *Opt. Express*, **29**, 21212-21224.

CONTENTS

1 Introduction **1**
- 1.1 Self-Assembly of Hard Spheres . . . 2
- 1.2 Beyond Hard-Sphere Colloids . . . 6
- 1.3 Patchy Particles and Open Crystals . . . 7
  - 1.3.1 The Quest for the Holy Grail: Colloidal Diamond . . . 10
- 1.4 Colloidal Gels and Empty Liquids . . . 13
  - 1.4.1 Water and its Anomalies . . . 14
  - 1.4.2 Patchy Particles that Never Freeze . . . 15
- 1.5 Aim and Objectives . . . 16

2 Theory and Methodology **17**
- 2.1 The Potential Energy Surface . . . 18
  - 2.1.1 Identifying Local Minima — Geometry Optimisation . . . 20
  - 2.1.2 Basin-Hopping Global Optimisation . . . 23
- 2.2 Monte Carlo Methods . . . 25
  - 2.2.1 The Metropolis Method . . . 25
  - 2.2.2 Isothermal-Isobaric Ensemble . . . 32
  - 2.2.3 Cluster Move Monte Carlo . . . 34
- 2.3 Free Energy Methods . . . 36
  - 2.3.1 Thermodynamic Integration . . . 37
  - 2.3.2 Hamiltonian Integration . . . 38
  - 2.3.3 Einstein Crystal Method: Free Energy of Solids . . . 39
  - 2.3.4 Schilling-Schmid Method: Free Energy of Fluids . . . 44
- 2.4 Structure Characterisation and Order Parameters . . . 47
  - 2.4.1 Tetrahedral Order Parameter . . . 47
  - 2.4.2 Steinhardt Bond Order Parameters . . . 47
- 2.5 Photonic Crystals and the Photonic Band Gap . . . 49
  - 2.5.1 Plane Wave Expansion Method . . . 49
  - 2.5.2 Origin of the PBG . . . 52

3 Programmed Assembly of Rod-Connected Diamond **57**
- 3.1 Retrosynthesis of Rod-Connected Diamond . . . 59
- 3.2 Hierarchical Self-Assembly of Rod-Connected Diamond . . . 67
- 3.3 Crystallisation *via* Specific Interactions . . . 74

3.4 Photonic Properties of Rod-Connected Diamond . . . 76
3.4.1 Photonic Crystals Robust to Stacking Faults . . . 80
3.5 Discussion . . . 81

4 Clear Pathways to Colloidal Diamond 87
4.1 Rational Design of Building Blocks to Yield Diamond . . . 88
4.2 Self-Assembly of Colloidal Diamond . . . 92
4.3 Thermodynamic Driving Force Aiding Crystallisation . . . 96
4.3.1 Chromatic Patchy Particles . . . 101
4.4 Diamond Polytype Selection using Patchy Widths . . . 102
4.5 Discussion . . . 105

5 Colloidal Water 107
5.1 Designing a Colloidal Model of Water . . . 108
5.2 Thermodynamic Anomalies of Colloidal Water . . . 112
5.3 Topological Nature of the Liquid-Liquid Transition . . . 119
5.4 Discussion . . . 128

6 Self-Assembly of Rectangular Patchy Particles 131
6.1 Photonic Properties of Colloidal Gyroid . . . 134
6.2 Reverse Engineering Colloidal Gyroid . . . 140
6.2.1 Rectangular Patchy Particles . . . 143
6.3 Self-Assembly of Colloidal Gyroid and Empty Liquids . . . 145
6.4 Self-Assembly of Chiral Entangled Liquids . . . 149
6.5 Discussion . . . 153

7 Conclusions 155
7.1 Summary . . . 155
7.2 Outlook . . . 157

A Unit Cell Information for Crystals 163
A.1 Bravais Lattices . . . 163
A.1.1 Simple Cubic . . . 163
A.1.2 Face-Centred Cubic . . . 164
A.1.3 Hexagonal . . . 164
A.1.4 Orthorhombic . . . 165
A.1.5 Body-Centred Cubic . . . 165
A.2 Basis for Crystal Structures . . . 166
A.2.1 Cubic Tetrastack / Rod-Conected Diamond . . . 166
A.2.2 Hexagonal Tetrastack / Rod-Conected Diamond . . . 167
A.2.3 Double Hexagonal Tetrastack / Rod-Conected Diamond . . . 168
A.2.4 Gyroid . . . 169

List of Figures

1.1 Phase behaviour for a system of hard sphere colloids 4
1.2 Illustration of DNA-functionalised tetrahedral patchy particle synthesis . 9

2.1 Orientational reference free energy for particles with $D_{\infty h}$ and T_d symmetry. 43
2.2 Cartoon depicting the origin of the band gap in a multilayer film 53

3.1 Reverse engineering of rod-connected diamond (RCD) and closely related crystal structures 59
3.2 Schematic of the triblock patchy rod model 61
3.3 Energy per particle for different clusters of AB-triblock patchy rods as a function of the half-opening angle of the patches 63
3.4 Views of different polytypes of segmented rod-connected diamond (sRCD) crystal 65
3.5 Entropy of the cubic and hexagonal sRCD crystals as a function of aspect ratio 66
3.6 Triblock patchy rod particles with a hierarchy of interactions forming a crystalline structure in two stages, the first being the formation of tetrahedra 69
3.7 Promotion of crystallisation by hierarchical self-assembly strategy 70
3.8 Self-assembly of AB-triblock patchy rods (TPRs) with polydisperse patch half-opening angles 72
3.9 Snapshots of low-temperature configurations in systems of AB-triblock patchy rods (TPRs) with polydisperse patch half-opening angles 73
3.10 Two-step nucleation of the segmented rod-connected diamond structure from the fluid phase of triblock patchy rods with specificity of interactions upon cooling 75
3.11 Dependence of the photonic band gap in the sRCD structures on the aspect ratio 78
3.12 Dependence of the photonic band gap in the sRCD structures on the aspect ratio 79
3.13 Photonic properties of stacking hybrids of sRCD structures, showing complete photonic band gaps 81
3.14 Photonic band gap dependence on cubicity for sRCD structures 82
3.15 Photonic band structures for rod-connected diamond crystals 84

4.1 Ring selection rules for facile assembly of colloidal diamond 91

4.2 Self-assembly of one- and two-component systems of tetrahedral patchy particles with narrow patches . . . 94
4.3 Self-assembly of one- and two-component systems of tetrahedral patchy particles with wide patches . . . 96
4.4 Thermodynamic driving force for crystallisation in one- and two-component systems of tetrahedral patchy particles . . . 98
4.5 Bonding probabilities for one- and two-component systems of tetrahedral patchy particles . . . 99
4.6 Comparison of fluid-solid coexistence in one- and two-component systems of tetrahedral patchy particles . . . 100
4.7 Self-assembly of chromatic tetrahedral patchy particles . . . 102
4.8 Diamond polytype selection in two-component systems of tetrahedral patchy particles . . . 104

5.1 Colloidal water model . . . 108
5.2 Evolution of cluster distributions with temperature in systems of triblock patchy particles for different A-patch widths . . . 111
5.3 Thermodynamic anomalies of colloidal water . . . 113
5.4 Liquid-liquid phase transition of colloidal water . . . 115
5.5 Liquid-liquid critical point of colloidal water . . . 118
5.6 Links and knots in colloidal water . . . 120
5.7 Visualisation of the Gauss linking integral . . . 124
5.8 Topological nature of the liquid-liquid phase transition . . . 125
5.9 Pressure dependence of the topological properties of colloidal water . . . 126
5.10 Identifying links and knots in molecular water . . . 129

6.1 Reverse engineering colloidal single network gyroid . . . 132
6.2 Chiroptical properties for single colloidal gyroid structures . . . 135
6.3 Chiroptical properties for single colloidal gyroid structures . . . 139
6.4 Limitation of triblock patchy particles for the assembly of gyroid . . . 141
6.5 Relative stability of crystal polymorphs formed by triblock patchy particles 142
6.6 Designer spherical patchy particle with two rectangular patches . . . 145
6.7 Crystallisation of rectangular patchy particles . . . 147
6.8 Distribution of rings in networks formed by rectangular patchy particles . 148
6.9 Characteristic clusters in amorphous networks of rectangular patchy particles 149
6.10 Trefoil knots . . . 150
6.11 Topological properties of rectangular patchy particle networks . . . 151
6.12 Chirality of rectangular patchy particle networks . . . 152
6.13 Trefoil theta-curves formed in rectangular patchy particle networks . . . 153

CHAPTER 1

INTRODUCTION

The emergence of order from disorder is a common theme in nature – the formation of cell membranes from phospholipids, the crystallisation of water molecules into snowflakes and the intertwining of DNA strands into helices are just a few examples. The term "self-assembly" refers to the spontaneous formation of an ordered structure or pattern from its initially disordered components without any human intervention.[1] In this thesis we are particularly concerned with the self-assembly of colloidal building blocks. A number of definitions regarding what qualifies to be considered colloidal have been suggested. For instance, one working definition suggested is that "*particles that are individually unremarkable but collectively interesting*" are colloidal.[2] It is therefore interesting that the collective behaviour of humans can, in some instances, bear a striking resemblance to the collective behaviour of particular colloidal systems[3–6] (the reader can make of this what they will). However, this brings us to the crux of what makes colloidal self-assembly such an interesting phenomenon to investigate: the ability of these "unremarkable" particles to form intricate structures and display complex phase behaviour. Colloidal systems can therefore be used as a conduit to deliver insights into the more general question of *how does matter become organised*?.

A more conventional definition characterises particles to be colloidal if they have at least one dimension which is of the order $0.01 - 10\ \mu$m. This size range is not arbitrary, and the lower and upper limits have two key consequences. When dispersed in a solvent

medium, such as water, the size of the colloidal particles compared to the solvent molecules must be so small that the time scales of the solvent molecules and the colloidal particles are far enough apart that we can "integrate out" the degrees of freedom for the solvent molecules from our description of the system. Instead, we describe the solvent as a continuum. Therefore, the lower limit for the size of the colloidal particles is set by the size of the solvent molecules. The upper size limit is determined by the size at which external fields, such as gravity, overshadow the effects of Brownian motion. If one was to observe a dilute suspension of spherical colloidal particles, they would see that each particle moves with an irregular, but continuous, random motion. This motion is known as Brownian motion.[7,8] The phenomenon is named after Robert Brown, a botanist who observed this motion while looking at plant pollen in 1827.[9] Albert Einstein offered an explanation for this observation in 1905. He attributed the random motion to a constantly fluctuating net force on the particles due to constant collisions with the solvent molecules.[10]

1.1 | Self-Assembly of Hard Spheres

Hard spheres have become the quintessential model of colloidal particles – impenetrable spheres that cannot overlap with one another. In 1957, Wood & Jacobson[11] and Alder & Wainwright (together with Mary Ann Mansigh)[12] demonstrated in computer simulations that a fluid-crystal transition exists in such a system. An ordering transition from a fluid phase to a crystalline phase in a hard sphere system has to be solely driven by entropy, which was somewhat counter-intuitive. The experimental evidence of hard sphere crystallisation was provided by Pusey and van Megen after three decades, using a suspension of poly(methylmethacrylate) spheres coated by thin brushes of a flexible polymer, which can be treated as nearly hard sphere colloids.[13] They found four distinct phases, as shown in Figure 1.1. Moving from lower to higher packing fraction, ϕ: a fluid

phase, a fluid-solid coexistence region, a solid region, and a glass region. There are two different close-packed structures with maximum packing fraction of 74%, the face-centred cubic (fcc, also known as the cubic close-packed structure) and hexagonal close-packed (hcp) structures. Both structures can be thought of as being built up from layers of spheres forming a triangular lattice, where the two structures arise due to differences in the stacking of these layers. Experimentally it is observed that these close-packed colloidal crystals have randomly stacked layers, and are referred to as random hcp (rhcp) crystals.[14,15] This random phase arises as the difference in free-energy between the two structures is very small. While fcc is reported to have the lower free-energy, this has been a topic of much controversy due to the difference being very small (for example, $\Delta F_{\text{hcp-fcc}} = 0.00134$ for crystals with a number density of $\rho = 1.099975309$).[16–18]

An example of a naturally occurring colloidal crystal is the gemstone opal, which is known for its fascinating optical properties. The striking, iridescent colour of opals originates from the Bragg diffraction of the crystalline lattice assembled from silica colloids that display no colour themselves.[19] We say that opals are photonic crystals, periodic structures formed by macroscopic media of different dielectric constants ε. The interfaces between the different dielectric media act as scattering centres, and so in certain instances a photonic crystal may prevent the propagation of light in certain directions. The frequency range in which a photon is prohibited to propagate through the crystal is said to form a "photonic band gap" (PBG).[20–22] If these prohibited frequency ranges along all directions overlap, then the photonic crystal blocks light propagation in all directions and is said to possess a complete PBG. Opals possess a number of narrow partial PBGs along different crystallographic axes, but their frequency ranges do not overlap and so it does not possess a complete PBG. However, it is the narrowness and directionality of these partial gaps leads to the striking iridescence of opals.



Figure 1.1: **Phase behaviour for a system of hard sphere colloids.** Snapshots of polymer coated poly(methylmethacrylate) spheres suspended in a mixture of liquids chosen to nearly match their refractive index so that the suspensions are nearly transparent when the particles are in a fluid phase. Nine samples of different volume fractions (ϕ) were prepared, and row (a) shows the samples immediately after mixing, (b) after 1 day, and (c) after 4 days. Adapted from Ref. [23].

This iridescence can be used to follow the fluid-solid transition in colloidal systems which form "synthetic" opals.[13,23] Figure 1.1 shows how the fluid-solid transition is visually apparent for a suspension of amorphous poly(methylmethacrylate) particles, as the system transitions from the dull fluid phase to an iridescent crystal.[13,23] It is also worth pointing out that the timescale associated with colloidal crystallisation is much longer than that of atomic or molecular systems: it is not until four days after the suspension is formed that crystals have formed. Following the fabrication of a synthetic opal, it is possible to "invert" the structure by infiltrating the space between the spheres with a high dielectric

material, for instance silicon.[24,25] The colloidal spheres are then dissolved away, leaving behind an inverse opal. Whereas the "direct" fcc structure does not have a complete PBG, its inverse structure does. Similarly, the inverse hexagonal close-packed (hcp) structure also has a complete PBG.[15,20,26]

While crystals with complete PBGs have traditionally been the targets for colloidal self-assembly,[25,27–31] recently there has been an increased interest in colloidal glasses.[32–36] This interest is largely driven by the ability of these colloidal glasses to display angle-independent structural colours making them attractive materials for a range of applications spanning industries involving cosmetics, displays, and coatings.[32,33,37] Unlike colloidal crystals that are iridescent (their colour depends on the angle at which they are viewed), some amorphous structures that possess short-range correlations can display structural colour that seemingly does not change with the angle between the light source and viewer.[34,35,38] However, the structural colours formed by colloidal glasses, while angle-independent, often have much lower saturation than their crystalline counterparts as there is a trade-off between colour saturation and angle-independence.[35] The physical origins underpinning this trade-off is not fully understood, however, it was recently shown that the first peak in the structure factor plays a key role in determining both the colour saturation and angle-independence of structurally coloured materials.[35] Materials with narrow first peaks in the structure factor have greater colour saturation and those with higher peaks have greater angle-dependence. However, in general, sharper peaks are also higher and so it is not straightforward to design materials that are both highly angle-independent and saturated. One strategy that has been used to alleviate this issue is to introduce broadband absorbers, such as carbon black, to the system as this will increase the transport length of the light, which in turn increases the colour saturation of the material.[35,38]

1.2 | BEYOND HARD-SPHERE COLLOIDS

While hard sphere colloids have been extensively studied and have proven extremely useful as a model system for understanding the role of entropy in crystallisation and polytype selection,[39–43] they involve practically excluded-volume interactions only, thereby limiting the crystal structures they form. Therefore, there has been much effort placed in developing systems where attractive interactions are at play between colloidal particles to engineer their phase behaviour and widen the variety of colloidal crystal structures. One of the most powerful, and simple, ways to introduce attractive interaction between hard bodies is provided by the so-called depletion interaction. The addition of non-adsorbing co-solutes (called depletants), that are intermediate in size compared to the solvent molecules and the colloidal particles, can induce an entropic attraction between the colloidal particles. The depletant particles can only get so close to the colloidal particles due to excluded volume effects, resulting in an "exclusion zone" around the colloidal particles of thickness R (where R is the radius of the depletants). An entropic attraction arises when two colloidal particles approach one another such that their exclusion zones overlap. The volume of space available to the depletants in the system increases, and as a result the entropy of the system increases also.

An alternative approach to endowing colloidal particles with attractive interactions is to alter their surface chemistry. In 1996 two seminal papers presented the idea that DNA could be used as a "glue" between nanocolloids.[44,45] In one paper, Mirkin and coworkers, provided the first example of DNA-coated nano-particles. By exploiting the thiol-gold conjugation reaction, they were able to immobilise single-stranded DNA (ssDNA) with a thiol end-group onto the surface of gold nano-particles. They fabricated two distinct populations of DNA-coated colloids (DNACCs), which were coated with

non-complementary ssDNA. The reversible aggregation of the particles was then facilitated by the introduction of linker ssDNA complementary to both populations. Importantly, they showed that the aggregation could be reversed by increasing the temperature.[44] However, the use of a linker is not absolutely necessary. The same result could have been achieved by coating the particles with partially, or fully, complementary DNA. In the same issue of Nature, Alivisatos *et al.*, showed that small gold clusters with a single DNA strand grafted to their surface assemble into dimers and trimers (which they referred to as "nanocrystal molecules").[45] These two papers birthed a new field of research: crystal engineering with DNA. However, engineering crystal structures with DNACCs is not quite so straightforward. Many early attempts to fabricate crystal structures from DNACCs failed, instead producing random, amorphous aggregates.[46–50] This was especially true for micron-sized DNACCs.[50,51] The first crystal structure produced from micron-sized DNACCs was not reported until 2005 by Crocker and coworkers.[52] A number of synthetic routes to fabricate DNACCs are present in the literature. However, the general recipe for the nucleic acids is always the same: a binding group, a spacer and single-stranded probe DNA.[53,54]

1.3 | Patchy Particles and Open Crystals

The fcc structure was initially considered to be the best candidate for a structure with a complete PBG.[20] However, it was later shown in the early 1990s by Ho, Chan and Soukoulis to only have a partial PBG.[55] The first structure confirmed to possess a complete PBG was in fact diamond.[55] The structure was composed of dielectric spheres, with a refractive index of $n = 3.6$, positioned on diamond lattice points, and embedded in air. This structure was reported to have a band gap–midgap ratio (the ratio of the width of the band gap and the midgap frequency of the band gap) of 15%, although this value was later disputed and shown to actually only be 3.5%.[56] However, the inverse structure (i.e.,

diamond lattice of air spheres embedded in a high dielectric medium) was reported to have a band gap–midgap ratio of 29%, which still stands as one of widest PBGs reported.[55] The only structure to have a wider band gap is the so-called "rod-connected diamond" structure, which has a band gap–midgap ratio of 30%.[57,58] This is a structure composed of dielectric spheres that lie on diamond lattice points, and are connected to their nearest neighbours by dielectric cylinders. A recent computational study sought to identify what structures provide optimal complete PBGs via topology optimisation, where each voxel of the unit cell was a degree of freedom. The rod-connected diamond structure was found to be the optimal structure with a band gap–midgap ratio of 30.2%.[58] Despite being the crystal structure with widest PBG (which has earned it the moniker "champion photonic crystal"), rod-connected diamond has proven difficult to fabricate. This has led to a family of alternative photonic crystals, based on diamond, that are more easily fabricated. A thorough review of the diamond family of photonic crystals is provided in Ref. [57].

Therefore, much effort has been placed in fabricating crystals beyond that of close-packed structures. However, in order to move away from these close-packed structures it is necessary to introduce some form of anisotropy to the system.[59,60] Fortunately, the interactions between colloidal particles are tunable, and so colloidal particles can be rationally designed to self-assemble into a range of different structures.[61–63] To move away from close-packed structures, and towards open structures such as cubic diamond, the spherical symmetry of the particles must first be broken. It is possible to fabricate particles with anisotropic interactions that have a number of attractive or repulsive patches on their surface; these are often referred to as "patchy" particles.[64] The patches introduce directionality to the inter-particle interactions, facilitating their assembly into a myriad of structures.[27,28,64–72] However, these particles are not routinely fabricated and so far have mostly been investigated through computational studies.

Wang *et al.*, built on the concept of DNA-mediated interactions, and through the use of the avidin-biotin reaction, fabricated micrometre-sized particles with symmetrically arranged, "sticky" patches of DNA on their surfaces, as shown in Figure 1.2. The synthetic protocol begins with creating different, highly symmetric, clusters of amine-modified polystyrene spheres. A chemically distinct polymer is then grown from the center of the clusters using a swelling and cross-linking process, to the extent that only small patches remain exposed from the original amine-modified polystyrene spheres. These amidine patches are then converted into biotin patches which ultimately form DNA patches. These particles display specific directional bonding so that when they assemble into clusters they form "molecular colloids". The valency of the colloidal atoms, and hence what colloidal molecules they can form, is controlled by the number of patches on their surface and the size of the patches. The addition of the specificity of DNA hybridisation to the valency ensures that the interactions adds another layer of control which can be exploited to direct the assembly of these particles.[73]

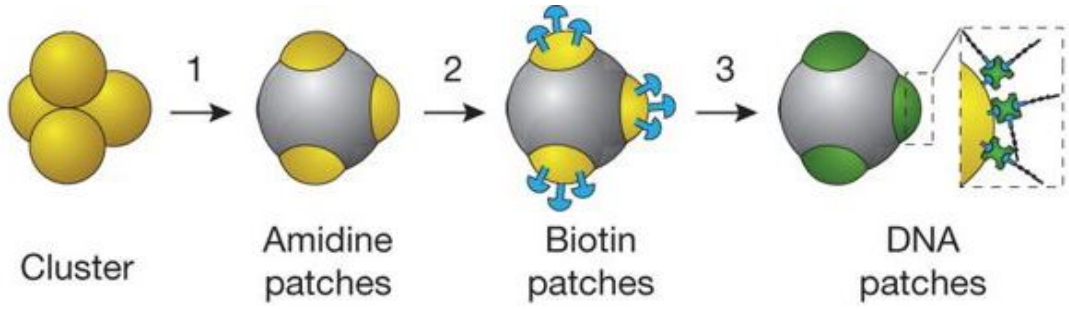


Figure 1.2: **Illustration of DNA-functionalised tetrahedral patchy particle synthesis. 1**. A tetrahedral cluster of amidinated polystyrene microspheres are swollen with styrene, such that only small protrusions from the original cluster remain. The styrene is polymerised leaving a patchy particle with tetrahedrally arranged amidine patches. **2**. The amidine patches are functionalised with biotin. **3**. The biotin functionalised patchy particles are functionalised with DNA using the lock-and-key avidin-biotin reaction. Figure adapted from Ref. [73]

.

The patches introduce directionality to the inter-particle interactions, meaning that altering the number, size, shape and relative geometry of the patches will also alter the potential structures that the particles can form. Additionally, we must also consider the strength of the inter-particle interactions: if they are too strong, the particles will become kinetically trapped in disordered structures, whilst if they are too weak, assembly will not occur.[59] The strength of the interactions must be correctly tuned so as to allow for bond reversibility, which ensures that incorrectly positioned particles can be re-positioned.

1.3.1 The Quest for the Holy Grail: Colloidal Diamond

Experimental studies investigating the self-assembly of colloidal structures have been predominantly focused on 2D systems.[67,74–76] However, much effort has also been placed in devising fabrication routes to diamond-structured colloidal crystals,[24,77–79] driven by their applications in visible photonics.[55,57] For nearly three decades the cubic polytype of diamond has often been considered as the Holy Grail of colloidal self-assembly. Particular effort has been spent on investigating the assembly of colloidal particles with four identical patches arranged in a tetrahedral geometry.[27,28,65,66,69] These particles are the obvious choice for a potential precursor to cubic diamond, and so hold the promise of a self-assembling system with a large complete PBG.

Glotzer *et al.* studied the assembly of patchy particles with a hard core and patches with a tetrahedral arrangement using Monte Carlo simulations.[27] They observed that, for fast cooling rates, the diamond structure is not observed; instead, only kinetically arrested, disordered structures are obtained. However, for slow cooling rates, cubic diamond was formed in 55% of the runs in the presence of a crystalline seed. This was clear evidence for the potential of these particles as precursors for cubic diamond; however, only a single parameter set was investigated.[27]

Despite their promise, the self-assembly of a diamond crystal from such tetrahedral patchy particles has proved to be challenging. The self-assembly of a diamond crystal from tetrahedral patchy particles faces challenges that can be of both thermodynamic and kinetic origins, as suggested by a number of computer simulation studies.[28,80–82] When the particles possess narrow patches, 5-membered rings form more readily than 6-membered rings, and clathrate structures are thus kinetically favoured over a diamond structure.[82] On the other hand, when patches are too wide, there is not a sufficiently large thermodynamic driving force for spontaneous crystallisation to occur.[28] A significant degree of supercooling is then required for the free-energy barrier to crystal nucleation to reach an accessible barrier height that would allow for spontaneous crystallisation to take place.[80] As a result, crystallisation is pre-empted by the dynamic arrest of the system into an amorphous glassy network when the attractive patches are too wide.[28,80,82] Patchy particles are an example of a system of particles with directional interactions, by this we mean that the particles form bonds that have a well defined position and orientation in space and that there is some concept of valency so the particles can only form a finite number of bonds. In such a system the particles form extended networks which contain rings – paths in the networks where the start point and end point are the same.[83] The glassy network has a distribution of rings, including even- and odd-membered rings.[84] As diamond crystals comprise exclusively even-membered rings, the tetrahedral patchy particles become dynamically arrested due to frustration between the local order of the fluid and the global order of the crystal.[85]

Unlike tetrahedral patchy colloids, triblock patchy particles (particles with two attractive circular patches at the poles separated by a repulsive middle band) have routinely been synthesised in bulk by the glancing angle deposition (GLAD) method.[86] In seminal work by Chen *et al.*, triblock patchy particles with equal-sized patches on the poles across a

charged middle band and a kagome lattice was self-assembled from these patchy particles in a quasi-two-dimensional system.[67] Subsequently, the self-assembly of a kagome lattice was observed in computational studies.[71,87] The mechanical stability of the kagome lattice was attributed to rotational entropy, and it can be favoured over the close-packed hexagonal lattice due to vibrational entropy.[68,88]

The self-assembly of triblock particles into three-dimensional crystal structures has been studied extensively with computational methods. In particular, there have been many attempts to programme their self-assembly into the cubic tetrastack structure (also known as pyrochlore) since it is known to also possess a wide PBG like diamond.[89] However, the issues of polytype selection and kinetic accessibility can also be an issue for triblock patchy particles since the cubic tetrastack structure is in competition with hexagonal tetrastack, with both having comparable free energies (less than 0.2 $k_{\mathrm{B}}T$).[72] The cubic tetrastack comprises corner-shared tetrahedra in such a way that each particle has six neighbours in a staggered configuration, whereas the hexagonal tetrastack involves some eclipsed configurations in addition to staggered configurations. Romano and Sciortino laid out one route to selectively assemble one of the tetrastack structures with their 'patterning symmetry' concept, which imposed geometric constraints on the patches in order to control the relative arrangements of the nearest neighbours of the two patches.[30] Instead of circular patches, Romano and Sciortino considered two triangular patches on the poles orientated in a staggered configuration to destabilise the hexagonal tetrastack, thus facilitating the self-assembly of the cubic tetrastack lattice.[30] If the two triangular patches were eclipsed, neither of the tetrastack crystals was observed, as both require some staggered motifs. Instead clathrate-like structures were observed.

By proceeding *via* one or more stable/metastable phases, hierarchical approaches to self-assembly are able to better navigate kinetic traps that may hinder the assembly of the target

structure.[90] Due to their modular design space, it is also possible to programme triblock spherical particles to follow hierarchical self-assembly pathways to target structures.[31,91,92] Recently, Chakrabarti and coworkers have shown that two-stage self-assembly schemes, whereby the first stage involves the self-limited formation of uniform discrete tetrahedral clusters, facilitates crystallisation into open colloidal crystals.[31,92] They showed that, by forming a tetrahedral cluster fluid in a first stage of assembly, crystallisation into tetrastack crystals is promoted by suppressing formation of 5- and 7-membered rings.[31] This is due to the fact that the tetrahedral clusters can only form chains of particles that are multiples of two, therefore, only even-membered rings can form in a monodisperse system of tetrahedral clusters.

1.4 | Colloidal Gels and Empty Liquids

While studies on the self-assembly of patchy particles have predominantly focused on the self-assembly of open crystals, there has also been interest in understanding their assembly into network liquids, or empty liquids – systems whose thermodynamic and structural properties originate from the formation of a random network mediated by directional interactions.[93–95] Much of the motivation for studying the formation of empty liquids using patchy particles originates from the desire to understand the properties of network liquids formed by molecular systems, in particular that of water.

Unlike systems with isotropic interactions (for instance, the noble gases or colloids interacting *via* depletion), which form *simple* liquids, systems where directional bonding mediates bonding between the building blocks can give rise to so-called *empty* liquids.[93,95] The use of patchy particles to study empty liquids was initiated by Bianchi *et al.*,[93] who investigated the phase behaviour of patchy particles, with varying number of patches, in order to probe the prospect of forming liquids with low volume fractions. They found that patchy

particles with low valence were able to form disordered structures, and that such a system could act as an avenue to forming persistent gel networks that are thermodynamically stable at low temperatures.

1.4.1 WATER AND ITS ANOMALIES

While the phrase "empty liquid" was first coined to describe liquid networks formed by patchy particle models, it has now become synonymous with a number of atomic and molecular liquids, in particular with water. Liquid water, while being the liquid which we all are most familiar with (due to its role as the elixir of life), seems to be the most complex of all liquids. The most famous of water's "quirks" is the fact that it expands upon cooling below 4°C, while most liquids simply gradually compress as they cool.[95–100] More generally, water displays anomalous behaviour in its thermodynamic response functions, such as the heat capacity, when cooled.[101] These thermodynamic response functions essentially measure the magnitude of the fluctuations of the internal properties of the liquid – such as the volume and enthalpy of the liquid. While the magnitude of the fluctuations in these properties steadily decrease upon cooling in simple liquids, they increase when liquid water is cooled below a certain temperature. This anomalous behaviour becomes more pronounced when water is supercooled (when a liquid is cooled below its freezing point without crystallising) and have been linked to the presence of a metastable liquid-liquid critical point in the supercooled region of its phase diagram.[101–104] This two liquid hypothesis suggests that a phase transition line separates two metastable liquid phases formed of transient hydrogen-bond networks – the low-density liquid and high-density liquid – and terminates at a liquid-liquid critical point.[102]

1.4.2 PATCHY PARTICLES THAT NEVER FREEZE

The idea that water's anomalies are due to a metastable liquid-liquid critical point has been a topic of controversy, with some suggesting that the liquid-liquid phase transition was actually a misinterpreted liquid-solid phase transition[103,105,106] and others suggesting that the phase transition is continuous and so no critical point exists.[107] The doubt over the validity of this hypothesis has been further compounded by the issues facing experiments with liquid water in the relevant region of the phase diagram – at such low temperatures and high pressures water crystallises too rapidly (it is, after-all, a metastable phase transition).[108] As a result of this controversy, Sciortino and coworkers looked to design a system that could unequivocally show that a liquid-liquid phase transition was possible.[81,109]

The first step was to mitigate the issues with crystallisation. Smallenburg and Sciortino[81] showed that patchy particles that can form extremely flexible bonds, but are still limited to forming only one bond per patch, never actually crystallise. These particles are able to form fully connected liquid networks (i.e., a liquid network where every particle has formed the maximum number of bonds possible) and so the liquid phase is iso-energetic with the crystalline phases. However, while there is only one way to form a particular crystal structure, the liquid phase represents an ensemble of random fully connected networks. As a result, the liquid phase is lower in free energy than the crystal phases due to having an additional configurational entropy contribution.

They followed up this work with a second study that exploited this ability of patchy particles with flexible patches to form thermodynamically stable empty liquids in which they designed a model system of tetrahedral particles that displays a liquid-liquid phase transition and critical point.[109] It is important to stress that the empty liquids formed by these patchy particles are equilibrium phases, and are not dynamically arrested structures as is the case with a glassy system and some colloidal gels.[81,110]

1.5 Aim and Objectives

In this introduction we have briefly covered the application of patchy particles to study the self-assembly of open crystals and empty liquids. The overarching goal of this thesis was to build on this past work and push the frontiers of programmed self-assembly of open crystals and empty liquids. To this end, the objectives of this thesis are as follows:

1. to design colloidal patchy particles that hew to current experimental capabilities and are capable of self-assembling into 3D open crystals that support wide PBGs;

2. to establish a colloidal model system for liquid water that is able to reproduce supercooled water's thermodynamic anomalies and liquid-liquid phase transition;

3. to identify what microscopic features fundamentally distinguish the two liquid phases of supercooled water.

This thesis is organised as follows: Chapter 2 provides an overview of the key methods underpinning the body of work presented in this thesis. Chapter 3 presents the programmed self-assembly of the rod-connected diamond structure. In Chapter 4 we demonstrate the facile crystallisation of colloidal diamond by tetrahedral patchy particles through the introduction of ring selection rules. Chapter 5 presents the use of patchy particles as a colloidal analogue to water and their suitability to study the liquid-liquid phase transition of supercooled water. Additionally, we introduce a novel order-parameter that reveals the topological nature of the liquid-liquid phase transition. Chapter 6 introduces rectangular patchy particles and explores their self-assembly behaviour in the quest for a chiral photonic crystal. Finally, Chapter 7 concludes with a summary of the results presented in this thesis and an outlook for future work.

CHAPTER 2

THEORY AND METHODOLOGY

In the physical and applied sciences, we are often interested in the macroscopic behaviour of systems consisting of many interacting particles. However, models describing such systems are few and far between and usually cannot be solved analytically. There are only a few example systems that can be solved in such a manner (*e.g.*, the ideal gas or the two-dimensional Ising model[111]). It is here that computer simulations play a key role in providing "almost exact" results for otherwise unsolvable problems. In a computer simulation we try to represent the real world using a model for the system we wish to study. Additionally, we tell the computer which physical laws must be obeyed and the thermodynamic conditions that we are interested in (*i.e.*, pressure, temperature, density). We then perform a "simulated experiment", where we let the computer calculate how our system evolves in time, and we make measurements of the quantities of interest.[112,113]

Simulations can therefore act as a bridge between experiments and theory, and they are particularly useful for predicting the properties of existing or new materials. Computer simulations can also be used to predict new phenomena, which can stimulate new experiments and the development of new theories, for instance the freezing transition of hard spheres.[11,12] In this section we outline the theory which underpins our simulations, as well as the methods developed into the software used to generate the results. In particular, we focus on Monte Carlo methods used in this thesis to study the equilibrium properties of our colloidal systems.

2.1 THE POTENTIAL ENERGY SURFACE

In this thesis we look to model systems of colloidal particles and investigate their self-assembly. Due to their size, we can treat colloidal particles as classical bodies and so we may write the Hamiltonian $\mathcal{H}$ for a system of N colloidal particles as the sum of the kinetic and potential energy functions of the set of momenta $\{\mathbf{p}_i\}$ and coordinates $\{\mathbf{q}_i\}$, respectively. We choose to adopt the condensed notation:

$$q^N = (\mathbf{q}_1, \mathbf{q}_2, ..., \mathbf{q}_N); \quad p^N = (\mathbf{p}_1, \mathbf{p}_2, ..., \mathbf{p}_N) \tag{2.1}$$

Then we can write the Hamiltonian as:

$$\mathcal{H}(p^N, q^N) = \mathcal{K}(p^N) + \mathcal{V}(q^N) \tag{2.2}$$

We can take the kinetic energy to be of the form:

$$\mathcal{K}(p^N) = \sum_{i=1}^{N} \frac{\mathbf{p}_i^2}{2m_i} \tag{2.3}$$

where m_i is the mass of particle i. Depending on the system, the generalised coordinates q^N may simply be the set of Cartesian coordinates $r^N \equiv \{\mathbf{r}_i\}$ for each particle. However, in order to completely capture the interactions between particles in our model, we may also require a set of variables $\Omega^N \equiv \{\mathbf{\Omega}_i\}$ that specify the orientation of the particles. The potential energy function $\mathcal{V}$ captures how the particles interact with one another. We model a system of colloidal particles using a pairwise additive potential energy function:

$$\mathcal{V}(q^N) = \sum_{i=1}^{N-1} \sum_{j>i}^{N} v(q_{ij}) \tag{2.4}$$

where $v(q_{ij})$ is the pairwise interaction and q_{ij} defines the relative geometry of particles i and j. For instance, in the simple case where the potential energy is simply a function of Cartesian coordinates this would be the centre-to-centre separation between particles i and j, $r_{ij} = |\mathbf{r}_{ij}| = |\mathbf{r}_i - \mathbf{r}_j|$. The potential energy function defines a Nd surface, where d is the number of geometric degrees of freedom for the system of interest. This "potential energy surface" (PES) forms the underpinning of a number of computational frameworks which we can use to understand what drives self-assembly. Stationary points on the PES are defined as regions where the gradient vanishes:

$$\nabla \mathcal{V}(q^N) = 0, \quad \text{where } \nabla \equiv \left(\frac{\partial}{\partial q_1}, \cdots, \frac{\partial}{\partial q_{dN}} \right) \tag{2.5}$$

Additionally, we define the internal forces acting on particle i due to all other particles in the system as:

$$\boldsymbol{\mathcal{F}}_i = \sum_{j \neq i} \boldsymbol{\mathcal{F}}_{ij}(q_{ij}) = -\sum_{j \neq i} \nabla_i v(q_{ij}) \tag{2.6}$$

Therefore, stationary points correspond to configurations of the system where the total force acting on the system is zero (otherwise known as mechanical equilibrium), with local minima corresponding to configurations which are mechanically stable (*i.e.*, the system will relax back to such a configuration following any small perturbation). The lowest-lying minima correspond to likely candidates for the thermodynamically most stable structure, and so identifying these minima can provide valuable insight into the system under investigation.

2.1.1 IDENTIFYING LOCAL MINIMA — GEOMETRY OPTIMISATION

The most commonly used methods to locate local minima on the PES exploit the fact that we only need to search in the directions where $\mathcal{V}$ is decreasing. This is easy to do as we can simply follow $\boldsymbol{\mathcal{F}}$ along the PES until we reach a minimum. Given an initial configuration q_0^N, these gradient based optimisation algorithms iteratively update the coordinates of the system along a search direction, $\boldsymbol{d}$, that points towards a local minimum, and then determine how far in that direction to move. We define a general update scheme for these algorithms as: $q_{k+1}^N = q_k^N + \alpha_k \boldsymbol{d}_k$, where k denotes the step iteration, α_k is the step-length, and each step should satisfy the condition: $\mathcal{V}(q_{k+1}^N) < \mathcal{V}(q_k^N)$. We therefore require $\boldsymbol{d}_k$ to be a *descent direction*, meaning that $\boldsymbol{d}_k \cdot \mathbf{g}_k < 0$, where $\mathbf{g}_k = \nabla\mathcal{V}(q_k^N)$, as this guarantees that $\mathcal{V}(q_k^N)$ can be reduced along this direction. We can break down these search methods into three steps: (i) *compute the step-length*; (ii) *compute the step direction*; (iii) *update the coordinates of the system.* This process is repeated until a termination condition is satisfied. The step length α_k is a positive scalar that is usually computed in such a way as to give a considerable decrease in $\mathcal{V}(q_k^N)$, but not require too much computational time. This gives rise to what are known as *inexact line search* methods, where an α_k that satisfies certain sufficient descent conditions is identified.

Different gradient based optimisation algorithms are characterised according to the nature of the search direction used. Here we use Nocedal's limited memory Broyden-Fletcher-Goldfarb-Shanno algorithm (L-BFGS). This algorithm uses a quasi-Newton approach, where the first and the second derivatives of the potential energy function are used to define a local approximation to the PES using Taylor's theorem:

$$\mathcal{V}_{k+1}(\boldsymbol{d}_k) \equiv \mathcal{V}(q_k^N + \boldsymbol{d}_k) \approx \mathcal{V}(q_k^N) + \boldsymbol{d}_k^{\mathrm{T}}\mathbf{g}_k + \tfrac{1}{2}\boldsymbol{d}_k^{\mathrm{T}}\mathbf{H}_k\boldsymbol{d}_k \tag{2.7}$$

where, $\mathbf{H}_k$ is the Hessian matrix, a square matrix of partial second derivatives:

$$\mathbf{H} = \begin{bmatrix} \dfrac{\partial^2 \mathcal{V}}{\partial q_1^2} & \dfrac{\partial^2 \mathcal{V}}{\partial q_1 \partial q_2} & \cdots & \dfrac{\partial^2 \mathcal{V}}{\partial q_1 \partial q_{dN}} \\ \vdots & \vdots & \ddots & \vdots \\ \dfrac{\partial^2 \mathcal{V}}{\partial q_{dN} \partial q_1} & \dfrac{\partial^2 \mathcal{V}}{\partial q_{\mathrm{n}} \partial q_2} & \cdots & \dfrac{\partial^2 \mathcal{V}}{\partial q_{dN}^2} \end{bmatrix} \tag{2.8}$$

Differentiating Eqn. (2.7) with respect to the step direction we get:

$$\nabla \mathcal{V}_{k+1}(\boldsymbol{d}_k) = \mathbf{g}_k + \mathbf{H}_k \mathbf{d}_k \tag{2.9}$$

When $\nabla \mathcal{V}(q_k^N + \boldsymbol{d}_k) = 0$ we have a stationary point, and so solving Eqn. (2.9) gives us the Newton-Raphson step:

$$\mathbf{d}_k = -\mathbf{H}_k^{-1} \mathbf{g}_k \tag{2.10}$$

If the PES is quadratic, only a single update is required to find the minimum. However, the PES is rarely quadratic and so multiple steps are often required to reach a minimum. Computing the Hessian at each iteration will be computationally expensive. Instead, methods that use an approximation of the Hessian – quasi-Newton methods – are employed. The search direction for quasi-Newton methods can be generally defined as:

$$\boldsymbol{d}_k = -\boldsymbol{B}_k^{-1} \mathbf{g}_k \tag{2.11}$$

where $\boldsymbol{B}_k$ is a symmetric and positive definite matrix. For each set of new coordinates,

q^N_{k+1}, we generate a new quadratic model of the PES that takes the form:

$$E_{k+1}(\boldsymbol{d}_k) = \mathcal{V}(q^N_k) + \boldsymbol{d}_k \cdot \mathbf{g}_{k+1} + \tfrac{1}{2}\boldsymbol{d}_k \cdot \boldsymbol{B}_k \boldsymbol{d}_k \tag{2.12}$$

To ensure that this new model is valid we require that the gradient of E_{k+1} is the same as that of the true PES for the last two iterates q^N_k and q^N_{k+1}. The second condition can be written as $\nabla E_{k+1}(\mathbf{0}) = \mathbf{g}_{k+1}$, and so is automatically satisfied, and the first condition is the same as setting $\boldsymbol{d}_k$ to be the negative of the displacement from the previous iteration:

$$\nabla E_{k+1}(-\alpha_k \boldsymbol{d}_k) = \mathbf{g}_{k+1} - \alpha_k \boldsymbol{B}_{k+1}\boldsymbol{d}_k = \mathbf{g}_k \tag{2.13}$$

By rearranging, we get:

$$\boldsymbol{C}_{k+1}\mathbf{y}_k = \mathbf{s}_k \tag{2.14}$$

where $\boldsymbol{B}_k^{-1} = \boldsymbol{C}_k$, $\mathbf{s}_k = \alpha_k, \boldsymbol{d}_k = q^N_{k+1} - q^N_k$ and $\mathbf{y}_k = \mathbf{g}_{k+1} - \mathbf{g}_k$. These are the *secant conditions*, and they ensure that $\boldsymbol{C}_{k+1}$ behaves, at least, like the Hessian at q^N_k and q^N_{k+1}. We want any potential approximation to the Hessian to satisfy the secant conditions. Additionally, we impose the constraint that $\boldsymbol{C}_{k+1}$ must be a symmetric and positive definite matrix. Then to determine $\boldsymbol{C}_{k+1}$ uniquely, we impose one final condition: $\min_{\boldsymbol{C}} \|\boldsymbol{C} - \boldsymbol{C}_k\|$ where $\|\cdot\|$ is the weighted Frobenius norm. This condition simply states that out of all possible symmetric matrices that satisfy the secant condition, $\boldsymbol{C}_{k+1}$ is the one which is closest to the current matrix $\boldsymbol{C}_k$. The unique solution to all of these conditions is then:

$$\boldsymbol{C}_{k+1} = (\boldsymbol{I} - \rho_k \cdot \mathbf{s}_k \otimes \mathbf{y}_k) \cdot \boldsymbol{C}_k \cdot (\boldsymbol{I} - \rho_k \cdot \mathbf{y}_k \otimes \mathbf{s}_k) + \rho_k \mathbf{s}_k \otimes \mathbf{s}_k \tag{2.15}$$

where $\rho_k = 1/\mathbf{y}_k \cdot \mathbf{s}_k$ and $\otimes$ represents the dyadic product between two vectors. This is known as the BFGS step, named after its discoverers Broyden, Fletcher, Goldfarb and

Shanno. A complete discussion regarding the derivation and the convergence properties of the BFGS method can be found in Ref. [114]. There is no special definition for $\boldsymbol{C}_0$ which works in all cases, and it is often easiest to simply set it to be the identity matrix. Rather than storing the full $N \times N$ Hessian, we can implicitly represent the matrix by saving a certain number, m, of the vectors $\mathbf{s}_i$ and $\mathbf{y}_i$, from which the product $\boldsymbol{C}_k \cdot \mathbf{g}_k$ can be calculated. After each iteration of the algorithm the oldest set of vectors $\{\mathbf{s}_i, \mathbf{y}_i\}$ is replaced by those calculated from the current step, $\{\mathbf{s}_k, \mathbf{y}_k\}$. This way the approximation to the Hessian contains the curvature information from the m most recent steps. This is known as the limited-memory BFGS (L-BFGS) method.[114]

2.1.2 BASIN-HOPPING GLOBAL OPTIMISATION

Ideally, we would be able to identify all local minima on the PES for a given system. However, the number of minima grows exponentially with the number of dimensions dN of the PES. Instead, we concern ourselves only with the lowest energy minima, and in particular, the global minimum, as these are the configurations most likely to have a dominant contribution to the equilibrium properties of the system. In order to find the lowest-lying structures on the PES we must couple the local minimisation algorithm with some way of searching the PES: we call this a *global optimisation algorithm*. Throughout this thesis we make use of one such strategy – basin-hopping global optimisation – for the identification of global minima.[115] We define a basin as a region of the PES associated with a local minimum such that optimisation from any point in the basin gives the same local minimum. The PES can be deformed into a function of its basins so as to produce a new potential energy function, $\widetilde{\mathcal{V}}(q^N)$, that resembles a step function. The energy of the global minimum is unchanged and the relative energies of the local minima are also unchanged. This transformed PES is given by the complete set of local minima on the

original PES:

$$\widetilde{\mathcal{V}}(q^N) = \left\{ \min_{q^N} \mathcal{V}(q^N) \right\} \tag{2.16}$$

Combining this transformation with a search strategy is known as basin-hopping global optimisation.[116] We use a search strategy based on Monte-Carlo sampling (see Section 2.2.1) with the acceptance probability of each random step given by the Metropolis criterion, $\exp(-\beta\Delta\mathcal{V})$, where $\beta = 1/k_{\mathrm{B}}T$, T is a fictitious temperature and k_{B} is Boltzmann's constant. The basin-hopping optimisation algorithm involves the following steps:

1. Starting from an initial configuration with energy $\mathcal{V}_{\mathrm{old}}$, randomly perturb the system to obtain a new configuration.

2. Minimise this new configuration to obtain $\mathcal{V}_{\mathrm{new}}$.

3. If $\mathcal{V}_{\mathrm{new}} < \mathcal{V}_{\mathrm{old}}$, accept the step. Otherwise, the new minimum is accepted or rejected based on the Metropolis criterion.

4. If the new configuration is accepted, $\mathcal{V}_{\mathrm{old}} = \mathcal{V}_{\mathrm{new}}$.

5. Return to Step 1 for a preset number of iterations. A record of the lowest minima visited is kept.

In order to properly search the PES the coordinates of the system are randomly perturbed at each iteration of the algorithm. Each perturbation should be a uniform step in that parameter space, and so it necessary to account for the differences in translational, rotational and lattice parameters during this step.[116,117] It is important to note that the temperature T is fictitious, with no physical meaning. It is used solely to control the acceptance probability of the Metropolis criterion,[118] where the optimal value for T would depend on the topography of the landscape.

2.2 | MONTE CARLO METHODS

Global optimisation allows us to predict candidate structures that are likely to be responsible for any observed equilibrium properties, at low temperatures, for our systems of interest. However, it does not allow us to sample and evaluate the aforementioned equilibrium properties of the identified low energy configurations. Following their initial development at the end of the Second World War (to study the diffusion of neutrons in fissionable material) Monte Carlo (MC) methods have become the standard technique by which to study systems at thermal equilibrium in soft matter and statistical physics.

2.2.1 THE METROPOLIS METHOD

We begin by considering a classical system of N indistinguishable particles, where a microscopic state (or microstate) of the system is characterised by a point in *phase space* – a state specified by listing the coordinates and momenta of all the classical degrees of freedom of the system:

$$(\mathbf{q}_1, \mathbf{q}_2, ..., \mathbf{q}_N; \mathbf{p}_1, \mathbf{p}_2, ..., \mathbf{p}_N) = (q^N, p^N)$$
$$= \text{point in phase space for an } N \text{ particle system.}$$

The particles are contained within a cell, and periodic boundary conditions are employed (*i.e.*, if a particle passes the boundaries defined by the cell, it will appear at the opposite face to which it left). The Hamiltonian describing such a system is given by:

$$\mathcal{H}(p^N, q^N) = \sum_{i=1}^{N} \frac{\mathbf{p}_i^2}{2m} + \mathcal{V}(q^N) \tag{2.17}$$

where m_i is the mass of the particles. The canonical partition function, $\mathcal{Q}(N,V,T)$, represents the total number of accessible microstates for a system with a fixed number of particles N, volume V and temperature T. We write down the classical partition function for a system of particles described by Eqn. 2.17 as:

$$\mathcal{Q}(N,V,T) = \frac{1}{h^{dN}N!}\int \mathrm{d}p^N \mathrm{d}q^N \mathrm{e}^{-\beta\mathcal{H}(p^N,q^N)} \tag{2.18}$$

where $\beta = 1/k_\mathrm{B}T$ (k_B is the Boltzmann constant), h is some constant with the dimensions of momentum times length, d is the number of degrees of freedom possessed by each particle and the factor of $N!$ is included to account for the possible permutations of indistinguishable particles.[112,119] The probability of a state in such a system is $f(p^N,q^N)\mathrm{d}p^N\mathrm{d}q^N$, where $f(p^N,q^N)$ is the probability distribution for observing the system at some point in phase space. From statistical mechanics we can derive this probability distribution to be:

$$f(p^N,q^N) = \frac{\mathrm{e}^{-\beta\mathcal{H}(p^N,q^N)}}{\int \mathrm{d}p^N \mathrm{d}q^N \mathrm{e}^{-\beta\mathcal{H}(p^N,q^N)}} \tag{2.19}$$

Usually we are concerned with calculating equilibrium properties of the system. The equilibrium value of some mechanical observable A can be expressed as an ensemble average given by:

$$\langle A\rangle = \frac{\int \mathrm{d}p^N \mathrm{d}q^N \mathrm{e}^{-\beta\mathcal{H}(p^N,q^N)} A(p^N,q^N)}{\int \mathrm{d}p^N \mathrm{d}q^N \mathrm{e}^{-\beta\mathcal{H}(p^N,q^N)}} \tag{2.20}$$

In general, we cannot directly evaluate the integrals in Eqn. 2.20 using standard numerical integration techniques. However, the integration over momenta can be performed analytically using $\int \exp(-ax^2)\mathrm{d}x = \sqrt{\pi/a}$, giving:

$$\int \mathrm{d}p^N \exp\left[-\beta\left(\sum_{i=1}^{N}\frac{\mathbf{p}_i^2}{2m}\right)\right] = \left(\frac{2\pi m}{\beta}\right)^{dN/2} \tag{2.21}$$

where d is the dimensionality of the system. Therefore, the difficulty, and use of MC simulations, lies in computing the averages of properties which depend on the coordinates of the particles, $X(q^N)$, such as energy or pressure. As such we denote the configurational partition function, $\mathcal{Z}(N,V,T)$, of a system as:

$$\mathcal{Z}(N,V,T) = \frac{1}{h^{dN}N!}\int \mathrm{d}q^N \mathrm{e}^{-\beta\mathcal{V}(q^N)} \tag{2.22}$$

Eqn. 2.20 can then be re-written as:

$$\langle X\rangle = \frac{\int \mathrm{d}q^N \mathrm{e}^{-\beta\mathcal{V}(q^N)} X(q^N)}{\int \mathrm{d}q^N\, \mathrm{e}^{-\beta\mathcal{V}(q^N)}} \tag{2.23}$$

Rather than evaluating each integral in Eqn. 2.23, we can directly calculate the ratio of two integrals. One may be tempted to think we can evaluate Eqn. 2.23 simply by generating a random sequence of configurations of length l, $\{q_1^N,\, q_2^N,\, \cdots,\, q_l^N\}$, and rewriting the ensemble average as:

$$\langle X\rangle = \lim_{l\to\infty} \frac{\sum_{i=1}^{l} \mathrm{e}^{-\beta\mathcal{V}(q_i^N)} X(q_i^N)}{\sum_{i=1}^{l} \mathrm{e}^{-\beta\mathcal{V}(q_i^N)}} \tag{2.24}$$

However, this is often not a viable method as the Boltzmann factor, $\exp(-\beta\mathcal{V})$, will almost always equal zero. A much better method becomes apparent if we notice that the probability distribution of finding the system at some point in configuration space is:

$$f_c(q^N) \equiv \frac{\mathrm{e}^{-\beta\mathcal{V}(q^N)}}{\int \mathrm{d}q^N \mathrm{e}^{-\beta\mathcal{V}(q^N)}} \tag{2.25}$$

If we are able to generate configurations in such a way that the probability of generating some configuration q_i^N is proportional to its Boltzmann weight, $\exp[-\beta\mathcal{V}(q_i^N)]$, then the

ensemble average can be re-written as:

$$\langle X \rangle = \lim_{n\to\infty} \frac{\sum_{i=1}^{n} X(q_i^N)}{n} \tag{2.26}$$

This means that although we cannot calculate the absolute probability of visiting a particular state q_i^N, we can calculate the relative probability of visiting particular configurations. This way of sampling configurations is the underlying principle of the Metropolis method.[118]

In general, Metropolis Monte Carlo algorithms make use of a *Markov chain* – a sequence of trials where the system evolves from state to state, with the outcome of each trial depending only on the outcome of the preceding trial. Consider a system of N particles starting in an initial state $o \equiv q_o^N$ with a (non-zero) Boltzmann weight $\exp[-\beta\mathcal{V}(o)]$. This is our first link in the Markov chain. Now we generate a new *trial* state $n \equiv q_n^N$ (for instance by randomly moving one particle) whose Boltzmann weight is $\exp[-\beta\mathcal{V}(n)]$. If we accept this new state then the next link in our Markov chain will be q_n^N, otherwise it will be q_o^N (*i.e.*, two neighbouring links in the chain can correspond to the same state). Once the system relaxes to an equilibrium distribution of states, average properties of the system are then calculated as averages over the elements of the Markov chain using Eqn. 2.26. To ensure that the system does eventually reach equilibrium, we devise an acceptance criterion which satisfies the conditions of *detailed balance* – in equilibrium the average number of accepted trial moves leaving state o to state n is equal to the average number of accepted trial moves leaving state n to state o. This can be written as:

$$f_c(o) \times \pi(o \to n) = f_c(n) \times \pi(n \to o) \tag{2.27}$$

where $\pi(o \to n)$ denotes the probability of transitioning from state o to n, which can be split into two components: the probability $\alpha(o \to n)$ to perform a trial move from o to n,

and the probability $\mathrm{acc}(o \to n)$ of accepting a trial move from state o to n:

$$\pi(o \to n) = \alpha(o \to n) \times \mathrm{acc}(o \to n) \tag{2.28}$$

A similar set of statements can be made for $\pi(n \to o)$. In the Metropolis algorithm we choose α such that it represents a symmetric probability matrix, which means the probability of proposing a trial move from o to n and from n to o are equal (*i.e.*, $\alpha(o \to n) = \alpha(n \to o)$). Taking this into consideration and rearranging Eqn. 2.27:

$$\frac{\mathrm{acc}(o \to n)}{\mathrm{acc}(n \to o)} = \frac{f_c(n)}{f_c(o)} = \mathrm{e}^{-\beta\left(\mathcal{V}(n)-\mathcal{V}(o)\right)} \tag{2.29}$$

We ensure α is symmetric by randomly displacing randomly chosen particles. There are multiple choices for $\mathrm{acc}(o \to n)$ which satisfy Eqn. 2.29, but Metropolis *et al.*,[118] chose:

$$\mathrm{acc}(o \to n) = \begin{cases} f_c(n)/f_c(o) & \text{if } f_c(n) < f_c(o) \\ 1 & \text{otherwise} \end{cases} \tag{2.30}$$

This can be alternatively written down as:

$$\mathrm{acc}(o \to n) = \min\left\{1, \mathrm{e}^{-\beta\left(\mathcal{V}(n)-\mathcal{V}(o)\right)}\right\} \tag{2.31}$$

where $\min(a,b) = a$ when $a < b$, and b otherwise. This means that new configurations with lower energy are always accepted, and new configurations that increase the energy of the system are accepted with a certain probability that depends of the difference in energy with the previous state in the Markov chain and the temperature. In practice, for each trial move, we generate a random number u, from a uniform distribution in the interval $[0,1)$. Then, if $u < \mathrm{acc}(o \to n)$ we accept the move, otherwise we reject it.

We are now left with deciding how to generate trial states. So far we have discussed the coordinates of the particles in a general way. We will consider particles which are fully described by translational and orientational coordinates. By translational coordinates, $\mathbf{r}^N$, we are referring to the particle's centre of mass, which is described by a set of Cartesian coordinates $\mathbf{r}$. The displacement of some particle i is achieved by the addition of a random vector to its centre of mass:

$$\mathbf{r}_{i,n} = \mathbf{r}_{i,o} + \Delta_{\max}\mathbf{v} \tag{2.32}$$

where $\Delta_{\max}$ defines the maximum possible displacement to each component of the centre of mass and $\mathbf{v}$ is a vector whose components are uniformly generated on the interval [-1,1]. If we are simulating particles with anisotropic interaction potentials, or rigid bodies, we must also generate trial moves we alter the particle orientations. Orientational moves require more care than translational moves as we must ensure trial moves are generated in such a way so as to satisfy the symmetry requirement of the Markov chain imposed by detailed balance. Rotational coordinates, $\mathbf{\Omega}^N$, encode the orientation of the particles, which can be expressed as a rotation with respect to some fixed frame of reference. There are multiple ways of performing rigid body rotations, by far the most straightforward method is with rotation matrices. However, it is not particularly convenient to express the orientaional coordinates of the particles using rotation matrices. In this work we represent the orientations of the particles using quaternions, which we then convert to a rotation matrix as and when we need to perform a rotation. Unit quaternions can be thought of as a unit vector in four-dimensional space:

$$\mathbf{a} = (a_0, a_1, a_2, a_3) \quad \text{with} \quad a_0^2 + a_1^2 + a_2^2 + a_3^2 = 1 \tag{2.33}$$

We define quaternion multiplication as:

$$\mathbf{a} \otimes \mathbf{b} = (a_0 b_0 - \mathbf{a} \cdot \mathbf{b},\ a_0 \mathbf{b} + b_0 \mathbf{a} + \mathbf{a} \times \mathbf{b}) \tag{2.34a}$$

$$= \begin{pmatrix} a_0 & -a_1 & -a_2 & -a_3 \\ a_1 & a_0 & -a_3 & a_2 \\ a_2 & a_3 & a_0 & -a_1 \\ a_3 & -a_2 & a_1 & a_0 \end{pmatrix} \begin{pmatrix} b_0 \\ b_1 \\ b_2 \\ b_3 \end{pmatrix} \tag{2.34b}$$

It is possible to directly rotate some vector $\mathbf{e}$, expressed as a pure quaternion: $\mathbf{e} = (0, \mathbf{e})$, by a unit quaternion using the equation:

$$\mathbf{e}' = \mathbf{a} \otimes \mathbf{e} \otimes \mathbf{a}^{-1} \quad \text{with } \mathbf{a}^{-1} = (a_0, -a_1, -a_2, -a_3) \tag{2.35}$$

We can rewrite this equation, using Eqn. 2.34b, in the form: $\mathbf{e}' = \mathbf{R}^{\mathrm{T}} \cdot \mathbf{e}$, where $\mathbf{R}$ is a rotation matrix defined in terms of a unit quaternion:

$$\mathbf{R} = \begin{pmatrix} a_0^2 + a_1^2 - a_2^2 - a_3^2 & 2(a_1 a_2 + a_0 a_3) & 2(a_1 a_3 - a_0 a_2) \\ 2(a_1 a_2 - a_0 a_3) & a_0^2 - a_1^2 + a_2^2 - a_3^2 & 2(a_2 a_3 + a_0 a_1) \\ 2(a_1 a_3 + a_0 a_2) & 2(a_2 a_3 - a_0 a_1) & a_0^2 - a_1^2 - a_2^2 + a_3^2 \end{pmatrix} \tag{2.36}$$

It is possible to define a rotation by an angle θ about an arbitrary axis, defined by a unit vector, $\hat{\mathbf{n}}$ in terms of a unit quaternion:

$$\mathbf{c} = \left(\cos\frac{\theta}{2},\ \hat{\mathbf{n}} \sin\frac{\theta}{2} \right) \tag{2.37}$$

Therefore, given a particle whose orientation is defined by the quaternion $\mathbf{a}$, a trial orienta-

tional move can be constructed as:

$$\mathbf{a}' = \mathbf{a} \otimes \mathbf{c} \tag{2.38}$$

where the rotation axis is a uniformly sampled random unit vector[120,121] and θ is uniformly generated on the interval $[-\theta_{\max}, \theta_{\max}]$, with $\theta_{\max} \leq \pi/2$.

While the moves we have outlined so far facilitate the movement and equilibration of particles, it is worth restating that these moves are purely stochastic in nature. This means that there is no explicit measure of time in Monte Carlo simulations, instead we usually expresses the simulation "time" in terms of the number of Monte Carlo cycles performed. Additionally, unlike molecular dynamics simulations, there is no need for the moves to be physically realistic. And so, there is the question of whether Monte Carlo simulations can be used to capture the realistic dynamics of particle systems. It has been shown that, if the Monte Carlo simulation is restricted to only consist of physically meaningful moves (for instance, small single particle displacements) Monte Carlo produces trajectories equivalent to those produced by Brownian dynamics.[122,123] Therefore, as long as the move sets are appropriately chosen, Monte Carlo simulations can be used for simulating dynamical processes and to quantitatively measure translational and rotational diffusion.[122–126]

2.2.2 Isothermal-Isobaric Ensemble

We have just described the Metropolis MC algorithm scheme in the canonical (*NVT*) ensemble. However, the MC method can easily be adapted to study systems in different ensembles. Another commonly employed ensemble is the isothermal-isobaric (*NPT*) ensemble, where a fixed pressure *P* is specified instead of a fixed volume *V*. Importantly, it is often convenient to use MC simulations in the *NPT* ensemble to study phase transitions,

as at constant pressure (given sufficient time) the system is able to completely transform into the state of lowest Gibbs free energy. However, at constant *NVT* the system may be at a density where it would prefer to phase separate. When discussing a system in the isothermal-isobaric ensemble it is convenient use scaled coordinates $\mathbf{s}^N$ defined as:

$$\mathbf{r}_i = L\mathbf{s}_i \tag{2.39}$$

where we have assumed our simulation cell is a cubic box of volume $V = L^3$ (however, this is easily extended to consider arbitrary parallelepipeds). The partition function can then be written as:

$$\mathcal{Q}(N,P,T) = \frac{\beta P}{h^{dN}N!}\int \mathrm{d}V \mathrm{e}^{-\beta PV} V^N \int \mathrm{d}\mathbf{s}^N \mathrm{d}\boldsymbol{\Omega}^N \mathrm{e}^{-\beta \mathcal{V}(\mathbf{s}^N;L,\boldsymbol{\Omega}^N)} \tag{2.40}$$

MC simulations performed in the *NPT* ensemble simply treat V as an additional coordinate of the system for which we construct trial moves. Just as we did for the canonical ensemble, we can define a probability distribution of finding the system at some point in phase space:

$$f(\mathbf{s}^N;V,\boldsymbol{\Omega}^N) \propto \mathrm{e}^{-\beta PV} V^N \mathrm{e}^{-\beta \mathcal{V}(\mathbf{s}^N;L,\boldsymbol{\Omega}^N)} \tag{2.41a}$$

$$= \mathrm{e}^{N\ln(V)-\beta PV-\beta \mathcal{V}(\mathbf{s}^N;L,\boldsymbol{\Omega}^N)} \tag{2.41b}$$

Assuming volume trial moves involve an attempted change in volume from V_o to $V_n = V_o + \delta V$, where δV is a uniformly sampled random number in the interval $[-\delta V_{\max}, \delta V_{\max}]$, the Metropolis criterion becomes:

$$\mathrm{acc}(V_o \to V_n) = \min\left\{1, \mathrm{e}^{N\ln(V_n/V_o)-\beta P\Delta V-\beta\Delta\mathcal{V}}\right]\right\} \tag{2.42}$$

where $\Delta\mathcal{V} = \mathcal{V}(n) - \mathcal{V}(o)$ and $\Delta V = \delta V = V_n - V_o$. Alternatively, one may wish to perform trial moves in the logarithm of the volume such that:[112,127]

$$\ln(V_n) = \ln(V_o) + \delta V = \ln(V_o + \Delta V) \tag{2.43}$$

These trial moves would be equally valid; however, the acceptance criterion becomes:[112,127]

$$\mathrm{acc}(V_o \rightarrow V_n) = \min\left\{1, \mathrm{e}^{(N+1)\ln(V_n/V_o) - \beta P\Delta V - \beta\Delta\mathcal{V}}\right\} \tag{2.44}$$

where N in Eqn. 2.42 has been replaced by $(N+1)$. To clarify, MC simulations in the *NPT* ensemble involve trial moves where the coordinates of the particles are changed, which make use of Eqn. 2.31. Additionally, trial moves where the volume of the system is altered are also attempted, here Eqns. 2.42 or 2.47 are used. In our simulations, for each trial move, there is a $1/N$ probability of performing a volume move instead of a particle move.

2.2.3 CLUSTER MOVE MONTE CARLO

A major issue with the simulation of strongly interacting systems is that, at low temperatures, particles aggregate into clusters which diffuse extremely slowly through the simulation cell. In this case, standard MC moves may be inadequate at sampling configuration space, preventing the system from reaching equilibrium. In order to combat this issue we can introduce "cluster moves", where we define a cluster as a group of particle coordinates which are altered collectively by a single MC move (*i.e.*, the intra-cluster interactions do not change). We must therefore specify a rule for generating clusters, which provides us with the probability that particles i and j are bonded (*i.e.*, belong to same cluster) with probability $\mathrm{P}(i,j)$ and are disconnected with probability $1 - \mathrm{P}(i,j)$. This rule must ensure that $\mathrm{P}(i,j)$ is unchanged following a cluster move, regardless of whether

either particle belongs to the cluster under consideration. The detailed balance condition requires that:

$$\mathrm{e}^{-\beta\mathcal{V}(o)}\prod_{i,j}\left[1-\mathrm{P}_o(i,j)\right]\mathrm{acc}(o\to n)=\mathrm{e}^{-\beta\mathcal{V}(n)}\prod_{i,j}\left[1-\mathrm{P}_n(i,j)\right]\mathrm{acc}(n\to o) \tag{2.45}$$

The Metropolis criterion for a cluster move then becomes:

$$\mathrm{acc}(o\to n)=\min\left\{1,\mathrm{e}^{-\beta\left(\mathcal{V}(n)-\mathcal{V}(o)\right)}\prod_{i,j}\frac{1-\mathrm{P}_n(i,j)}{1-\mathrm{P}_o(i,j)}\right\} \tag{2.46}$$

In this work we are mostly concerned with the hierarchical self-assembly of colloidal particles, which goes via two stages. In the first stage we form a phase of discrete clusters of a specific geometry, for instance tetrahedra. In the second stage these clusters act as effective particles which then aggregate to form extended structures. Since we know a priori what kind of clusters will form in our systems, we can construct a simple rule to move the discrete clusters. We take $\mathrm{P}(i,j)=1$ if the particles satisfy some geometric conditions based on their relative distance and orientations, otherwise $\mathrm{P}(i,j)=0$. It should be clear that any cluster moves where $\mathrm{P}_o(i,j)=0$ and $\mathrm{P}_n(i,j)=1$ (or vice versa) will be rejected. As a result, these cluster moves will not able to alter the total number of particles in a cluster, and so we combine these cluster moves with single particle moves.

Alternatively, we could have used the virtual move Monte Carlo (VMMC)[128,129] algorithm, which has been used to great effect for systems of patchy particles.[92,130,131] In VMMC, $\mathrm{P}(i,j)$ does not only take values of 0 and 1 and instead clusters are built by recursively adding particles to the cluster with a probability that depends on the difference in energy of the cluster move with and without the particle in the cluster. This makes VMMC a much more general approach to including cluster moves in a Monte Carlo simulation, and can be applied to study a diverse range of systems where aggregation takes

place.[130,132–136] However, it is much more expensive from a computational perspective and so we use the simplified cluster move scheme outlined above.

Additionally, in *NPT* simulations, we will include one volume move, on average, per cycle where we scale the positions of the particles in tandem with the simulation cell. If we are simulating a system where discrete clusters are forming, we would like to displace particles as clusters during the volume move. Therefore, rather than scaling the positions of the particles individually, we first identify all clusters in the system and compute their centre of mass. We then scale the position of clusters centre of mass during the volume moves and move the particles associated with each cluster accordingly. Cluster volume moves were accepted with probability:[137]

$$\mathrm{acc}(V_o \to V_n) = \min\left\{1, \mathrm{e}^{(N_{\mathrm{clstr}}+1)\ln(V_n/V_o)-\beta(P\Delta V+\Delta\mathcal{V})}\prod_{i,j}\frac{1-\mathrm{P}_n(i,j)}{1-\mathrm{P}_o(i,j)}\right\} \tag{2.47}$$

where N_{clstr} is the number of discrete clusters identified in the system.

2.3 | FREE ENERGY METHODS

A major application of computer simulations is to predict the phase behaviour of a given system of particles. In fact, one of the initial discoveries by Monte Carlo simulations was the existence of a fluid-solid transition for a system of hard spheres in 1957.[12] Since then, various methods have been developed to study phase transitions through the computation of free energies. The Helmholtz free energy is defined as:

$$F(N,V,T) = -k_{\mathrm{B}}T\ln\mathcal{Z}(N,V,T) \tag{2.48a}$$

$$= -k_{\mathrm{B}}T\ln\left(\frac{\int \mathrm{d}q^N \mathrm{e}^{-\beta\mathcal{V}(q^N)}}{h^{dN}N!}\right) \tag{2.48b}$$

In principle, we could determine the free energy by directly evaluating the integral in Eqn. 2.48b. However, we have already stated that this is intractable (except for a few trivial cases such as the ideal gas or Einstein crystal). Instead, we are able to calculate free energy differences via a set of methods referred to collectively as thermodynamic integration.

2.3.1 THERMODYNAMIC INTEGRATION

Thermodynamic integration exploits standard thermodynamic relations, such as:

$$\left(\frac{\partial F}{\partial V}\right)_{N,T} = -P \tag{2.49a}$$

or (2.49b)

$$\left(\frac{\partial (F/T)}{\partial T}\right)_{N,V} = -\frac{\mathcal{V}}{T^2} \tag{2.49c}$$

to calculate the free energy difference between two states/systems connected by a reversible thermodynamic pathway. Assuming that the free energy of one of the states/systems is already known and can act as a reference, the free energy of the other state/system can then be determined. For a closed system, with a fixed number of particles, two thermodynamic variables are required to define the state of the system (*e.g.*, P and T or V and T). When performing thermodynamic integration, we keep one of the pair of thermodynamic variables constant and integrate over the other. If the Helmholtz free energy is known at a reference density $\rho_1 = N/V_1$, the free energy at another density $\rho_2 = N/V_2$ can be obtained via a reversible path at constant temperature. The free energy for state 2 can be calculated using:[138]

$$\frac{F(\rho_2,T)}{Nk_\mathrm{B}T} = \frac{F(\rho_1,T)}{Nk_\mathrm{B}T} + \frac{1}{k_\mathrm{B}T}\int_{\rho_1}^{\rho_2} \left\langle \frac{P(\rho)}{\rho^2} \right\rangle_\rho \mathrm{d}\rho \tag{2.50}$$

The integrand can be calculated using a series of *NVT* simulations, where the equilibrium pressure can be determined for each density studied using the virial expression for pressure. Similarly, we could integrate along an isochore by varying the temperature and keeping the density fixed. Here, the free energy for state 2 can be calculated using:

$$\frac{F(T_2,V)}{Nk_\mathrm{B}T_2} = \frac{F(T_1,V)}{Nk_\mathrm{B}T_1} - \int_{T_1}^{T_2} \left\langle \frac{\mathcal{V}(T)}{Nk_\mathrm{B}T^2} \right\rangle_T \mathrm{d}T \tag{2.51}$$

which again can be easily evaluated via *NVT* simulations.

2.3.2 HAMILTONIAN INTEGRATION

In simulations, we are not limited to using a physically realistic thermodynamic integration path. We can evaluate the free energy of a system of interest by coupling it to a reference system with a known free energy. We construct a new Hamiltonian, $\mathcal{H}'$, by combining our original Hamiltonian $\mathcal{H}$ with the reference Hamiltonian $\mathcal{H}_\mathrm{ref}$, whose contributions are scaled by a coupling parameter λ:[39,139]

$$\mathcal{H}'(\lambda) = (1-\lambda)\mathcal{H} + \lambda\mathcal{H}_\mathrm{ref} \tag{2.52}$$

We can see that when $\lambda = 0$ we recover our Hamiltonian of interest, and when $\lambda = 1$ we obtain the reference Hamiltonian for which the free energy is known. We can then express the partition function for a system interacting via our new Hamiltonian as a function of the coupling parameter:

$$\mathcal{Q}(N,V,T,\lambda) = \frac{1}{h^{dN}N!}\int \mathrm{d}p^N \mathrm{d}q^N \mathrm{e}^{-\beta\mathcal{H}'(\lambda)} \tag{2.53}$$

The derivative of the Helmholtz free energy with respect to the coupling parameter can be written as:

$$\begin{aligned}\left(\frac{\partial F(\lambda)}{\partial \lambda}\right)_{N,V,T} &= -\frac{\partial}{\partial \lambda}\frac{\ln \mathcal{Q}(N,V,T,\lambda)}{\beta} \\ &= \frac{\int \mathrm{d}p^N \mathrm{d}q^N (\partial \mathcal{H}'(\lambda)/\partial \lambda)\mathrm{e}^{-\beta \mathcal{H}'(\lambda)}}{\int \mathrm{d}p^N \mathrm{d}q^N \mathrm{e}^{-\beta \mathcal{H}'(\lambda)}} \\ &= \left\langle \frac{\partial \mathcal{H}'(\lambda)}{\partial \lambda} \right\rangle_{\lambda}\end{aligned} \tag{2.54}$$

We can then calculate the free energy of the system of interest by integrating Eqn. 2.54:

$$F(N,V,T) = F_{\mathrm{ref}}(N,V,T) - \int_{\lambda=0}^{\lambda=1} \mathrm{d}\lambda \left\langle \frac{\partial \mathcal{H}'(\lambda)}{\partial \lambda} \right\rangle_{N,V,T,\lambda} \tag{2.55}$$

2.3.3 EINSTEIN CRYSTAL METHOD: FREE ENERGY OF SOLIDS

We use the Einstein crystal method to determine the free energy for crystal structures of interest.[39,140] This method has been applied to study a vast range of systems, such as hard spherocylinders,[141,142] molecular models of water,[143,144] and patchy colloidal particles,[31,65,72,145] just to name a few. In this method, the free energy of a crystal structure, F, can be obtained by computing the free energy changes along a path from a reference crystal with known free energy, F_{ref}, to the crystal structure of interest, involving three steps:

$$F = F_{\mathrm{ref}} + \Delta F_1 + \Delta F_2 + \Delta F_3 \tag{2.56}$$

Here F_{ref} is the free energy of the reference ideal Einstein crystal with fixed centre of mass (COM). ΔF_1 corresponds to the free energy difference between the interacting Einstein crystal and the ideal Einstein crystal, each having a fixed COM. There are no interparticle interactions in an ideal Einstein crystal, in which the particles are bound to their lattice

positions and orientations by a harmonic potential of the form:

$$\mathcal{V}_{\text{ref}}(\kappa_{\text{tr}}, \kappa_{\text{or}}) = \mathcal{V}_{\text{ref}}^{\text{tr}}(\kappa_{\text{tr}}) + \mathcal{V}_{\text{ref}}^{\text{or}}(\kappa_{\text{or}}) \tag{2.57}$$

where κ_{tr} and κ_{or} are the spring constants of the translational and orientational harmonic fields, which have units of ε/σ^2 and ε, respectively (with ε being the unit of energy and σ the unit of length). The free energy change in the second step (ΔF_2) involves gradually reducing the spring constants for the interacting Einstein crystal to obtain the crystal structure of interest, while retaining the fixed COM. Finally, ΔF_3 gives the free energy difference in the third step in which the constraint of fixed COM is relaxed. A detailed discussion of the method is given in Ref. [146]. The translational component of the reference potential energy is

$$\mathcal{V}_{\text{ref}}^{\text{tr}} = \kappa_{\text{tr}} \sum_{i=1}^{N} (|\boldsymbol{r}_i - \boldsymbol{r}_{i,0} - \Delta\boldsymbol{r}_{\text{cm}}|)^2 \tag{2.58}$$

where N is the number of particles in the system, $\boldsymbol{r}_i$ is the centre of mass of particle i, $\boldsymbol{r}_{i,0}$ is its reference position and $\Delta\boldsymbol{r}_{\text{cm}}$ is the accumulated drift of the COM. In practice, we do not explicitly fix the COM, but instead update $\Delta\boldsymbol{r}_{\text{cm}} \to \Delta\boldsymbol{r}_{\text{cm}} + \delta\boldsymbol{r}_i/N$ each time a particle i moves by $\delta\boldsymbol{r}_i$, where we assume particles have equal masses.[112] Over the course of a simulation, when a particle at a distance of $\Delta\boldsymbol{r}_i = \boldsymbol{r}_i - \boldsymbol{r}_{i,0} - \Delta\boldsymbol{r}_{\text{cm}}$ from its reference site is displaced by $\delta\boldsymbol{r}$, the change in the reference energy can be directly computed using

$$\Delta\mathcal{V}_{\text{ref}}^{\text{tr}} = \kappa_{\text{tr}} \left(2\Delta\boldsymbol{r}_i \cdot \delta\boldsymbol{r}_i + \frac{N-1}{N} \delta\boldsymbol{r}_i^2 \right) \tag{2.59}$$

The free energy of the ideal Einstein crystal with fixed centre of mass is known analytically and is given by[39,112,146]

$$\frac{\beta F_{\text{ref}}^{\text{tr}}}{N} = -\frac{3}{2}\frac{N-1}{N}\ln\left(\frac{\pi}{\beta\kappa_{\text{tr}}\sigma^2}\right) - \frac{3}{2N}\ln N \tag{2.60}$$

where $\beta = 1/k_{\text{B}}T$, k_{B} is Boltzmann's constant and T is the temperature.

In this thesis we will consider particles that also have orientational degrees of freedom, and so we must also apply an orientational harmonic field, which couples the particles to their ideal orientations, $\mathcal{V}_{\text{Ein,or}}$. The exact form of the orientational field depends on the symmetry of the particles considered. The orientational component of the free energy of the ideal Einstein crystal can be written generally as

$$\frac{\beta F_{\text{ref}}^{\text{or}}}{N} = -\ln\left[\frac{1}{8\pi^2}\int_{-1}^{1}\mathrm{d}\cos\theta\int_0^{2\pi}\mathrm{d}\phi\int_0^{2\pi}\mathrm{e}^{-\beta v_{\text{ref}}^{\text{or}}}\mathrm{d}\chi\right] \tag{2.61}$$

Here θ, ϕ and χ are the Euler angles defining the orientation of the particle and $v_{\text{ref}}^{\text{or}}$ is the orientational Einstein field for a single particle. We will mostly be concerned with particles that have $\mathrm{C}_{\infty\text{v}}$ or $\mathrm{D}_{\infty\text{h}}$ symmetry. The orientational component of the free energy of the ideal Einstein crystal composed of particles with $\mathrm{C}_{\infty v}$ symmetry is given in Ref. [147] as:

$$\frac{F_{\text{Ein,or}}^{\mathrm{C}_{\infty\text{v}}}}{Nk_{\text{B}}T} = -\ln\left\{\frac{1-\mathrm{e}^{-2\beta\kappa_{\text{or}}}}{2\beta\kappa_{\text{or}}}\right\} \tag{2.62}$$

For an ideal Einstein crystal composed of particles with $\mathrm{D}_{\infty h}$ symmetry the orientational component of the free energy of the ideal Einstein crystal can be written as:[146]

$$\frac{F_{\text{Ein,or}}^{\mathrm{D}_{\infty\text{h}}}}{Nk_{\text{B}}T} = -\ln\left\{\frac{1}{4\pi}\int_{-1}^{1}\mathrm{d}\cos\theta\int_0^{2\pi}\mathrm{e}^{-\beta\kappa_{\text{or},a}\sin^2(\psi_a)}\mathrm{d}\phi\right\} \tag{2.63}$$

If we associate the angle ψ_a with the polar angle θ, we can simplify this integral into a one-dimensional problem:

$$\frac{F_{\mathrm{Ein,or}}^{\mathrm{D}_{\infty\mathrm{h}}}}{Nk_{\mathrm{B}}T} = -\ln\left\{\int_0^1 \mathrm{e}^{-\beta\kappa_{\mathrm{or},a}(x^2-1)}\mathrm{d}x\right\} \tag{2.64}$$

The integrals in Eqns. 2.61 and 2.64 can be evaluated numerically (in this thesis we use the VEGAS Monte Carlo integration technique).[146,148] Romano *et al.* reported that the values of $F_{\mathrm{Ein,or}}^{\mathrm{T_d}}/Nk_{\mathrm{B}}T$ as a function of $\kappa_{\mathrm{or}}/k_{\mathrm{B}}T$ are well described by a logarithmic function.[65] In Fig. 2.1 we show that this is also true for $\mathrm{D}_{\infty h}$ particles:

$$\frac{F_{\mathrm{Ein,or}}^{\mathrm{D}_{\infty\mathrm{h}}}}{Nk_{\mathrm{B}}T} = \quad 0.6921(2) + \ln\left(\beta\kappa_{\mathrm{or}}\right) \tag{2.65a}$$

$$\frac{F_{\mathrm{Ein,or}}^{\mathrm{T_d}}}{Nk_{\mathrm{B}}T} = \quad 0.4530(3) + \frac{3}{2}\ln\left(\beta\kappa_{\mathrm{or}}\right) \tag{2.65b}$$

The total free energy of the ideal Einstein crystal with fixed centre of mass is then

$$\frac{\beta F_{\mathrm{ref}}}{N} = -\frac{3}{2}\frac{N-1}{N}\ln\left(\frac{\pi}{\beta\kappa_{\mathrm{tr}}\sigma^2}\right) - \frac{3}{2N}\ln\left(N\right) + \frac{F_{\mathrm{Ein,or}}}{Nk_{\mathrm{B}}T} \tag{2.66}$$

We can now establish a path from the reference system to the systems of interest by coupling these system to the Einstein crystal using

$$\mathcal{V}'(\lambda) = \mathcal{V} + \lambda\mathcal{V}_{\mathrm{ref}} \tag{2.67}$$

where λ is the coupling parameter, and takes a value between zero and unity, and $\mathcal{V}$ is the potential energy of the system of interest (note that the COM is still fixed). We also note that under the constraint of a fixed COM we do not explicitly use periodic boundary

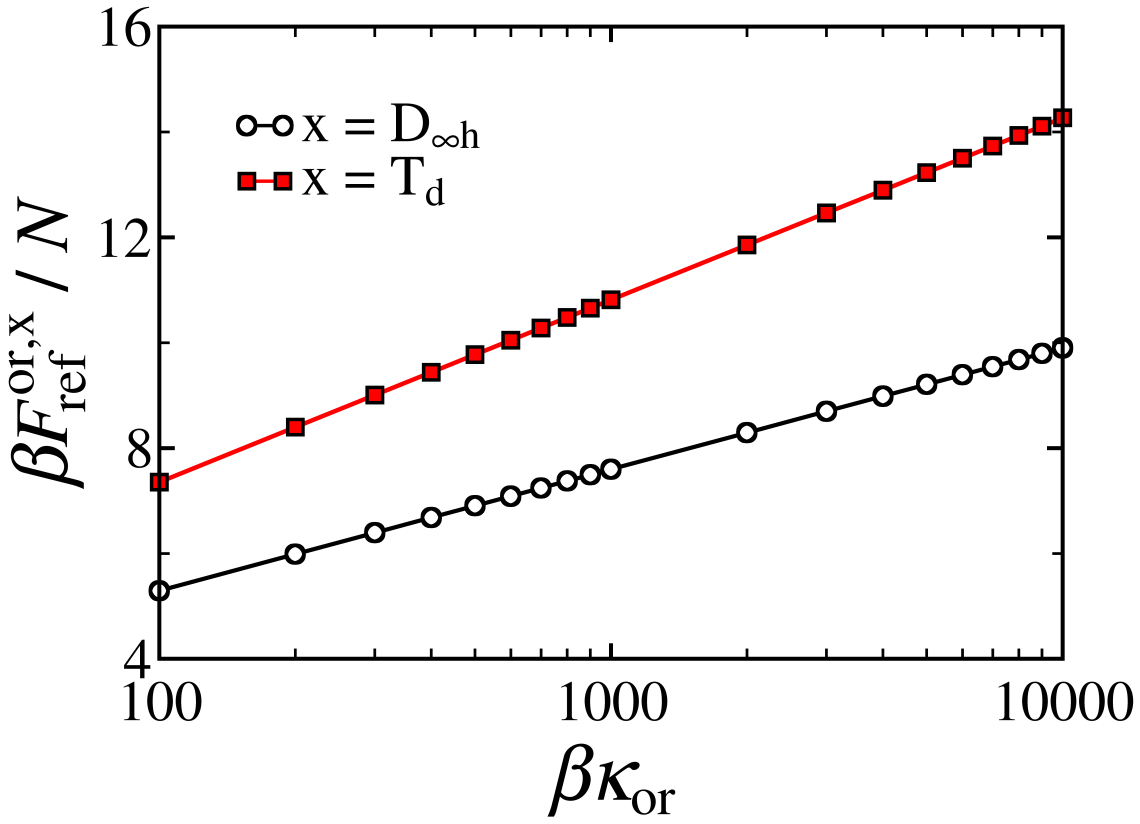


Figure 2.1: **Orientational reference free energy for particles with $D_{\infty h}$ and T_d symmetry.** Orientational reference free energy ($\beta F^{\mathrm{or}}_{\mathrm{ref}}/N$, where $\beta = 1/k_{\mathrm{B}}T$ and N is the number of particles) as a function of the orientational spring constant (κ_{or}) for particles with $D_{\infty h}$ and T_d symmetry. The lines represent fits to the following functions: $\beta F^{\mathrm{or,D_{\infty h}}}_{\mathrm{ref}}/N = a + \ln(\beta\kappa_{\mathrm{or}})$ and $\beta F^{\mathrm{or,T_d}}_{\mathrm{ref}}/N = b + \frac{3}{2}\ln(\beta\kappa_{\mathrm{or}})$, where $a = 0.692$ and $b = 0.453$.

conditions as this would cause a discontinuous change in the energy of Einstein crystal. However, when calculating pair potentials in the coupled system with fixed COM we can still use the minimum image convention to compute the distance between particles.

The first step along this path involves calculating the free energy difference between the reference Einstein crystal and the "fully" coupled system (*i.e.*, when $\lambda = 1$) using

$$\Delta F_1 = \mathcal{V}_{\mathrm{Latt}} - k_{\mathrm{B}}T \ln \left\langle \mathrm{e}^{-\beta(\mathcal{V}-\mathcal{V}_{\mathrm{Latt}})} \right\rangle_{\mathrm{ref}} \tag{2.68}$$

where $\mathcal{V}_{\text{Latt}}$ is the potential energy of the system of interest in the reference configuration and $\langle\cdot\rangle_{\text{ref}}$ denotes an ensemble average along a simulation for the reference system. The final step involves calculating the free energy difference between the fully coupled system and the system of interest. This free energy difference can be evaluated using

$$\Delta F_2 = -\int_{\ln(c)}^{\ln(\kappa_{\text{E}}+c)} \mathrm{d}\ln(\lambda\kappa_{\text{E}}+c)\left(\langle\mathcal{V}_{\text{ref}}^{\text{tr}}\rangle_{N,V,T,\lambda}+\eta\langle\mathcal{V}_{\text{ref}}^{\text{or}}\rangle_{N,V,T,\lambda}\right)\frac{\lambda\kappa_{\text{E}}+c}{\kappa_{\text{E}}} \tag{2.69}$$

where we have defined $\kappa_{\text{E}} = \kappa_{\text{tr}} = \kappa_{\text{or}}/\eta$, with η a multiplicative factor (with the units of σ^2) relating the translational and rotational spring constants, c is a user-selected constant and $\langle\cdot\rangle_{N,V,T,\lambda}$ denotes an ensemble average along a simulation for the coupled system defined in Eq. 2.67. Had the COM of the system not been fixed, then the integrand in Eq. 2.69 would diverge as $\lambda \to 0$ making the evaluation of the integral difficult. In order to complete the path from the reference system to the system of interest we must also account for the free energy difference between a crystal with fixed COM and a crystal with an unconstrained COM. This free energy difference is invariant to the details of the system being studied and can be simply defined as

$$\frac{\beta\Delta F_3}{N} = \frac{1}{N}\ln\left(\frac{N\sigma^3}{V}\right) \tag{2.70}$$

where V is the volume.

2.3.4 SCHILLING-SCHMID METHOD: FREE ENERGY OF FLUIDS

A similar method to the Einstein crystal method, which can also be applied to systems where the particles are freely diffusing – such as fluids – as well as crystals was developed by Schilling and Schmid.[149–151] In this approach, attractive potential wells are centred at each of the reference positions of the particles, and the translational component of the

reference potential energy is given by:[150]

$$\mathcal{V}_{\text{ref}}^{\text{tr}} = \kappa_{\text{tr}} \sum_{i=1}^{N} \min \left\{ \frac{|\boldsymbol{r}_i - \boldsymbol{r}_{i,0}|}{r_{\text{c}}} - 1, 0 \right\} \tag{2.71}$$

where r_{c} is the radius of the attractive potential well. The orientational field applied to particles with rotational degrees of freedom is the same as for the Einstein crystal method, and so the reference free energy for the orientational component of the reference system will also be same. The translational free energy of this new reference system is:[150]

$$\frac{\beta F_{\text{ref}}^{\text{tr}}}{N} = \ln(\rho\sigma^3) - 1 - \ln\left[1 + \frac{(4/3)\pi r_{\text{c}}^3}{V} g(\beta\kappa_{\text{tr}})\right] \tag{2.72}$$

where,

$$g(\beta\kappa_{\text{tr}}) = 3(\beta\kappa_{\text{tr}})^3(\mathrm{e}^{\beta\kappa_{\text{tr}}} - 1 - \beta\kappa_{\text{tr}} - (\beta\kappa_{\text{tr}})^2/2 - (\beta\kappa_{\text{tr}})^3/3) \tag{2.73}$$

The exponential in the expression for $g(\beta\kappa_{\text{tr}})$ can be challenging to compute numerically for large κ_{tr}, and so it is useful to use an approximate expression for the reference free energy in this case:[151]

$$\frac{\beta F_{\text{ref}}^{\text{tr}}(\kappa_{\text{tr}} \gg 1)}{N} \approx \ln(\rho\sigma^3) - 1 - \kappa_{\text{tr}} - \ln\left(\frac{(4/3)\pi r_{\text{c}}^3}{V} \frac{6}{\kappa_{\text{tr}}^3}\right) \tag{2.74}$$

In principle, we can proceed exactly as before with the Einstein crystal method and compute the free energy of the system of interest using: $F = F_{\text{ref}} + \Delta F_1 + \Delta F_2$, where ΔF_3 no longer contributes as the COM of the system is not fixed when using the Schilling-Schimd method. While ΔF_1 can be computed exactly as before for the Einstein crystal method, it becomes convenient to subtract the reference free energy from ΔF_2 before evaluating the integral, as the integrand diverges at large λ.[151] Therefore, in order to subtract the reference free energy from the integrand we must first compute the derivative of the reference free energy

with respect to κ_{tr}:

$$h(\kappa_{\mathrm{tr}}) = \frac{\partial \beta F_{\mathrm{ref}}^{\mathrm{tr}}/N}{\partial \kappa_{\mathrm{tr}}} = \frac{3\frac{(4/3)\pi r_{\mathrm{c}}^3}{V}\left[6+2\mathrm{e}^{\kappa_{\mathrm{tr}}}(-3+\kappa_{\mathrm{tr}})+4\kappa_{\mathrm{tr}}+\kappa_{\mathrm{tr}}^2\right]}{\kappa_{\mathrm{tr}}\left[-\kappa_{\mathrm{tr}}^3+\frac{(4/3)\pi r_{\mathrm{c}}^3}{V}(6-6\mathrm{e}^{\kappa_{\mathrm{tr}}}+6\kappa_{\mathrm{tr}}+3\kappa_{\mathrm{tr}}^2+\kappa_{\mathrm{tr}}^3)\right]} \tag{2.75}$$

and

$$h(\kappa_{\mathrm{tr}} \gg 1) \approx \frac{3}{\kappa_{\mathrm{tr}}} - 1 \tag{2.76}$$

We can now rewrite the integral as:

$$\begin{aligned}\frac{\beta(\Delta F_2 + F_{\mathrm{ref}})}{N} = &-\int_{\ln(c)}^{\ln(\kappa_{\mathrm{E}}+c)} \mathrm{d}\ln(\lambda\kappa_{\mathrm{E}}+c) \\ &\left[\frac{\beta}{N}\left(\langle\mathcal{V}_{\mathrm{ref}}^{\mathrm{tr}}\rangle_{N,V,T,\lambda} + \eta\langle\mathcal{V}_{\mathrm{ref}}^{\mathrm{or}}\rangle_{N,V,T,\lambda}\right) - h(\beta\lambda\kappa_{\mathrm{E}}+c)\right]\frac{\lambda\kappa_{\mathrm{E}}+c}{\kappa_{\mathrm{E}}} \\ &+\ln(\rho\sigma^3) - 1 + \frac{\beta F_{\mathrm{Ein,or}}}{N}\end{aligned} \tag{2.77}$$

Finally, when performing Monte Carlo simulations to compute ΔF_1 and ΔF_2, we include additional swap moves (*i.e.*, moves where the potential well associated with one particle is swapped with another).[149,151] Note that this means that particles are indistinguishable (a key difference from the Einstein crystal method) which has been accounted for when computing the reference free energy.

2.4 | STRUCTURE CHARACTERISATION AND ORDER PARAMETERS

Here we outline the key order-parameters used through this thesis to follow cluster formation and crystallisation in systems of interest.

2.4.1 TETRAHEDRAL ORDER PARAMETER

In Chapters 3 and 5, we investigate the hierarchical self-assembly of triblock patchy particles, where the particles form a tetrahedral cluster fluid in a first stage of assembly. In these systems we identified tetrahedral clusters using the local order parameter, q_{Td}, defined as:[152]

$$q_{\mathrm{Td}} = 1 - \frac{3}{8}\sum_{i=1}^{N_c-1}\sum_{j=i+1}^{N_c}\left(\cos\psi_{ij} + \frac{1}{3}\right)^2 \tag{2.78}$$

where $N_c = 4$ is the number of particles in the cluster under consideration, ψ_{ij} is the angle subtended at the centre of the cluster by the two vectors joining the centre of particle i and particle j. $q_{\mathrm{Td}} = 1$ for a perfect tetrahedron. We identified a set of neighbours for each particle i using a cut-off for the radial distance of $d_c = 1.3$ between any pair including i. q_{Td} was then calculated for all distinct combinations of four particles including i from this set. All unique sets of four particles satisfying the condition of $q_{\mathrm{Td}} > 0.99$, were considered to form a tetrahedron.

2.4.2 STEINHARDT BOND ORDER PARAMETERS

In order to identify crystalline particles, we used the Steinhardt bond-orientational order-parameters (BOOPs):[153,154]

$$q_{lm}(i) = \frac{1}{N_{\mathrm{B}}}\sum_{j=1}^{N_{\mathrm{B}}(i)} Y_{lm}(\mathbf{r}_{ij}) \tag{2.79}$$

where N_{B} is the number of first nearest-neighbours of particle i, $\mathbf{r}_{ij}$ is the vector connecting the centres of particles i and j and Y_{lm} is the spherical harmonic with total angular momentum l and projection $-l \leq m \leq l$.

The global orientational order parameters are defined as:

$$Q_{lm} = \frac{\sum_{i \in N} N_{\mathrm{B}}(i) q_{lm}(i)}{\sum_{i \in N} N_{\mathrm{B}}(i)} \tag{2.80}$$

We can then define the rotationally invariant global order parameter as:

$$Q_l = \sqrt{\frac{4\pi}{2l+1} \sum_{m=-l}^{l} |Q_{lm}|^2} \tag{2.81}$$

Which value of l should be chosen depends on the system of interest, and the crystal structure that is expected to be formed. In general, we use Q_4 or Q_6 in this thesis to distinguish between liquid-like and solid phases.

In addition to this global order-parameter, the translational-order correlation parameter $d_l(i,j)$ was used to directly count the number of solid particles in a crystalline system.[41] This analysis is based on the complex vectors given by Eq. 2.79, in terms of which the translational-order correlation between the particles is defined as:[30,41,109,155]

$$d_l(i,j) = \mathrm{Re}\left(\frac{\mathbf{q}_l(i) \cdot \mathbf{q}_l^*(j)}{|\mathbf{q}_l(i)||\mathbf{q}_l(j)|} \right) \tag{2.82}$$

where the $*$ indicates the complex conjugate and $\mathbf{q}_l(i) \cdot \mathbf{q}_l^*(j) = \sum_{m=-l}^{l} q_{lm}(i) \cdot q_{lm}^*(j)$. In this analysis, $d_l(i,j)$ is used to determine whether the local environments of particles i and j are sufficiently similar, and hence share a crystalline bond. Those particles which possess a certain threshold number of crystalline bonds are labelled as *crystalline*.

2.5 | PHOTONIC CRYSTALS AND THE PHOTONIC BAND GAP

Our key motivation for investigating the self-assembly of colloidal open crystals is their application as PBG materials. We are therefore interested in computing the photonic band structures of our crystals of interest. In this section, we briefly introduce some of the key concepts required to understand how photonic band structures are computed and the emergence of a PBG.

2.5.1 PLANE WAVE EXPANSION METHOD

In this thesis we make a number of assumptions regarding the response of our crystals of interest to electromagnetic waves. Namely, we assume our photonic crystals of interest are to be composed of linear and isotropic materials. Additionally, we ignore any frequency dependence of the materials. Instead, we use dielectric constants in our calculations that are realistic for colloidal particles interacting with visible light. Having made these assumptions, to investigate the response of photonic crystals to electromagnetic waves we start with the Helmholtz equation which can be derived from Maxwell's equations:[26]

$$\nabla \times \frac{1}{\varepsilon(\mathbf{r})} \nabla \times \mathbf{H}(\mathbf{r}) = \frac{\omega^2}{c^2} \mathbf{H}(\mathbf{r}). \tag{2.83}$$

where $\mathbf{H}(\mathbf{r})$ is an eigenmode corresponding to spatial distribution of the magnetic field, ω is the corresponding angular frequency, $\varepsilon(\mathbf{r})$ is the dielectric function for a non-uniform medium, $\mathbf{r}$ corresponds to some point in the unit cell and c is the vacuum speed of light. The equation is derived from Maxwell's equations, for a thorough derivation and discussion of this equation and where it comes from see Ref. [26]. The Helmholtz equation is an eigenvalue equation with $(\omega/c)^2$ being the eigenvalue and $\nabla \times \varepsilon(\mathbf{r})^{-1} \nabla \times$ the operator, which is Hermitian and positive-definite if $\varepsilon(\mathbf{r})$ is real and positive. Thus,

the same principles applied in quantum mechanics to compute electronic band structures can be applied here. The only difference is that a transversality condition is enforced ($\nabla \cdot \mathbf{H}(\mathbf{r}) = 0$) to ensure eigenmodes with free magnetic charges are forbidden.[26]

The dielectric function describes the spatial distribution of the materials that make up the photonic crystal. Since the photonic crystal is a 3D periodic structure with a unit cell defined by a set of primitive lattice vectors $\mathbf{a}_i$ where $i = 1,2,3$, the dielectric function is also periodic $\varepsilon(\mathbf{r}) = \varepsilon(\mathbf{r} + \mathbf{a}_i)$. Due to this periodicity, Bloch's theorem can be used to expand the eigenmodes in the Helmholtz equation as a Fourier series over reciprocal lattice vectors:[55,156–158]

$$\mathbf{H}_{\boldsymbol{k}}(\mathbf{r}) = \left(\sum_{\mathbf{G}} \mathbf{h}_{\boldsymbol{k}}(\mathbf{G}) \mathrm{e}^{i\mathbf{G}\cdot\mathbf{r}}\right) e^{i\boldsymbol{k}\cdot\mathbf{r}} \tag{2.84}$$

where $\mathbf{G} = \sum_{j=1}^{3} m_i \mathbf{b}_j$ is a reciprocal lattice vector obtained from the primitive reciprocal lattice vectors $\mathbf{b}_j$ and the integers m_j, $\boldsymbol{k}$ is a Bloch wavevector and $\mathbf{h}_k(\mathbf{G})$ are the Fourier coefficients for an envelope function with the same periodicity of the crystal. The inverse dielectric function can also be expanded in a similar fashion:

$$\frac{1}{\varepsilon(\mathbf{r})} = \sum_{\mathbf{G}} \eta(\mathbf{G}) \mathrm{e}^{i\mathbf{G}\cdot\mathbf{r}} \tag{2.85}$$

Substituting $\mathbf{G} = \mathbf{G}' - \mathbf{G}$ into Eqns. 2.84 and 2.85, we are able to rewrite Eqn. 2.83 as an eigenvalue problem in reciprocal space:[158]

$$-\sum_{\mathbf{G}} \eta(\mathbf{G}' - \mathbf{G})(\boldsymbol{k} + \mathbf{G}') \times \left((\boldsymbol{k} + \mathbf{G}) \times \mathbf{h}_{n,\boldsymbol{k}}(\mathbf{G})\right) = \frac{\omega_{n,\boldsymbol{k}}^2}{c^2} \mathbf{h}_{n,\boldsymbol{k}}(\mathbf{G}') \tag{2.86}$$

Solving Eqn. 2.86 for a given wavevector will give us the set of eigenfrequencies $\{\omega_{n,\boldsymbol{k}}\}$, where $\omega_{0,\boldsymbol{k}} \leq \omega_{1,\boldsymbol{k}} \leq \omega_{2,\boldsymbol{k}}, \ldots$ and n is the band index.[26] We therefore have a discrete

eigenfrequency spectrum for each $\boldsymbol{k}$ (much like how the energy levels of 'the particle in a box' are quantized or how a rigidly held string has an infinite number of normal modes). We expect the frequency to vary continuously with $\boldsymbol{k}$ for a given n, and so we say that each family of continuous functions $\{\omega_n(\boldsymbol{k})\}$ form bands, which collectively form the photonic band structure.

Equation 2.86 represents an infinite system of linear equations, and so the set of wavevectors and reciprocal lattice vectors must be limited in some way. It is possible to show that due to the symmetries of crystal we need only consider wavevectors in the irreducible Brillouin zone of the crystal – a region of the first Brillouin zone which contains wavevectors that are not related by the symmetry of the crystal.[156,157] However, since we are primarily concerned with identifying PBGs we are able to further limit the set of wavevectors we consider when solving Eqn. 2.86. The minima and maxima of a given band (which determine the existence of a PBG) usually appear at the edges of the Brillouin zone.[26] As a result, band structures are usually computed only for wavevectors that lie on the edge of the irreducible Brillouin zone.[26]

We can then solve Eqn. 2.86 numerically by truncating the sum over the reciprocal lattice vectors and disregarding reciprocal lattice vectors that have a magnitude larger than some cutoff value $|\mathbf{G}_{\max}|$ under the assumption that they have a negligible contribution to the Fourier coefficients of the eigenmodes.[158] In this thesis we compute photonic band structures using the MIT Photonic Bands (MPB) package,[159] which uses an iterative solver utilising the conjugate gradient method to determine the eigenmodes of Maxwell's equations.

2.5.2 ORIGIN OF THE PBG

The opening of a PBG in photonic crystals is understood to be due to an interplay between macroscopic Bragg scattering and the Mie resonances of the individual scattering centres. Here we briefly outline the these two mechanisms.

Bragg Scattering Mechanism

The physical origin of a PBG can be easily understood by considering the multilayer film, where we have a structure of alternating dielectric constant, ε_1 and ε_2, such that $\varepsilon_1 > \varepsilon_2$. The unit cell of this one-dimensional crystal contains two "particles", one of each dielectric material, and has a length of a. We can extend this conceptual crystal into a 3D structure by considering the particles to be slabs of infinite height and width, but of depth $a/2$. We align the slabs so that the crystal has continuous translational symmetry in the x-y plane, and discrete translational symmetry along the z-axis. As the crystal only has periodicity along the z-axis, our problem is one-dimensional (1D) as we only have a single non-zero primitive lattice vector, $\mathbf{a} = (0,0,a)$, and primitive reciprocal lattice vector, $\mathbf{b} = (0,0,2\pi/a)$. We also only consider electromagnetic waves with wave vectors aligned with the z-axis, $\boldsymbol{k} = (0,0,k)$ (*i.e.*, the direction of the waves is perpendicular to the surface of the slabs). Due to the 1D nature of the problem we can express our eigenmodes as

$$\mathbf{E}(z) = \mathbf{e}(z)\mathrm{e}^{ikz}. \tag{2.87}$$

In 1D the Bragg condition, $(\boldsymbol{k}+\mathbf{G})^2 = k^2$, for the diffraction of a wave becomes:

$$k = \pm\frac{1}{2}G = \pm\frac{n\pi}{a}, \tag{2.88}$$

where, $G = 2\pi n/a$ is a reciprocal lattice vector and $n \in \mathbb{Z}$. Therefore, electromagnetic waves with wave vectors $k = \pm\pi/a$ will be reflected, creating two standing waves

$$\mathbf{E}_+(z) \propto e^{i\pi z/d} + e^{-i\pi z/d} = 2\cos(\pi z/a)$$
$$\text{and} \tag{2.89}$$
$$\mathbf{E}_-(z) \propto e^{i\pi z/d} - e^{-i\pi z/d} = 2i\sin(\pi z/a).$$

The standing waves are labelled (+) or (-) according to whether or not they change sign when z is replaced by -z. We see in Figure 2.2 that the $\mathbf{E}_+(z)$ mode is more concentrated in the higher dielectric region than $\mathbf{E}_-(z)$. Therefore, due to Eqn. (2.90), the $\mathbf{E}_+(z)$ mode will have a lower frequency than the $\mathbf{E}_-(z)$ mode. We refer to the bands associated with the two modes as the lower "dielectric" band and higher "air" band, and the size of the band gap increases as the dielectric contrast increases.[160]

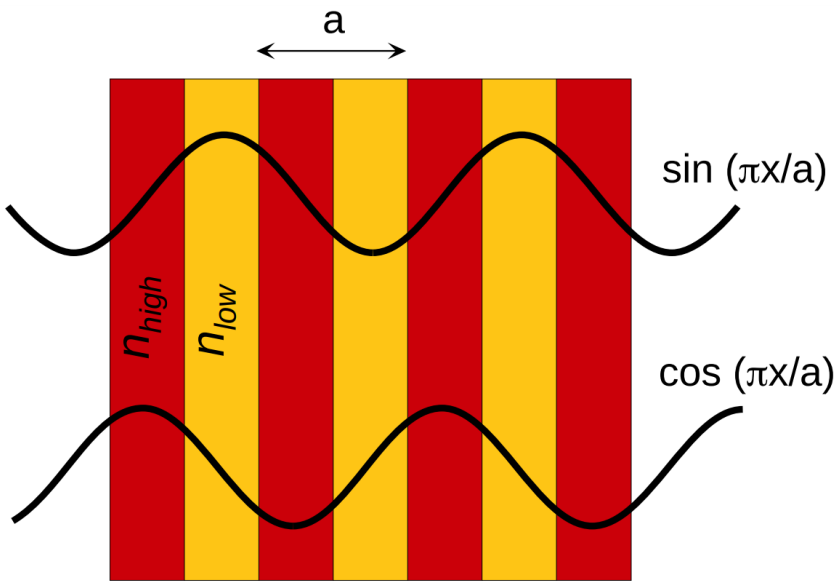


Figure 2.2: **Cartoon depicting the origin of the band gap in a multilayer film**. The pair of degenerate $k = \pm\pi/a$ planewaves split into $\cos(\pi x/a)$ and $\sin(\pi x/a)$ standing waves due to the periodicity of the film. The former has electric-field peaks in the high dielectric region (n_{high}) and so lies at a lower frequency than the latter (which peaks in the low dielectric region). Adapted from Ref. [161]

We can understand how this gives rise to the existence of a PBG by considering the electromagnetic variational theorem, which states that the lowest eigenfrequency mode has a field pattern that minimises the Rayleigh quotient U_f:[26,159,160]

$$U_f(\mathbf{H}) = \frac{\int \mathrm{d}^3\mathbf{r}|\nabla \times \mathbf{E}(\mathbf{r})|^2}{\int \mathrm{d}^3\mathbf{r}\ \varepsilon(\mathbf{r})|\mathbf{E}(\mathbf{r})|^2}. \tag{2.90}$$

Therefore, the lowest-frequency eigenmodes concentrate their electric energy in the high dielectric regions to maximise $\int \mathrm{d}^3\mathbf{r}\ \varepsilon(\mathbf{r})|\mathbf{E}(\mathbf{r})|^2$ and minimise their spatial oscillations to minimise $\int \mathrm{d}^3\mathbf{r}|\nabla \times \mathbf{E}(\mathbf{r})|^2$. We know that the modes with $n > 1$ are also constrained to be orthogonal to the lower bands from the variational theorem:[26]

$$\langle \mathbf{H}_{m,\boldsymbol{k}}, \mathbf{H}_{n,\boldsymbol{k}} \rangle = \langle \mathbf{E}_{m,\boldsymbol{k}}, \varepsilon(\mathbf{r})\mathbf{E}_{n,\boldsymbol{k}} \rangle = 0, \quad m < n \tag{2.91}$$

Therefore, band gaps arise (between adjacent bands) as the dielectric bands will be more concentrated in the high dielectric regions and so the air bands are forced into the low dielectric regions due to the orthogonality constraint. Additionally, lower frequency bands will, generally, have smaller spatial oscillations, when compared to higher frequency bands. We see that the PBG opens up at the edge of the Brillouin zone ($\omega = \pi c/a$) for the one-dimensional photonic crystal. We could, therefore, also expect to open up a band gap for 3D photonic crystals if the edge of the Brillouin zone has the same magnitude in all directions, corresponding to a spherical Brillouin zone. However, there is no 3D crystal with a perfectly spherical Brillouin zone and so stop gaps in different directions do not usually overlap perfectly with one another. However, if the dielectric contrast is large enough then it is possible to make these different gaps wide enough so that there is some overlap in frequency ranges, thus, giving rise to a complete PBG. The fcc lattice

has a Brillouin zone that is almost spherical (it is a truncated octahedron) and so the cubic diamond and tetrastack structures are very good candidates for a structures with a 3D PBG. It has also been suggested that in order to maximise the band gap, the crystal should be composed of high dielectric particles that have a thin vein-like shape along which the electric field lines can traverse. This means that the lowest bands can be strongly confined to the high dielectric region, whereas the upper bands are moved to higher frequency as the particles will be unable to accommodate multiple orthogonal modes (except for two orthogonal polarisations).[26,162]

Mie Scattering Mechanism

We have just explained the existence of PBGs in terms of Bragg scattering of plane waves. However, for the Bragg condition to be met, and for standing waves to form, the reciprocal lattice of the structure must have delta function like peaks (*i.e.*, it must be crystalline). This might suggest that amorphous dielectric materials are unable to possess a complete PBG. However, this is not the case. Therefore, Bragg scattering is not necessarily the only mechanism at play when considering the opening of a PBG in dielectric media.

The general solution to Maxwell's equations for an isolated sphere of arbitrary radius and refractive index was given in 1908 by Gustav Mie, who developed the theory to explain the scattering of light by small colloidal gold particles suspended in water.[163] A full description of Mie theory is beyond the scope of this thesis (the reader is instead referred to Ref. [164]). Mie theory provides an exact analytical solution for Maxwell's equations for the case of a plane wave incident on a spherical particle.[164] According to Mie theory, a dielectric sphere can possess strong scattering resonances, with the scattering proprieties of the sphere dependent on its dielectric constant and size relative to the wavelength of the incident light.[165]

We can consider a dielectric sphere to act as a localised basis for a photon with a wavelength corresponding to one its scattering resonances (much like an atomic orbital does for an electron). Although, the electromagnetic field is not truly localised as the field decays inversely with the distance from the centre of the sphere. These bound states of photons, and accompanying leak, are known as Mie modes.[166] If multiple scatterers are brought together, their individual resonant modes will hybridise, and energy bands will form. Then the ideas of the linear combination of atomic orbitals (LCAO) can be extended to the problem of electromagnetic waves, forming the tight binding model of photonic crystals.[167–171] The Mie scattering mechanism therefore allows us to understand the opening of PBGs in structures that do not possess any periodicity. Additionally, this argument has not been limited to structures composed of spheres or cylinders, the idea has been extended to consider network structures where Mie-type resonances are understood to be vital in the opening of a PBG in both the crystalline and amorphous network gyroid and diamond structures.[172,173]

We have seen that there are two key mechanisms at play when discussing the opening of PBGs - Bragg and Mie scattering mechanisms. Therefore, photonic crystals with the widest PBGs are those which allow for a synergistic interplay between single scattering Mie resonances and macroscopic Bragg scattering. This is best achieved when the dielectric fill fraction of the crystal is optimised to allow for an overlap between the spectral ranges associated with the two mechanisms.[174]

CHAPTER 3

PROGRAMMED ASSEMBLY OF ROD-CONNECTED DIAMOND

The cubic diamond structure is a much sought-after self-assembly target as it supports a photonic band gap (PBG) at a much lower refractive-index contrast than other crystals.[25,55,57,77,175] Therefore, the diamond structure provides more flexibility in terms of materials selection and ensures that the PBG is less sensitive to disorder[55,57] – both being of great importance when considering the self-assembly of colloidal particles.[24,77,78]

However, existing self-assembly approaches face several challenges. While methods have been developed to make spherical particles decorated with four patches in tetrahedral symmetry,[176] which are known to stabilise a cubic diamond structure along with its hexagonal counterpart,[27,28,66] such tetrahedral patchy particles must be reduced in size by an order of magnitude to make 3D photonic crystals that operate in the visible range. Furthermore, simulations have shown that the self-assembly of a diamond crystal from tetrahedral patchy particles faces competition with a kinetically arrested amorphous phase.[28,80] If successful, such a bottom-up route typically yields a mixed phase of cubic and hexagonal polytypes, owing to the small difference in the free energy between these polytypes.[28] Similar observations have been made in the context of closely related tetrastack crystals, which can be self-assembled from triblock patchy particles, unless an involved design approach is invoked.[29,30] The stacking faults present in such a mixed phase make the PBG vulnerable, limiting the practical applications of the self-assembled photonic materials. Thus, alternative self-assembly strategies are needed.

More generally, there are three problems that must be solved to design a self-assembling diamond-structured material with a complete PBG. First, particles must be designed that can be feasibly synthesised and that self-assemble into the diamond-like structure. Second, the PBG of the resulting crystal must be insensitive to defects such as stacking faults. Third, the crystal structure must have a PBG that opens up at an experimentally attainable refractive index. Because these three problems are linked together, they must be addressed simultaneously. In this chapter we address these issues using a multi-pronged computational approach involving reverse engineering, Monte Carlo simulation, and photonic band structure calculations. We start by targeting the rod-connected diamond (RCD) structure, comprising dielectric rods connecting nearest-neighbour sites in the cubic diamond lattice.[57] The RCD structure is known as the "champion" 3D photonic crystal structure because it supports a PBG at the lowest refractive-index contrast.[57,58,177] We use a reverse engineering approach, constrained by how feasible it is to synthesise the building blocks, to arrive at designer colloidal triblock patchy rods (TPRs) as the self-assembling particles. Such particles are similar to other asymmetric patchy particles that have previously been synthesised.[72,74,91,92,178,179]

Because one of the most difficult experimental challenges is functionalising the patches, we demonstrate two different bottom-up routes for the fabrication of RCD-like structures, corresponding to different types of patch-patch interactions. One involves a hierarchy of interactions and the other exploits specificity, as found in DNA-grafted systems.[73] Using Monte Carlo simulations, we show that both of these routes proceed *via* the formation of tetrahedral clusters, and both promote crystallisation over the formation of a kinetically arrested amorphous phase. Surprisingly, we find that the complete PBGs supported by these crystal structures are robust to stacking faults - an important feature for practical applications of self-assembled colloidal photonic crystals.

3.1 | RETROSYNTHESIS OF ROD-CONNECTED DIAMOND

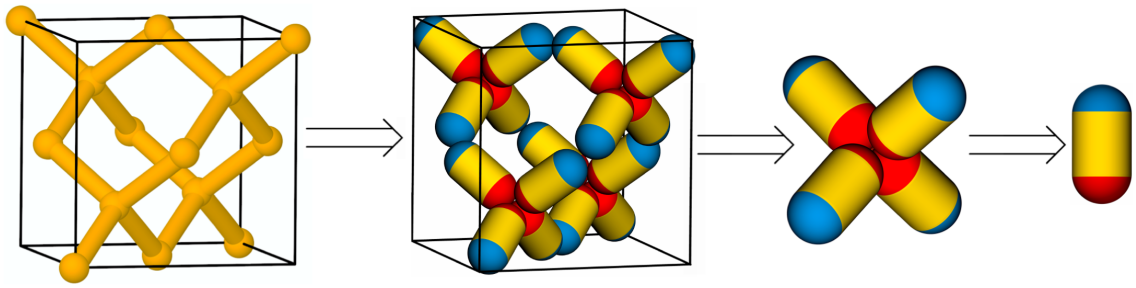


Figure 3.1: **Reverse engineering of rod-connected diamond (RCD) and closely related crystal structures.** Schematic representation of the reverse engineering approach to the rod-connected diamond (RCD) structure, identifying colloidal triblock patchy rods as the designer building blocks. Each TPR has equal-size patches which form bonds of different strengths. Patch A, coloured red, forms stronger bonds with patch A relative to those formed between patches of type B, coloured blue; the bonds between patch A and patch B are of an intermediate strength.

Inspired by the well-known retrosynthetic analysis practised in organic chemistry, we reverse engineer the RCD structure, as schematically outlined in Fig. 3.1. We rely upon a two-stage (dis)assembly scheme, involving tetrahedral subunits as the secondary building blocks, which we envisage to be assembled from colloidal TPRs. Such designer building blocks are anticipated to yield, *via* the corresponding forward approach, a crystal structure that closely resembles RCD, where each cylinder is replaced by a spherocylinder and each sphere by a tetrahedral void. We refer to this structure as segmented rod-connected diamond (sRCD). Our primary building blocks have a repulsive spherocylindrical core and two attractive patches on the opposite hemispherical caps, as shown schematically in Fig. 3.1.

We employed the well-established one-component description for the colloidal suspensions considered here with a pairwise effective potential.[59] Triblock patchy rods are modelled as rigid bodies consisting of a repulsive core, which is spherocylindrical in

shape and decorated with two distinct patches, A and B, located on opposing poles. The interaction between the cores is modelled by the truncated and shifted Kihara potential v_{K}.[180–182] The diameter of the spherocylinder is denoted by σ and its length by L, the aspect ratio of the spherocylinder is then $L^* = L/\sigma$. Patches A and B can differ in terms of their surface coverage, characterised by the angles α and β which describe their half-patch widths, respectively. The effective potential for a pair of patchy rods is shown in Fig. 3.2 and given by:

$$v(\mathbf{r}_{IJ}, \hat{\mathbf{u}}_I, \hat{\mathbf{u}}_J) = v_{\mathrm{K}}(\mathbf{r}_{IJ}, \hat{\mathbf{u}}_I, \hat{\mathbf{u}}_J) + \sum_{i=\mathrm{A}}^{\mathrm{B}} \sum_{j=\mathrm{A}}^{\mathrm{B}} v_{ij}(r_{ij}) \cdot \frac{(1+\Phi_i)(1+\Phi_j)}{4} \tag{3.1}$$

where,

$$v_{\mathrm{K}}(d_{IJ}) = \begin{cases} 4\varepsilon_{\mathrm{K}}\left[\left(\dfrac{\sigma}{d_{IJ}}\right)^{100} - \left(\dfrac{\sigma}{d_{IJ}}\right)^{50} + \dfrac{1}{4}\right] & \text{if} \quad d_{IJ} < \sqrt[50]{2}\sigma \\ 0 & \text{otherwise} \end{cases} \tag{3.2}$$

$$v_{ij}(r_{ij}) = \begin{cases} -\varepsilon_{ij} & \text{if } (r_{ij} - \lambda) < 0 \\ -\frac{1}{2}\varepsilon_{ij}[1 + \cos(\pi(r_{ij} - \lambda)s)] & \text{if } 0 \leq (r_{ij} - \lambda) \leq s^{-1} \\ 0 & \text{otherwise} \end{cases} \tag{3.3}$$

$$\Phi_a = \begin{cases} -1 & \text{if } -\hat{\mathbf{r}}_{ij} \cdot \hat{\mathbf{u}}_i < \cos\delta \\ -\cos\left(\dfrac{\pi[-\hat{\mathbf{r}}_{ij} \cdot \hat{\mathbf{u}}_i - \cos\delta]}{1 - \cos\delta}\right) & \text{otherwise} \end{cases} \tag{3.4}$$

where $\mathbf{r}_{IJ}$ and d_{IJ} are the centre-to-centre separation vector and the shortest distance[183] between particles I and J, respectively.

The orientation of each patch on particle I is defined by a unit vector $\hat{\mathbf{u}}_I$ parallel to its line segment, where we then define the orientation of the patches as $\hat{\mathbf{u}}_{\mathrm{A}} = \hat{\mathbf{u}}_I$ and

$\hat{\mathbf{u}}_B = -\hat{\mathbf{u}}_I$. The positions of the rigid-body sites for a patchy rod of length L is then: $\mathbf{r}_A = (L/2)\hat{\mathbf{u}}_A$ and $\mathbf{r}_B = -(L/2)\hat{\mathbf{u}}_A$, and the inter-patch vector between patches i and j on spherocylinders I and J is then given by: $\mathbf{r}_{ij} = \mathbf{r}_{IJ} + (\mathbf{R}_i \cdot \mathbf{r}_i - \mathbf{R}_j \cdot \mathbf{r}_j)$ where $\mathbf{R}_i$ and $\mathbf{R}_j$ represent the 3×3 rotation matrix for patch i on particle I and patch j on particle J, respectively. The angular dependence of the patch-patch interaction is described by Φ, as prescribed in Ref. [184], and more recently used in Ref. [92], and δ assumes the value of α and β. The form of Φ_j is similar to that of Eqn. 3.4, where $-\hat{\mathbf{r}}_{ij} \cdot \hat{\mathbf{u}}_i$ is replaced by $\hat{\mathbf{r}}_{ij} \cdot \hat{\mathbf{u}}_j$. The depth of the patch-patch interaction is given by ε_{ij}, where we set $0.2\varepsilon_{AA} = \varepsilon_{BB} = \varepsilon_K$ and $\varepsilon_{AB} = \sqrt{\varepsilon_{AA}\varepsilon_{BB}}$. The distance dependence of the patch-patch interaction is governed by the function v_{ij}, where λ is the largest separation at which the attraction between patches i and j is at its strongest and the parameter s controls the range over which this attraction decreases to zero. In the present study, we set $\lambda = 1.01\sigma$ and $s = 5$. We express length in the units of σ, energy in the units of ε_K, the temperature as $T^* = k_B T / \varepsilon_K$ and density as $\rho^* = N\sigma^3/V$, where V is the volume.

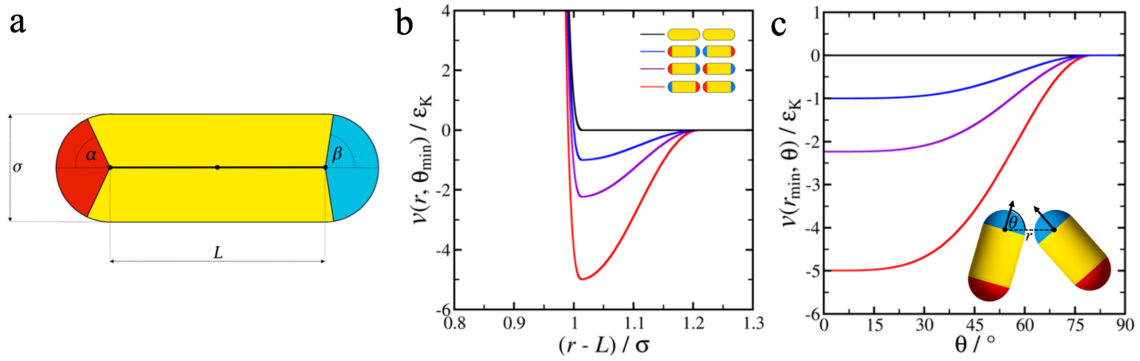


Figure 3.2: **Schematic of the triblock patchy rod model.** (**a**) Triblock patchy rod (TPR) model, where L is the length of the line segment (thick black line) that connects the centres of the spherocylinder caps, and σ is the diameter. Attractive circular patches, distinguished by colour-coding, are placed on opposite poles. The sizes of the patches, characterised by the half-opening angles α and β, and strengths of the interactions between the patches can vary. The effective pair potential as a function of (**b**) the center-to-center distance (r) and (**c**) the angle θ for one TPR shown in the inset, while the corresponding angle for the other TPR is set to θ_{min}, where $r_{min} = \sqrt[50]{2}\sigma$ and $\theta_{min} = 0°$.

The hierarchical self-assembly scheme we intend to exploit, as shown in Fig. 3.1 can be encoded in the designer TPRs by introducing a hierarchy of interaction strengths to the patch-patch interactions,[31,92] that is $\varepsilon_{AA} > \varepsilon_{AB} > \varepsilon_{BB}$. The success of the two-stage self-assembly strategy presented in Fig. 3.1 depends crucially upon the self-limiting formation of tetrahedral clusters in the first stage of assembly.[31,92,185] To this end, we first ensure that the two stages of assembly, driven by the interactions between the two different types of patches, are well separated in strengths by setting $\varepsilon_{AA} = 5\varepsilon_{BB}$, with $\varepsilon_{AB} = \sqrt{\varepsilon_{AA}\varepsilon_{BB}}$. The valency of the patches can then be programmed by judiciously choosing the interaction range and the size of the patches.[31,92] For the TPR model used here, the range of the patch-patch interactions is governed by a parameter s, which we set to $s = 5$. This, in turn, sets the range of the patch-patch interactions to $\sim 1.2\sigma$ for patches facing each other, as evident in Fig. 3.2. The size of the patches is characterised by the patch half-angles α and β for patches A and B, respectively. We used equal-size patches with $\delta = \alpha = \beta = 80^\circ$ as this choice ensures that the formation of tetrahedral clusters is energetically favourable when compared to competing motifs (as shown in Fig. 3.3).

To assess whether these parameters support the formation of the sRCD structure, we first predicted candidate crystal structures for our designer TPRs *via* global optimisation on the crystal energy landscape.[186,187] We found two polytypes as degenerate global minima. One polytype has cubic symmetry, corresponding to the target structure presented in Fig. 3.1, and the other has hexagonal symmetry. Representative views of the (cubic) segmented rod-connected diamond structure (c-sRCD) are shown in Fig. 3.4a, and views of the hexagonal structure (h-sRCD) are shown in Fig. 3.4b. These representations highlight the structural similarities of the two polytypes; in particular, how both structures are built from stacked layers of tetrahedra. In the cubic polytype, successive layers of tetrahedra are staggered relative to one another, and in the hexagonal polytype, they are eclipsed. Thus,

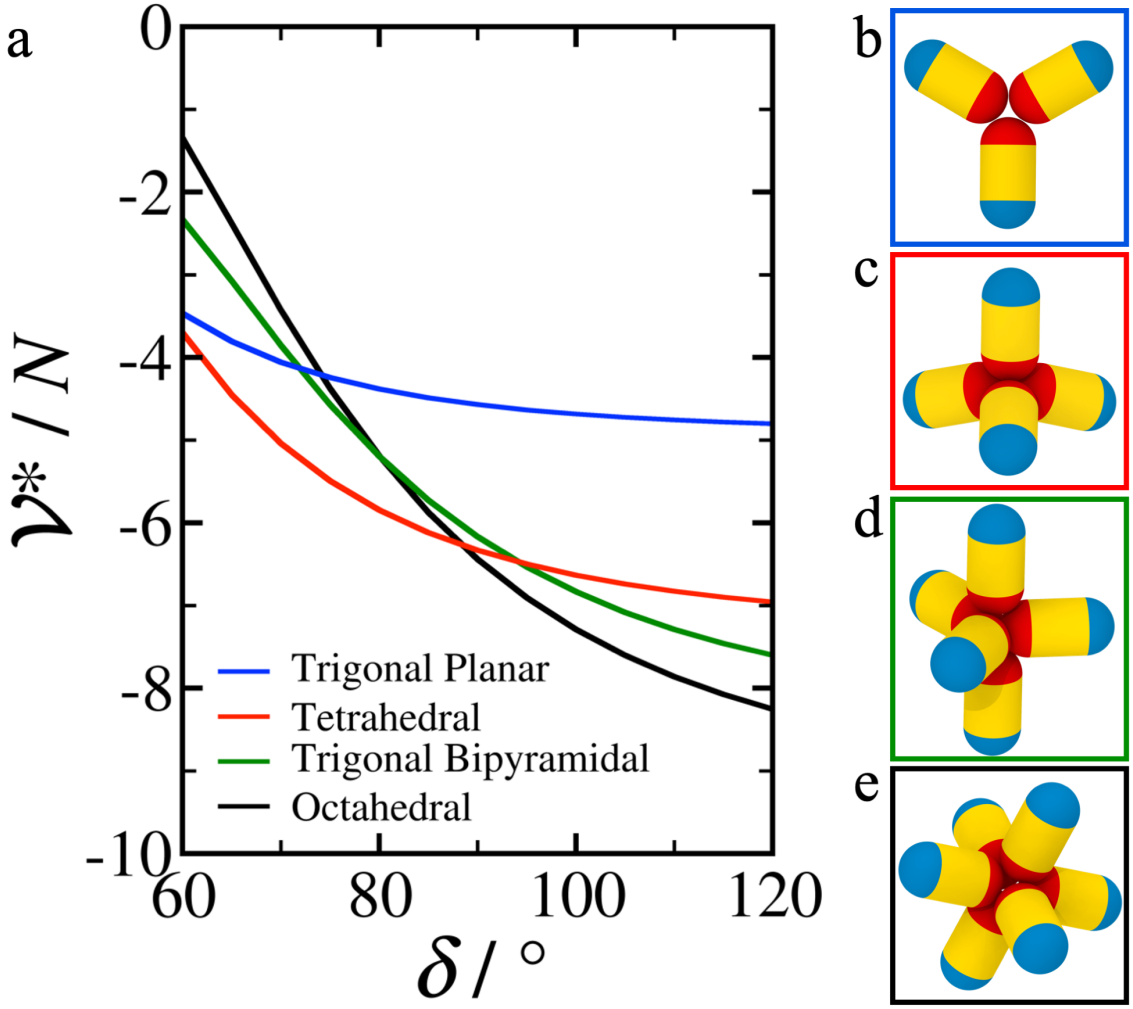


Figure 3.3: **Energy per particle for different clusters of AB-triblock patchy rods as a function of the half-opening angle of the patches. a**) The potential energy per particle ($\mathcal{V}^*/N$) is shown for trigonal planar, tetrahedral, trigonal bipyramidal and octahedral clusters as minima on the potential energy landscapes for AB-triblock patchy rods (TPRs) as a function of the half-opening angle (δ) of the patches. The potential energy is independent of the aspect ratio, as long as it is large enough to ensure that the particle can accommodate two non-overlapping patches. Snapshots of **b**) trigonal planar, **c**) tetrahedral, **d**) trigonal bipyramidal and **e**) octahedral clusters of TPRs are also shown.

the centres of the tetrahedral subunits follow an ABCABC… stacking sequence in the cubic polytype, whereas they follow an ABABAB… pattern in its hexagonal counterpart. However, due to these structural similarities it is also possible for stacking hybrids to

arise where neither of these sequences is strictly followed. For instance, Fig. 3.4c shows a structure where the centres of the tetrahedral subunits follow an ABACABAC… stacking sequence. In this case, the layers of tetrahedra alternate between staggered and eclipsed arrangements. This structure has a spherical close-packed counterpart in the form of the double hexagonal structure.[15,188] We therefore refer to it as double-hexagonal segmented rod-connected diamond (dh-sRCD). It belongs to the same $P6_3/mmc$ space group as h-sRCD, whereas the cubic polytype belongs to the $Fd3m$ space group. As the two polytypes are iso-energetic, any difference in free energy will be due to a difference in entropy, which we anticipate to be small due to their structural similarities.[30,72]

The Helmholtz free energies, A, of the crystal structures of interest were calculated using the Einstein crystal method[39,65,146] for systems of $N = 192$ particles at $T^* = 0.1$, in an orthorhombic cell with $L^* \in [0-1]$. The reference rotational Hamiltonian was chosen to have the same symmetry as our designer patchy particles, *i.e.*, $C_{\infty v}$.[147] Additionally, the orthorhombic cell was chosen such that both the cubic and hexagonal structures were commensurate with its dimensions, where the [111] and [001] axes of the cubic and hexagonal structures, respectively, were aligned with the **c**-axis of the orthorhombic cell (as shown in Fig. 3.4). The density of each system $\rho^* = N\sigma^3/V$ was set to the ideal density of the crystals at zero temperature and pressure, as determined by global optimisation. Integrals were evaluated by means of a 20-point Gauss-Legendre quadrature, and averages were calculated using 10^8 Metropolis Monte Carlo sweeps in the NVT ensemble. The entropies of the crystals were then determined using: $S/Nk_B = (A-\mathcal{V})/(Nk_BT)$. The potential energy for each crystal was determined using 2×10^7 Metropolis Monte Carlo sweeps, with $N = 192$ and $T^* = 0.1$. Indeed, we find that the entropy difference between the cubic and hexagonal polytypes is small at all aspect ratios (L^*) and δ considered (see Fig. 3.5). We also find that the entropy of these structures decreases with L^*. This is

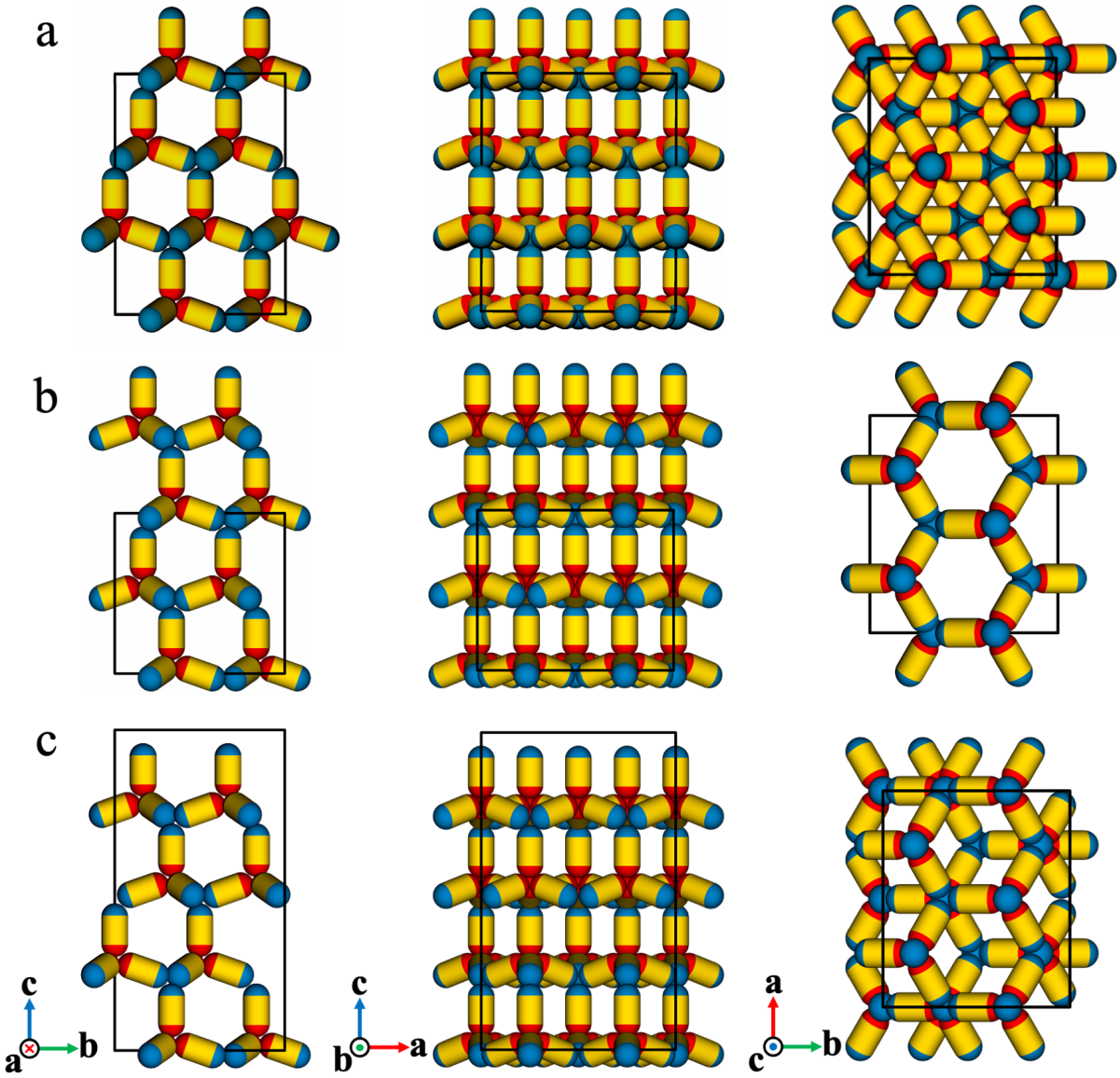


Figure 3.4: **Views of different polytypes of segmented rod-connected diamond (sRCD) crystal.** Orthorhombic unit cells of the (**a**) cubic, (**b**) hexagonal and (**c**) double-hexagonal sRCD structures are shown where the black lines outline the unit cell. The unit cell of the cubic polytype is composed of three stacked layers of tetrahedra, where all adjacent layers are staggered relative to one another. The hexagonal sRCD structure has two layers of stacked tetrahedra, where all adjacent layers are eclipsed relative to one another. The double-hexagonal sRCD structure has four layers of stacked tetrahedra, where each layer has one adjacent staggered layer and one adjacent eclipsed layer. For example, the second layer in panel (**c**) is staggered relative to the 1st layer and eclipsed relative to the 3rd layer.

presumably related to a decrease in the rotational entropy of the crystal structures, imposed by a trade-off with an energetic penalty. Each TPR will incur an energetic penalty for any rotation about an arbitrary axis, other than the axis of cylindrical symmetry, as this causes a displacement of the patches from their ideal positions or orientations (Fig. 3.5, insets). The magnitude of this energy penalty for a given rotation angle increases with the aspect ratio, thus reducing the rotational freedom with increasing aspect ratio.

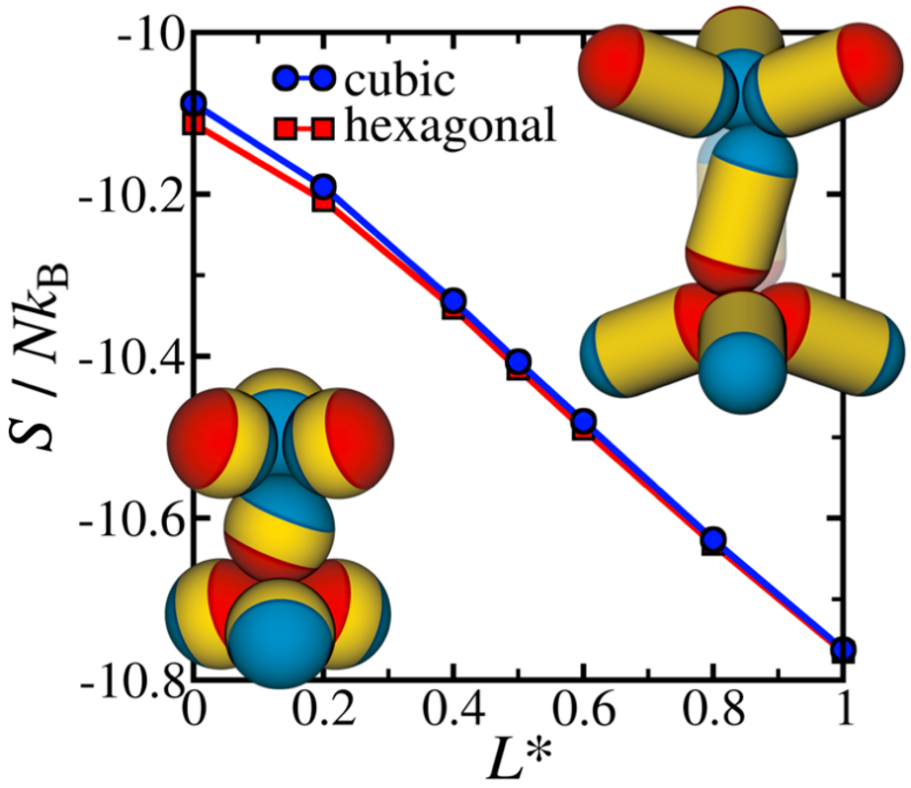


Figure 3.5: **Entropy of the cubic and hexagonal sRCD crystals as a function of aspect ratio.** Entropy S/k_B per particle for the ideal cubic and hexagonal sRCD crystals as a function of aspect ratio at $T^* = 0.1$. Note that the entropies are negative as these are classical systems and the kinetic contributions have been omitted.[65] The insets show two corner-sharing tetrahedra for particles with an aspect ratio of zero and unity, where the central pivot particle is displaced from its ideal orientation. At the spherical limit only the orientation of the patches on the central pivot particle changes when the particle is rotated, whereas for particles with an elongated core, both the position and orientation of the patches are altered when the particle is rotated, as highlighted by the translucent particle in the bottom right inset.

3.2 | HIERARCHICAL SELF-ASSEMBLY OF ROD-CONNECTED DIAMOND

To investigate whether these crystal structures can be self-assembled, we use Monte Carlo sampling of systems of TPRs. To this end, we devised an efficient cluster-move algorithm to sample effectively in the context of emergent structural hierarchy (see Section 2.2.3). A series of Monte Carlo simulations were performed with the systems of $N = 2000$ triblock patchy particles in the canonical ensemble by subjecting the system to gradual cooling. In each case, the simulations were carried out with the system contained in a cubic box under periodic boundary conditions using the minimum image convention. The orientational degrees of freedom were represented by quaternions. Each Monte Carlo cycle consisted of N single-particle or cluster moves, either of which could be translational or rotational, chosen at random with equal probabilities. The potential energy was calculated using a spherical cutoff of $1.3\sigma + L^*$, and a cell-list was used for efficiency.

We performed a series of five independent Monte Carlo simulations with three systems of $N = 2000$ AB-TPRs (AB-TPRs refers to particles where we have set $\varepsilon_{AA} = 5\varepsilon_{BB}$) corresponding to different values of the aspect ratio $L^* = \{0, 0.5, 1\}$. For each independent run, we followed the following annealing protocols: $T^* = 1.0 \to 0.6$ with $\Delta T^* = -0.2$; $T^* = 0.5 \to 0.4$ with $\Delta T^* = -0.1$; $T^* = 0.38 \to 0.30$ with $\Delta T^* = -0.02$; $T^* = 0.25 \to 0.20$ with $\Delta T^* = -0.05$; $T^* = 0.18 \to 0.16$ with $\Delta T^* = -0.02$, with 1.5 million Monte Carlo cycles run for temperatures between [0.5-1.0] and 3 million Monte Carlo cycles run for temperatures between [0.18-0.4]. For the $L^* = 0$ system, 10 million Monte Carlo cycles were run at $T^* = 0.16$, followed by 3 million Monte Carlo cycles for $T^* = 0.14 \to 0.1$ with $\Delta T^* = -0.02$. For the $L^* = 0.5$ system, 3 million Monte Carlo cycles were run at $T^* = 0.16$, followed by 10 million Monte Carlo cycles at $T^* = 0.14$, and then 3 million Monte Carlo Cycles were run at $T^* = 0.12$ and 0.10. For the $L^* = 1$ system, 3 million

Monte Carlo cycles were run for each temperature in the range $T^* = 0.16 \to 0.14$ with $\Delta T^* = -0.02$; 10 million Monte Carlo cycles were performed at $T^* = 0.12$, followed by 3 million Monte Carlo cycles at $T^* = 0.11$ and 0.10. We also carried out a series of five independent Monte Carlo simulations with a system of $N = 2000$ AA-TPRs (AA-TPRs refers to particles where we have set $\varepsilon_{\mathrm{AA}} = \varepsilon_{\mathrm{BB}}$), for $L^* = 0.5$. The following annealing protocol was followed: $T^* = 1.0 \to 0.6$ with $\Delta T^* = -0.2$; $T^* = 0.5 \to 0.4$ with $\Delta T^* = -0.1$; $T^* = 0.35 \to 0.2$ with $\Delta T^* = -0.05$; $T^* = 0.18 \to 0.14$ with $\Delta T^* = -0.02$; $T^* = 0.13 \to 0.10$ with $\Delta T^* = -0.01$. 1, 3 and 5 million Monte Carlo cycles were run at each temperature between [0.2-1.0], [0.13-0.18] and [0.10-0.12], respectively.

In order to establish the success of the design principles laid out in Fig. 3.1, we followed the number of tetrahedral clusters in the system. The simulations show that as the temperature T^* decreases, assembly occurs in two stages. First, the average number of tetrahedral clusters in the system ($\langle \mathcal{N}_{\mathrm{Td}} \rangle$) gradually grows with decreasing temperature until it reaches a plateau around $\langle \mathcal{N}_{\mathrm{Td}} \rangle \approx N/4$ at $T^* = 0.3$, as shown in Fig. 3.6a. The plateau signals the completion of the first stage of assembly, driven by the stronger patch-patch interactions, leading to the formation of a cluster phase comprising exclusively tetrahedral clusters.

Then, both the number of tetrahedral clusters and the average energy per particle change sharply with decreasing T^*, signalling a first-order phase transition. The assembled phase is a crystalline structure containing multiple stacking variants. Analysis based on the Steinhardt bond-orientational order parameters confirms the occurrence of crystallisation (see Fig. 3.7a). We find that the self-assembled crystal structures have the designer particles in different local environments, labelled as *cubic*, *hexagonal*, and *interfacial*, as shown in Fig. 3.6b. The formation of a mixed phase follows from the small free-energy difference between the cubic and hexagonal polytypes.

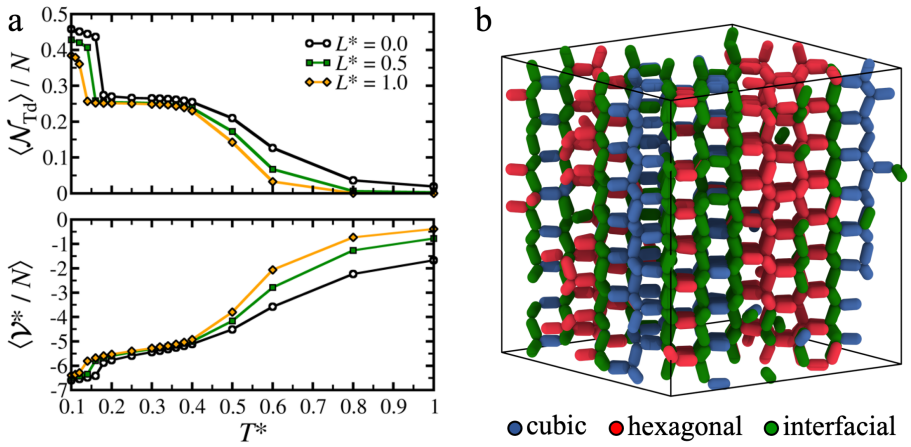


Figure 3.6: **Triblock patchy rod particles with a hierarchy of interactions forming a crystalline structure in two stages, the first being the formation of tetrahedra.** (**a**) The evolution of the average number of tetrahedra $\mathcal{N}_{\mathrm{Td}}$ and energy per particle $\mathcal{V}^*/N$ for a system of $N = 2000$ particles, as a function of temperature T^* for TPR systems with an aspect ratio of $L^* = 0.0, 0.5, 1.0$, which have densities of $\rho^* = 0.674, 0.241, 0.11$, respectively. (**b**) Representative crystalline configuration sampled in Monte Carlo simulations of the AB-triblock patchy rod (TPR) system with $N = 2000$ AB-TPRs with $L^* = 0.5$ at $T^* = 0.1$ and $\rho^* = 0.241$. Here the particles are coloured blue, red and green according to whether they are in locally cubic, hexagonal and interfacial environments, respectively.

The two-stage self-assembly route promotes crystallisation by avoiding competition with an amorphous glassy state, which we find to form when all the interaction strengths are similar.[31] To show that a hierarchy of interaction strengths is necessary, we perform a series of Monte Carlo simulations for a system of TPRs with $L^* = 0.5$ and $\varepsilon_{\mathrm{AA}} = \varepsilon_{\mathrm{BB}} = \varepsilon_{\mathrm{AB}} = 1$. Hereafter, we refer to TPR systems with a hierarchy of interaction strengths as "AB-systems" and those without a hierarchy as "AA-systems." We examine the number of rings ($\mathcal{N}_{\mathrm{R}_l}$) of length l that are formed during the assembly, because 5- and 7-membered rings are absent in the perfect crystal structures of c-sRCD, h-sRCD and dh-sRCD. We calculate the number of rings of length l, $\mathcal{N}_{\mathrm{R}_l}$, where $l \in \{5,6,7,8\}$, by means of a graph-theoretical approach, where we describe an N-particle system as a periodic undirected graph, with each vertex representing a particle centre and the edges representing a bond between two particles.[31] Comparison of the ring statistics presented in Figs. 3.7c and 3.7d

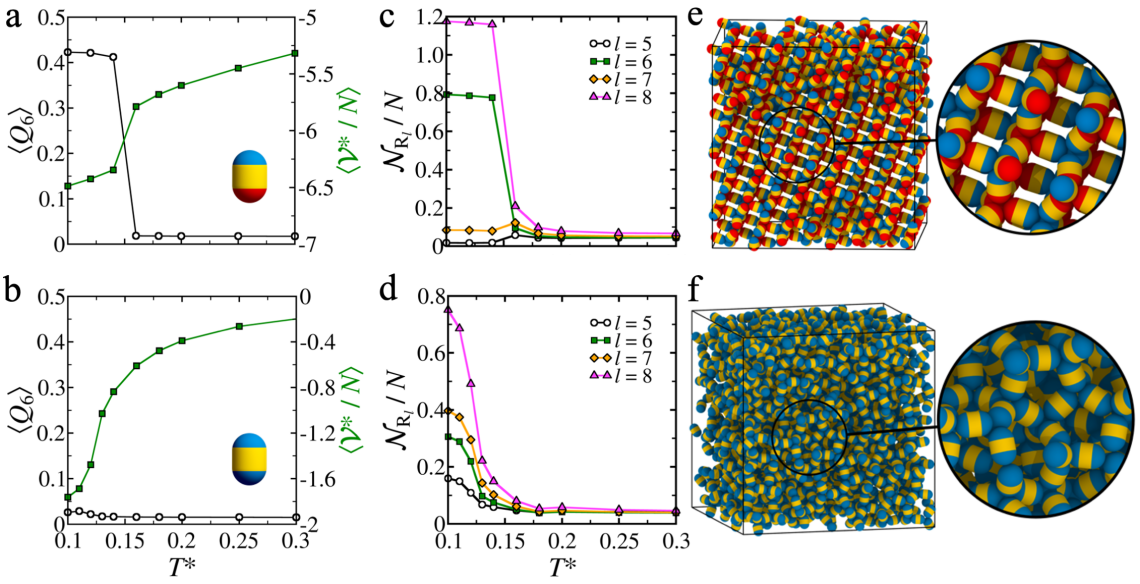


Figure 3.7: **Promotion of crystallisation by hierarchical self-assembly strategy.** Evolution of the average energy per particle $\mathcal{V}^*/N$ and the global bond-orientational order parameter Q_6 with temperature T^* for the (**a**) AA-system and (**b**) AB-system with $L^\star = 0.5$, $N = 2000$ and $\rho^* = 0.241$. The insets show the corresponding TPRs. The evolution of the number of rings of length l, $\mathcal{N}_{\mathrm{R}_l}$, where $l \in \{5,6,7,8\}$, with temperature T^* for the (**c**) AB- and (**d**) AA-systems with $L^* = 0.5$. As shown by the snapshot in (**e**), the hierarchical (AB) system yields a crystalline structure at $T^* = 0.1$ with $L^* = 0.5$. Without the hierarchy, the system forms an amorphous glassy state, as shown by the snapshot in (**f**), obtained at $T^* = 0.1$ and $\rho^* = 0.241$, with $N = 2000$ particles and $L^* = 0.5$ for a system where $\varepsilon_{\mathrm{AA}} = \varepsilon_{\mathrm{BB}} = 1$. The expanded view highlights examples of 5- and 7-membered rings, which prevent the emergence of long-range order when there is no hierarchy of interactions.

shows that 5- and 7-membered rings are suppressed in the AB-system and not in the AA-system, explaining the promotion of crystallisation in the AB-system. The 5- and 7-membered rings are suppressed in the AB-system because the tetrahedral clusters formed in the first stage of assembly can only form chains of particles that are multiples of two. Odd-membered rings in the AB-system can occur only if A-patches are available to bond to B-patches, owing to an incomplete or incorrect first stage of assembly. Figures 3.7e and 3.7f show representative configurations, sampled in Monte Carlo simulations for the AB- and AA-systems, to highlight the contrasting scenarios.

In order to assess the robustness of our design principles to imperfection to the fabrication of triblock patchy rods (TPRs), we investigated the self-assembly of TPRs with polydisperse patch half-opening angles. In Ref. [178], Chaudhary *et al.* were able to synthesise a monodisperse system of colloidal Janus matchsticks with a patch angle distribution of $2\delta = 116^\circ \pm 12^\circ$. We therefore studied three systems of AB-TPRs, each having a Gaussian distribution for patch half-angles with the standard deviation $\sigma_\delta = 5^\circ$, around the mean values of $\bar{\delta} = 70^\circ, 80^\circ, 90^\circ$. Hereafter, we will refer to these systems as AB_1, AB_2 and AB_3, respectively. All three systems contained $N = 1000$ particles having an aspect ratio of $L^* = 0.5$, $\rho^* = 0.241$, $\varepsilon_{AA} = 5\varepsilon_{BB}$ and $\varepsilon_{AB} = \sqrt{\varepsilon_{AA}\varepsilon_{BB}}$.

Figure 3.8 shows the self-assembly of AB-TPRs with polydisperse patch angles when subjected to gradual cooling in Monte Carlo simulations and the corresponding distributions of patch half-angles. We find that, as observed in the case for monodisperse patches with the half-angle of $\delta = 80^\circ$, these systems gradually transition from a fluid phase composed primarily of dimers and trimers at high temperatures, to a tetrahedral cluster phase at lower temperatures. However, we also find that for the AB_1 system there are trimers in a sizeable number at the end of the first stage of assembly, which is to be expected for a system of patchy particles with narrow patches that still allow for three contacts to form.[189] By contrast, there is a small population of pentamers in the AB_3 system, showing that higher coordination clusters begin to become more prevalent as the size of the patches increases. These observations reinforce the importance of optimally designing the geometry of the patches in order to program the self-assembly of the particles into a phase of self-limiting tetrahedral clusters, and that there exists a "Goldilocks" window of patch half-angles that sufficiently stabilises tetrahedral clusters over trigonal planar clusters and higher coordination clusters.

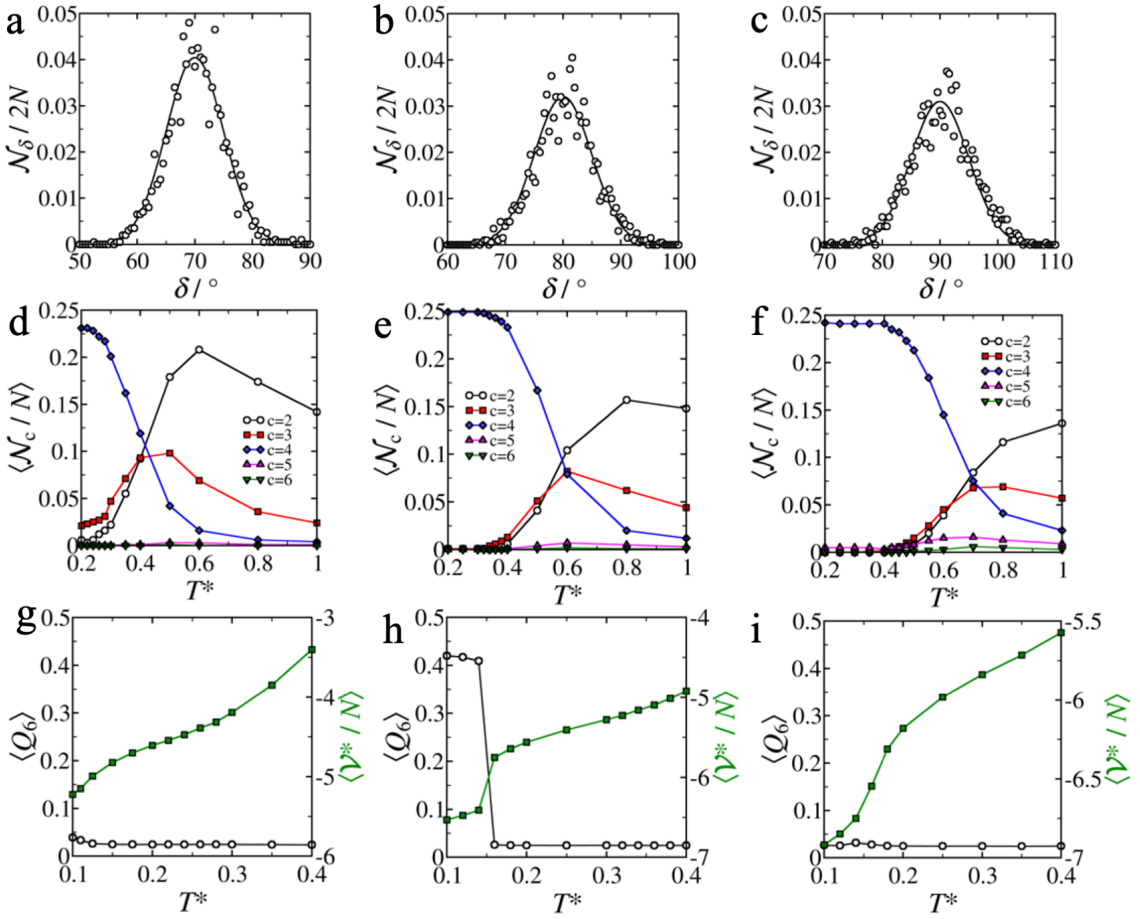


Figure 3.8: **Self-assembly of AB-triblock patchy rods (TPRs) with polydisperse patch half-opening angles.** Data are presented for three different systems of $N = 1000$ AB-TPRs with the aspect ratio $L^* = 0.5$ and polydisperse patch half-angles (δ) having different values of the mean $\bar{\delta}$ but the same standard deviation $\sigma_\delta = 5^\circ$ at $\rho^* = 0.241$. **a**, **d** and **g** correspond to $\bar{\delta} = 70^\circ$; $\bar{\delta} = 80^\circ$ for **b**, **e** and **h**; $\bar{\delta} = 90^\circ$ for **c**, **f** and **i**. (**a**-**c**) show the distributions of patch-half-angles with a fit to a Gaussian distribution with mean $\bar{\delta}$ and standard deviation σ_δ for the three systems; (**d**-**f**) show the evolution of the average number of clusters ($\mathcal{N}_c$) of size c$= 2,3,4,5,6$ through the first stage of assembly in these systems; (**g**-**i**) show the evolution of the average energy ($\mathcal{V}^*$) per particle and the global bond-orientational order parameter (Q_6) at low temperatures for these systems.

Figures 3.8g-i show the evolution of $\langle \mathcal{V}^*/N \rangle$ and $\langle Q_6 \rangle$ as a function of temperature for the AB_1, AB_2 and AB_3 systems. We see that, following the first stage of assembly, only the AB_2 system crystallises into a s-RCD crystal. This is evident from the absence of a discontinuous drop in $\langle \mathcal{V}^*/N \rangle$ at low temperatures for the AB_1 and AB_3 systems,

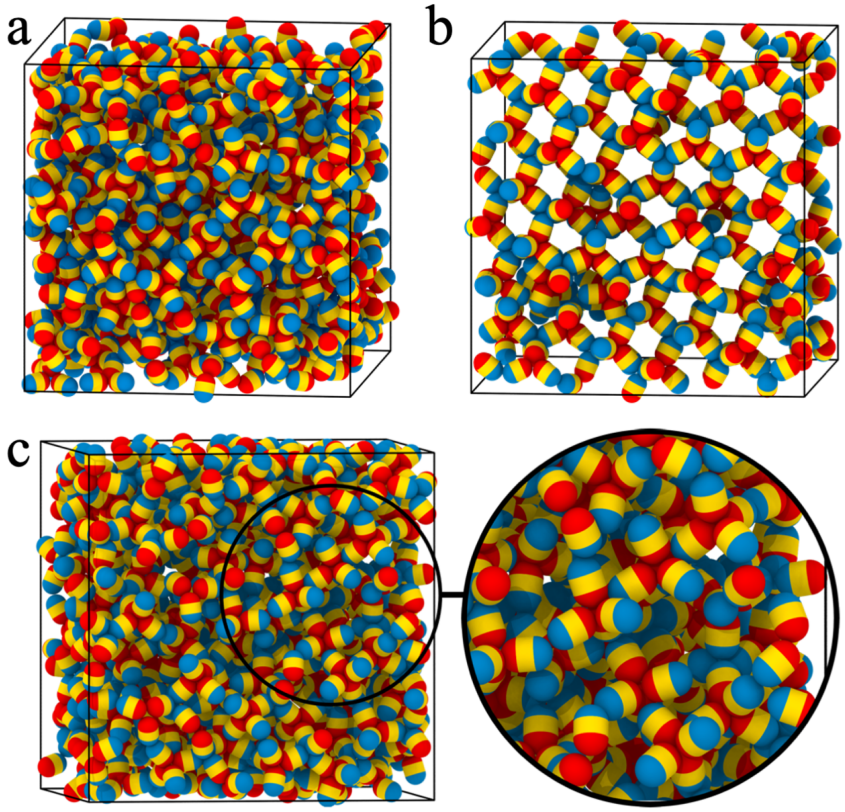


Figure 3.9: **Snapshots of low-temperature configurations in systems of AB-triblock patchy rods (TPRs) with polydisperse patch half-opening angles.** The configurations were obtained from systems of $N = 1000$ AB-TPRs with $L^* = 0.5$ at $T^* = 0.1$ and $\rho^* = 0.241$ with the patch half-angles (δ) having mean values: (**a**) $\bar{\delta} = 70°$, (**b**) $\bar{\delta} = 80°$, (**c**) $\bar{\delta} = 90°$, and the same standard deviation $\sigma_\delta = 5°$. The expanded view in panel (**c**) highlights the distorted trigonal bipyramidal motifs formed by the system of AB-TPRs with $\bar{\delta} = 90°$ following the first-stage of assembly. These distorted trigonal bipyramidal motifs can be considered as being formed *via* vertex-face bonds between the tetrahedral clusters, facilitated by patch A-patch B interactions.

while $\langle \mathcal{V}^*/N \rangle$ suddenly decreases for the AB_2 system at $T^* \approx 0.15$. The drop in energy in the AB_2 system is accompanied by a sudden and large increase in $\langle Q_6 \rangle$, signalling that this drop in energy is due to crystallisation. In contrast, $\langle Q_6 \rangle$ for the AB_1 and AB_3 systems remains close to zero for all temperatures considered, confirming that they have not crystallised.

We find that the AB_1 system struggles to form the emergent vertex-sharing tetrahedra, which drive crystallisation in the second stage of assembly. Instead, the system becomes arrested in an amorphous structure, as shown in Fig. 3.9a. This inability of the AB_1 system to crystallise is further exacerbated by the presence of persistent trimers following the first stage assembly. Unlike the AB_2 system, the AB_3 system also fails to crystallise; however, the reason for this failure is different from that for the AB_1 system. Figure 3.9c shows that the AB_3 system fails to crystallise due to the preferential formation of distorted trigonal bipyramidal motifs over the vertex-sharing tetrahedra required for the s-RCD crystals. These motifs are formed *via* vertex-face bonds between the tetrahedral clusters, facilitated by patch A-patch B interactions. Due to the wider patches in the AB_3 system, and because the strength of the interactions were such that $\varepsilon_{BB} < \varepsilon_{AB} < \varepsilon_{AA}$, it is more favourable for the system to form three distorted AB-bonds in the trigonal bipyramidal motifs than the three BB-bonds of the desired vertex-sharing tetrahedra.

3.3 | CRYSTALLISATION *VIA* SPECIFIC INTERACTIONS

Understanding of the physical mechanism by which the hierarchical self-assembly strategy promotes crystallisation led us to the following hypothesis: introducing specific interactions that prevent the formation of AB bonds would also facilitate the self-assembly of the target crystal. To validate our hypothesis, we set $\varepsilon_{AA} = \varepsilon_{BB} = 1$ and $\varepsilon_{AB} = 0$, thereby ensuring that there are no thermodynamic driving forces for the formation of AB bonds. Such specificity in the patch-patch interactions could be realised using DNA-mediated interactions in synthetic colloids.[53,73]

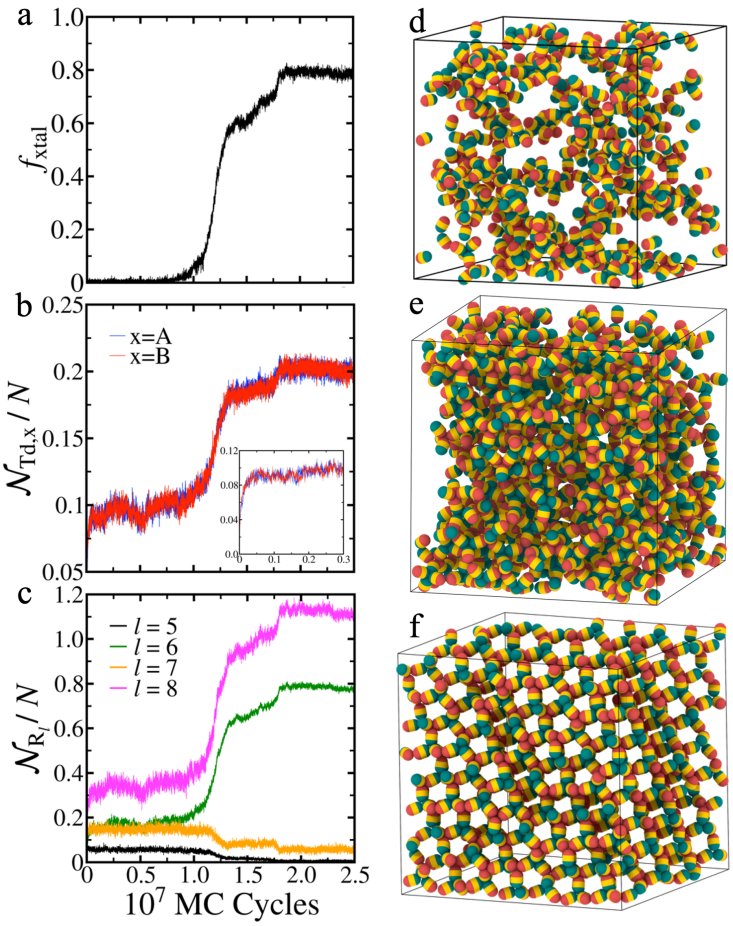


Figure 3.10: **Two-step nucleation of the segmented rod-connected diamond structure from the fluid phase of triblock patchy rods with specificity of interactions upon cooling.** Monte Carlo simulations show that designer TPRs with specific interactions nucleate a crystal from a fluid phase of self-assembled tetrahedra. Here $N = 2000$ particles, $L^* = 0.5$, $\rho^* = 0.241$, $\varepsilon_{AA} = \varepsilon_{BB} = 1$, and $\varepsilon_{AB} = 0$. The panels show the evolution of the system following a drop in temperature from $T^* = 1$ to $T^* = 0.118$: (**a**) fraction of particles in the largest crystalline cluster f_{xtal}; (**b**) the number of tetrahedral clusters $\mathcal{N}_{Td}$ formed by AA bonds and B-B bonds. The total number of tetrahedral clusters in the system is given by $\mathcal{N}_{Td} = \mathcal{N}_{Td,A} + \mathcal{N}_{Td,B}$; (**c**) the number of rings of length l, $\mathcal{N}_{R_l}$, for $l = 5,6,7,8$. The upper bounds on these three parameters correspond to values found in a perfect crystal: $\mathcal{N}_{Td} = N/2$, $\mathcal{N}_{R_6} = N$ and $\mathcal{N}_{R_8} = 3N/2$. Note that the values of all of the parameters, normalised to these upper bounds after 2.5×10^7 MC steps, are close to 0.8, which is also the final fraction of particles in the largest crystalline cluster f_{xtal} (see Methods). Thus the values of these three parameters give similar quantitative estimates of the *crystallinity* of the system, affirming the robustness of the analysis. The formation of the tetrahedral fluid occurs rapidly, as highlighted by the inset on panel (**b**) where we show the evolution of the number of tetrahedral clusters for the first 3×10^6 Monte Carlo cycles. Representative snapshots of the system are shown for (**d**) 25,000, (**e**) 1.25×10^7 and (**f**) 2.5×10^7 Monte Carlo cycles, showing only the tetrahedral clusters formed.

We find that this system, which we refer to as the AA′-system, indeed undergoes a phase transition when cooled from $T^* = 1$. Figure 3.10a shows the nucleation of a crystal from the fluid in a Monte Carlo simulation of a system of $N = 2000$ particles with $L^* = 0.5$ at $\rho^* = 0.241$ and $T^* = 0.118$. The resulting crystal structures are a mixed phase of the sRCD structures, as is the case with the AB-system. The AA′-system evolves through a phase of tetrahedral clusters before a nucleus is formed. As shown in Fig. 3.10b, two sets of tetrahedral clusters, one bound by AA bonds and the other by B-B bonds, are equally abundant as the system evolves to a crystalline state. Crystallisation is then driven by the formation of 6- and 8-membered rings from the fluid of tetrahedral clusters (Fig. 3.10c), similar to what we observe in the AB-system. Representative snapshots of the tetrahedral clusters along the Monte Carlo trajectory are shown in Figs. 3.10d-f.

The emergence of local tetrahedral ordering before nucleation is a signature of two-step nucleation pathways, which are well-established for crystallisation of proteins such as lysozyme[190] and are also observed in some colloidal systems.[191–193] In the two-step nucleation observed here, the first step – the formation of a fluid of tetrahedral clusters – occurs rapidly, while the subsequent formation of the nucleus within the tetrahedral fluid phase is slow and rate-determining. Note that we do not explicitly encode a two-stage assembly scheme; instead, the two-step nucleation process is emergent. We also find that this two-step nucleation process occurs even in the presence of polydispersity in patch half-angles.

3.4 | PHOTONIC PROPERTIES OF ROD-CONNECTED DIAMOND

Having shown that two different types of designer TPRs can assemble into crystalline sRCD phases, we now examine the conditions under which a PBG opens. Because the self-assembled crystals correspond to neither a pure cubic nor a pure hexagonal sRCD phase, we

examine the band structures of both polytypes as well as that of the dh-sRCD structure. The photonic band structures were computed using the MIT MPB package,[159] and the primitive unit cells of the crystals were used for the calculations. Appendix A provides details on the lattice vectors, crystal basis, and $\boldsymbol{k}$-vectors used in the calculations.[194] Additionally, we computed the minimum refractive-index (n_{min}) required to open a PBG for the three structures as a function of L^* using a binary search algorithm with a convergence criterion of 10^{-4}.

We find that all three sRCD structures display PBGs, though these gaps open at different n_{min} and L^* (Fig. 3.11a). However, we also find that the frequency ranges associated with the PBGs of all three sRCD structures overlap, as shown in Fig. 3.11b. Given these observations, we anticipate that two conditions must be met for a PBG to open in a mixed-phase system: first, each polytype must show a PBG; and second, the PBGs of the different polytypes must spectrally overlap. We also note that for both sets of structures, the double-hexagonal structure requires a much smaller refractive-index contrast than the pure hexagonal crystal to support a complete PBG, despite belonging to the same space group. Additionally, the size of the PBG for dh-sRCD is comparable to that of c-sRCD, these observations are at odds with the conventional wisdom that crystal structures with cubic symmetry are the best candidates for wide PBGs.[26,58] It also suggests that the local order of the crystal plays a critical role in determining its photonic properties, an observation which aligns with previous studies that investigated the photonic properties of amorphous networks.[173,195,196]

We also observe that the minimum index varies non-monotonically with the aspect ratio: for each structure, there is an optimal aspect ratio (Fig. 3.11a). An aspect ratio around 0.75 maximises the PBG for the h-sRCD structure with a refractive index contrast of $n_c = 3$

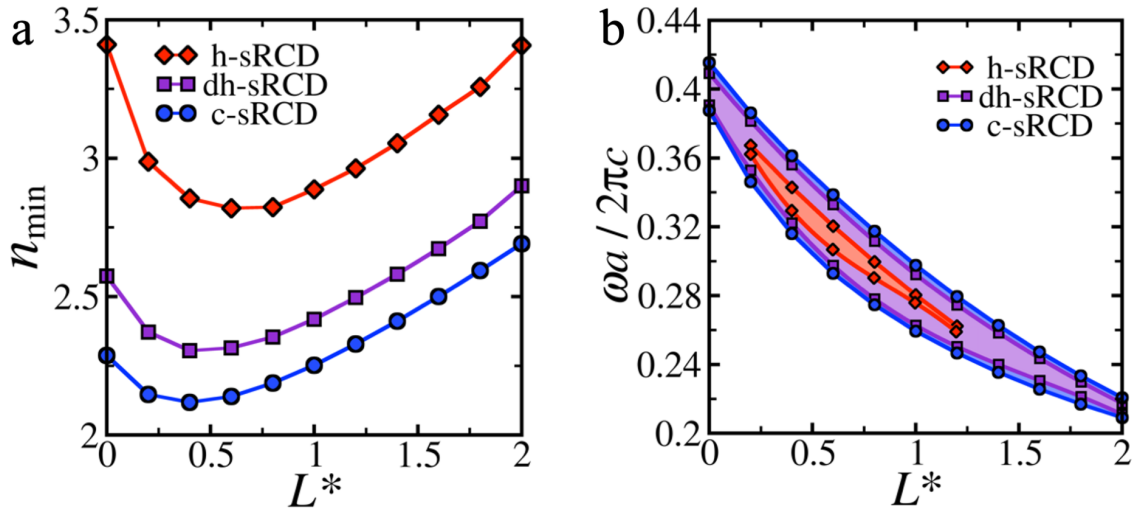


Figure 3.11: **Dependence of the photonic band gap in the sRCD structures on the aspect ratio.** (**a**) Minimum refractive index required to open a photonic band gap (PBG) n_{min} for the cubic (c-sRCD), hexagonal (h-sRCD) and double hexagonal (dh-sRCD) structures as a function of aspect ratio L^*. (**b**) Photonic bandgap map for c-sRCD, dh-sRCD and h-sRCD with $n_c = 3$, where the lower-frequency line corresponds to the dielectric band of the PBG and the higher-frequency line to the air band.

while maintaining a wide gap for c-sRCD and dh-sRCD (Fig. 3.11b). To understand the non-monotonic behaviour with L^*, we analyse the electromagnetic modes of the dielectric bands (those immediately below the PBG) and air bands (those immediately above the PBG) for these structures. From the spatial variations of the electric-field energy density on the kagome planes of the c-sRCD and h-sRCD structures (Fig. 3.12a), it is evident that the electric-field energy above the PBG is mostly localised in the low-index regions, while the energy below the PBG is in high-index regions. The frequency of a particular electromagnetic mode is closely associated with the degree to which its electric-field energy is localised in the high-index regions, which can be quantified using the dimensionless concentration factor:

$$f = \frac{\int_{V_{n_c}} \mathrm{d}^3\mathbf{r}\, \mathbf{E}^*(\mathbf{r}) \cdot \mathbf{D}(\mathbf{r})}{\int_V \mathrm{d}^3\mathbf{r}\, \mathbf{E}^*(\mathbf{r}) \cdot \mathbf{D}(\mathbf{r})}, \tag{3.5}$$

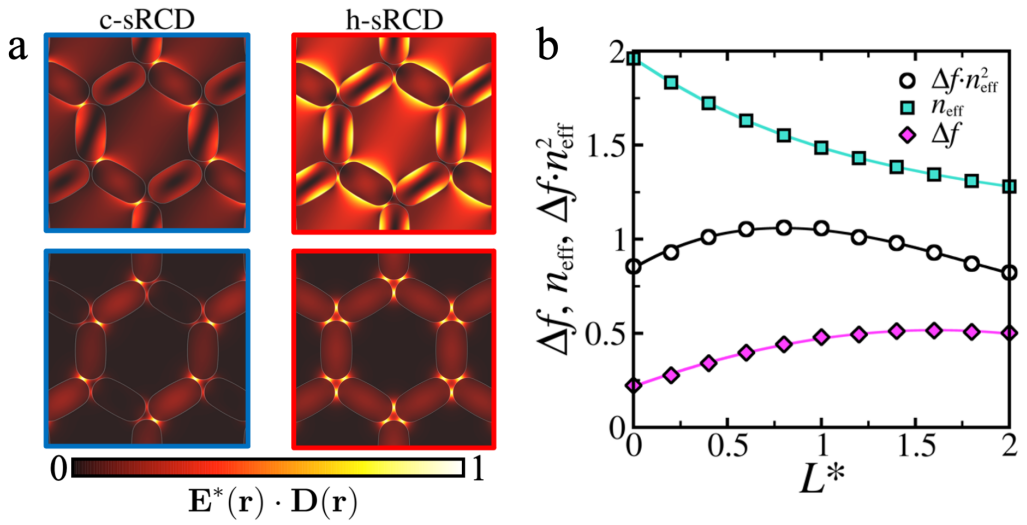


Figure 3.12: **Dependence of the photonic band gap in the sRCD structures on the aspect ratio.** (**a**) Slices of the normalised electric-field energy density are shown for the c-sRCD (left panels with blue borders) and h-sRCD (right panels with red borders) with $L^* = 1$, where the top sub-panels correspond to the air bands and the bottom to the dielectric band. The slices are taken through a Kagome plane to which the [111] and [001] axis of the cubic and hexagonal unit cells are normal, respectively. (**b**) Plots of the difference in concentration factor between the top of the dielectric band and bottom of the air band $\Delta f = f_{\text{diel}} - f_{\text{air}}$, effective refractive index n_{eff} (taken as the mean refractive index of the primitive unit cell) and their product $\Delta f \cdot n_{\text{eff}}^2$ as a function of L^* for c-sRCD with $n_c = 3$. The lines are fits to guide the eye.

where $\mathbf{E}(\mathbf{r})$ is the electric field, $\mathbf{D}(\mathbf{r})$ is the displacement field, V is the volume of the unit cell, and V_{n_c} is the volume occupied by the high-index material.[160] The width of the PBG should therefore depend on $\Delta f = f_{\text{diel}} - f_{\text{air}}$, where f is the concentration factor corresponding to the dielectric or air band.[160] Another relevant parameter is the effective refractive index n_{eff}, which is the mean refractive index of the primitive unit cell. We find that Δf and n_{eff} have opposing dependencies on L^* in the cubic polytype (Fig. 3.12b). Consequently, the product of the two, $\Delta f \cdot n_{\text{eff}}^2$, shows a maximum at an aspect ratio near where the PBG is largest (Fig. 3.12b). This correspondence suggests that the non-monotonic variation of the width of the PBG with L^* is governed by a trade-off between the two factors, Δf and n_{eff}.

3.4.1 PHOTONIC CRYSTALS ROBUST TO STACKING FAULTS

The observation that the band gaps for all three crystal structures overlap (Fig. 3.11b) raises the question of whether randomly stacked structures, such as those self-assembled in our simulations, also support a complete PBG. We therefore examine the band structures for two sRCD structures derived *via* random stacking, using an orthorhombic unit cell for the calculations. We find that such structures can indeed support complete PBGs (Figures 3.13a and 3.13b). We further calculate the band structures for a series of such structures with $L^* \in [0,1]$. We find that the PBGs are robust to stacking faults for refractive index contrasts as low as 2.6 when $L^* > 0$ (Fig. 3.13c).

In order to probe how the presence of stacking faults influences the size of the PBG in sRCD structures, we computed the photonic band structures for a number of random stacking structures with different levels of cubicity (the fraction of cubic particles in the structure) and a refractive-index contrast of $n_c = 3.6$. Figure 3.14 shows the relative gap width of these random stacking structures as a function of cubicity. We see that for each value of the cubicity there are multiple data points for $\langle \Delta\omega/\omega_{\mathrm{m}} \rangle$ that can span a wide range of values as there are multiple unique ways to distribute the cubic and hexagonal layers throughout the crystal. We find that, it is not only the cubicity that is important in determining the photonic properties of the crystal, but also how the layers of cubic and hexagonal diamond are distributed relative to one another. The insets of Fig. 3.14 show two structures with a Cubicity of 0.5, however, one structure has a relative gap width of $\sim 15\%$ and the other $\sim 11\%$. Particles in these structures are colour-coded according to whether they are in a cubic, hexagonal or interfacial local environment. We see that structures where hexagonal layers are grouped together to form a large hexagonal block have a much narrower PBG as compared to structures where the hexagonal layers are separated.

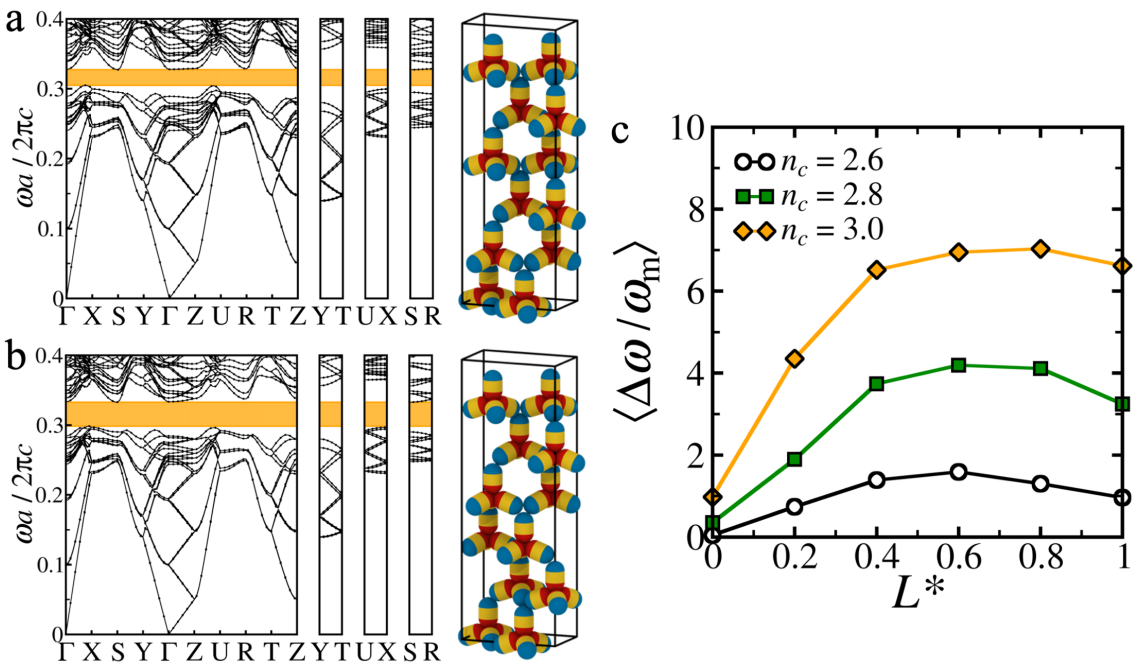


Figure 3.13: **Photonic properties of stacking hybrids of sRCD structures, showing complete photonic band gaps.** Panels (**a**) and (**b**) show two example photonic band structures for randomly stacked sRCD structures composed of particles with an aspect ratio of 0.6 and a refractive-index contrast of $n_c = 3$. Both structures are built from 6 randomly stacked layers of tetrahedra, where each layer can either be staggered (S) or eclipsed (E) relative to the preceding layer. The structure in panel (**a**) follows a S-E-S-E-E-E pattern and has a relative gap width of 7.1%. The structure in panel (**b**) follows a S-S-E-S-S-E pattern and has a relative gap width of 10.8%. Schematic visualisations of the unit cells used in the calculations are shown to the right of their respective photonic band structures. (**c**) The average relative gap width $\langle \Delta\omega / \omega_m \rangle$, expressed as a percentage, for randomly stacked sRCD structures as a function of L^* for three refractive-index contrasts of $n_c = 2.6, 2.8, 3.0$. The points represent averages over 100 structures composed of 12 randomly stacked layers of tetrahedra.

3.5 | DISCUSSION

Our designer TPRs have three properties that make them promising candidates for the self-assembly of materials with a PBG in the visible range. First, they do not form an amorphous glassy phase. Instead, owing to the two-stage crystallization mechanism, they form crystalline sRCD, though with a mixture of polytypes. Second, the self-assembled

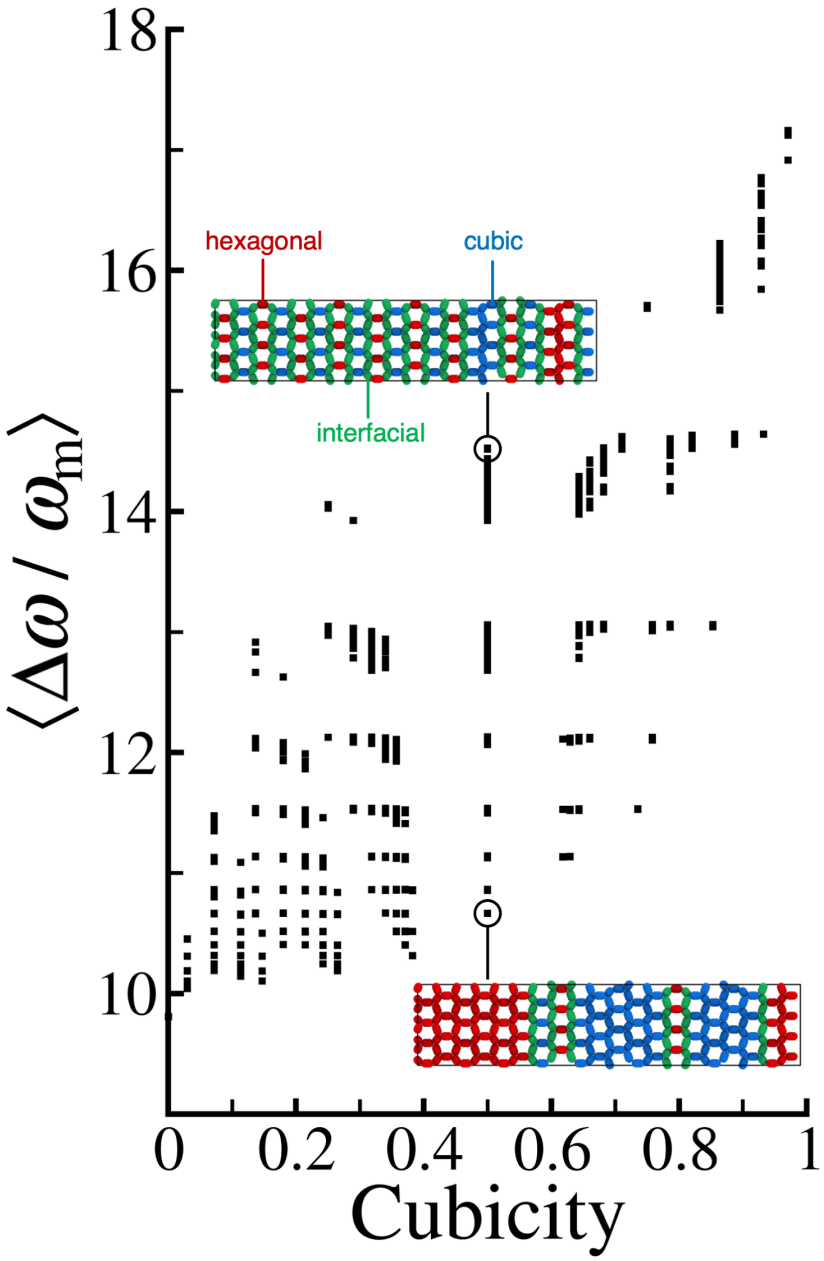


Figure 3.14: **Photonic band gap dependence on cubicity for sRCD structures.** Photonic band gap (PBG) width (expressed as a percentage) as a function of cubicity (number of cubic particles/number of hexagonal particles) for random stacking sRCD structures composed of particles with an aspect ratio of 0.5 with 20 layers and a refractive-index contrast of $n_c = 3.6$. For each value of the cubicity there are multiple data points as there are multiple ways to distribute the cubic and hexagonal layers within the crystal. The insets show two configurations that have the same cubicity but different PBG width.

crystals have a PBG, even when they contain a mixture of polytypes. Third, the width of the band gap can be controlled through the aspect ratio without compromising the ability to self-assemble.

At the limit of $L^* = 0$, the TPR particles reduce to the well-studied spherical triblock patchy particles, and their associated crystal structures correspond to the tetrastack crystals.[30,31,72] These particles are also capable of self-assembling into randomly stacked tetrastack crystals, but as we show in Fig. 3.13, the required refractive-index contrast to open a PBG ($n_{\text{min}} \approx 3$) in these crystals is too high to be realised in the visible region of the spectrum. However, by using the aspect ratio as a control knob, one can reduce the minimum refractive index required to open the gap to $n_{\text{min}} = 2.6$ for randomly stacked sRCD structures. This seemingly small reduction in n_{min} greatly improves the prospects for a colloidal photonic crystal with a PBG in the visible range. The most straightforward strategy to make a material with this refractive index is to assemble TPRs made from titanium dioxide. The refractive index of 2.6 may be achievable with anatase titania, which is much easier to synthesise than the rutile phase and has minimal absorption above 400 nm.[24] We find that both randomly stacked structures presented in Fig. 3.13 have a midgap frequency of $\omega^*_{\text{m}} = 0.316$ (where $\omega^* = \omega a/2\pi c$ and $a \approx 2\sigma$). Therefore, if we take the wavelength corresponding to the midgap frequency to be 450 nm, the estimated diameter of the TPRs required to fabricate a photonic crystal with a PBG in the visible regime is $\sigma \approx 70$ nm.

A more promising strategy for fabrication of photonic crystals using TPRs involves lowering the required refractive-index contrast by filling the gaps between particles, thereby producing a true RCD structure. By depositing materials onto the surfaces of the particles, the tetrahedral voids formed in the first stage of assembly would decrease in size, and the dielectric filling fraction would increase.[197] This post-assembly processing, which can

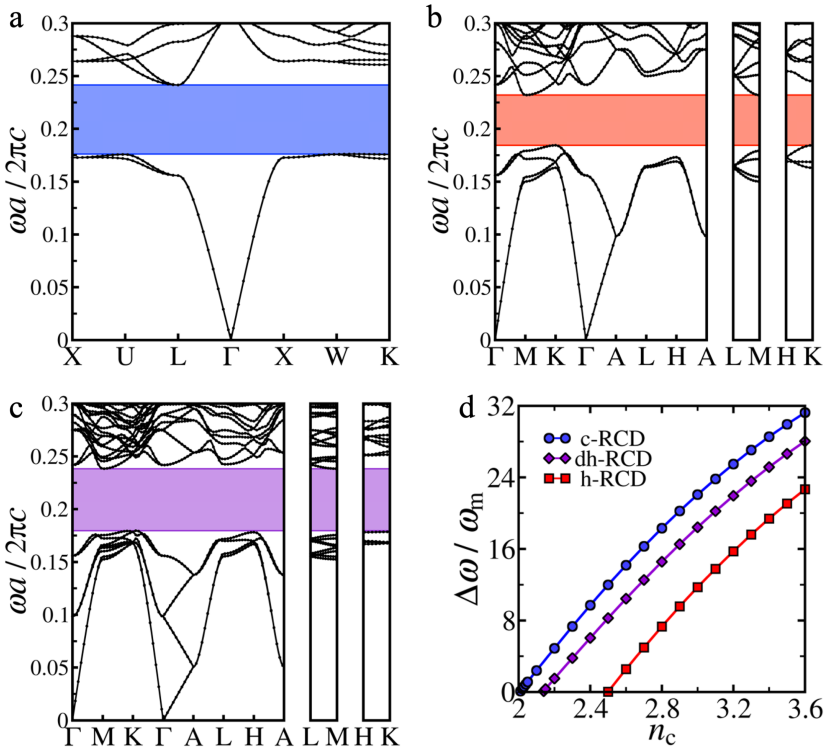


Figure 3.15: **Photonic band structures for rod-connected diamond crystals.** Photonic band structures for the (**a**) cubic, (**b**) double-hexagonal and (**c**) hexagonal rod-connected diamond structures for a refractive-index contrast of $n_c = \sqrt{13}$ with $L^* = 1.2$ and an effective particle diameter of 1.2σ. The relative gap width of the complete PBG for the c-RCD structure converges on the previously quoted value of 31% at $n_c = \sqrt{13}$.[55,173] Moreover, the dh-RCD structure assumes the "near-champion" status as it supports a relative gap width of 28% at $n_c = \sqrt{13}$, the same as the single-network gyroid structure.[173] This is surprising, as only crystal structures with cubic symmetry have hitherto been sought after for their well-documented ability to support such a wide complete PBG.[58] (**d**) Evolution of the relative gap width $\Delta\omega/\omega_m$, expressed as a percentage, with the refractive index contrast n_c for the cubic, double-hexagonal and hexagonal RCD structures.

be thought of as "swelling" the particles so that they overlap, would recover the RCD structures as a limiting case. The photonic band structures of these swollen RCD crystal structures are shown in Fig. 3.15, where we have used the primitive unit cells for the calculations. We find that a PBG opens up for the cubic RCD structure at $n^{\mathrm{c}}_{\mathrm{min}} \approx 2$, for the hexagonal RCD at $n^{\mathrm{h}}_{\mathrm{min}} \approx 2.5$, and for the double-hexagonal RCD at $n^{\mathrm{dh}}_{\mathrm{min}} \approx 2.2$. Based on these values, we estimate the refractive index contrast at which a PBG would open in

a randomly stacked RCD structure to be $n_c \approx 2.2$. This lower refractive index contrast could be achieved with even sol-gel-derived, nanocrystalline titania,[198] which is readily synthesised with no need for high heat treatment. Because it is performed in solution, the sol-gel method could be used both to make the TPRs as well as to coat the assembled structures and fill in the voids.

We note also that our results challenge the notion that cubic structures are optimal for PBGs.[26] The critical refractive index that we find for the double hexagonal RCD structure, $n_{\text{min}}^{\text{dh}} \approx 2.2$, is comparable to that of the much sought-after network gyroid structure, $n_{\text{min}} = 2.2$,[58,199] which has cubic symmetry. This result shows that there are hexagonal structures that compete favourably with cubic structures in terms of photonic properties. Future studies that investigate how and why double hexagonal structures obtain such wide band gaps may yield valuable design principles for photonic crystals.

CHAPTER 4

CLEAR PATHWAYS TO COLLOIDAL DIAMOND

Cubic diamond has been well established as a target structure for self-assembly, with over 30 years of effort being dedicated to this endeavour.[25,27,28,55,57,80–82,200] The initial interest in devising a self-assembly route to cubic diamond structures was predominantly driven by their attractive photonic properties.[55,57,200] Tetrahedral patchy particles[27,28,73,176] were the obvious candidate building blocks for assembling cubic diamond crystals, however, the self-assembly of a diamond crystal from tetrahedral patchy particles faces a number of challenges that can be of both thermodynamic and kinetic origins, as suggested by a number of computer simulation studies.[28,80–82] The kinetics of self-assembly pose a major challenge, with competition from an amorphous glassy phase, as well as clathrate crystals, leaving a narrow widow of patch widths where tetrahedral patchy particles can self-assemble into diamond crystals.[28,80,84,85] Recently, He *et al.* devised an experimental system of patchy tetrahedral clusters that was able to selectively self-assemble into a structure with cubic diamond symmetry, and avoids any competition with hexagonal polytype.[25]

While the original driving force for studying tetrahedral patchy particles may have have been to fabricate photonic band gap materials, assembling diamond crystals with these particles now represents a fundamental challenge for programmable self-assembly. In this chapter, we explore whether introducing ring selection rules to a system of tetrahedral patchy particles can facilitate their self-assembly into diamond crystals.

4.1 | RATIONAL DESIGN OF BUILDING BLOCKS TO YIELD DIAMOND

In the previous chapter, we showed that crystallisation of diamond crystals is promoted by suppressing the formation of 5- and 7-membered rings.[31,201] The frustration caused by a distribution of ring sizes could be a generic mechanism by which crystallisation into an open lattice is hindered. In the present chapter, we sought to demonstrate the generality of this hypothesis by investigating the self-assembly of diamond crystals in a system that contains two types of designer tetrahedral patchy particles, each having four identical patches, in a 1:1 mixture. We introduce specific interactions, such that bond formation can only occur between the two different types of particles, labelled A and B. Such specificity in bond formation can be realised using DNA-mediated interactions.[73,202,203] We refer to a system of tetrahedral patchy particles with these specific interactions as a two-component system and a system where these interactions are not at play (*i.e.*, a standard system of tetrahedral patchy particles) as a one-component system.

Our tetrahedral patchy particles are represented by the widely used Kern-Frenkel model,[204] where the particles of different types interact *via* a combination of a hard-core repulsion, with diameter σ, and a square-well attraction between the patches, with a half-angle θ, modulated by an angular factor. The angular factor is unity only when the patches face each other, and zero otherwise. Only hard-sphere repulsion is at play between particles of the same type. The effective potential for a pair of patchy particles v_{ij} is given by:

$$v_{ij}(\mathbf{r}_{ij},\mathbf{\Omega}_i,\mathbf{\Omega}_j) = v_{ij}^{\mathrm{hs}}(r_{ij}) + v_{ij}^{\mathrm{sw}}(r_{ij}) \sum_{\alpha,\beta=1}^{4} f(\mathbf{r}_{ij},\hat{\mathbf{n}}_i^{\alpha},\hat{\mathbf{n}}_j^{\beta}) \tag{4.1}$$

where $r_{ij} = |\mathbf{r}_{ij}|$ is the center-to-center distance between particles i and j and $\mathbf{\Omega}_i$ and $\mathbf{\Omega}_j$ describe the orientations of particles i and j, respectively. v_{ij}^{hs} is the hard-sphere pair

potential

$$v_{ij}^{\mathrm{hs}}(r_{ij}) = \begin{cases} \infty & \text{if } r_{ij} < \sigma \\ 0 & \text{otherwise} \end{cases} \tag{4.2}$$

with σ representing the hard-sphere diameter. v_{ij}^{sw} is a square-well potential given by

$$v_{ij}^{\mathrm{sw}}(r_{ij}) = \begin{cases} -\varepsilon & \text{if } \sigma \leq r_{ij} \leq (1+\delta)\sigma \\ 0 & \text{otherwise} \end{cases} \tag{4.3}$$

where ε is the well-depth and δ controls the range of the attraction and is set to $\delta = 0.2\sigma$. Finally, the factor $f(\mathbf{r}_{ij}, \hat{\mathbf{n}}_i^{\alpha}, \hat{\mathbf{n}}_j^{\beta})$ controls the angular dependence of the interaction between two patches, and is given by

$$f(\mathbf{r}_{ij}, \hat{\mathbf{n}}_i^{\alpha}, \hat{\mathbf{n}}_j^{\beta}) = \begin{cases} 1 & \text{if } \hat{\mathbf{n}}_i^{\alpha} \cdot \hat{\mathbf{r}}_{ij} > \cos\theta \text{ and } \hat{\mathbf{n}}_j^{\beta} \cdot \hat{\mathbf{r}}_{ji} > \cos\theta \\ 0 & \text{otherwise} \end{cases} \tag{4.4}$$

where $\hat{\mathbf{n}}_i^{\alpha}$ is a normalised vector from the center of particle i in the direction of the center of patch α on its surface, and thus depends on $\mathbf{\Omega}_i$. Similarly, $\hat{\mathbf{n}}_j^{\beta}$ is a normalised vector from the center of particle j in the direction of the center of patch β, and thus depends on $\mathbf{\Omega}_j$. The width of the patches is controlled by θ, which represents the half-opening angle of the patches. The pairwise additive approximation is used to obtain the total potential energy of the system, $\mathcal{V}$.

For the one-component system, all particles are considered to be identical, and are decorated with patches that are taken to be of equal size, range and strength. In the two-component system, the two types of particles, labelled A and B, are distinct, despite having the same size and attractive patches equal in size and range of interactions. The particles are distinct as $\varepsilon_{\mathrm{AA}} = \varepsilon_{\mathrm{BB}} = 0$ and $\varepsilon_{\mathrm{AB}} = \varepsilon$). That is, only particles of different

types have attractive interactions between them . In the present study, we used reduced units: the length in units of σ, the energy in units of ε, the temperature in units of $\varepsilon/k_{\mathrm{B}}$, with the Boltzmann constant k_{B} taken to be equal to one.

Chains of particles in the two-component system considered here can only form closed bond loops in the cases where the first and last particles in the chain are of different types. The contrasting scenarios between the formation of rings in a one-component and a two-component system of tetrahedral patchy particles are shown in Figs. 4.1a and 4.1b, vividly demonstrating the selection of even-membered rings imposed by the constraint of inter-type binding only. The two-component system of tetrahedral patchy particles can of course form cubic and hexagonal diamond crystals, representative views of which are shown in Figs. 4.1c and 4.1d, respectively. Additionally, we recognise that the two-component system of tetrahedral patchy particles should effectively suppress the formation of s-I and s-II clathrates (both lattices requiring odd-membered rings), but it can still stabilise the s-III clathrate, which is composed of 4- and 6-membered rings, as shown in Fig. 4.1d[205]. However, due to the presence of 4-membered rings, this structure can only form when $\theta \geq 9.75^{\circ}$; additionally, the 6-membered rings found in this structure are planar, unlike the boat and chair conformations found in the diamond crystals (as shown in Figs. 4.1c and 4.1d).[28] Due to the frustration associated with the formation of 4- and planar 6-membered rings, we anticipate our design rules for diamond will not suffer any competition from the clathrate s-III crystal.

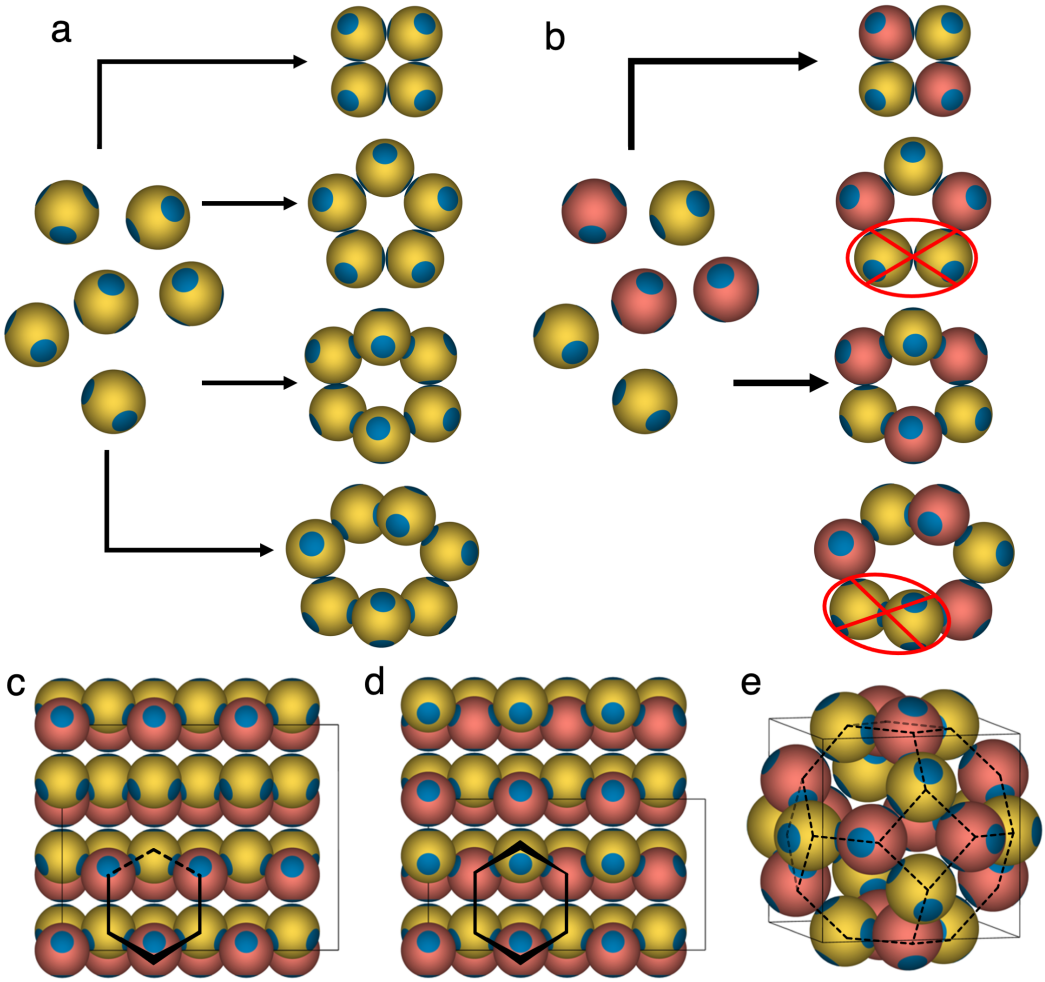


Figure 4.1: **Ring selection rules for facile assembly of colloidal diamond.** (**a**) Examples of 4-, 5-, 6- and 7-membered rings that can form in a one-component system of tetrahedral patchy particles. (**b**) Examples 4- and 6-membered rings that can form in a two-component system of tetrahedral patchy particles, where bonds can form only between distinct types, labelled A (coloured yellow) and B (coloured pink). Examples of 5- and 7-membered rings are also shown to highlight that odd-membered rings cannot form in such a two-component system of tetrahedral patchy particles as they require AA or BB bonds. (**c**-**e**) Example crystal structures that can be stabilised by a two-component system of tetrahedral patchy particles: (**c**) cubic diamond; (**d**) hexagonal diamond; (**e**) clathrate s-III. The thin black lines represent the edges of the respective unit cells of the crystal structures. We highlight representative 6-membered rings present in the cubic and hexagonal diamond crystals in the chair and boat conformations, respectively. Additionally, we show the underlying network in the clathrate s-III structure as dashed lines to highlight that the four- and six-membered rings in the unit cell are arranged such that they form a truncated octahedron.

4.2 | SELF-ASSEMBLY OF COLLOIDAL DIAMOND

A two-component system of tetrahedral patchy particles with specificity of interactions then appears as a propitious route to a diamond crystal. To explore whether this is indeed the case, we carried out Monte Carlo simulations of one-component and two-component systems of $N = 1000$ tetrahedral patchy particles in the *NVT* ensemble. We used an equal number of A and B particles in the two-component system (*i.e.*, $N_A = N_B = 500$). Additionally, we considered systems where the patch half-angles for the tetrahedral patchy particles were chosen such that diamond was not expected to be kinetically accessible in the one-component system.

We performed a series of Monte Carlo simulations for one- and two-component systems of $N = 1000$ tetrahedral patchy particles with patch half-angle $\theta = 12^\circ$ and at a density of $\rho^* = N\sigma^3/V = 0.3$. Each system was gradually cooled to a temperature of $T^* = k_B T/\varepsilon = 0.1$, starting from an equilibrium configuration obtained by melting a simple cubic lattice at $T^* = 1$. For the one-component system, the following cooling protocol was followed in steps: $T^* = 1.0 \to 0.2$ with $\Delta T^* = -0.2$, $T^* = 0.18 \to 0.14$ with $\Delta T^* = -0.02$, $T^* = 0.135 \to 0.13$ with $\Delta T^* = -0.005$, and $T^* = 0.12 \to 0.1$ with $\Delta T^* = -0.01$. At each temperature between $T^* = 1.0$ and $T^* = 0.16$, 1 million Monte Carlo cycles were run, then 3 million Monte Carlo cycles were run at $T^* = 0.14$ and 30 million Monte Carlo cycles were run at $T^* = 0.135$, before running 2 million Monte Carlo cycles at each temperature between $T^* = 0.13$ and $T^* = 0.1$. For the two-component system, we followed the following cooling protocol in steps: $T^* = 1.0 \to 0.2$ with $\Delta T^* = -0.2$, $T^* = 0.18 \to 0.14$ with $\Delta T^* = -0.02$, $T^* = 0.135 \to 0.13$ with $\Delta T^* = -0.005$, and then at $T^* = 0.128, 0.125, 0.12, 0.1$ in the sequence. We carried out 1 million Monte Carlo cycles at each temperature between $T^* = 1.0$ and $T^* = 0.14$, 3 million Monte Carlo

cycles at $T^* = 0.135$, 10.5 million Monte Carlo cycles at $T^* = 0.13$ and $T^* = 0.128$, and 2 million Monte Carlo cycles at each temperature between $T^* = 0.125$ and $T^* = 0.1$. Additionally, we performed a series of Monte Carlo simulations for the one-component system of $N = 1000$ tetrahedral patchy particles with $\theta = 12^\circ$ at $\rho^* = 0.5$, starting from an equilibrium configuration at $T^* = 1$. We followed the following cooling protocol in steps: $T^* = 1.0 \rightarrow 0.2$ with $\Delta T^* = -0.2$, $T^* = 0.18 \rightarrow 0.16$ with $\Delta T^* = -0.02$, $T^* = 0.15 \rightarrow 0.145$ with $\Delta T^* = -0.005$, and then at $T^* = 0.144$, before lowering the temperature further: $T^* = 0.14 \rightarrow 0.1$ with $\Delta T^* = -0.01$. We carried out 1 million Monte Carlo cycles at each temperature between $T^* = 1.0$ and $T^* = 0.16$, 10 million Monte Carlo cycles run at each temperature between $T^* = 0.15$ and $T^* = 0.144$, and then 3 million Monte Carlo cycles at each temperature between $T^* = 0.14$ and $T^* = 0.1$.

In Fig. 4.2, we compare the self-assembly observed of the two systems. We find that both systems undergo a first-order phase transition upon gradual cooling, the one-component system forming a clathrate structure, while the two-component system forming a diamond structure instead. This is reflected in Figs. 4.2a and 4.2d, where we compare the evolution of the average number of rings of length l ($\mathcal{N}_{\mathrm{R}_l}$) with temperature for the one-component and two-component systems, respectively. The first-order phase transition in the one-component system is marked by a dominant growth of 5-membered rings as one would expect for a clathrate structure.[82] By contrast, a sharp increase in 6- and 8-membered rings in the two-component system signals the self-assembly into a diamond crystal. The characteristic peaks in the probability distribution for the translational-order correlation parameter, d_3 (defined in the Section 2.4), as evident in Fig. 4.2b and Fig. 4.2d, confirm the respective crystal structures. Figures 4.2c and 4.2f show representative snapshots of the clathrate and diamond structures self-assembled in the one-component and two-component systems, respectively.

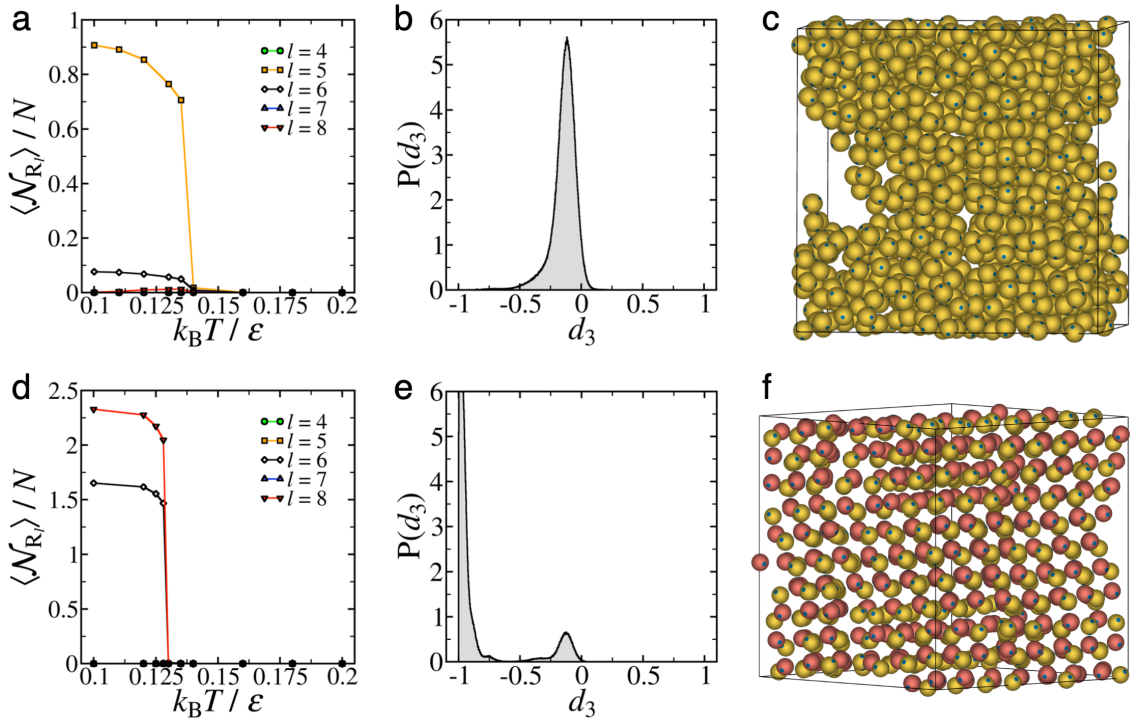


Figure 4.2: **Self-assembly of one- and two-component systems of tetrahedral patchy particles with narrow patches.** Self-assembly in (**a**-**c**) one-component and (**d**-**f**) two-component systems of $N = 1000$ tetrahedral patchy particles with patch half-angle $\theta = 12^\circ$ at $\rho^* = N\sigma^3/V = 0.3$. (**a**,**d**) Evolution of the average number of rings of length l ($\mathcal{N}_{Rl}$) with temperature. (**b**,**e**) Probability distribution function of the translational-order correlation parameter d_3, defined in Section 2.4, at a temperature of $k_B T/\varepsilon = 0.1$. (**c**,**f**) Representative snapshots of the crystals at a temperature of $k_B T/\varepsilon = 0.1$.

The distribution of d_3 (see Section 2.4) is routinely used to identify the formation of diamond in systems of tetrahedral patchy particles as a pure cubic diamond structure has a single peak at $d_3 = -1$, while hexagonal diamond and also random stacking diamond have an additional peak centred at $d_3 = -0.115$[27,28,65,80,136]. The peak at $d_3 = -1$ arises from the presence of bonded pairs of particles (*i.e.*, two particles that share a patch-patch bond) with staggered patches, while the peak at $d_3 = -0.115$ corresponds to bonded particles with eclipsed patches. Figure 4.2b reveals that the one-component system contains exclusively eclipsed bonds, a characteristic of the clathrate structures.[30] By contrast, Fig. 4.2d shows that the two-component system contains predominantly staggered bonds, with some

eclipsed bonds, suggesting that a mixture of cubic and hexagonal diamond has formed. At higher densities, we find that the one-component system may crystallise into a diamond structure alongside an amorphous clathrate phase.[82]

We also performed a series of Monte Carlo simulations for one- and two-component systems of $N = 1000$ tetrahedral patchy particles with a larger patch half-angle of $\theta = 25^\circ$ and at a density of $\rho^* = 0.5$. This θ value is well into the regime where a one-component system of tetrahedral patchy particles is known to become dynamically arrested into a glassy state upon cooling.[28,82] Each system was gradually cooled to a temperature of $T^* = 0.1$, starting from an initial simple cubic lattice which was melted at $T^* = 1$. For both systems, the following cooling protocol in steps was followed: $T^* = 1.0 \rightarrow 0.6$ with $\Delta T^* = -0.2$, $T^* = 0.5 \rightarrow 0.2$ with $\Delta T^* = -0.1$, $T^* = 0.18 \rightarrow 0.16$ with $\Delta T^* = -0.02$, $T^* = 0.155 \rightarrow 0.15$ with $\Delta T^* = -0.005$, and $T^* = 0.14 \rightarrow 0.1$ with $\Delta T^* = -0.01$. We carried out 1 million Monte Carlo cycles at each temperature between $T^* = 1.0$ and $T^* = 0.3$, 5 million Monte Carlo cycles at each temperature between $T^* = 0.2$ and $T^* = 0.16$, 15 million Monte Carlo cycles at $T^* = 0.155$ and 0.15, and 5 million Monte Carlo cycles at each temperature between $T^* = 0.14$ and $T^* = 0.1$.

Figure 4.3a shows that a distribution of rings with $l \in [4-8]$ indeed emerges in the one-component system, with no signature of crystallisation taking place, as revealed in Fig. 4.3b by the lack of well-resolved peaks in the distribution of d_3. The broad distribution suggests that there are a number of particles which form bonds that are neither staggered nor eclipsed. This implies that the resulting structure is truly amorphous, and not disordered because of polycrystallinity. By contrast, the two-component system readily crystallises into a diamond structure; with the evolution of the number of rings with temperature, and the distribution of d_3 at low temperatures, closely matching that of the two-component system with narrower patches, as evident in Fig. 4.3d and Fig. 4.3e, respectively.

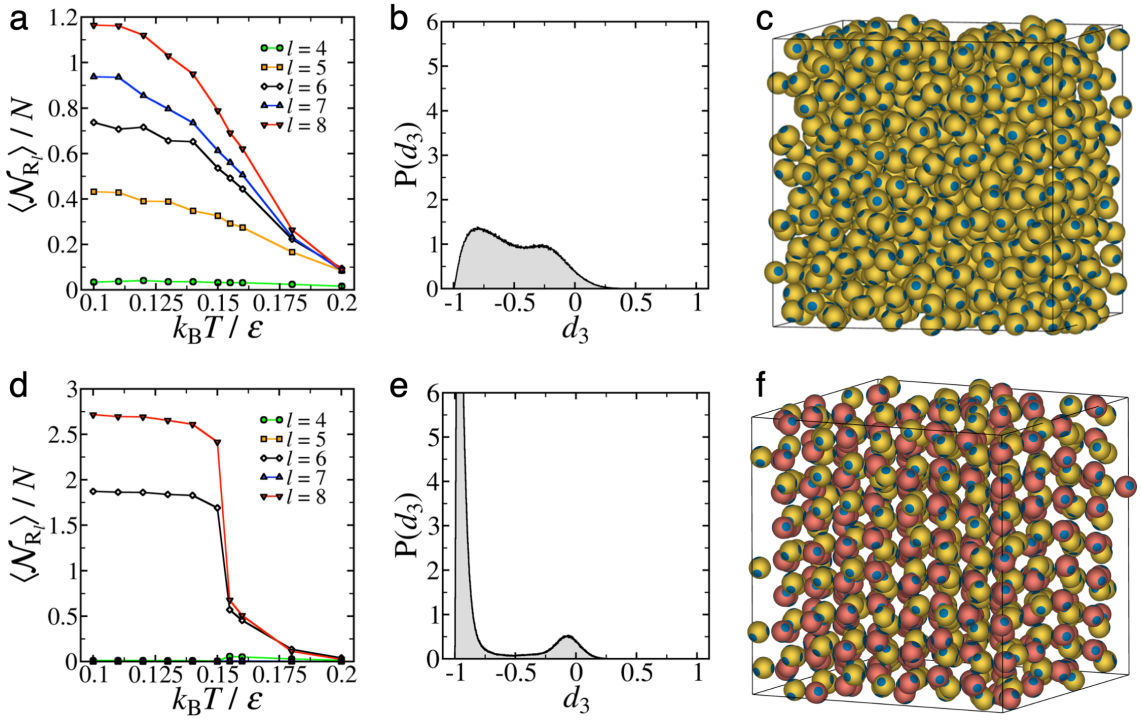


Figure 4.3: **Self-assembly of one- and two-component systems of tetrahedral patchy particles with wide patches.** Self-assembly in (**a**-**c**) one-component and (**d**-**f**) two-component systems of $N = 1000$ tetrahedral patchy particles with patch half-angle $\theta = 25^\circ$ at $\rho^* = N\sigma^3/V = 0.5$. (**a**,**d**) Evolution of the average number of rings of length l ($\mathcal{N}_{Rl}$) with temperature. (**b**,**e**) Probability distribution function of the translational-order correlation parameter d_3 at a temperature of $k_B T/\varepsilon = 0.1$. (**c**,**f**) Representative snapshots of the configurations in the two systems at a temperature of $k_B T/\varepsilon = 0.1$.

4.3 | THERMODYNAMIC DRIVING FORCE AIDING CRYSTALLISATION

We have thus established that our two-component system of designer tetrahedral patchy particles readily crystallises into diamond, even for patch half-angles where the diamond crystals are kinetically inaccessible for the one-component system. The facile crystallisation of diamond for a two-component system of tetrahedral patchy particles can be predominantly attributed to the removal of kinetic traps containing odd-membered rings from the energy landscape. However, in order to assess whether crystallisation is also facilitated in the two-component system from thermodynamic considerations, we evaluate

the thermodynamic driving force for crystallisation (*i.e.*, the chemical potential difference between the crystal and fluid phases, $\Delta\mu = \mu_{\text{crystal}} - \mu_{\text{fluid}}$). Figures 4.4a and 4.4b show the temperature and θ dependence of $\Delta\mu$ for the one-component ($\Delta\mu_{1c}$) and two-component ($\Delta\mu_{2c}$) systems, respectively. At higher temperatures, where the fluid is more stable than the crystal, we see that $\Delta\mu_{2c} > \Delta\mu_{1c}$ for all θ, implying that the two-component fluid phase is more stable than its one-component counterpart, relative to their respective crystalline phases. This additional stability can be mainly attributed to the entropy of mixing: $S_{\text{mix}}/(Nk_{\text{B}}) = -\sum_{i=\text{A,B}} \frac{N_i}{N} \ln(\frac{N_i}{N})$ which is present in the two-component fluid, but not in the one-component fluid.[206,207]

By contrast, at low temperatures where the crystal is the stable phase, we find that $\Delta\mu_{2c} < \Delta\mu_{1c}$. This is most clearly evident for the systems with the widest patch half-angle ($\theta = 26°$), where there is very little driving force for crystallisation in the one-component system. This is because the one-component system with wide patches is able to form a fully connected liquid phase, whose stability competes with that of the crystal phase.[28,80,81] Above a threshold θ, the fully connected liquid becomes the thermodynamically favoured phase at low temperatures due to a configurational entropy contribution to the free energy, thereby preventing crystallisation into diamond.[81] However, even for patch half-angles narrower than this threshold value, crystallisation is not observed, as we have shown in Fig. 4.3a-c. Additionally, the highly associative nature of these particles leads to significantly slowed dynamics at low temperatures, resulting in nucleation barriers that are too high to overcome, making the system essentially a guaranteed glass-former.[80,84]

In the two-component system, each particle has only $N/2$ potential bonding partners as compared to $N-1$ in the one-component system. As a result, the probability of forming a bond in the two-component fluid must be reduced relative to that of the one-component fluid. Figure 4.5 shows the bonding probability (p_b) in the two systems as a function

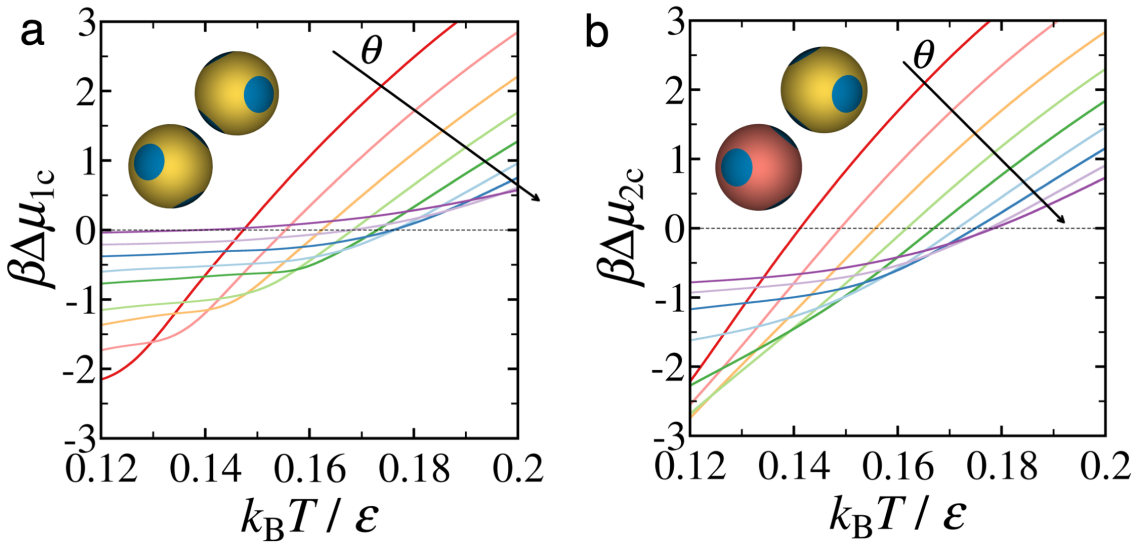


Figure 4.4: **Thermodynamic driving force for crystallisation in one- and two-component systems of tetrahedral patchy particles.** Dependence of the chemical potential difference between the cubic diamond and fluid phases for (**a**) one-component ($\Delta\mu_{1c}$) and (**b**) two-component ($\Delta\mu_{2c}$) systems of $N = 216$ tetrahedral patchy particles on temperature (k_BT/ε) and patch width (θ) at a pressure of $P^* = P\sigma^3/\varepsilon = 0.03$. Here, $\Delta\mu = \mu_{cd} - \mu_{fluid}$ and $\theta = 10°, 12°, 14°, 16°, 18°, 20°, 22°, 24°, 26°$. The arrows show the direction of increasing θ.

of temperature as determined by Monte Carlo simulations and Wertheim's perturbation theory.[206–212] Indeed, we see that the bonding probability for the one-component system with $\theta = 25°$ is larger than that of the corresponding two-component system prior to crystallisation. At low temperatures Wertheim's theory begins to break down (as shown by the increasing deviation of the bonding probabilities calculated numerically from Monte Carlo in Fig. 4.5) since it neglects the formation of rings in the system.[206,207] Additionally, at low temperatures there is seemingly a switch in the relative bonding probabilities of the one- and two-component systems where p_b in the two-component system is greater than that of the one-component system. This switch occurs when crystallisation takes place in the two-component system, and so our intuition that the one-component fluid is "more connected" than the two-component fluid remains valid.

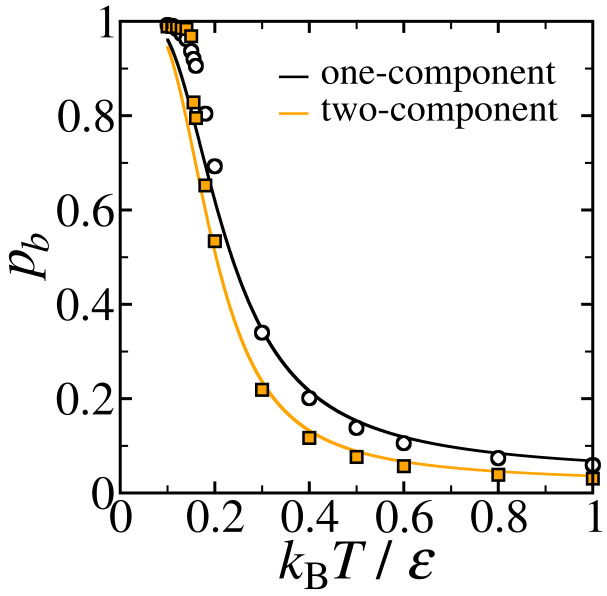


Figure 4.5: **Bonding probabilities for one- and two-component systems of tetrahedral patchy particles.** Bonding probabilities for one- and two-component systems of tetrahedral patchy particles with patch half-angle $\theta = 25^\circ$ at a density of $\rho^* = N\sigma^3/V = 0.5$ as a function of temperature. The data points correspond to bonding probabilities determined from Monte Carlo simulations of the systems of $N = 1000$ tetrahedral patchy particles and the lines correspond to bonding probabilities determined using Wertheim's theory.[206–212]

This explains why there is a greater thermodynamic driving force for crystallisation in the two-component system upon cooling to moderately low temperatures – the liquid phase is simply less "connected". Therefore, introducing specificity of interactions to program even-ring selection rules promotes crystallisation not only by reducing the frustration experienced by the system, through the removal of kinetic traps, but also by providing an additional thermodynamic driving force.

Additionally, we note that as we move from the one-component to the two-component system, through the introduction of specific interactions, the coexistence temperature at $P^* = 0.03$ changes. As shown in Fig. 4.6, the coexistence temperature shifts to lower and higher values for narrower and wider patches, respectively, with the crossover occurring around 22°. Again, this can be understood by considering how the relative contributions of

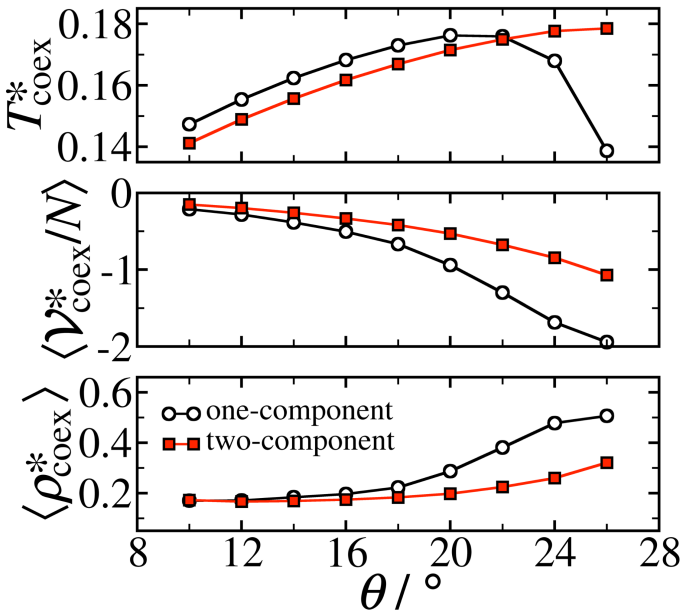


Figure 4.6: **Comparison of fluid-solid coexistence in one- and two-component systems of tetrahedral patchy particles.** Dependence of the coexistence temperature, T^*_{coex}, the fluid potential energy ($\mathcal{V}^*_{coex}$) and the fluid density (ρ^*_{coex}) at the coexistence temperature on the patch half-angle θ for the one-component and two-component systems at $P^* = 0.03$.

energy and entropy to the free energy of the respective fluid phases affect the behaviour of the system. The two-component system is less prone to bonding, as shown in Fig. 4.5 and apparent from the energies per particle of the fluid phases at the coexistence temperature.

Figure 4.6 also shows that the coexistence is with a "gas" phase in the case of the one-component system for low θ values, but crosses to one with a dense liquid phase for higher θ values when we compare the coexistence densities with the corresponding critical densities.[213] For the two-component system, the coexistence appears to be always with the "gas" phase. As a result, crystallisation occurs *via* different nucleation mechanisms in the two models, leading to the different θ dependence of T_{coex}, and to the consequent crossing of T_{coex} between the two models. For one-component systems with wider patches, where a network fluid can form, the energy in the liquid phase reaches values similar to the one of the crystal and crystal formation becomes essentially controlled by an entropic balance.[81]

4.3.1 CHROMATIC PATCHY PARTICLES

Our finding that there is an additional thermodynamic driving force for crystallisation in the two-component system when interactions are specific raises the question of whether augmentation of specific interactions would further favour the self-assembly of a diamond crystal. In order to address this question, we considered a two-component system of tetrahedral patchy particles where the four patches are of distinct "colours", allowing for the formation of bonds only between patches of the same colour, provided that the patches belong to particles of different types. This two-component system of "chromatic" patchy particles, which resembles systems that have previously been investigated for the self-assembly of a diamond crystal,[79,214,215] maintains the same ring selection rules previously imposed to favour crystallisation, while increasing the specificity of the interactions. Therefore, we might expect the thermodynamic driving force for crystallisation in such a system to be even greater than the two-component system where the patches are not distinguished.[214]

Figure 4.7 shows the results of our Monte Carlo simulations of a two-component (1:1) system of $N = 1000$ chromatic tetrahedral patchy particles in the *NVT* ensemble with $\theta = 25^{\circ}$. We find that indeed only even-membered rings form as per our ring selection strategy, but we do not observe crystallisation during the course of our simulations, suggesting that this chromatic two-component system is "over-specific" and particles struggle to identify four neighbours in their immediate vicinity with the right patches available for bonding. This observation also suggests the possibility of a trade-off between increasing the height of the kinetic barriers associated with crystallisation and increasing the thermodynamic driving force for crystallisation upon introducing specific interactions to a system of tetrahedral patchy particles.

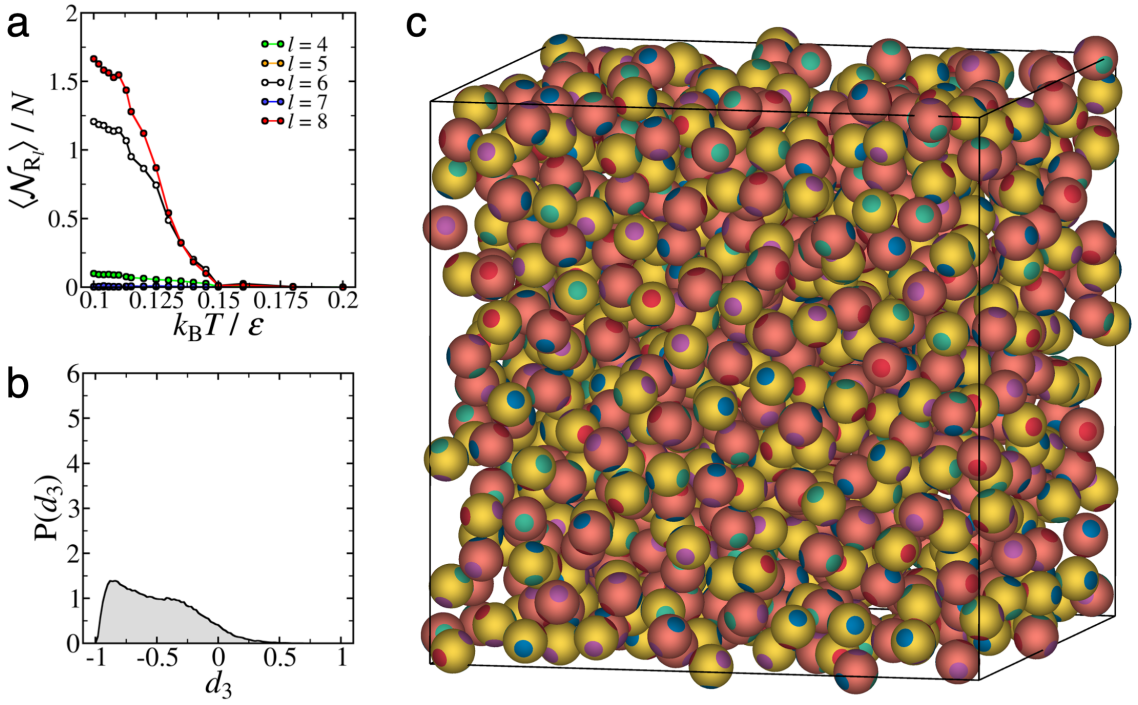


Figure 4.7: **Self-assembly of chromatic tetrahedral patchy particles.** Self-assembly in a two-component systems of $N = 1000$ chromatic tetrahedral patchy particles with patch half-angle $\theta = 25^\circ$ at $\rho^* = N\sigma^3/V = 0.5$. (**a**) Evolution of the average number of rings of length l ($\mathcal{N}_{R_l}$) with temperature. (**b**) Probability distribution function of the translational-order correlation parameter d_3, defined in Section 2.4, at a temperature of $k_B T/\varepsilon = 0.1$. (**c**) Representative snapshot of the resulting amorphous network at a temperature of $k_B T/\varepsilon = 0.1$.

4.4 | DIAMOND POLYTYPE SELECTION USING PATCHY WIDTHS

The two main diamond polytypes, cubic and hexagonal diamond, differ only in a single dimension, and can in fact be viewed as the limiting cases of a series of diamond polytype structures.[216,217] These different polytype structures can be considered as stacking hybrids of cubic and hexagonal diamond; however, the periodicity of any such polytype can always be described by a hexagonal unit cell.[217] Generally, it has been observed that the self-assembly of tetrahedral patchy particles into diamond gives rise to one of these hybrid diamond polytype structures, rather than a pure cubic or hexagonal diamond

crystal.[28,69,80] It is reasonable to anticipate that self-assembled diamond structures will consist of approximately equal proportions of cubic and hexagonal polytypes, due to a marginal free energy difference between them.[28] Similar observations and arguments have been made for the related tetrastack crystals formed from triblock patchy particles.[30,31,72] However, it was shown that the geometry of the patches was found to influence the relative stability of the cubic and hexagonal tetrastack structures,[72] with cubic tetrastack found to become more stable relative to hexagonal tetrastack with increasing patch width, most likely due to the cubic polytype having a more favourable rotational entropy.[68,72]

The influence of patch geometry on the relative stability of the two diamond polytypes composed of tetrahedral patchy particles, and their relative abundance in self-assembled diamond crystals, has not previously been investigated. This is presumably due to the limited window of patch widths where the spontaneous crystallisation of diamond can be observed for a one-component system of tetrahedral patchy particles.[27,28,82] As we have established, the two-component system under consideration here provides access to the diamond crystals, *via* self-assembly, for a much wider range of patch half-angles.

Figure 4.8a shows the dependence of the chemical potential difference between the cubic and hexagonal diamond structures ($\Delta\mu_{\mathrm{cd-hd}} = \mu_{\mathrm{cd}} - \mu_{\mathrm{hd}}$) as a function of the patch half-angle θ. As expected, we find that the chemical potential difference is relatively small, and is in fact of the same order as the free energy difference between the face-centred cubic and hexagonal close-packed structures formed by hard-spheres.[218,219] The hexagonal diamond is found to be marginally more stable for systems with narrow patches ($\theta \lesssim 12^{\circ}$), whereas cubic diamond is the more stable polytype for larger θ values.

Given the small chemical potential difference, we would not anticipate one polytype to be noticeably favoured over the other in self-assembled diamond crystals. To verify whether this is indeed the case, we show in Fig. 4.8b the θ dependence of the relative

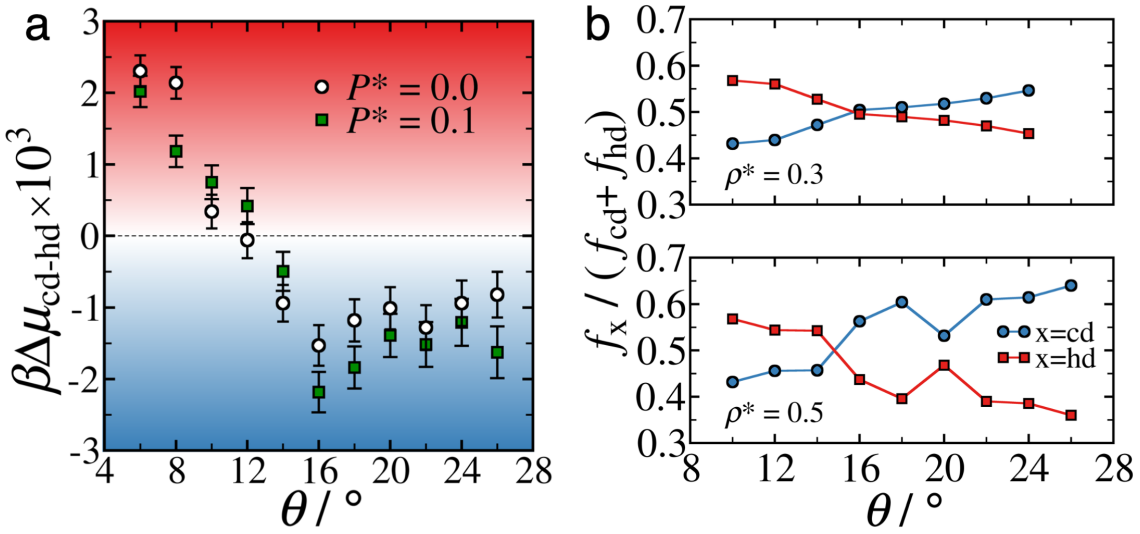


Figure 4.8: **Diamond polytype selection in two-component systems of tetrahedral patchy particles.** (**a**) Patch half-angle (θ) dependence of the chemical potential difference ($\Delta\mu$) between the cubic diamond (cd) and hexagonal diamond (hd) crystal structures of a two-component system of $N = 1800$ tetrahedral patchy particles at a temperature of $k_{\text{B}}T/\varepsilon = 0.1$ and pressures of $P^* = P\sigma^3/\varepsilon = 0.0, 0.1$. The error bars represent the standard error in the values, as determined by block-averaging. (**b**,**c**) Relative fraction of particles in a local cubic diamond (f_{cd}) and hexagonal diamond (f_{hd}) environment following spontaneous crystal formation in systems of $N = 4000$ two-component tetrahedral patchy particles with varying θ, at a constant density of (**b**) $\rho^* = N\sigma^3/V = 0.3$ and (**c**) $\rho^* = 0.5$. Each data point corresponds to an average over 25 independent simulations. Note that spontaneous nucleation is observed at different temperatures for different densities and patch half-angles.

fraction of particles in cubic diamond (f_{cd}) and hexagonal diamond (f_{hd}) environments following spontaneous crystallisation in two-component systems of $N = 4000$ tetrahedral patchy particles in Monte Carlo simulations. We investigated tetrahedral patchy particles with $\theta = 10°, 12°, ..., 26°$, where, for each of the nine values of θ considered, we performed 25 independent simulations at two different densities: $\rho^* = 0.3$ and $\rho^* = 0.5$. We find that the hexagonal diamond is more abundant than cubic diamond for systems with narrow patches ($\theta \lesssim 14°$), while the opposite is true for systems with wider patches. Additionally, the relative proportion of cubic diamond gradually increases (and hence, the relative proportion of hexagonal diamond gradually decreases) with increasing θ at both densities

considered. This trend generally agrees with our free energy calculations; however, we find that $\Delta\mu_{\mathrm{cd-hd}}$ plateaus around $\theta = 16°$. Therefore, it is likely that there is an additional kinetic driving force whose effect is also dependent on the patch width. This mirrors observations that have been reported regarding the crystallisation of ice, where it has been shown that kinetics play a dominant role in determining the relative fraction of cubic and hexagonal ice in large crystallites.[220,221]

4.5 | DISCUSSION

The self-assembly of the diamond lattice, either cubic or hexagonal or mixed, from a melt of identical tetrahedral patchy particles, despite being thermodynamically favoured, is hampered by the propensity for forming disordered arrested states for wide patches,[81] and for forming five-membered ring rich structures (clathrates) for small patches.[82] We have established here the conditions to overcome these two bottlenecks and suggested a reliable bottom-up route to diamond, simply by going from a one-component to a two-component system of tetrahedral patchy particles, where interactions are only allowed between patches on particles of different types.

Our two-component system of designer tetrahedral patchy particles crystallises into diamond much more readily than the one-component system, due to two reasons: (i) there is no driving force for the formation of odd-membered rings, thereby removing kinetic traps from the energy landscape; (ii) there is an enhanced thermodynamic driving force for crystallisation from the fluid phase due to a decrease in the concentration of potential bonding partners (*i.e.*, particles of another type) for each particle. The removal of kinetic traps from the energy landscape is "programmed" into the design of the two-component system, while the enhanced thermodynamic driving force can be considered an emergent feature of our design rules that also favours the formation of diamond. Understanding the

mechanism for promotion of crystallisation *via* the selection of correct ring sizes in the context of colloidal diamond will have general implications for programmed self-assembly of colloidal open crystals. Such mechanistic understanding also provides insight into the crystallisation process at the molecular level in related systems (e.g. tetrahedral networking forming liquids, including water, silica and silicon).

The specificity in the interactions between patches on different types of tetrahedral patchy particles in the two-component system can be experimentally realised through the use of DNA-mediated interactions.[73,203] The two-component system therefore presents itself as a synthetically feasible approach for the self-assembly of a diamond lattice of spheres, which remains a major outstanding problem. Our simulations predict the self-assembly of a mixture of cubic and hexagonal diamond by this route. However, the width of the patches can be used as a handle to control their relative proportions, with wider patches leading to a greater proportion of the cubic polytype. This is likely to be of particular importance in the context of the photonic applications of the self-assembled structures since random stacking diamond structures can display complete photonic band gaps, with those possessing more cubic character generally having superior photonic properties.[201]

CHAPTER 5

COLLOIDAL WATER

A salient feature of liquid water is the anomalous behaviour of its thermodynamic response functions upon cooling, the most famous being the density maximum at ambient pressure.[russo2021physics, 96–100] In an effort to explain the origin of water's thermodynamic anomalies, enhanced in supercooled states, Poole *et al.* suggested the presence of a first-order liquid-liquid phase transition (LLPT) line in the supercooled region of the pressure–temperature ($P-T$) phase diagram.[102] In this scenario, this transition line separates two liquid phases formed of transient hydrogen-bond networks – the low-density liquid (LDL) and high-density liquid (HDL) – and terminates at a liquid-liquid critical point (LLCP).[102] The anomalous behaviour of liquid water, along with water polyamorphism, was then suggested to be a manifestation of the presence of this LLPT. Recent numerical studies,[103,104] as well as experiments,[108,222,223] have provided strong support to this fascinating hypothesis.

However, due to the rapid formation of ice around the predicted critical temperature and pressure conditions, unambiguous verification of this two-liquid hypothesis in experiments has proved to be very challenging. Because of this, there has been much debate over the years as to whether the hypothesis holds water (see for example Refs. [103] and [224]). Therefore, there has also been much effort to design systems that unambiguously display this phenomenon without the hindrance of crystallisation.[81,109,225,226]

The work presented in this chapter was carried out in collaboration with Professor Francesco Sciortino, who performed the molecular dynamics simulations for TIP4P/Ice that were used to generate Fig. 5.10.

5.1 DESIGNING A COLLOIDAL MODEL OF WATER

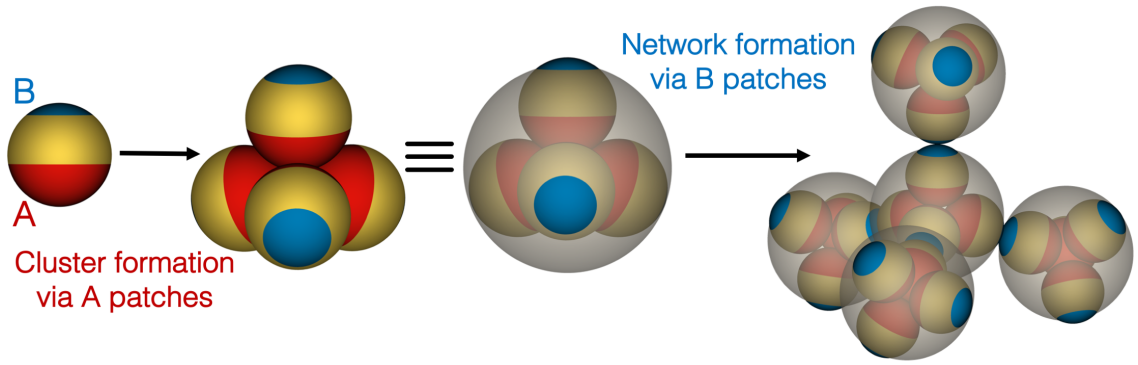


Figure 5.1: **Colloidal water model.** Schematic representation of the hierarchical self-assembly of triblock patchy particles leading to a colloidal model of water. The two patches, labelled A and B, are of different sizes and form bonds of different strengths. The A-patches (coloured red) form stronger bonds than the B-patches (coloured blue) so as to encode two-stage assembly upon cooling.

Colloidal patchy particles, due to their capacity to form network liquids *via* encoded self-assembly information,[81] combined with their synthetic availability,[73,86,91,176,227] are ideally suited to investigate universal aspects of the LLPT, as well as potentially facilitating detailed experimental investigations at single-particle resolution. Therefore, guided by recent advances in programming their hierarchical self-assembly[136] and in understanding the necessary conditions for facilitating a LLPT – bond flexibility[81,109] and network interpenetration[109,225] – we rationally designed a colloidal analogue of water. Figure 5.1 schematically illustrates this "colloidal water" model. We considered designer triblock patchy particles[67,86,91] with two distinct attractive patches that encode tetrahedrality – key to the uniqueness of water.[100] The tetrahedrality emerges as the triblock patchy particles undergo two-stage assembly upon cooling. The energetics and geometry of the patches, labelled A and B, encode the desired staged-assembly information into the particles.[31,136,201] The energetics are chosen to facilitate the formation of discrete

tetrahedral clusters, initially driven by strong AA interactions, and then a tetrahedral network fluid *via* weaker BB interactions, as shown in Fig. 5.1. The width of the A-patches is judiciously chosen so as to favour the formation of a tetrahedral cluster fluid upon completion of the first stage of assembly.[31,136,201]

The width of each B-patch is instead chosen to favour its interaction with only one other B-patch. The discrete tetrahedral clusters then behave as secondary building blocks, similar to tetrahedral patchy particles, that can interact with one another via B-patches at lower temperatures to drive a second stage of assembly, leading to the formation of a liquid network. In this case, the patch widths are chosen not only to enforce the desired valency constraints, but also to maximise the flexibility of the bonds to hinder the onset of crystallisation.[81] As a result, the tetrahedral clusters formed by the triblock patchy particles can deviate from the ideal tetrahedral symmetry. Note that the volume occupied by a tetrahedral cluster is less than that of a spherical patchy particle of equivalent size, as shown in Fig. 5.1, thereby easing the formation of locally interpenetrating networks.

We employed the Kern-Frenkel pair potential,[204] which has been extensively used to study patchy particles, to model the triblock patchy particles. Each particle, with a hard core diameter σ, has, at opposite poles, two distinct circular attractive patches, labelled A and B, having half-angles of θ_{A} and θ_{B}, respectively. The effective potential for a pair of patchy particles v_{ij} is

$$v_{ij}(\mathbf{r}_{ij},\mathbf{\Omega}_i,\mathbf{\Omega}_j) = v_{ij}^{\mathrm{hs}}(r_{ij}) + \sum_{\alpha,\beta=\{A,B\}} v_{\alpha\beta}^{\mathrm{sw}}(r_{ij}) f(\mathbf{r}_{ij},\hat{\mathbf{n}}_i^{\alpha},\hat{\mathbf{n}}_j^{\beta}) \tag{5.1}$$

where $r_{ij} = |\mathbf{r}_{ij}|$ is the centre-to-centre distance between particles i and j and $\mathbf{\Omega}_i$ and $\mathbf{\Omega}_j$ describe the orientations of particles i and j, respectively. In Eqn. 5.1, v_{ij}^{hs} is the hard-sphere

pair potential and v_{ij}^{sw} is a square-well potential, given by

$$v_{\alpha\beta}^{\mathrm{sw}}(r_{ij}) = \begin{cases} -\varepsilon_{\alpha\beta} & \text{if } \sigma \leq r_{ij} \leq (1+\delta_{\alpha\beta})\sigma \\ 0 & \text{otherwise} \end{cases} \tag{5.2}$$

where $\varepsilon_{\alpha\beta}$ and $\delta_{\alpha\beta}$ control the depth and range, respectively, of the attraction of a patch α-patch β interaction. The factor $f(\mathbf{r}_{ij}, \hat{\mathbf{n}}_i^{\alpha}, \hat{\mathbf{n}}_j^{\beta})$ controls the angular dependence of the interaction between two patches, and is given by

$$f(\mathbf{r}_{ij}, \hat{\mathbf{n}}_i^{\alpha}, \hat{\mathbf{n}}_j^{\beta}) = \begin{cases} 1 & \text{if } \hat{\mathbf{n}}_i^{\alpha} \cdot \hat{\mathbf{r}}_{ij} > \cos\theta_{\alpha} \text{ and } \hat{\mathbf{n}}_j^{\beta} \cdot \hat{\mathbf{r}}_{ji} > \cos\theta_{\beta} \\ 0 & \text{otherwise} \end{cases} \tag{5.3}$$

where $\hat{\mathbf{n}}_i^{\alpha}$ is a normalised vector from the centre of particle i in the direction of the centre of patch α on its surface, and thus depends on $\mathbf{\Omega}_i$. Similarly, $\hat{\mathbf{n}}_j^{\beta}$ is a normalised vector from the centre of particle j in the direction of the centre of patch β, and thus depends on $\mathbf{\Omega}_j$. The total potential energy of the system was calculated by summing over the contributions from all distinct pairs ($\mathcal{V} = \sum_{i \neq j} v_{ij}$).

We employed $\varepsilon_{\mathrm{AA}} = 5\varepsilon_{\mathrm{BB}}$ along with $\varepsilon_{\mathrm{AB}} = 0$ to encode a two-stage self-assembly process upon cooling[136]. The choice of $\varepsilon_{\mathrm{AB}} = 0$, realisable *via* DNA-mediated interactions, facilitates staged assembly and allows for the use of a wider A patch without compromising the formation of self-limiting tetrahedral clusters at intermediate temperatures. The ranges of the interactions are set by $\delta_{\mathrm{AA}} = 0.05$ and $\delta_{\mathrm{BB}} = 0.2$ (the value of δ_{AB} being irrelevant since $\varepsilon_{\mathrm{AB}} = 0$). The longer range of BB interactions facilitates the formation of a tetrahedral network liquid at low temperatures. In the present study, we used reduced units: the length in units of σ, the energy in units of $\varepsilon_{\mathrm{BB}}$, the temperature in units of $\varepsilon_{\mathrm{BB}}/k_{\mathrm{B}}$, with the Boltzmann constant $k_{\mathrm{B}} = 1$.

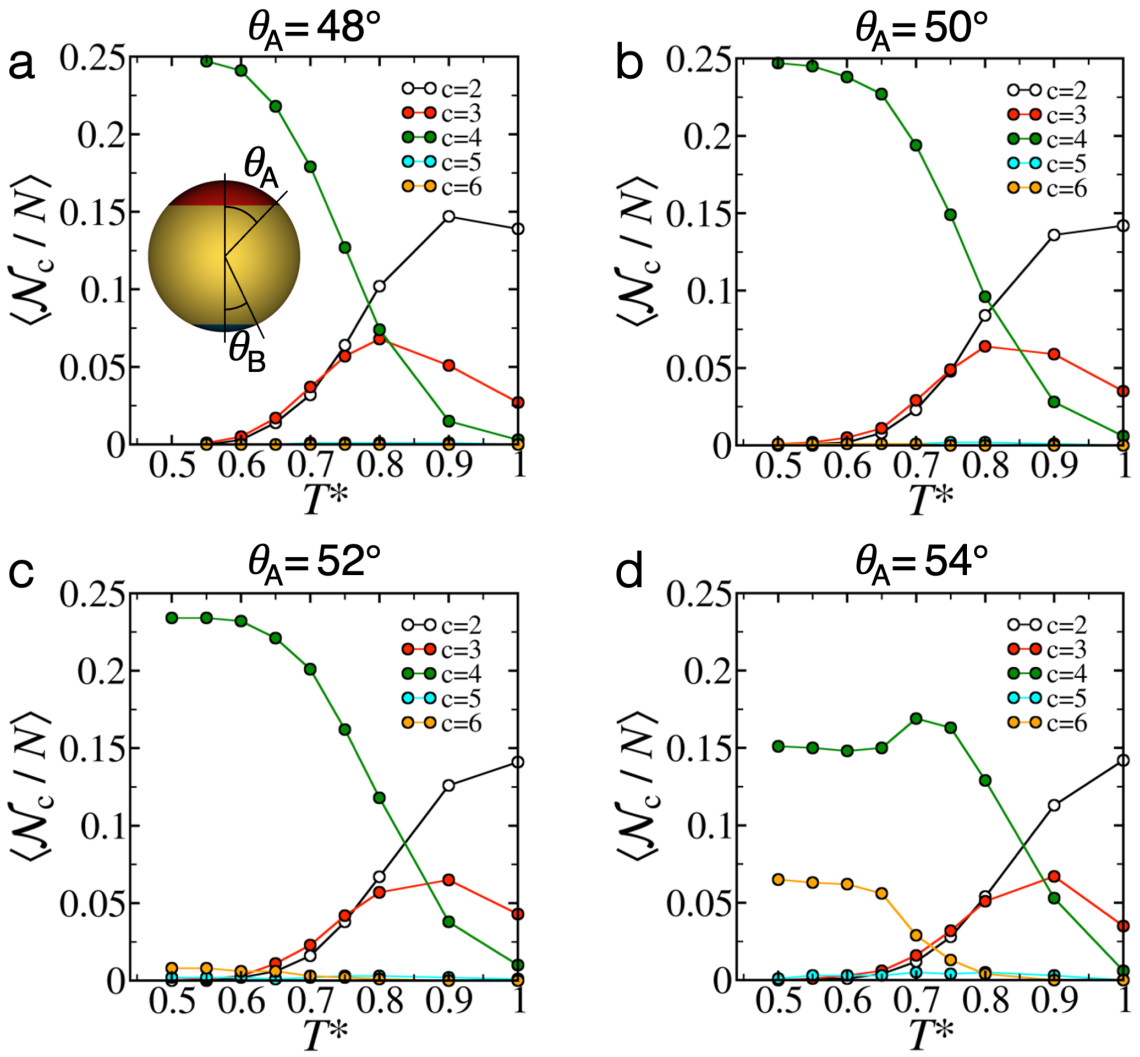


Figure 5.2: **Evolution of cluster distributions with temperature in systems of triblock patchy particles for different A-patch widths.** Evolution of the average number of clusters ($\mathcal{N}_c$) of size c $= [2-6]$ with temperature (T^*) along a series of NVT simulations for systems of $N = 1000$ triblock patchy particles with $\delta_{AA} = 0.05\sigma$, $\delta_{BB} = 0.2\sigma$, $\varepsilon_{AA} = 5\varepsilon_{BB}$, $\varepsilon_{AB} = 0$, $\theta_B = 26^\circ$ and $\theta_A =$ (**a**) 48°, (**b**) 50°, (**c**) 52°, (**d**) 54° at a density of $\rho^* = 0.2$. The inset on panel **a** shows a representative triblock patchy particle with $\theta_A = 48^\circ$ and $\theta_B = 26^\circ$.

To ensure the success of the hierarchical self-assembly scheme laid out in Fig. 5.1, we tuned the widths of the patches so that the formation of tetrahedra was favoured over other clusters, such as trimers or octahedra. We carried out a series of NVT simulations

at a density of $\rho^* = 0.2$ for systems of $N = 1000$ triblock patchy particles with different sets of parameters having distinct θ_A values: $\delta_{AA} = 0.05\sigma$, $\delta_{BB} = 0.2\sigma$, $\varepsilon_{AA} = 5\varepsilon_{BB}$, $\varepsilon_{AB} = 0$, $\theta_B = 26^\circ$ and $\theta_A = 48^\circ, 50^\circ, 52^\circ, 54^\circ$. Figure 5.2 shows the evolution of cluster distributions in the size range c $= [2,6]$ (where $\mathcal{N}_c$ is the number of clusters of size c) with temperature (T^*). A comparison of Figs. 5.2b and 5.2c reveals that for $\theta_A > 50^\circ$, octahedral clusters begin to compete with tetrahedra in the first stage of assembly. Therefore, we selected the value $\theta_A = 50^\circ$ for the present body of work. Additionally, we chose $\theta_B = 26^\circ$ to allow for maximal flexibility in the BB-bonds. Since it is only just above the threshold value beyond which more than one bond may form ($\theta_{max} \approx 24.6^\circ$, as given by the inequality $\sin(\theta_{max}) \leq [2(1+\delta)]^{-1}$ when $\delta = 0.2\sigma$), this choice ensured that our design criterion of a single BB-bond per B patch was met.

5.2 | THERMODYNAMIC ANOMALIES OF COLLOIDAL WATER

In order to establish that the chosen system of triblock patchy particles can indeed be considered as a colloidal analogue of water, we first demonstrate that it is able to capture water's thermodynamic anomalies using Monte Carlo simulations. All Monte Carlo simulations were carried out with systems of $N = 1000$ triblock patchy particles contained in a cubic box under periodic boundary conditions, using the minimum image convention. Each triblock patchy particle was treated as a rigid body, whose orientational degrees of freedom were represented by quaternions. The potential energy was calculated using a spherical cutoff of $\sigma(1+\delta_{BB})$ and a cell-list was used for efficiency[112]. To enhance sampling in systems composed of clusters, we employed a combination of translational and rotational single-particle and cluster moves.

Figure 5.3a shows the reduced temperature ($T^* \equiv k_B T / \varepsilon_{BB}$, where k_B is the Boltzmann constant and ε_{BB} the well depth of patch B-patch B interactions) dependence of the reduced

density ($\rho^* \equiv \rho\sigma^3$) along different isobars as determined by Monte Carlo simulations. At low temperatures ($T^* \leq 0.12$), two sets of simulations were carried out over the same range of state points, starting from a tetrahedral cluster fluid of triblock patchy particles, where the initial density was set to $\rho^* = 0.2$ for one set of simulations and to $\rho^* = 0.4$ for the other set. For each of these simulations, 3×10^8 Monte Carlo cycles were performed in order to ensure that equilibrium was attained. At higher temperatures, 1×10^8 Monte Carlo cycles were performed, starting with a density of $\rho^* = 0.4$.

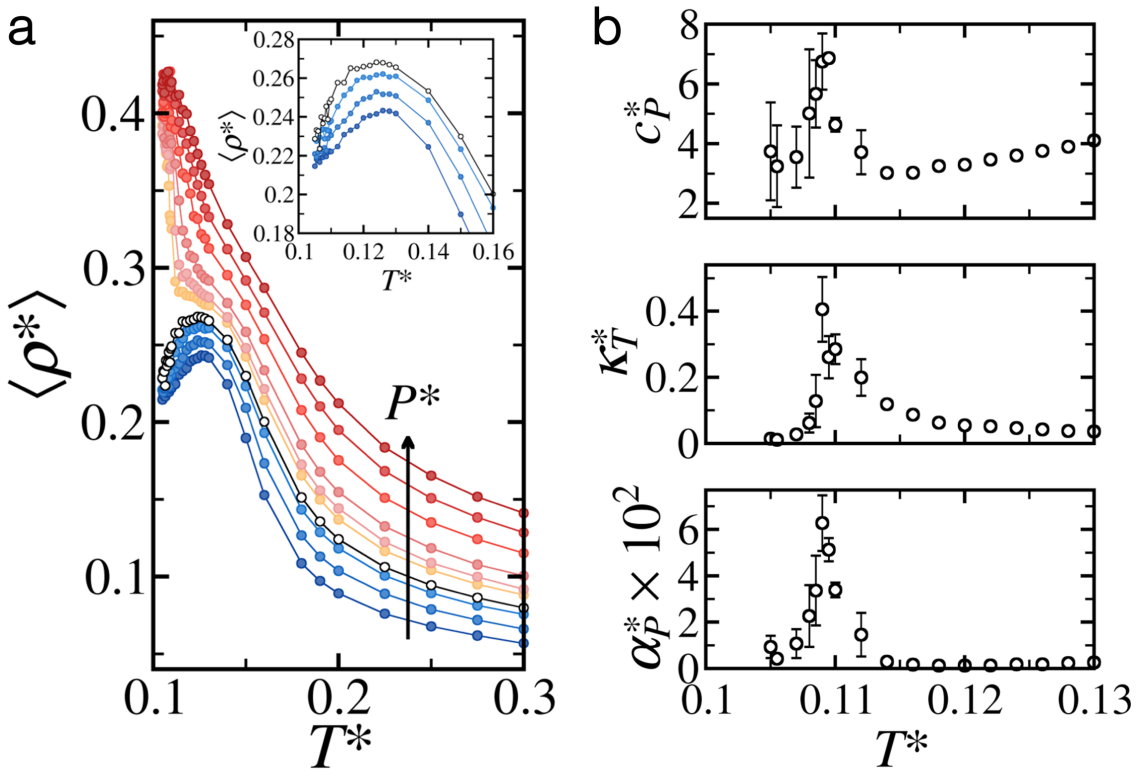


Figure 5.3: **Thermodynamic anomalies of colloidal water.** (**a**) Evolution of the reduced density ρ^* as a function of reduced temperature T^* for different reduced pressures P^*, where $P^* \times 10^3 = 5, 6, 7, 7.5, 8.5, 9, 10, 12, 14, 16$. The arrow indicates the direction of increasing P^*. The inset highlights the density maximum for $P^* \times 10^3 = 5, 6, 7, 7.5$. (**b**) Evolution of the reduced thermal expansion coefficient (α_P^*), isothermal compressibility (κ_T^*) and the isobaric heat capacity (c_P^*) as a function of T^* at $P^* = 0.0085$ (which is above the critical pressure). Error bars represent the standard deviation over 5 sets of Monte Carlo trajectories, each comprising 1×10^8 MC cycles.

Below a certain reduced pressure ($P^* \equiv P\sigma^3/\varepsilon_{\mathrm{BB}}$), the colloidal water model displays a density maximum upon cooling. Upon further cooling, ρ^* approaches either a low or a high density value depending on the pressure. From the *NPT* simulations, we calculated the reduced isobaric thermal expansion coefficient (α_P^*), isothermal compressibility (κ_T^*) and the isobaric heat capacity (c_P^*) by computing the covariance and variance in the volume and enthalpy (H) as:

$$\alpha_P = \frac{\langle HV\rangle - \langle H\rangle\langle V\rangle}{N\langle V\rangle k_{\mathrm{B}}T^2} = \frac{k_{\mathrm{B}}}{\varepsilon_{\mathrm{BB}}}\alpha_P^* \tag{5.4}$$

$$\kappa_T = \frac{\langle V^2\rangle - \langle V\rangle^2}{N\langle V\rangle k_{\mathrm{B}}T} = \frac{\sigma^3}{\varepsilon_{\mathrm{BB}}}\kappa_T^* \tag{5.5}$$

$$c_P = \frac{\langle H^2\rangle - \langle H\rangle^2}{Nk_{\mathrm{B}}T^2} = k_{\mathrm{B}}c_P^* \tag{5.6}$$

These thermodynamic quantities, as well as the average density, were computed from 5 independent *NPT* simulations, consisting of 1×10^8 Monte Carlo cycles, following equilibration at each temperature and pressure considered. Figure 5.3b shows the temperature dependence of the isobaric thermal expansion coefficient (α_P^*), isothermal compressibility (κ_T^*) and the isobaric heat capacity (c_P^*) at a select pressure, highlighting that, upon cooling, colloidal water shows non-monotonic behaviour in its thermodynamic response functions.

Figure 5.4 shows the dependence of ρ^* and the fraction of bonds f_b – defined as the fraction of bonded B patches, a quantity directly reflective of the potential energy of the system – on P^*. We find that, below a certain T^*, there is a discontinuous jump in ρ^* and f_b, as P^* changes, signalling a first-order phase transition. By contrast, ρ^* and f_b change continuously with P^* above this critical temperature, indicating that there is a LLCP. Interestingly, we note that fraction of bonds formed passes through a minimum at $T^* = 0.112$ as pressure is increased.

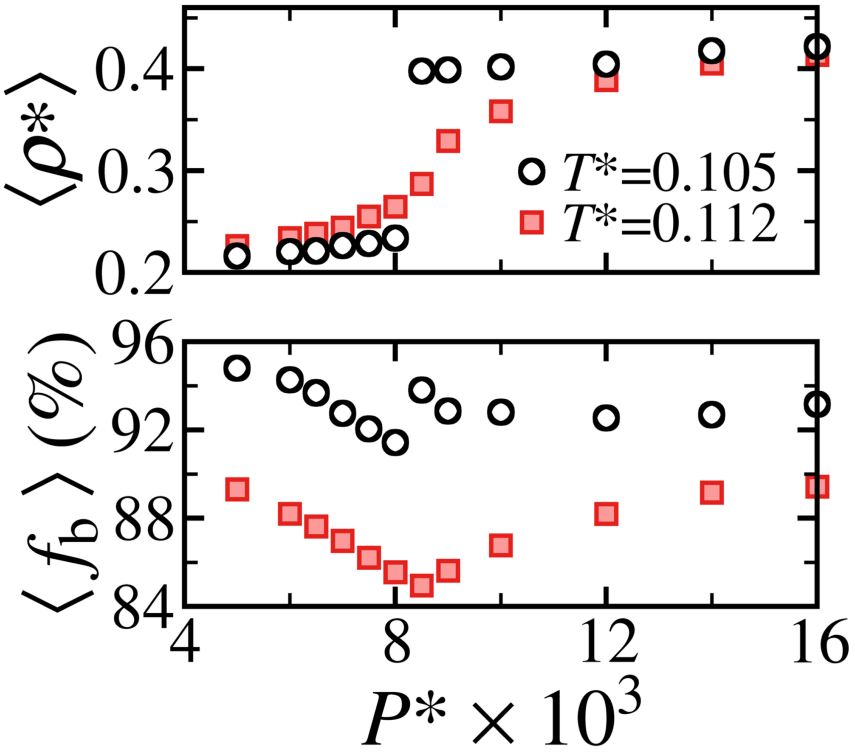


Figure 5.4: **Liquid-liquid phase transition of colloidal water.** Dependence of ρ^* and fraction of BB bonds formed (f_b) on P^*, at $T^* = 0.105$ and $T^* = 0.112$.

In order to identify the location of the liquid-liquid critical point in the colloidal water system, we merged information collected from the Monte Carlo simulations in order to generate an estimate of the density of states, $\hat{\Omega}(E,V)$. In the isothermal-isobaric (NPT) ensemble, the partition function at a given pressure, P, and temperature, T, is[104,228]

$$\mathcal{Z}(P,\beta) = \sum_E \sum_V \hat{\Omega}(E,V) \mathrm{e}^{-\beta(E+PV)} = \mathrm{e}^{-\beta G(P,\beta)} \tag{5.7}$$

where E is the energy of the system, V is the volume and G is the Gibbs free energy. We estimated the density of states by performing R simulations at different temperatures and pressures, where the total set of state points considered was given by $\{T_i, P_i\}, i = 1,\ldots,R$. For each simulation, a histogram (H_i) of the energies and volumes sampled was generated

using data from N_i equally spaced configurations along the trajectory. We defined an estimate for the density of states at discrete values of energy and volume, using data from a single simulation as

$$\Omega_i(E,V) = \frac{\mathrm{H}_i(E,V)}{\mathrm{N}_i}\mathrm{e}^{-\beta_i(E+P_iV)}\mathrm{e}^{+\beta_i G(P_i,\beta_i)} \tag{5.8}$$

However, each of the R simulations only provides information of the density of states for a finite portion of the phase space; hence, a better estimate was obtained by combining all the information gathered from the R simulations. This "best guess" for the density of states was written as a linear combination of these individual estimates, combined with a weight factor $\omega_i(E,V)$, as

$$\hat{\Omega}^b(E,V) = \sum_{i=1}^{R} \omega_i(E,V)\frac{\mathrm{H}_i(E,V)}{\mathrm{N}_i}\mathrm{e}^{-\beta_i(E+P_iV)}\mathrm{e}^{+\beta_i G(P_i,\beta_i)} \tag{5.9}$$

Conventionally, it is assumed that the "random" variable $\mathrm{H}_i(E,V)$ has Poisson statistics. Then it becomes possible to optimise Eqn. 5.9 by minimising the variance of $\hat{\Omega}^b(E,V)$ using the method of Lagrange multipliers, under the constraint that $\sum_i^R \omega_i = 1$. As a result

$$\hat{\Omega}^b(E,V)\frac{\sum_{i=1}^{R}\mathrm{H}_i(E,V)}{\sum_{i=1}^{R}\mathrm{e}^{-\beta_i(E+P_iV)}\mathrm{e}^{+\beta_i G(P_i,\beta_i)}\mathrm{N}_i} \tag{5.10}$$

and

$$\mathrm{e}^{-\beta_i G(P_i,\beta_i)} = \sum_E\sum_V \hat{\Omega}^b(E,V)\mathrm{e}^{-\beta_i(E+P_iV)} \tag{5.11}$$

When the number of samples used to generate each of the R histograms is the same (*i.e.*, $\forall i : \mathrm{N}_i = \mathrm{N}$), the above equations can be simplified by writing

$$S(E,V)/k_\mathrm{B} = \ln\left(\frac{\sum_{i=1}^{R}\mathrm{H}_i(E,V)}{\mathrm{N}}\right) - \ln\left(\sum_{i=1}^{R}\mathrm{e}^{-\beta_i(E+P_iV)}\mathrm{e}^{+\beta_i G(P_i,\beta_i)}\right) \tag{5.12}$$

and

$$G(P_i,\beta_i) = -k_{\mathrm{B}}T \ln\left(\sum_E \sum_V \mathrm{e}^{S(E,V)/k_{\mathrm{B}} - \beta_i(E+P_iV)}\right) \tag{5.13}$$

Evaluation of the exponential terms can be numerically unstable. Rewriting these equations in terms of the entropy allows us to make use of $\ln(\mathrm{e}^x) = a + \ln(\mathrm{e}^{x-a})$ in order to improve numerical precision. Eqns. 5.12 and 5.13 can then be solved self-consistently in an iterative procedure taking $G_i = 0$ for all i as an initial guess. We assume the values of the Gibbs free energies have converged once the sum squared difference between consecutive estimates is less than a tolerance value of 10^{-7}. The converged solutions provided an estimate for the values of $G(P,\beta)$ up to some additive constant c. From these estimates, we obtained values for the density of states. It was, therefore, possible to predict the probability of observing a state with energy E and volume V at any relevant state point (P,β) using

$$p(E,V|\beta,P) = \frac{\cancel{\mathrm{e}^{-c}}\,\mathrm{e}^{S(E,V)/k_{\mathrm{B}} - \beta(E+PV)}}{\sum_E \sum_V \cancel{\mathrm{e}^{-c}}\,\mathrm{e}^{S(E,V)/k_{\mathrm{B}} - \beta(E+PV)}} \tag{5.14}$$

Figure 5.5a shows the probability distribution of the density for various pressures at a temperature of $T^* \approx 0.1075$. We see that, for a pressure of $P^* = 0.0082$, the probability distribution of the density is bimodal, a signature of critical phenomena and signals that regions of different density can coexist in this system.

To then pinpoint the critical point, we followed a similar procedure recently applied in the study of a molecular model of water.[104] First we computed the approximate asymptotic expression for the probability distribution of the magnetisation for the Ising model, given by:

$$P_{\mathrm{Ising}}(M) = A \exp\left[-\left(\mathrm{a}\frac{M}{M_0} + \mathrm{c}\right)\left(\frac{M}{M_0} - 1\right)^2\right] \tag{5.15}$$

where $\mathrm{a} = 0.158$; $\mathrm{c} = 0.776$; $M_0 = 1.1341655$ (and is included to ensure the distribution has unit variance); and A is a normalisation factor, such that $\int P_{\mathrm{Ising}}(M)\mathrm{d}M = 1$. Then,

to identify the critical temperature (T_c) and critical pressure (P_c), we calculated the order parameter distribution $P(\mathrm{M})$, where $\mathrm{M} = \rho^* - sv^*$ is a combination of the density, potential energy per particle – $v^* = \mathcal{V}/(N\varepsilon_{\mathrm{BB}})$, where $\mathcal{V}$ is the total potential energy – and field-mixing parameter (s) using the probability distributions computed using Eqns. 5.12, 5.13 and 5.14 for various state points (β,P), ensuring to shift the distribution by its average value so it is centred at zero, and scaled according to its variance to make sure the distribution has unit variance.[229] We then performed a nonlinear fit of the parameters β, P and s until we found $P(\mathrm{M})$ that closely matches the distribution of the magnetisation at the critical point of the 3D Ising model given by $P_{\mathrm{Ising}}(M)$, as shown in Fig. 5.5b, confirming the presence of a LLCP in colloidal water.

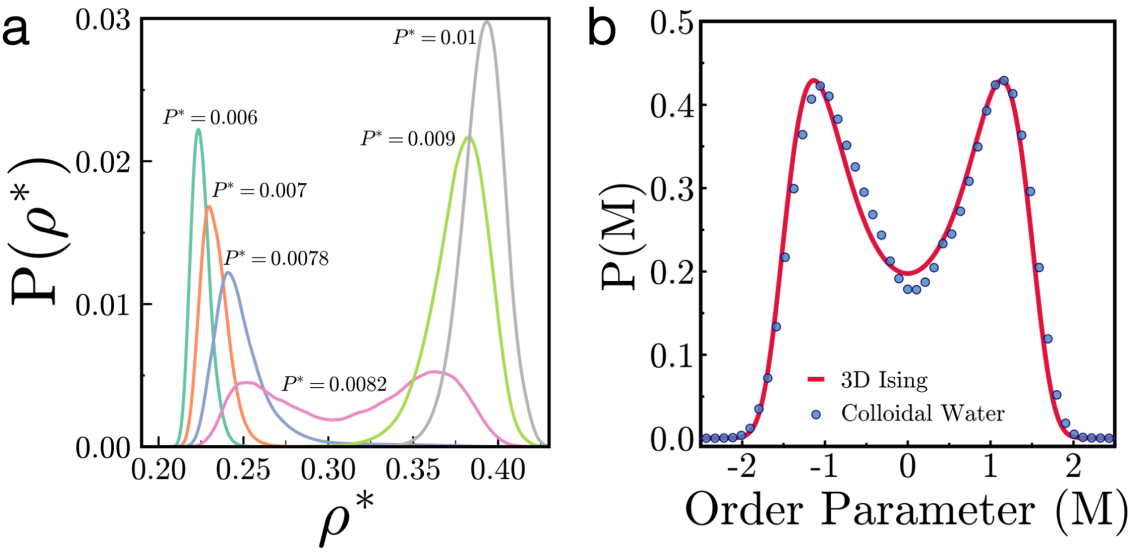


Figure 5.5: **Liquid-liquid critical point of colloidal water.** (**a**) Probability distribution of the density (ρ^*) for different pressures ($P^* \times 10^3 = 6, 7, 7.8, 8.2, 9, 10$), at a temperature of $T^* \approx 0.1075$, as calculated using histogram reweighting (see text). (**b**) Distribution of the order parameter M for colloidal water (blue symbols), calculated using histogram reweighing, with $T^* \approx 0.1075$, $P^* \approx 0.0082$ and $s \approx 0.627$ compared with the corresponding 3D Ising universal distribution (red solid line).

5.3 | TOPOLOGICAL NATURE OF THE LIQUID-LIQUID TRANSITION

Several order parameters, based on geometric or energetic criteria, have been proposed to characterise the transition.[230–237] In particular, the local structure index (LSI)[230] and the r_5-parameter[231] – two order parameters that effectively measure the distance between the first and second coordination shells – have been routinely applied. However, over the years, it has become increasingly apparent that a proper description of the LLPT requires the development of order parameters which include information beyond that of the single-molecule neighbourhood. This led to the introduction of other order parameters, such as ζ[238] and V_4,[232] which include information on the connectivity of the hydrogen-bond network.[236] It has also become clear that network interpenetration[225,239,240] plays a key role in the LLPT in tetrahedral liquids[81,109,225,241] with the LDL being composed of a single random tetrahedral network and the HDL consisting of two (or more[225]) disordered, but locally interpenetrating, networks. In this context, a structure-based order parameter that fundamentally distinguishes the two liquids at the microscopic level will be important to develop our understanding of the physical origin of the LLPT.

Topological concepts have become central in the description of physical,[242–244] biological,[245,246] social,[247] and financial[248,249] networks. The topological properties of the interaction matrix,[243] have been shown to affect the response of the system to external perturbation and to play a key role in phase transitions. In this context, a pertinent question is whether the LLPT also has a topological character. Therefore, in order to identify any topological features, we inspected configurations of the liquids, and found that linked and knotted ring structures were noticeably present in the HDL, but seemingly absent from the LDL. Figures 5.6a and 5.6b show representative snapshots of the two liquid phases, where examples of these topologically complex motifs in the HDL networks are

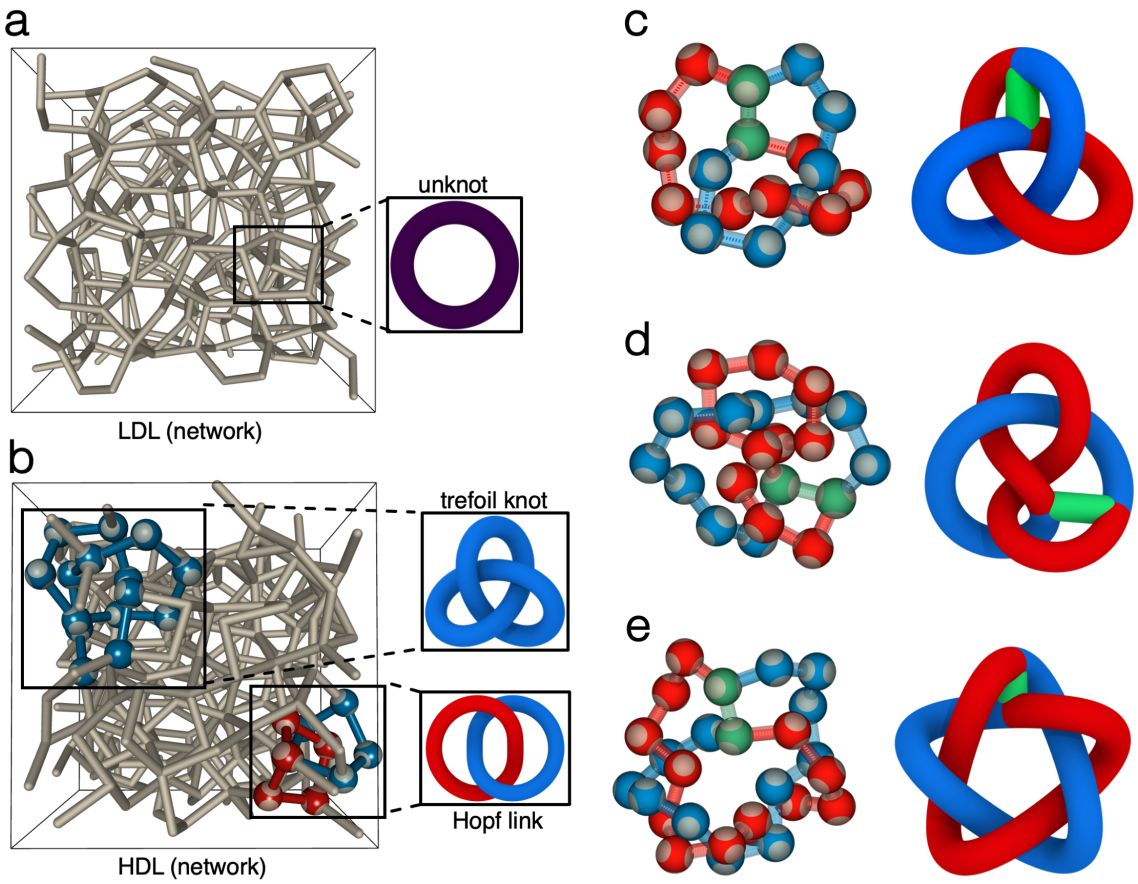


Figure 5.6: **Links and knots in colloidal water.** Representative snapshots of the (**a**) low-density liquid (LDL) and (**b**) high-density liquid (HDL) networks of colloidal water at a temperature below the critical temperature T_c and pressures either side of the critical pressure P_c ($T^* = 0.105$, $P^* = 0.005$ and $P^* = 0.016$, respectively). Here, vertices correspond to the centres of tetrahedral clusters, visualised in a reduced representation as tetrahedral patchy particles, while edges indicate existing BB bonds. In panel (**a**) a ring is highlighted in the LDL network, which can be considered to be an unknot. In panel (**b**) tetrahedral clusters in the HDL network forming a trefoil knot (top) and a Hopf link (bottom) are highlighted. (**c**-**e**) Illustrative snapshots of (**c**) trefoil, (**d**) figure-eight, and (**e**) cinquefoil theta-curves found in the HDL networks and their corresponding idealised representations.

highlighted: a trefoil knot and a Hopf link[250]. In addition to knots and links, we found a large number of knotted theta-curves[251,252] in the HDL networks, which can be viewed as two entangled fused rings (*i.e.*, rings that share at least two vertices). Examples of these knotted theta-curves are shown in Figs. 5.6c-e.

To investigate the importance of such topological features in the LLPT, we quantified the degree of "entanglement" in the LDL and HDL networks using the concept of helicity. The helicity has previously been used to provide a measure of the topological properties of vector fields, including magnetic fields[253] and vortex fields in fluids.[254] This scalar quantity measures the amount of entwining in the set of closed curves contained within a system. For the particle-based networks considered here, these closed curves correspond to the set of rings formed by bonded particles. Each pair of disjoint (and therefore distinct) rings R_i and R_j contributes to the helicity with a term proportional, in essence, to how many times the two rings wind around one another (alternatively, this can be thought of as the number of times ring R_i pierces the surface bounded by ring R_j). Also, each individual ring contributes with a term, which is proportional to how many times it loops around itself. Formally, the helicity is defined as a double sum over the total number of rings $\mathcal{N}_\mathrm{R}$ of the double line integral, known as the Gauss linking integral:

$$\mathcal{H} = \sum_{i=1}^{\mathcal{N}_\mathrm{R}} \sum_{j \geq i}^{\mathcal{N}_\mathrm{R}} \frac{1}{4\pi} \oint_{\mathrm{R}_i} \oint_{\mathrm{R}_j} \frac{r_j - r_i}{|r_j - r_i|^3} \cdot (\mathrm{d}r_j \times \mathrm{d}r_i) \tag{5.16}$$

where r_i and r_j are points on the two rings R_i and R_j, respectively. In Eqn. 5.16, $\mathrm{d}r_i$ and $\mathrm{d}r_j$ are infinitesimal vectors tangential to the two rings R_i and R_j located at points r_i and r_j, respectively. In the case where $i \neq j$, the Gauss linking integral gives the linking number (Lk_{ij}) of the two curves and takes on only integer values, and for $i = j$, it corresponds to the writhe (Wr_i) of a single curve and can take on any real value. Equation 5.16 can therefore be rewritten as the sum of the linking number and the writhe

$$\mathcal{H} = \sum_{i>j}^{\mathcal{N}_\mathrm{R}} Lk_{ij} + \sum_{i=1}^{\mathcal{N}_\mathrm{R}} Wr_i \tag{5.17}$$

In order to establish the prevalence of topologically complex motifs in a liquid network,

we have adapted the concept of the helicity to define two quantities: the network linking number[243] ($\mathcal{L}_n$) and the network writhe ($\mathcal{W}_n$). To emphasise the degree of entanglement in a network, $\mathcal{L}_n$ and $\mathcal{W}_n$ are computed by summing up the absolute values of Lk_{ij} and Wr_i, respectively, which as such can assume positive or negative values, to ignore the intrinsic orientation of the closed curves (in other words, we ignore the chirality of the topological objects). Additionally, the writhe is only computed for the set of $\mathcal{N}_\mathrm{k}$ knotted objects, which includes knotted rings and pairs of fused rings that contain a knotted path. Including the latter in $\mathcal{N}_\mathrm{k}$ ensures that the contributions of theta-curves (such as those shown in Figs. 5.6c-e) are captured by $\mathcal{W}_n$. We formally define $\mathcal{L}_n$ and $\mathcal{W}_n$ as

$$\mathcal{L}_n = \sum_{i>j}^{\mathcal{N}_\mathrm{R}} |Lk_{ij}| \quad \text{and} \quad \mathcal{W}_n = \sum_{i=1}^{\mathcal{N}_\mathrm{k}} |Wr_i| \tag{5.18}$$

We computed $\mathcal{L}_n$ and $\mathcal{W}_n$ by first identifying all rings in the system up to a maximum size of l_max (which defines the maximum number of particles forming a ring), and then calculating either (i) the linking number for all disjoint rings or (ii) the writhe for each ring that is knotted and for entangled fused rings (such as the knotted theta-curves shown in Figs. 5.6c-e). This then becomes akin to identifying linked and knotted paths in the spatial embedding of a graph.[252,255] The rings are composed of discrete line segments and so can be considered as closed polygonal paths. As a result, the linking number can be computed using the expression for polylines[256]:

$$Lk_{ij}(\mathrm{R}_i, \mathrm{R}_j) = \frac{1}{4\pi} \sum_{kl} \lambda_{kl} \tag{5.19}$$

where λ_{kl} is the contribution to the Lk_{ij} from a pair of line segments k and l belonging to rings i and j, respectively, and

$$\lambda_{kl} = \text{atan}\left(\frac{\mathbf{a}\cdot(\mathbf{b}\times\mathbf{c})}{|\mathbf{a}||\mathbf{b}||\mathbf{c}|+(\mathbf{a}\cdot\mathbf{b})|\mathbf{c}|+(\mathbf{c}\cdot\mathbf{a})|\mathbf{b}|+(\mathbf{b}\cdot\mathbf{c})|\mathbf{a}|}\right)+ \text{atan}\left(\frac{\mathbf{c}\cdot(\mathbf{d}\times\mathbf{a})}{|\mathbf{c}||\mathbf{d}||\mathbf{a}|+(\mathbf{c}\cdot\mathbf{d})|\mathbf{a}|+(\mathbf{a}\cdot\mathbf{c})|\mathbf{d}|+(\mathbf{d}\cdot\mathbf{a})|\mathbf{c}|}\right) \tag{5.20}$$

where $\mathbf{a} = r_l - r_k$, $\mathbf{b} = r_l - r_{k+1}$, $\mathbf{c} = r_{l+1} - r_{k+1}$, $\mathbf{d} = r_{l+1} - r_k$.[256]

The writhe has previously been used to study folding in protein systems[257] and supercoiling in DNA.[258] In these studies, proteins and DNA strands are modelled as polymer chains made up of straight line segments. Similarly, we computed the writhe using[258]

$$Wr_i(\mathrm{R}_i) = \frac{1}{2\pi}\sum_{k\neq l}\omega_{kl} \tag{5.21}$$

where ω_{kl} is the contribution to the writhe from the segments k and l on ring i defined as[258]

$$\omega_{kl} = \text{sgn}\{[(r_{l+1}-r_l)\times(r_{k+1}-r_k)]\cdot\mathbf{a}\}\left(\sin^{-1}(n_1\cdot n_2)+\sin^{-1}(n_2\cdot n_3)+\sin^{-1}(n_3\cdot n_4)+\sin^{-1}(n_4\cdot n_1)\right) \tag{5.22}$$

where sgn$(\cdot)$ is the sign function and

$$n_1 = \frac{\mathbf{a}\times\mathbf{d}}{|\mathbf{a}\times\mathbf{d}|}, \quad n_2 = \frac{\mathbf{d}\times\mathbf{c}}{|\mathbf{d}\times\mathbf{c}|}, \quad n_3 = \frac{\mathbf{c}\times\mathbf{b}}{|\mathbf{c}\times\mathbf{b}|}, \quad n_4 = \frac{\mathbf{b}\times\mathbf{a}}{|\mathbf{b}\times\mathbf{a}|} \tag{5.23}$$

where **a**, **b**, **c** and **d** are defined as before.

We made use of the freely available python package pyknotid in order to identify whether a ring (or a pair of rings sharing vertices) is knotted.[259] Using pyknotid, we computed the Gauss code for the ring, and following simplification by performing Reidemeister moves, we identified if a knot was present. If present, the identity of the knot

was determined using a knot lookup table, which includes information about all knots with up to 15 crossings. Only if the ring (or a pair of rings sharing vertices) was deemed to be knotted was the writhe then calculated. A visual representation of the Gauss linking integral for a set of closed loops, along with their corresponding writhe or linking number, is shown in Fig. 5.7.

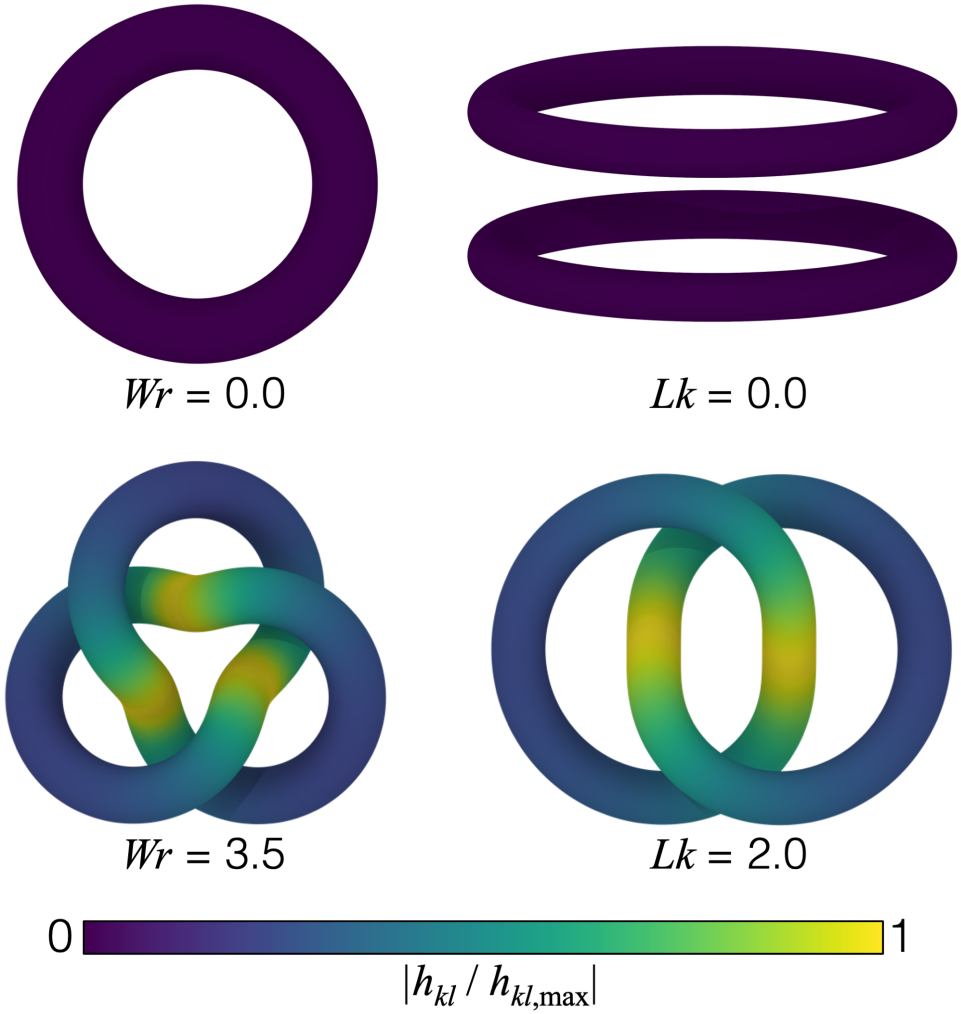


Figure 5.7: **Visualisation of the Gauss linking integral.** Linking number (Lk) or writhe (Wr) for an idealised unknot (top left), unlink (top right), trefoil knot (bottom left) and Hopf link (bottom right). Each point of the motifs is coloured according to the corresponding (relative) contribution to the Gauss integral (Equation 5.16), where $h_{kl} = \left[\oint_{\mathrm{R}_l}(r_l - r_k)/|r_l - r_k|^3 \cdot (\mathrm{d}r_l \times \mathrm{d}r_k)\right]/(4\pi)$.

Since we only identified links between rings of sizes $l \leq l_{\max}$ and knotted structures of sizes $l \leq (2l_{\max} - 2)$, the values of $\mathcal{L}_n$ and $\mathcal{W}_n$ depend on the chosen $l_{\max}$. The LDL and HDL networks have asymptotic limiting behaviour in their topological properties as a function of $l_{\max}$, above a critical value. Therefore, we computed $\mathcal{L}_n$ and $\mathcal{W}_n$ using the smallest $l_{\max}$ value that was found to be in the asymptotic regions of both the LDL and HDL phases ($l_{\max} \geq 13$). Figure 5.8a shows the average values of $\mathcal{L}_n$ and $\mathcal{W}_n$ as a function of pressure for $T < T_c$ and $T > T_c$ with $l_{\max} = 13$. Both $\mathcal{L}_n$ and $\mathcal{W}_n$ display a discontinuous change with P^* for sub-critical temperatures, concomitant with the discontinuity in the density (see Fig. 5.8a), while they change continuously for super-critical temperatures.

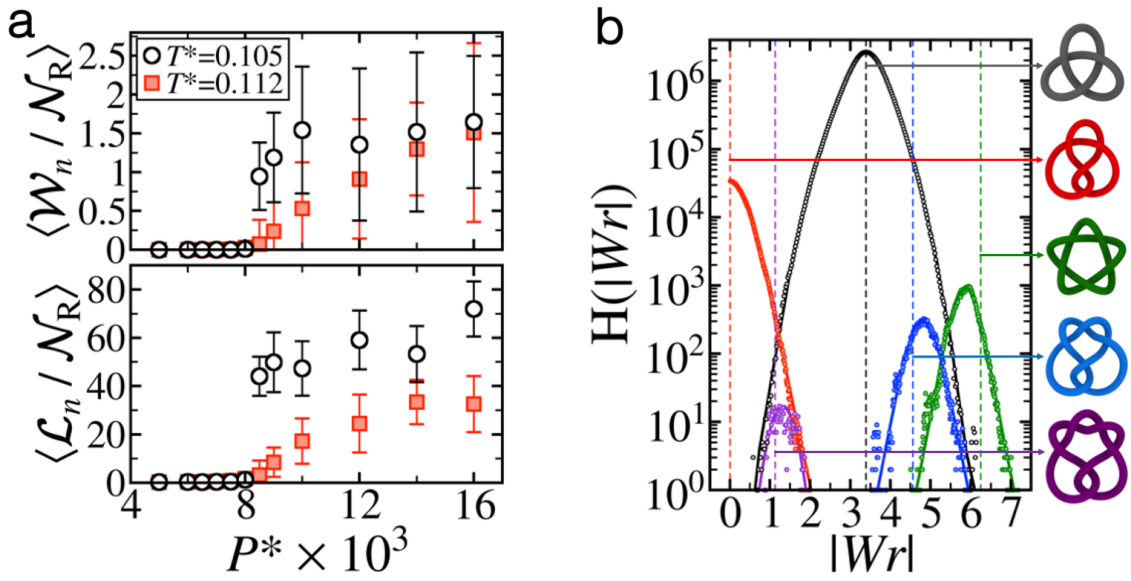


Figure 5.8: **Topological nature of the liquid-liquid phase transition.** (**a**) Dependence of the average network linking number ($\mathcal{L}_n$) and the network writhe ($\mathcal{W}_n$) normalised by the total number of rings in the network ($\mathcal{N}_R$) as a function of P^* at $T^* = 0.105$ ($T < T_c$) and $T^* = 0.112$ ($T > T_c$). $\mathcal{L}_n$ and $\mathcal{W}_n$ were computed using rings of sizes up to $l_{\max} = 13$. Error bars represent the standard deviation over 2 sets of Monte Carlo trajectories, each comprising 4×10^7 MC cycles. (**b**) Frequency distribution for the writhe (Wr), separated for different unique knotted structures observed in the HDL network, at $T^* = 0.105$ with $l_{\max} = 15$. The idealised knot associated with each distribution is colour-coded and shown to the right of the plot. The dashed lines indicate the writhe values of the idealised knots [260], and the solid lines are a guide to the eye.

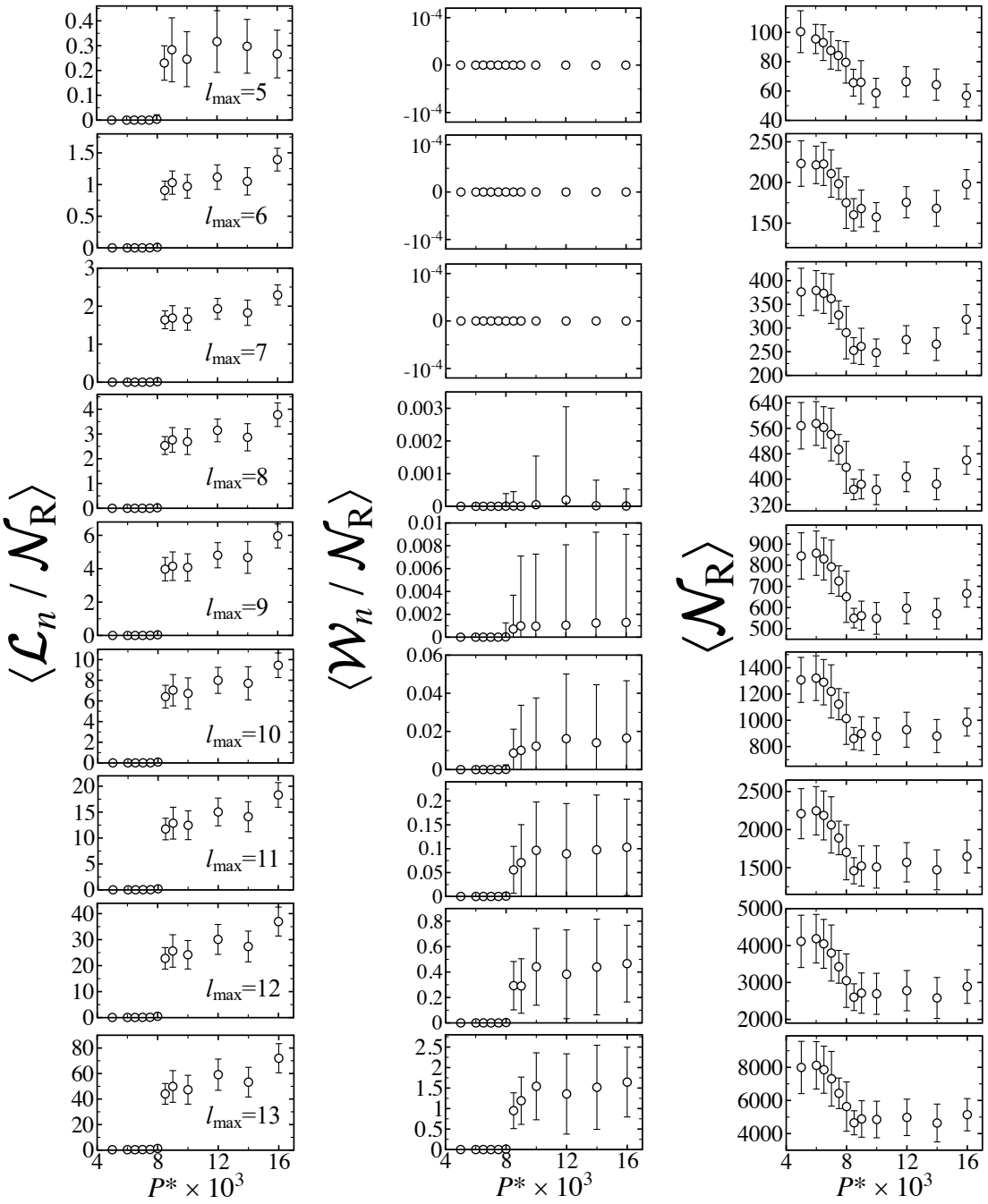


Figure 5.9: **Pressure dependence of the topological properties of colloidal water.** Pressure dependence of $\langle \mathcal{L}_n / \mathcal{N}_R \rangle$, $\langle \mathcal{W}_n / \mathcal{N}_R \rangle$ and $\langle \mathcal{N}_R \rangle$ for the colloidal water model, for $5 \leqslant l_{max} \leqslant 13$ at a temperature of $T^* = 0.105$. Note that $\mathcal{W}_n = 0$ for all pressures when $l_{max} \leqslant 7$

The transition between the LDL and HDL phases is clearly captured by $\mathcal{L}_n$ when $l_{\max} \geq 5$ (as shown in Fig. 5.9). However, as knots require longer chains of particles to form, they require a larger $l_{\max}$ to be identified, and so, $\mathcal{W}_n$ only shows a clear discontinuity when $l_{\max} \geq 10$ (see Fig. 5.9). Additionally, this means that there are fewer knots than links in the network, which in turn, means that $\mathcal{W}_n$ is smaller than $\mathcal{L}_n$ for a given $l_{\max}$. Yet, there are a variety of knotted objects in the HDL networks that contribute to the nonzero value of $\mathcal{W}_n$. Figure 5.8b shows the frequency distribution of the writhe for different knotted objects found in the HDL network with $l_{\max} = 15$. The majority of these structures contain trefoil knots, but we also find figure-eight, cinquefoil, three-twist and Stevedore knots.[250] Similar to randomly generated knotted rings, the ensemble average of the writhe for each of these knots correlates well with the writhe of the corresponding idealised configuration (*i.e.*, one which allows the volume to surface area ratio to be maximised[261]).

It is clear that $\mathcal{L}_n$ and $\mathcal{W}_n$ can both serve as a topological order parameter to describe the LLPT in colloidal water, providing strong evidence that the LLPT is a transition from an "unentangled" to an "entangled" network. This raises the question whether entanglement also underpins the LLPT in supercooled water. Recently, it has been shown that the TIP4P/Ice[262] and TIP4P/2005[263] molecular models of water, which do not explicitly enforce tetrahedral coordination, both exhibit a first-order LLPT and corresponding LLCP.[104] We therefore performed a similar topological analysis for TIP4P/Ice. Figures 5.10a and 5.10b show representative snapshots of the hydrogen bond networks for the LDL and HDL of TIP4P/Ice. We find that the LDL contains a small number of links and practically no knotted structures (only one or two knots occasionally appearing in a frame), while the HDL contains trefoil knots and theta-curves in addition to links (which are also present in more abundance than in the LDL). Figure 5.10c shows that the ensemble average of the writhe for these trefoil motifs in the HDL of TIP4P/Ice also correlates well with the

writhe of the idealised trefoil knot, as was the case for colloidal water. Additionally, as for colloidal water, Fig. 5.10d shows that, for TIP4P/Ice, $\mathcal{L}_n$ and $\mathcal{W}_n$ both jump at the critical pressure, suggesting that entanglement also underpins the LLPT in molecular water.

A universal property of systems close to a second order critical point (when $T \approx T_c$ and $P \approx P_c$) are wide oscillations in relevant order parameters, as configurations belonging to both phases are sampled along the trajectory.[229] To check if the topological order parameter $\mathcal{L}_n$ does indeed properly distinguish between the two liquid phases of the TIP4P/Ice and TIP4P/2005 models, we calculated $\mathcal{L}_n$ along 40 μs molecular dynamics trajectories of supercooled water for different values of P close to T_c. Figure 5.10e shows the evolution of the ρ and $\mathcal{L}_n$ along the molecular dynamics trajectory for a system of $N = 300$ TIP4P/Ice molecules at three different pressures. Above and below the critical pressure, $\mathcal{L}_n$ displays quite different values, indicating a significant topological difference between the two liquids. At the critical pressure, wide fluctuations in $\mathcal{L}_n$ are observed, closely correlating with those of ρ.

5.4 | DISCUSSION

In summary, we have designed a colloidal analogue of water – a tetrahedral network liquid self-assembled from designer triblock patchy colloidal particles *via* tetrahedral clusters. This colloidal water model captures the anomalous thermodynamic behaviour of supercooled water, including the well-known density maximum, and displays two structurally different network liquid phases. With the synthetic feasibility of the triblock patchy particles under consideration,[91] colloidal water presents itself as an ideal model system, amenable to experimental investigation at the single-particle level, for gleaning a fundamental understanding of LLPTs in tetrahedral liquids.

By analysing configurations from this colloidal model and from a widely used molecu-

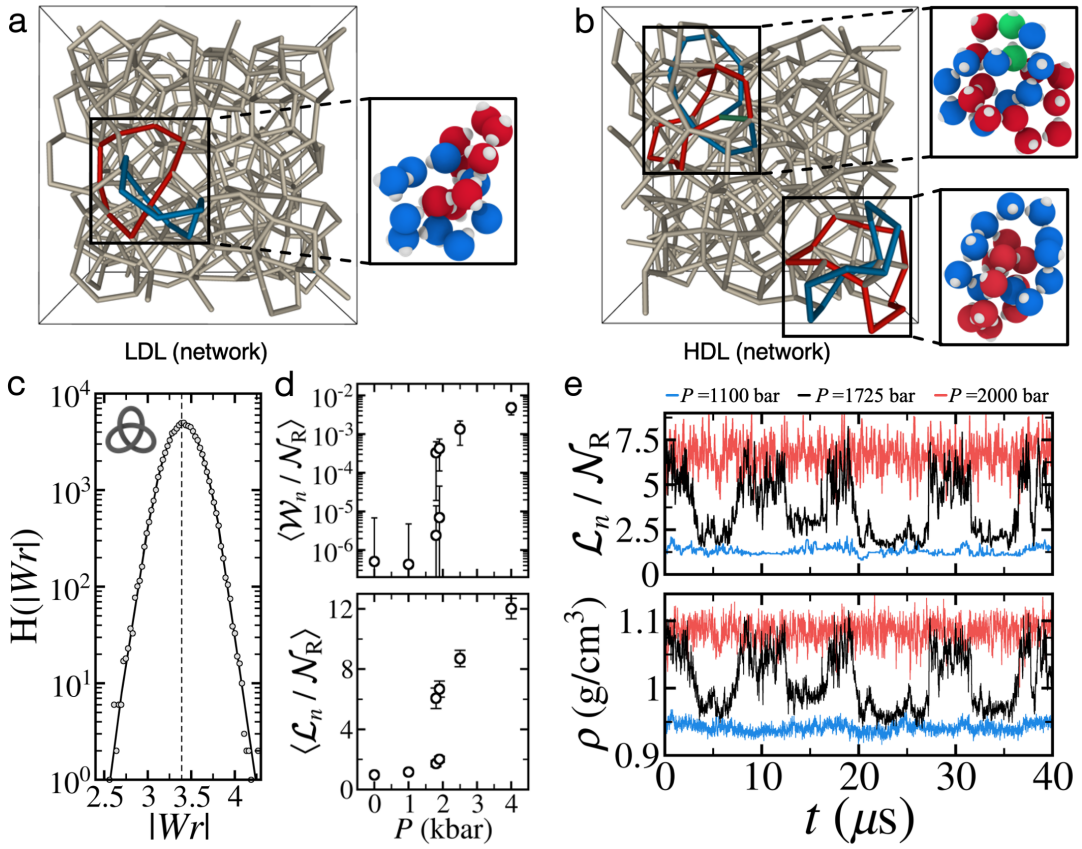


Figure 5.10: **Identifying links and knots in molecular water.** (**a,b**) Illustrative snapshots of the (**a**) low-density liquid (LDL) and (**b**) high-density liquid (HDL) networks of molecular water, simulated using the TIP4P/Ice potential, at $T = 188$ K and $P = 1100$ bar and $P = 2000$ bar, respectively. This temperature is slightly below the critical temperature ($T_c = 188.8$ K[104]) and the pressures are below and above critical pressure ($P_c = 1725$ bar[104]). In the LDL, only a few links are present - one is highlighted in panel **a**. In the HDL, both linked and knotted motifs are present, as highlighted in panel **b**. (**c**) Frequency distribution for the writhe (Wr) of the knotted paths found in the HDL network (essentially all being trefoil knots) at $T = 188$ K and $P = 2000$ bar. The inset shows the idealised configuration of a trefoil knot, and the dashed line indicates the value of the writhe for the idealised trefoil knot.[260] (**d**) Dependence of $\mathcal{L}_n$ and $\mathcal{W}_n$, computed using rings of sizes up to $l_{\max} = 13$, normalised by $\mathcal{N}_R$, as a function of P at $T = 188$ K for $N = 1000$ molecules. Error bars represent the standard deviation as calculated along the corresponding molecular dynamics trajectories. (**e**) Fluctuations in density (ρ) and $\mathcal{L}_n$ (computed using $l_{\max} = 13$) during isobaric-isothermal molecular dynamics simulations for $N = 300$ molecules of TIP4P/Ice water at a temperature of $T = 188$ K for $P = 1100$ bar, $P = 1725$ bar and $P = 2000$ bar.

lar model for water,[262] we have established that the LDL and HDL networks associated with the LLPT in all three cases are topologically distinguishable. The LDL in all these cases is an "unentangled network", consisting primarily of unknots, while the HDL is an "entangled network" containing an ensemble of topologically non-trivial motifs. For colloidal as well as molecular models, $\mathcal{L}_n$ and $\mathcal{W}_n$ – metrics able to capture the degree of entanglement – act as suitable order parameters, highlighting that the LLPT can be interpreted as a topological phase transition.

Uncovering the topological distinction between the LDL and HDL networks allows us to understand the physical mechanism underpinning the LLPT from a new perspective that sheds light on its microscopic origin. The LLPT occurs at low temperatures where the system tends to form a liquid network with the maximum number of bonds possible. At low pressures, it is well established that this is achieved by forming an open random tetrahedral network; however, as the pressure increases, the system tends to also minimise its volume. In tetrahedral liquids, associated with this drive to maximise the number of bonds is an increase in the number of rings in the network. Due to the directionality of the interactions, the system cannot minimise its volume by simply deforming the rings, while preserving the network connectivity, as there is a limit to the flexibility of the bonds. Instead, the system is able to simultaneously minimise its volume and maximise the number of bonds in the network by forming knots and links. Additionally, we note that, unlike knots and links formed by covalently bonded chains or networks[244], the LDL and HDL are transient networks (*i.e.*, bonds are constantly breaking and forming) and so their topological state is not constant. Despite this evolution, the topological signatures for each phase are properly defined.

CHAPTER 6

SELF-ASSEMBLY OF RECTANGULAR PATCHY PARTICLES

So far in this thesis, we have exclusively focused on the self-assembly of colloidal particles resulting in, at the very least, local tetrahedral order. This has been the case as the holy grail of colloidal self-assembly has been considered to be the diamond structure due to its highly desirable photonic properties.[58] Because the self-assembly of diamond with colloidal particles remained an unmet challenge for over 30 years (only very recently has an experimental system shown promise of scalably forming a structure possessing diamond symmetry with colloidal particles[25]), diamond has essentially been the prime target structure for those working in the field of colloidal self-assembly. However, other structures have been shown to possess photonic band gaps (PBGs) that are almost as wide as the rod-connected diamond structure.[58] One such structure is the single-network gyroid (SNG) structure, which has a body-centred cubic lattice with the space group $I4_132$ and supports a large PBG.[58] The SNG structure is also a chiral crystal meaning it has additional chiroptical properties that are not present in the diamond structures.[264–269] While the SNG structures have proven elusive, the double gyroid morphology, as a bicontinuous structure,[270] has been self-assembled from building blocks with elements of frustration, e.g. surfactants, block copolymers and mesogens.[271–274] Unlike the SNG structures, the double gyroid structure is neither chiral nor supports a complete PBG.

The work presented in this chapter was carried out partly in collaboration with Wesley Flavell, as reflected in a co-authored publication, but the data included here were produced independently.

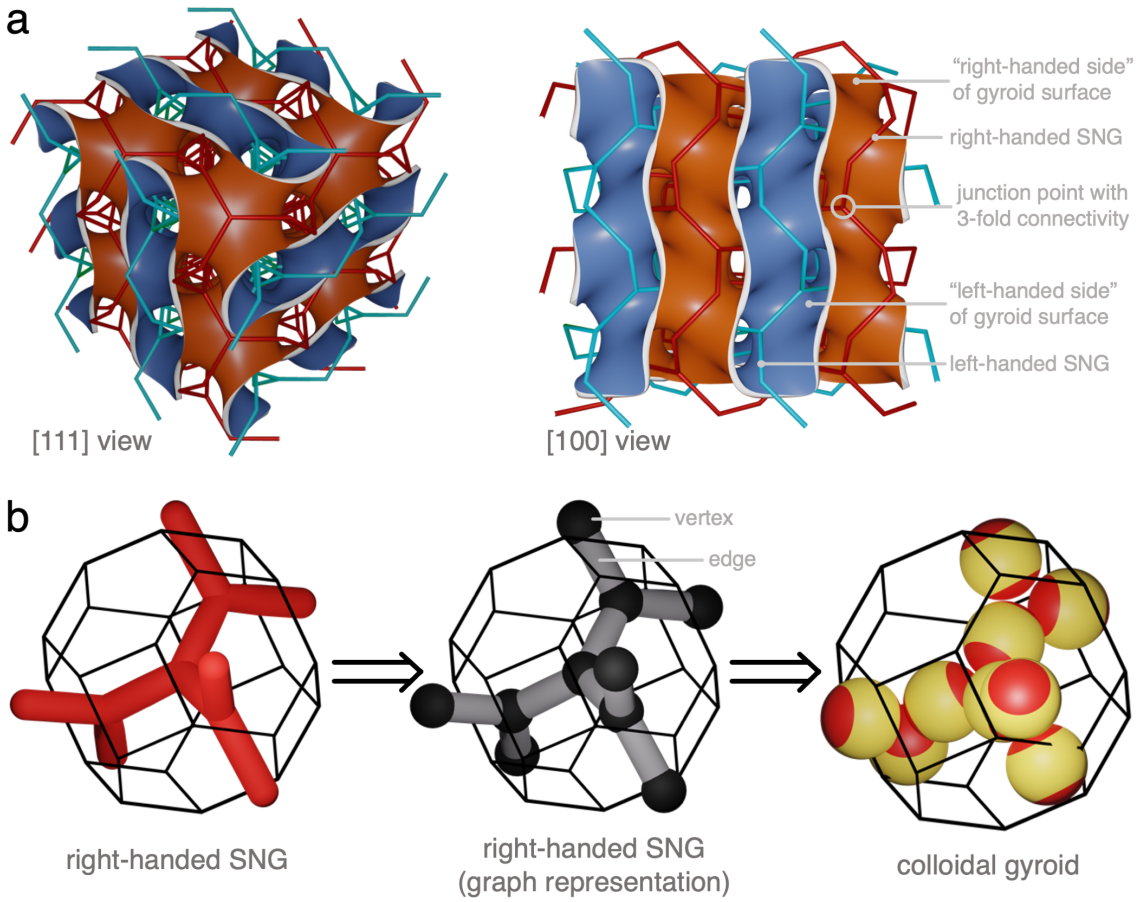


Figure 6.1: **Reverse engineering colloidal single network gyroid.** (**a**) Two views of the gyroid minimal surface along the [111] and [100] axes are shown. Additionally, the two single network gyroid (SNG) enantiomers are also shown. The two sides of the surface are colour matched with the SNG enantiomer that passes through the voids formed on that side of the surface. The space between the two sides of the gyroid surface is coloured grey. (**b**) Schematic representation of the reverse engineering approach to the colloidal SNG structure, identifying colloidal triblock patchy particles as the designer building blocks, starting from the Wigner-Seitz unit cell of the SNG structure. The SNG structure is first re-imagined in a graph representation where we place a vertex at regions of three-fold connectivity, and then draw an edge between each vertex. This graph representation is similar to the K_4 crystals formed by some sp^2 hybridised atomic systems such as carbon,[275] boron,[276] and phosphorus.[277] We then replace the edges of the graph with triblock patchy particles, where each particle forms two bonds per patch, to give the colloidal gyroid structure. We then have the centres of the vertex-sharing trigonal planar clusters formed by the triblock patchy located on the vertices of the colloidal gyroid graph.

Literature discussing gyroid will often be referring to the triply periodic minimal surface that partitions 3D space into a pair of intertwined labyrinths of vacant space, as shown in Fig. 6.1a.[278] If we trace two paths, each covering the vacant space on one side of the surface, we would define two enantiomorphic networks: these are the SNG structures (Fig. 6.1a). Each SNG structure can be decomposed into a graph representation, where we place a vertex at regions of three-fold connectivity and draw edges between neighbouring vertices, as shown in Fig. 6.1b. We see that the gyroid networks are characterised by trigonal planar local order (as opposed to the tetrahedral order found in diamond structures). The dihedral angles between adjacent nodes are all approximately equal to either 70.5° (right-handed) or 109.5° (left-handed), depending on which enantiomorph is under consideration.[274] When considering the graphical representation of the SNG structure in Fig. 6.1b, one could envisage each edge in the graph being replaced by a spherical colloidal particle. We refer to this structure single colloidal gyroid.

A single colloidal gyroid structure built from colloidal particles in the size range of hundreds of nanometres, as presented in Fig. 6.1b, promises to function as a synthetic chiral photonic crystal operating at optical frequencies. Here, we show that the structure does indeed have intriguing chiroptical properties which make it an attractive target for colloidal self assembly. We establish that designer colloidal spheres with staggered rectangular patchy particles can reliably self-assemble into a single colloidal gyroid structure when the skew angle between the patches is correctly chosen. Additionally, we show that these particles are also able to assemble into a diverse range of amorphous and crystalline structures simply by tuning the skew angle between the two rectangular patches. Finally, since these rectangular patchy particles are in general chiral, except for certain values for the skew angle, we also probe the possibility of assembling chiral entangled liquids and investigate their topological properties.

6.1 PHOTONIC PROPERTIES OF COLLOIDAL GYROID

While it is well documented that the SNG structure is a near-champion chiral photonic crystal, the photonic properties of the colloidal gyroid structure presented in Fig. 6.1b have not previously been probed. Therefore, in order to establish that colloidal gyroid is a worthy target structure for colloidal self-assembly we probe its photonic and chiroptical properties for the primitive unit cells of the direct and inverse structures (see Appendix A for details regarding the lattice vectors, crystal basis and the $\boldsymbol{k}$-points used to compute the band structures). By direct structure, we are referring to the structure formed *directly* by the particles which we can consider as spheres composed of a high-index material embedded in air. By inverse structure, we are referring to the *inverse* scenario where we have "air spheres" embedded in a high-index material, as has been done to fabricate inverse opals[14] and recently inverse diamond.[25]

Figure 6.2a shows the relative gap width, $\Delta f / f_{\mathrm{m}}$ expressed as a percentage, of the direct single colloidal gyroid structure (dielectric spheres in air) as a function of the refractive index contrast ($n_{\mathrm{c}} = n_{\mathrm{h}} / n_{\mathrm{l}}$). For the direct structure, we consider the maximum packing scenario. We find that a complete PBG opens up for $n_{\mathrm{c}} \approx 2.7$, which could potentially be realised with titania particles in order to open a PBG in the visible.[24] However, it is possible to further lower the required refractive-index contrast by depositing materials onto the surfaces of the particles, effectively increasing the dielectric filling fraction.[25,197] This "swelling" of the particles can also be used to fabricate the inverse structure, which involves backfilling the voids of the direct lattice with a high refractive-index material, after which the original material can be removed leaving air in its place.[25] The inverse single colloidal gyroid structure, composed of "air spheres" with a diameter of twice the original diameter (as shown by the inset of Figs. 6.2b), is a close approximation

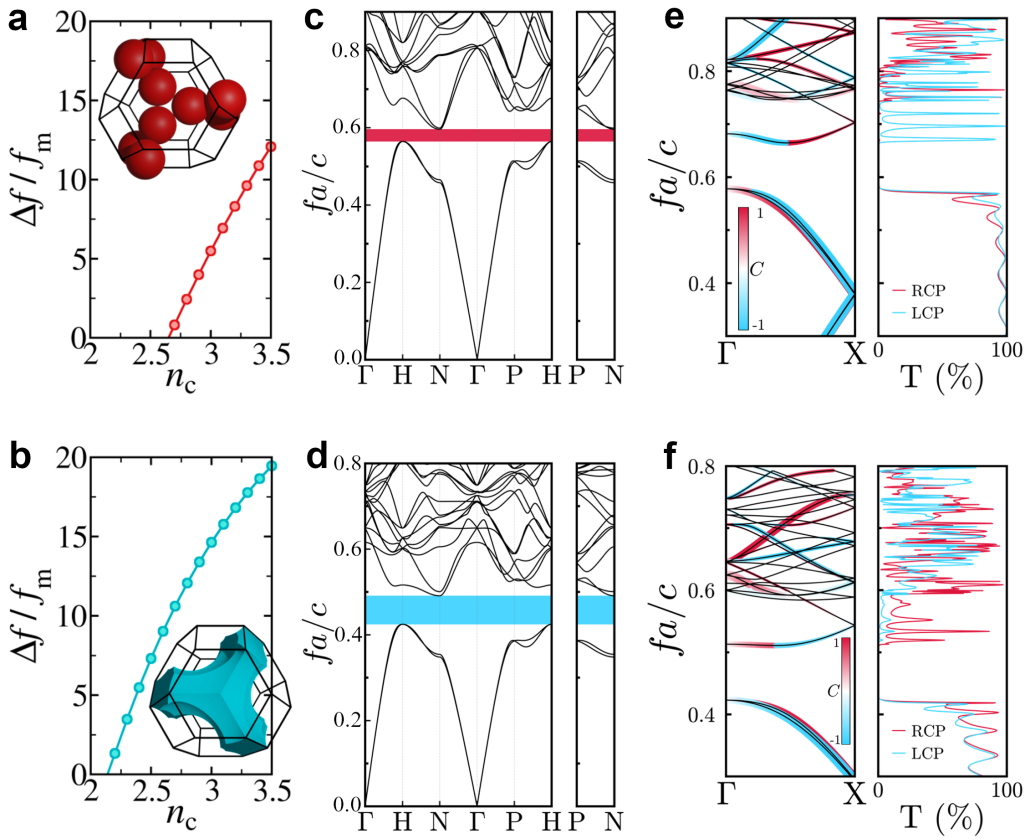


Figure 6.2: **Chiroptical properties for single colloidal gyroid structures.** (**a**, **b**) Dependence of the relative gap width ($\Delta f / f_m$), expressed as a percentage, on the refractive index contrast (n_c) for the (**a**) direct and (**b**) inverse single colloidal gyroid structures. (**c**, **d**) Photonic band structures of the direct (**c**) and inverse (**d**) gyroid structures with $n_c = 3$, showing complete photonic band gaps of approximately 5% and 15%, respectively. (**e**, **f**) The left panels show the photonic band structures of the conventional unit cells of the (e) direct and (f) inverse gyroid structures with $n_c = 3$ along the $\Gamma \rightarrow$ X direction (which corresponds to the $\Gamma \rightarrow$ H direction in the primitive unit cell). The colour of the lines in both band structures reflects the circular dichroism index (C), where right-circularly polarised (RCP) is red, left-circularly polarised (LCP) is blue, and unpolarised is black, and their thickness is proportionate to the coupling constant β. The right panels show the transmittance spectra for RCP (red) and LCP (blue) plane waves normally incident to a finite slab of the (**e**) direct and (**f**) inverse gyroid crystals with $n_c = 3$ along the [100] direction. For all calculations the direct colloidal gyroid structure is composed of touching dielectric spheres as shown by the inset of panel **a**. The inverse colloidal gyroid structure is composed of air spheres with a radius of $r = d^2/a$. The inset of panel **b** visually highlights that the inverse structure is a gyroid network of opposite handedness relative to the direct structure.

to SNG.[58,199] This is apparent from the fact that a complete PBG opens up for this inverse structure for $n_c \approx 2.2$, as shown in Figure 6.2b, similar to what has previously been reported for SNG.[58,199] Representative photonic band structures for both the direct and inverse single gyroid structures are shown in Fig. 6.2c and Fig. 6.2d, respectively, for the refractive index contrast $n_c = 3$, showing the presence of a complete PBG in each case.

We note that both the direct and inverse structures in this case are single gyroid-like structures, but are of opposite chirality. However, this is not immediately evident when comparing the dispersion relations in Figs. 6.2c and 6.2d. Therefore, in order to investigate the chiroptical properties of single colloidal gyroid we computed the transmittance spectra for circularly polarised light incident on finite slabs of the crystal with $n_c = 3$ using the freely available finite-difference time domain (FDTD) package MEEP.[279] For each simulation a finite slab of five conventional unit cells of colloidal gyroid, where periodic boundaries were imposed along the $\hat{\mathbf{x}}$ and $\hat{\mathbf{z}}$ directions of the simulation cell. The simulation cell was defined with a Yee grid of 42 points per unit cell and a size of $1 \times 15 \times 1$ unit cells, where perfectly matched layers were positioned on either side of the simulation cell where periodic boundaries were not imposed. A Gaussian source was defined on one side of the colloidal gyroid slab, with energy flux measured on the other side. Circularly-polarised sources were generated by overlapping two linearly-polarised sources which are 90° out of phase with one another and incident along the [100] direction of the simple cubic conventional unit cell. The conventional unit cell was used for the transmittance spectra calculations as MEEP does not have the capacity to treat non-orthogonal unit cells. Therefore, to check the results of our calculations, we also computed the photonic band structure of the conventional unit cell of single colloidal gyroid along with the circular dichroism index[280,281] for each band along the $\Gamma \rightarrow \mathrm{X}$ direction (which corresponds to the [100] direction in real space).

We are able to determine the handedness of the bands using the circular dichroism index ($C \in [-1,1]$),[280,281] which measures the preference of Bloch modes to couple to right-handed ($C \approx 1$) or left-handed ($C \approx -1$) light. We performed circular polarisation analysis on the photonic band structures of the gyroid crystals by calculating the circular dichroism index (C) and the coupling index (β) of the eigenmodes, where we define[280,281]

$$C = \mathrm{sgn}(\mathbf{q} \cdot \nabla_{\boldsymbol{k}} f_n) \left(\frac{C^{+}_{\boldsymbol{k},n} - C^{-}_{\boldsymbol{k},n}}{C^{+}_{\boldsymbol{k},n} + C^{-}_{\boldsymbol{k},n}} \right) \tag{6.1}$$

where n is the band index, $\boldsymbol{k}$ is the Bloch wave vector, $\nabla_{\boldsymbol{k}} f_n$ is the group velocity and $C^{\pm}_{\boldsymbol{k},n}$ is the overlap integral between Bloch modes and a circularly polarised plane wave with wave vector $\mathbf{q} \parallel \boldsymbol{k} = k\hat{\mathbf{b}}$. We define the overlap integral as[280,281]

$$C^{\pm}_{\boldsymbol{k},n} = \frac{\left| \int\int_P (\hat{\mathbf{a}} \pm i\hat{\mathbf{c}}) \cdot \mathbf{H}_{\boldsymbol{k},n}(P) \right|^2}{\left| \int\int_P (\hat{\mathbf{a}} \pm i\hat{\mathbf{c}}) \right|^2 \left| \int\int_P \mathbf{H}_{\boldsymbol{k},n}(P) \right|^2} \tag{6.2}$$

where $\mathbf{H}_{\boldsymbol{k},n}$ corresponds to a magnetic eigenmode. The integrals are performed over a plane P that is perpendicular to $\boldsymbol{k}$ and the unit vectors $\mathbf{a}$ and $\mathbf{c}$ are in the plane. Additionally, we fix the centre of the plane to be at the origin. For each eigenmode we can assign a handedness: if $C > 0.5$ it is right-handed (RH), if $C < -0.5$ it is left-handed (LH) and a mode remains unassigned otherwise. Additionally, we can define the coupling index

$$\beta = C^{+}_{\boldsymbol{k},n} + C^{-}_{\boldsymbol{k},n} \tag{6.3}$$

which measures the degree of coupling between an incident plane wave of either polarisation and the corresponding eigenmode. In plots of the photonic band structures and the circular dichroism index the colour of the symbols reflects the value of the circular dichroism index and the size of the symbols is proportional to the coupling index.

Figures 6.2e and 6.2f show the photonic band structures and transmittance spectra along the $\Gamma \rightarrow$ X direction for the conventional unit cells of the direct and inverse structures, respectively, with $n_c = 3$. Note that, the $\Gamma \rightarrow$ X direction along the simple cubic conventional unit cell of gyroid maps onto the $\Gamma \rightarrow$ H direction of its body-centred cubic primitive unit cell. This becomes clear when comparing Figs. 6.2c and 6.2d to the band structures in Figs. 6.2e and 6.2f, as we see that the stop gap along the relevant directions span the same frequency ranges. A close comparison between the left panels of Figs. 6.2e and 6.2f reveals that the handedness of the bands for the direct and inverse structures is flipped relative to one another, highlighting that the two structures are indeed of opposite chirality. This difference in chirality of the two structures is also revealed by the transmittance spectra for right-circularly polarised (RCP) and left-circularly polarised (LCP) plane waves normally incident to a finite slab of the direct and inverse gyroid crystals along the [100] direction, as shown in the right panels of Figs. 6.2e and 6.2f, respectively. For the direct structure, we observe a broad dip in the transmittance of RCP light across frequencies spanning both the unpolarised stop gap and the dichroic band gap of gyroid,[281] while the inverse structure displays a broad dip in the transmittance of LCP light.

In Figs. 6.3a-c, we show the transmittance spectra for the direct single colloidal gyroid structure along the [100], [110] ($\Gamma \rightarrow$ M) and [111] ($\Gamma \rightarrow$ R) directions of the conventional unit cell with the refractive index contrast of $n_c = 3$ at a density corresponding to the touching sphere limit. We see that a PBG is present in all three cases. However, along the [100] direction, there is an additional circular dichroism stop gap present that is absent from the other directions in the frequency range $0.69 \lesssim fa/c \lesssim 0.75$, where LCP light is transmitted, while RCP light is not. While this stop gap is not present along the other directions, we do see that there is partial circular dichroism along the [110] and [111] directions at frequencies of $fa/c \approx 0.8$ and $fa/c \approx 0.9$, respectively. Along the [110]

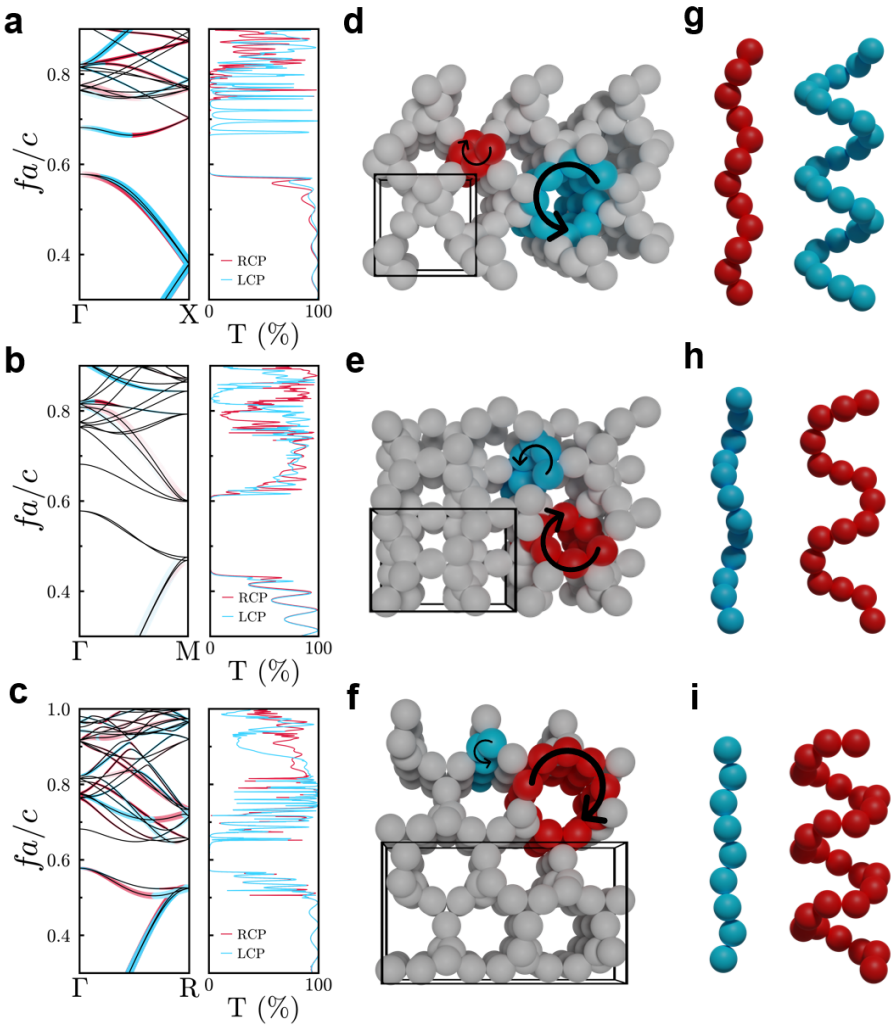


Figure 6.3: **Chiroptical properties for single colloidal gyroid structures.** (**a**-**c**) Photonic band structure and transmittance spectra of the conventional unit cells and transmittance spectra for RCP (red) and LCP (blue) plane waves normally incident to a finite slab of the direct single colloidal gyroid structure along the (**a**) [100], (**b**) [110], and (**c**) [111] directions at the refractive index contarst $n_c = 3$. For all calculations the direct single colloidal gyroid structure is composed of touching dielectric spheres. At the limit of touching spheres the density of the colloidal gyroid crystal is $\rho^* = 9\sqrt{6}/64 \approx 0.34$ and the edge length of the corresponding conventional unit cell is $a = 4d\sqrt{6}/3$, d being the diameter of the particles. (**d**-**f**) Views of the single colloidal gyroid structure along the (**d**) [100], (**e**) [110], and (**f**) [111] directions, where principal helices of the gyroid structure that have their axes parallel to the corresponding crystallographic axis are highlighted. These helices are also shown in panels (g-i) and are colour-coded according to their handedness (right handed coloured red and left handed coloured blue).

direction, we see two distinct regions where the transmissions of LCP and RCP light differ. However, along the [111] direction the circular dichroism is such that LCP light is less easily transmitted along this direction at frequencies $fa/c \approx 0.9$. This difference in the transmission of different polarisations of light along the different crystallographic axes of the crystal can be understood when looking at the helices that are present in the gyroid structure along these different directions. Figs. 6.3d-e shows views of the gyroid structure along the [100], [110] and [111] directions together with the principal helices formed by the particles along these directions. We see that handedness of the helices along the [100] and [111] directions are reversed, which is the likely cause of the reversal of the circular dichroism of the gyroid along these directions.[282]

6.2 | REVERSE ENGINEERING COLLOIDAL GYROID

It is clear that the colloidal gyroid structure has rich chiropical and photonic effects, making it a desirable target structure for colloidal self-assembly. In Fig. 6.1b, we show that triblock patchy particles, where the patches are narrow enough to favour the formation of only two bonds per patch, can stabilise the colloidal gyroid structure, and so may be a potential route to assembling colloidal gyroid. However, in a characteristic five-particle motif, containing two vertex-shared planar trimers, the circular patches allow for unrestricted rotation of one trimer with respect to the other, as shown schematically in Fig. 6.4.

As a result of this free rotation, we find that such particles can stabilise two other structures, one with *Fddd* symmetry and the other being two-dimensional kagome sheets. To determine the relative stability of these structures we computed their free energies over a range of pressures at a low temperature of $T^* = 0.05$ to ensure that bonds are never broken. Monte Carlo simulations in the *NPT* ensemble were performed at select pressures in the range $P^* = \{0.0 - 0.1\}$, using 8×10^7 Monte Carlo cycles and thermodynamic integration

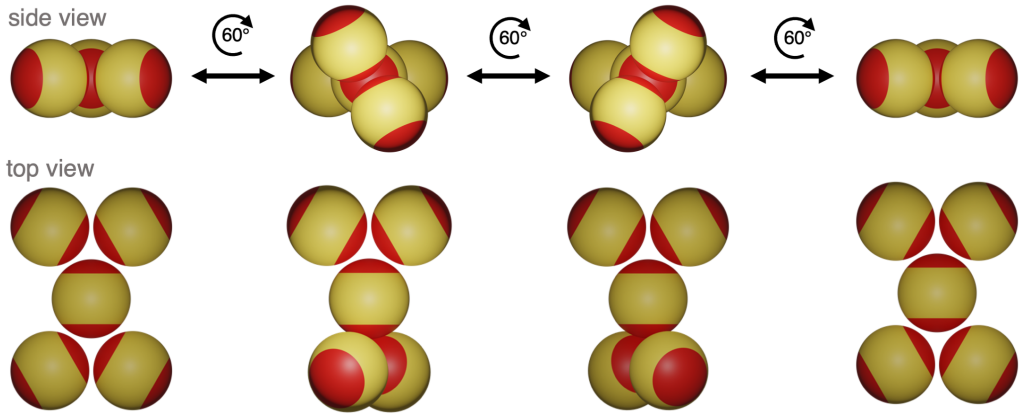


Figure 6.4: **Limitation of triblock patchy particles for the assembly of gyroid**. Five-particle motif containing vertex-shared planar trimers present in colloidal gyroid is shown. The triblock patchy particles with two circular patches allow for unrestricted rotation of one planar trimer relative to the other. This unrestricted rotation hinders the selection of the dihedral angle required for the self-assembly of a colloidal gyroid structure.

along an isotherm was used to determine the free energies of the crystals as a function of pressure. Reference free energies were computed at $T^* = 0.05$ and $P^* = 0.0$ using the Einstein crystal method for the gyroid and *Fddd* crystals, and the Schilling-Schmid method for the kagome sheets. Figure 6.5a shows the free energy of the three phases as a function of pressure, we see that the kagome sheets are thermodynamically favoured at all pressures considered. Figures 6.5b-d show representative snapshots of the three phases at $P^* = 0.1$ and $T^* = 0.05$, we see that, while the gyroid and *Fddd* structure are continuous network structures, the kagome sheets are discrete two-dimensional structures (*i.e.*, each sheet can move independently of the other). Therefore, despite all three structures being built from vertex-shared planar trimers, the kagome phase is considerably more stable. This is because the kagome phase is essentially a fluid phase of two-dimensional crystals, where the sheets can move independently of one another, and so the kagome phase possesses an additional configurational entropy contribution to its free energy. Therefore, while being able to stabilise the gyroid structure, triblock patchy particles are not suitable building blocks for the self-assembly of colloidal gyroid.

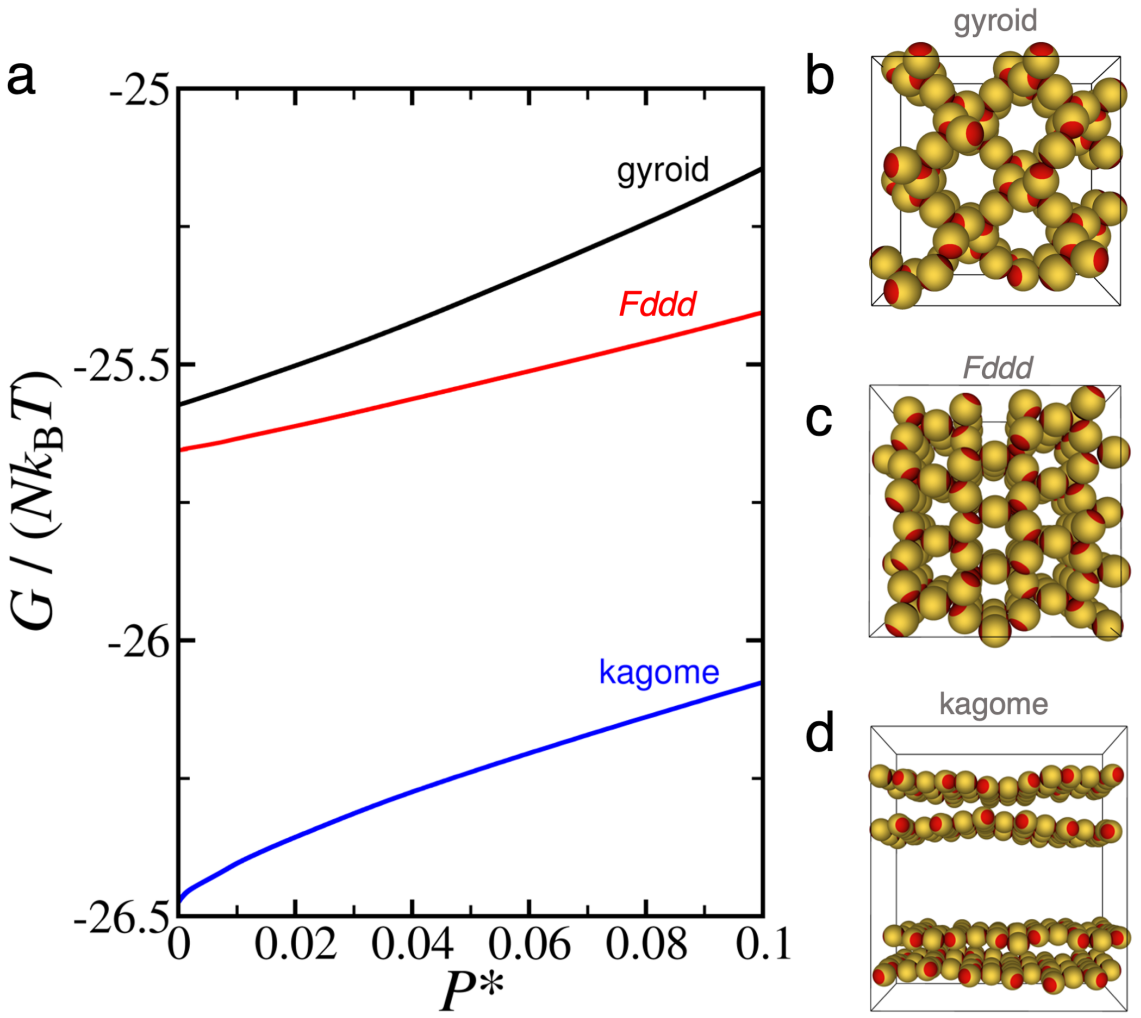


Figure 6.5: **Relative stability of crystal polymorphs formed by triblock patchy particles.** (**a**) Gibbs free energy of the gyroid, *Fddd* and kagome polymorphs as a function of pressure at $T^* = 0.05$ calculated using thermodynamic integration. Reference free energies for the structures were computed using the Einstein crystal method for the gyroid and *Fddd* structures and the Schilling-Schmid method for the kagome planes. Representative snapshots of the (**b**) gyroid, (**c**) *Fddd*, and (**d**) kagome phases at $T^* = 0.05$ and $P^* = 0.1$.

6.2.1 RECTANGULAR PATCHY PARTICLES

Faced with this issue, we conceived the particle design shown in Fig. 6.6 as our building block for colloidal gyroid. By replacing the two circular patches of triblock patchy particles with two staggered rectangular ones, we are able to restrict the relative rotation of vertex-shared planar trimers and thus enforce the selection of the dihedral angles required to assemble a single gyroid structure from colloidal spheres. This particle design was largely inspired by the patterning symmetry approach used by Romano and Sciortino, where they designed spherical colloidal particles with triangular patches to selectively form the cubic tetrastack structure.[30] Importantly, when designing these rectangular patchy particles we considered their synthetic feasibility, similar particles have been experimentally fabricated using the glancing-angle deposition method by Pawar and Kretzschmar.[283]

We developed an effective pair potential for these particles as an extension of the widely used Kern-Frenkel model.[204] In this new model, each rectangular patch is characterised by two half-opening angle values, θ_{p} and ϕ_{p}, that define the height and width of each rectangular patch, respectively. The relative orientation between the two patches is described by the skew angle χ, which is critical to the selection of dihedral angles. In our pair potential, we retain the same bonding condition as in the Kern-Frenkel model: for the patches to interact, the separation vector $\boldsymbol{r}_{ij}$ must pass through the patch surfaces on both particles. However, the orientational criteria that must be met to satisfy this condition become more involved due to the geometry of the patches. To check for these criteria, for each patch, we define a set of three orthogonal unit vectors $\boldsymbol{p}_{\mathrm{p},1}$, $\boldsymbol{p}_{\mathrm{p},2}$, $\boldsymbol{p}_{\mathrm{p},3}$ at the centre of the spherical particle i. The unit vector $\boldsymbol{p}_{\mathrm{p},1}$, is aligned with the vector from the centre of the particle to the point $\theta = 0^\circ$, $\phi = 0^\circ$ (the centre of the patch); the vector from the centre to $(\theta = 0^\circ, \phi = 90^\circ)$ is aligned with $\boldsymbol{p}_{\mathrm{p},2}$; the vector from the centre to $\theta = 90^\circ$ is aligned with $\boldsymbol{p}_{\mathrm{p},3}$ (the pole of the patch).

To allow for two patches on the opposite poles with their relative orientation defined *via* the skew angle χ, we align the coordinate frame of patch A with the body-fixed frame of the particle, and then define the coordinate frame for patch B as $\boldsymbol{p}_{\mathrm{B},1} = -\boldsymbol{p}_{\mathrm{A},1}$, $\boldsymbol{p}_{\mathrm{B},2} = R(\chi)\cdot\boldsymbol{p}_{\mathrm{A},2}$ and $\boldsymbol{p}_{\mathrm{B},3} = R(\chi)\cdot\boldsymbol{p}_{\mathrm{A},3}$, where $R(\chi)$ is a rotation matrix describing a clockwise rotation by the angle χ about the axis $\boldsymbol{p}_{\mathrm{A},1}$. A designer particle with two rectangular patches on the opposite poles, having the skew angle $\chi = 90^{\circ}$, is shown in Fig. 6.6 illustrating the critical parameters that define the shape, size and relative arrangement of the two rectangular patches.

Similar to the Kern-Frenkel potential, the effective pair potential is defined as a combination of a hard-sphere (v^{hs}), square-well (v^{sw}), and an angular modulation ($f_{\mathrm{pp}'}$) factor:

$$v_{ij}(\boldsymbol{r}_{ij},\hat{\boldsymbol{\Omega}}_i,\hat{\boldsymbol{\Omega}}_j) = v_{ij}^{\mathrm{hs}}(r_{ij}) + v_{ij}^{\mathrm{sw}}(r_{ij})\sum_{\mathrm{p}\in i}\sum_{\mathrm{p}'\in j} f_{\mathrm{pp}'}(\boldsymbol{r}_{ij},\hat{\boldsymbol{\Omega}}_i,\hat{\boldsymbol{\Omega}}_j) \tag{6.4}$$

The angular modulation factor is given by

$$f_{\mathrm{pp}'}(\boldsymbol{r}_{ij},\hat{\boldsymbol{\Omega}}_i,\hat{\boldsymbol{\Omega}}_j) = \begin{cases} 1 \quad \text{if} \quad \begin{cases} |\cos(\vartheta_{ij}^{\mathrm{p}})| < \cos(\vartheta_{\mathrm{p}}) \quad \text{and} \quad \cos(\phi_{ij}^{\mathrm{p}}) > \cos(\phi_{\mathrm{p}}) \\ \text{and} \quad |\cos(\vartheta_{ji}^{\mathrm{p}'})| < \cos(\vartheta_{\mathrm{p}'}) \quad \text{and} \quad \cos(\phi_{ji}^{\mathrm{p}'}) > \cos(\phi_{\mathrm{p}'}) \end{cases} \\ 0 \quad \text{otherwise} \end{cases} \tag{6.5}$$

where ϑ_{p} is the complementary angle to θ_{p}

$$\vartheta_{\mathrm{p}} = \pi/2 - \theta_{\mathrm{p}}, \tag{6.6}$$

and $\vartheta_{ij}^{\mathrm{p}}$ is the angle between $\boldsymbol{r}_{ij}$ and $\boldsymbol{p}_{\mathrm{p},3}$

$$\cos(\vartheta_{ij}^{\mathrm{p}}) = \hat{\boldsymbol{r}}_{ij}\cdot\boldsymbol{p}_{\mathrm{p},3}, \tag{6.7}$$

and ϕ_{ij}^{p} is the angle between $\boldsymbol{p}_{\mathrm{p},1}$ and the projection of $\boldsymbol{r}_{ij}$ into the $(\boldsymbol{p}_{p,1}, \boldsymbol{p}_{p,2})$ plane

$$\cos(\phi_{ij}^{\mathrm{p}}) = \hat{\boldsymbol{r}}_{ij}^{\mathrm{p}_{1,2}} \cdot \boldsymbol{p}_{\mathrm{p},1} \tag{6.8}$$

where,

$$\boldsymbol{r}_{ij}^{\mathrm{p}_{1,2}} = (\boldsymbol{p}_{\mathrm{p},1} \cdot \boldsymbol{r}_{ij})\boldsymbol{p}_{\mathrm{p},1} + (\boldsymbol{p}_{\mathrm{p},2} \cdot \boldsymbol{r}_{ij})\boldsymbol{p}_{\mathrm{p},2} \tag{6.9}$$

Similar expressions can be written in order to define $\vartheta_{ji}^{\mathrm{p}'}$, and $\phi_{ji}^{\mathrm{p}'}$.

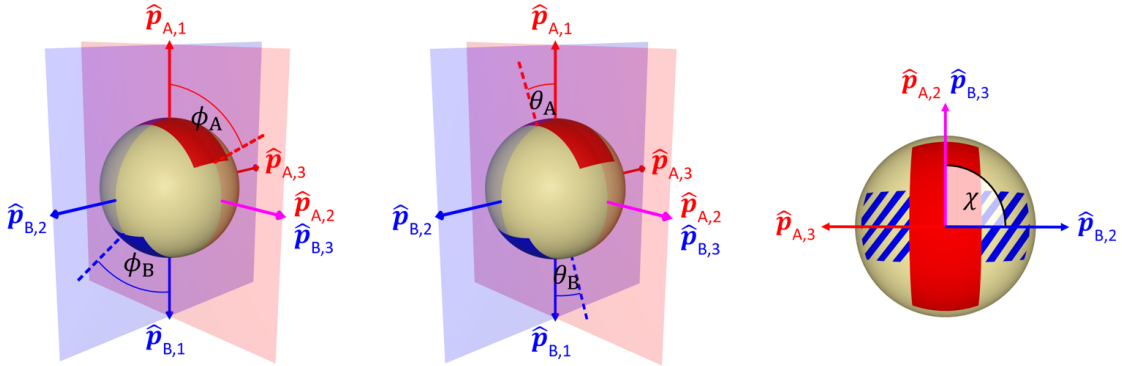


Figure 6.6: **Designer spherical patchy particle with two rectangular patches.** The two patches, labelled A and B, are shown in red and blue respectively, along with their pair of half-opening angles $(\theta_{\mathrm{A}}, \phi_{\mathrm{A}})$ and $(\theta_{\mathrm{B}}, \phi_{\mathrm{B}})$, their local coordinate systems and the skew angle χ, where χ defines the relative orientation of the patches. Here, $\phi_{\mathrm{A}} = \phi_{\mathrm{B}} = 60^{\circ}$, $\theta_{\mathrm{A}} = \theta_{\mathrm{B}} = 20^{\circ}$ and $\chi = 90^{\circ}$. In the right panel, the blue patch is dashed to indicate its location on the back face of the particle.

6.3 | SELF-ASSEMBLY OF COLLOIDAL GYROID AND EMPTY LIQUIDS

To explore whether these rectangular patchy particles can indeed self-assemble into colloidal SNG, we carried out a series of Monte Carlo simulations with $N = 4000$ particles with $\theta_{\mathrm{p}} = 10^{\circ}$, $\phi_{\mathrm{p}} = 44^{\circ}$ and $\chi \in \{0^{\circ} - 90^{\circ}\}$, in the *NVT* ensemble. For colloidal SNG, the maximum packing scenario (*i.e.*, where the dielectric spheres are touching) corresponds to a density of $\rho^{*} = 9\sqrt{6}/64 \approx 0.34$, and so we chose to perform the Monte

Carlo simulations at a density of $\rho^* = 0.3$. Here we considered only values of $\chi \leq 90^\circ$ as particles with $90^\circ < \chi < 180^\circ$ will show the same self-assembly properties, except that they will form structures of opposite handedness. Additionally, we note that the rectangular patchy particles are achiral when $\chi = 0^\circ$ and $\chi = 90^\circ$. We gradually cooled the systems from a reduced temperature of $T^* = 1$ to $T^* = 0.105$. Figure 6.7a shows the values of the global Steinhardt bond-order parameter Q_4 as a function of χ at $T^* = 0.105$. We see that, for $\chi < 15^\circ$ and $65^\circ \leq \chi \leq 75^\circ$, $\langle Q_4 \rangle > 0$, suggesting that these systems have crystallised, while for all other systems $\langle Q_4 \rangle \approx 0$. For systems where $\chi < 15^\circ$, planar kagome sheets form, as shown by the representative snapshot in Fig. 6.7b, while gyroid crystals are formed by systems with $65^\circ \leq \chi \leq 75^\circ$ (Fig. 6.7c). This confirms that we have successfully programmed the assembly of SNG gyroid into the particle design of the rectangular patchy particles. Additionally, we note that there is some robustness to the design as gyroid crystals form for a distribution of χ values.

While Q_4 only produces a signal only for systems forming kagome and gyroid structures, there may still be some kind of ordering occurring for the χ values that do not produce these two structures. In order to probe this, we compute the average number of of rings of length l ($\mathcal{N}_{\mathrm{R}_l}$) for $5 \leq l \leq 12$ as a function of χ for the resulting structures at $T^* = 0.105$. We see that for $\chi < 15^\circ$, there is a large number of 6-membered rings identified as these particles self-assemble into kagome sheets. However, we find that there are also a large number of 5- and 7-membered rings, suggesting that there are also many defects in these systems. Additionally, for $65^\circ \leq \chi \leq 75^\circ$ there is large peak in the number of 10-membered rings, as would be expected for the gyroid structures. Interestingly, we find that there is also a peak in the number of: (i) 11–membered rings when $\chi \approx 15^\circ$, (ii) 9- and 12-membered rings when $\chi \approx 55^\circ$, and (iii) 8-membered rings peaks for $\chi = 90^\circ$. This suggests that, while there is no long-range crystalline order within these structures

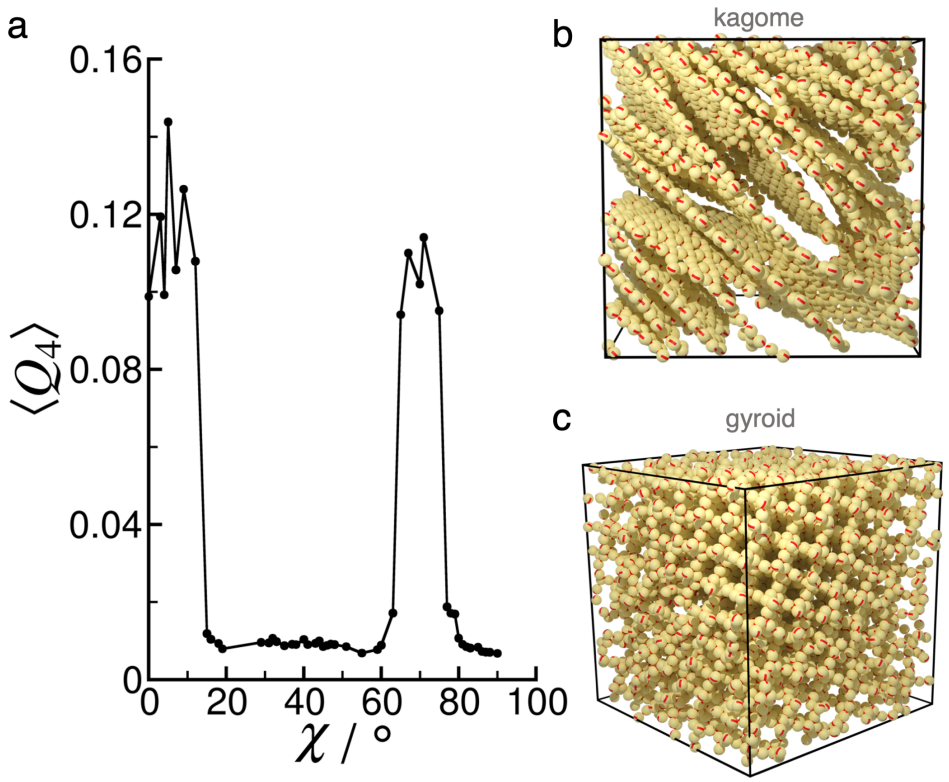


Figure 6.7: **Crystallisation of rectangular patchy particles.** (**a**) Average global Steinhardt bond order-parameter Q_4 as a function of the skew angle (χ) for systems of $N = 4000$ rectangular patchy particles at $T^* = 0.1$ and $\rho^* = 0.3$ for $0^\circ \leq \chi \leq 90^\circ$, $\theta_p = 10^\circ$ and $\phi_p = 44^\circ$. There are two peaks in the plot where $\langle Q_4 \rangle > 0$, the first appears for $\chi \leq 15^\circ$ where kagome sheets form, as shown by the representative configuration in (**b**) for a system with $\chi = 11^\circ$. The second peak appears between $65^\circ \leq \chi \leq 75^\circ$ where gyroid crystals form, as shown by the representative configuration in (**c**) for a system with $\chi = 70^\circ$

there is some medium-range ordering in the form of rings taking place. Figure 6.9a shows that the particles with $\chi = 15^\circ$ form right-handed helices, and 11-membered rings form when these helices connect to one another. Upon closer inspection of the 9-membered rings in the networks generated by particles with $\chi = 55^\circ$, we find that four of these rings come together to form a polyhedral cage with approximate tetrahedral symmetry, as shown in Fig. 6.9b. Alternatively, we could consider these cages as being formed from four trigonal planar clusters that are centred on the vertices of the tetrahedron, where each cluster is connected to the other three by a single "bridging" particle. Similarly, if we

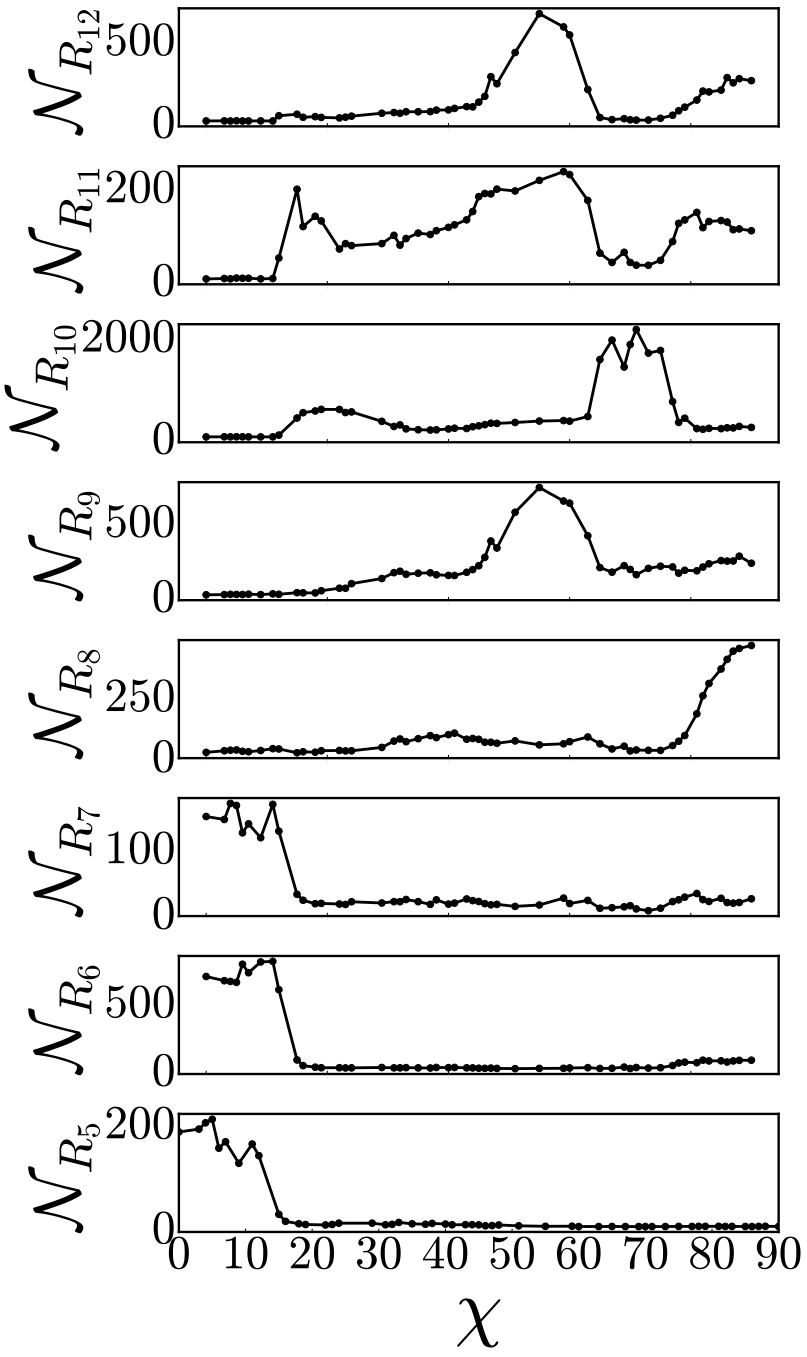


Figure 6.8: **Distribution of rings in networks formed by rectangular patchy particles.** Number of rings of length l ($\mathcal{N}_{\mathrm{R}_l}$) for $5 \leq l \leq 12$ as a function of χ for the resulting structures at $T^* = 0.105$ and $\rho^* = 0.3$.

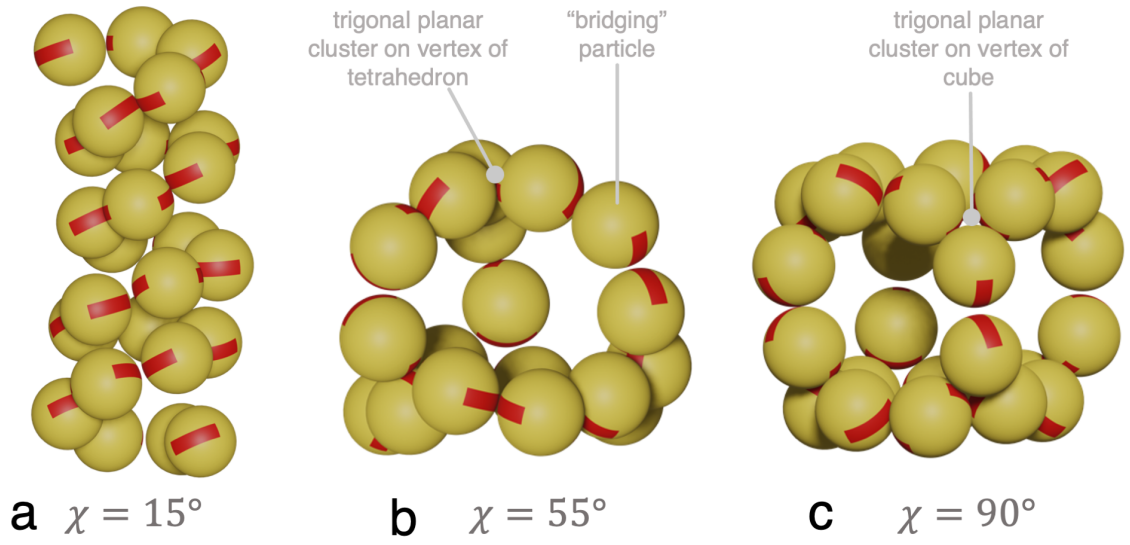


Figure 6.9: **Characteristic clusters in amorphous networks of rectangular patchy particles.** (**a**) Right-handed helix formed by particles with $\chi = 15°$. (**b**) Polyhedral cage with approximate tetrahedral symmetry formed by particles with $\chi = 55°$, where 4 trigonal planar clusters are centred on the vertex of a tetrahedron and 6 "bridging" particles connect these clusters together (*i.e.*, they are the edges of the tetrahedron). (**c**) Cubic cage formed by particles with $\chi = 90°$. It is possible to consider the cubic cage as being formed of eight trigonal planar clusters, where each cluster is centred on a vertex of the cube.

inspect the 8-membered rings formed by the rectangular patchy particles with $\chi = 90°$, we see that each ring forms the face of a deformed cube, as shown in Fig. 6.9c. Again, we can decompose these cages into eight trigonal planar clusters, one centred on each of the vertices of the cubes, rather than four 8-membered rings.

6.4 | SELF-ASSEMBLY OF CHIRAL ENTANGLED LIQUIDS

As alluded to in the previous chapter, knots and links can be chiral objects; for instance, Fig 6.10 shows the left- and right-handed trefoil knots. When considering the self-assembly of structures containing these topological motifs, we would not expect there to be any preference for one realisation over the other if the building blocks were achiral. However, as our rectangular patchy particles considered here are chiral, it is of interest to ask whether

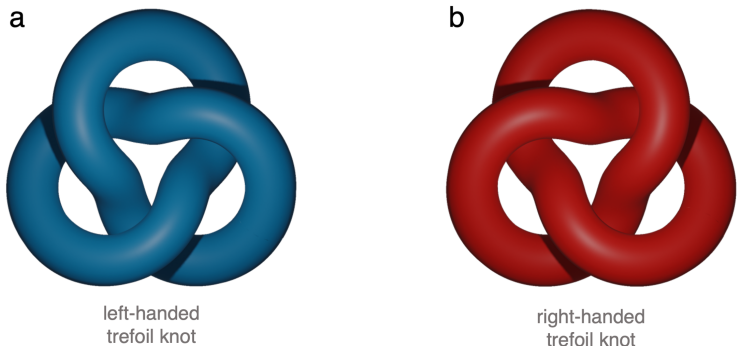


Figure 6.10: **Trefoil knots.** (**a**) Left-handed and (**b**) right-handed trefoil knots.

these particles are able to self-assemble into entangled fluids where knots and links of a particular chirality are favoured. We identify the knots and links present in the networks formed by the rectangular patchy particles from our Monte Carlo simulations, using configurations from $T^* = 0.105$ and $\rho^* = 0.6$. Figure 6.11 show the values of $\mathcal{L}_n$ and $\mathcal{W}_n$ as a function of χ. We see that for $\chi < 15$, both $\mathcal{W}_n \approx 0$ and $\mathcal{L}_n \approx 0$. This is because rectangular patchy particles forming planar kagome sheets that are able to stack on top of one another (see Fig. 6.5d). Therefore, if one is looking to design a system to form an entangled fluid with rectangular patchy particles, there is an optimal value of $\chi \approx 40^\circ$ that maximises the entanglement of the network.

We find that there is no preference for the formation of a link of one chirality over the other; however, we do find that the chirality of the particles has a clear influence on the probability of forming a knot of a particular chirality. Figure 6.12 shows that probability distribution for the writhe for networks generated with $N = 4000$ rectangular patchy particles at $T^* = 0.105$ and $\rho^* = 0.6$, for select values of χ. We see that, while there are two peaks in the distributions, one centred at $Wr \approx -3.4$ and the other at $Wr \approx +3.4$, there is a clear bias towards the formation of trefoil knots with positive (*i.e.*, right-handed) or negative (*i.e.*, left-handed) writhe if the particles are right- or left-handed, respectively.

Given that the particles are chiral, we might expect that only knots of one chirality

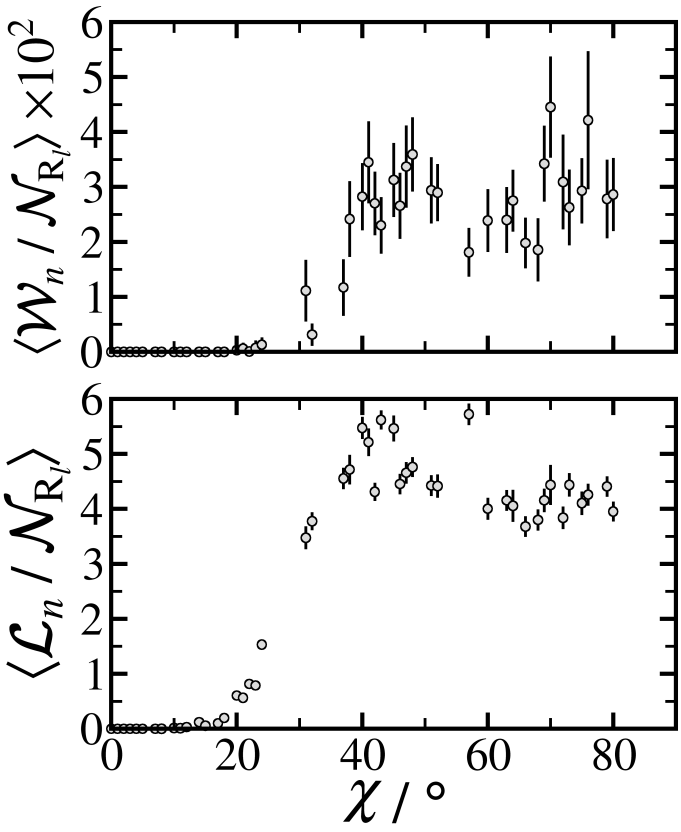


Figure 6.11: **Topological properties of rectangular patchy particle networks.** Skew angle (χ) dependence of $\langle \mathcal{L}_n / \mathcal{N}_{\mathrm{R}} \rangle$ and $\langle \mathcal{W}_n / \mathcal{N}_{\mathrm{R}} \rangle$ for systems of $N = 4000$ rectangular patchy particles at a temperature of $T^* = 0.105$ and density of $\rho^* = 0.6$. Topological properties were computed using rings with $4 \leqslant l_{\mathrm{max}} \leqslant 16$.

would form in the entangled networks of rectangular patchy particles. In order to understand why both enantiomers were forming, we inspected representative configurations of these knotted objects. Figure 6.13 shows two representative trefoil theta-curves (one of each chirality) formed by particles with $\chi = 50°$. We find that knots which have the "wrong" chirality are able to form since not every particle in the network has four neighbours. In order for the dihedral angle constraint of the patches to take effect the particles must form two bonds per patch. Some particles are thus free to rotate relative to their nearest neighbours.

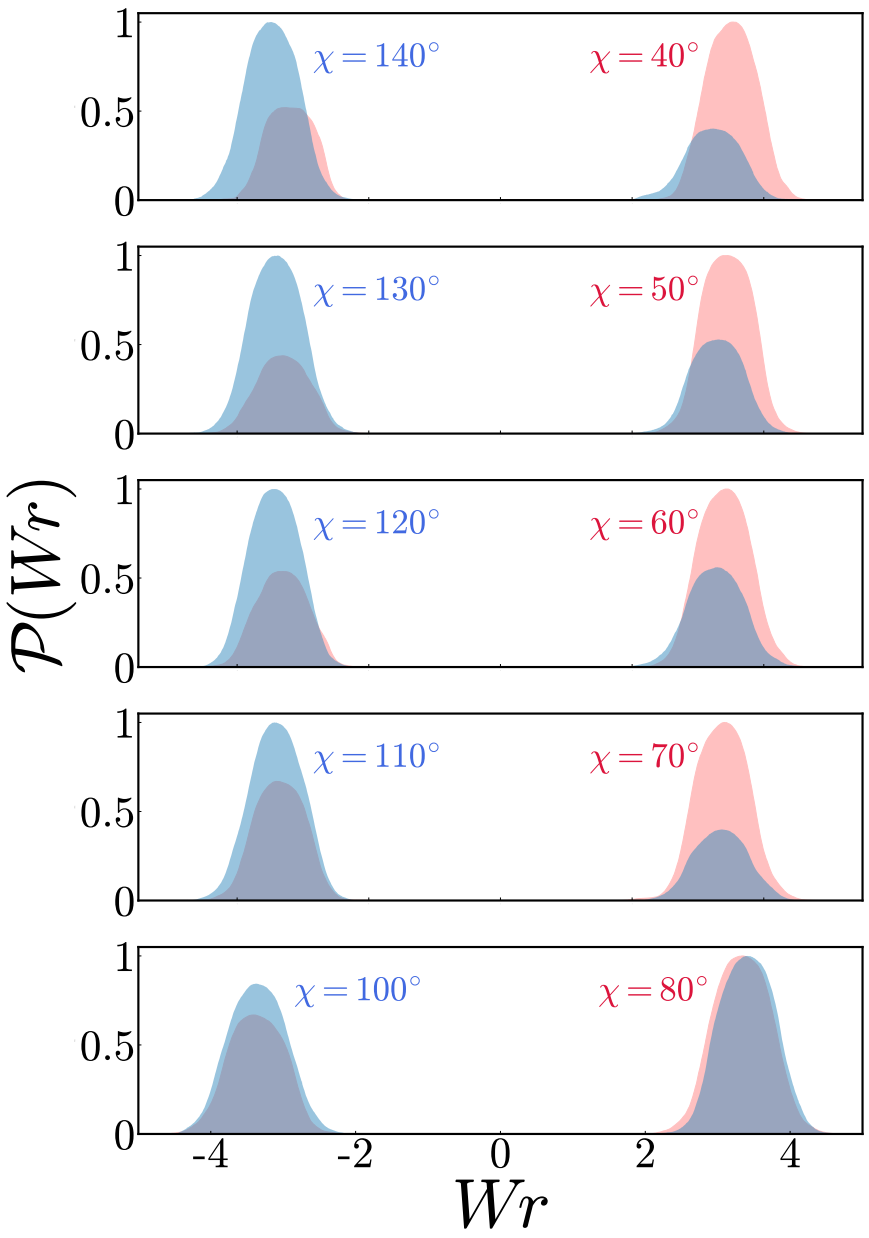


Figure 6.12: **Chirality of rectangular patchy particle networks.** Skew angle (χ) dependence of the probability distribution for the writhe of trefoil knotted objects in systems of $N = 4000$ rectangular patchy particles at a temperature of $T^* = 0.105$ and density of $\rho^* = 0.6$, where the trefoil knotted objects were extracted using rings with $l_{\text{max}} = 16$. The distributions are separated into right-handed (coloured red) and left-handed (coloured blue) pairs, where each pair of distributions are extracted from systems of particles that are mirror images of one another.

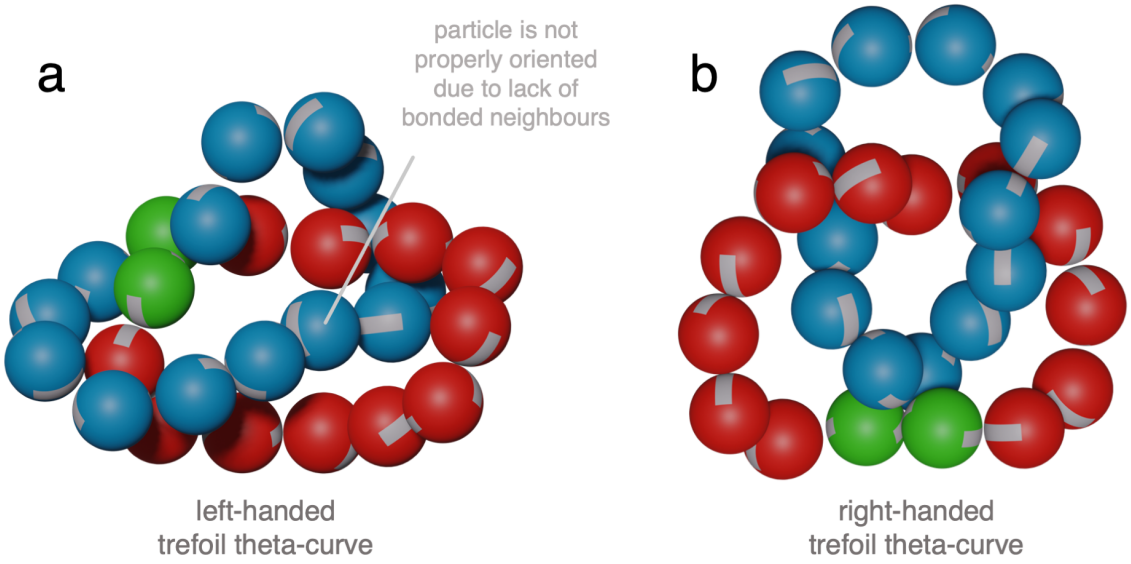


Figure 6.13: **Trefoil theta-curves formed in rectangular patchy particle networks.** (**a**) Left- and (**b**) right-handed trefoil theta-curves formed by rectangular patchy particles with $\chi = 50^\circ$ at a temperature of $T^* = 0.105$ and density of $\rho^* = 0.6$.

6.5 | DISCUSSION

In summary, we looked to program the self-assembly of colloidal gyroid structures using patchy particles. We showed that the single gyroid crystals built from colloidal spheres support a complete PBG at relatively low refractive index contrasts accessible to colloidal materials, and exhibit rich chiropical effects, thus presenting a new target structure for colloidal self-assembly which can find application as chiral devices operating at optical frequencies. We established that rectangular patchy particles, such as those synthesised by Pawar *et al.*,[86] are the ideal building block for this endeavour as, through a judicious choice of the skew angle (χ) between the patches, it is possible to eliminate competition from other crystal structures.

In order to study the self-assembly of these rectangular patchy particles we developed a pair potential based on the widely used Kern-Frenkel model.[204] While probing the self-assembly of rectangular patchy particles, we identified that these particles are able to form

a variety of different structures by tuning the skew angle. Of particular interest is their to form open liquids composed of polyhedral cages with tetrahedral and octahedral symmetry when $\chi = 55^\circ$ and $\chi = 90^\circ$, respectively. These structures bear a striking resemblance to the polyhedral cages that constitute the clathrate crystals formed by tetrahedral patchy particles. Finally, we showed that at higher densities rectangular patchy particles are able to form entangled liquid networks where there is a strong bias for the formation of knotted structures with the same chirality as the particles. Therefore, these particles may not only find application as building blocks for the self-assembly of colloidal gyroid, but may also provide access to a wide range of structures.

CHAPTER 7

CONCLUSIONS

7.1 SUMMARY

The overarching aim of this thesis has been to rationally design colloidal patchy particles to self-assemble into target open crystals and empty liquids. To successfully programme colloidal building blocks to self-assemble into a specific target structure, we must ensure that not only is the structure of interest thermodynamically favoured, but also kinetically accessible. In order to achieve this goal, a number of approaches have been utilised: we have exploited hierarchical self-assembly strategies to self-assemble open crystals and empty liquids with local tetrahedral order, specific interactions to encode the assembly of diamond crystals into patchy particle systems, and patterning symmetry – the rational design of patch shape and disposition – to programme the assembly of spherical colloidal particles into chiral photonic crystals and entangled liquids.

This thesis presents a series of computational studies that have addressed various challenges in the realm of programmed self-assembly, where we have made sure to maintain a close connection to current experimental capabilities. In Chapter 3 we have used reverse engineering to establish the design principles for the rod-connected diamond structure, the so-called "champion" photonic crystal. We have devised two distinct self-assembly routes for designer triblock patchy colloidal rods to yield crystals closely related to rod-connected diamond. Using Monte Carlo simulations we have shown how these routes avoid a metastable amorphous phase. Additionally, we have also shown that the

photonic band gaps of these crystals are robust to stacking faults, thus circumventing the requirement for polytype selection in a scalable fabrication method. Chapter 4 has built on the fundamental understanding developed in the context of programming self-assembly of rod-connected diamond structures. We have demonstrated that a two-component system of tetrahedral patchy particles, where bonding is allowed only between particles of different types to allow only the formation of even-membered rings, undergoes facile crystallisation into diamond crystals over a wide range of patch widths – something which was not previously possible with a one-component system of tetrahedral patchy particles. We have shown that the crystallisation in the two-component system is both thermodynamically and kinetically enhanced relative to the one-component system. Additionally, we have shown that it is possible to partially control the relative fractions of cubic and hexagonal diamond in the resulting crystals by tuning the width of the patches.

Chapter 5 has introduced a colloidal model for water that both reproduces the thermodynamic anomalies of water and displays a liquid-liquid phase transition. Additionally, we have introduced a novel order-parameter to demonstrate that the liquid-liquid phase transition in tetrahedral networks can be described as a transition between an unentangled low-density liquid and an entangled high-density liquid. We have demonstrated that this topological distinction is not only present in the colloidal model of water, but there is also a clear topological distinction between the two supercooled liquid networks of a molecular model of water. Finally, in Chapter 6 we have rationally designed a patchy colloidal building block, using patterning symmetry concepts, for the self-assembly of a single colloidal gyroid, a chiral photonic crystal. We have shown that the designer rectangular patchy particles are able to selectively form one enantiomorph of the single colloidal gyroid if the particle parameters are suitably chosen, and that the resulting crystal structures support a wide complete photonic band gap in addition to exhibiting rich chiroptical properties.

Additionally, using the topological order-parameter introduced to study the liquid-liquid phase transition, we have probed the prospect of using these chiral building blocks to self-assemble chiral entangled fluids.

7.2 | OUTLOOK

In the context of the body of work presented in this thesis, the role of rings in the self-assembly of network structures has emerged as a unifying theme. We have programmed the assembly of diamond crystals by encoding information into the building blocks that prevents the formation of odd-membereded rings, thereby removing kinetic traps that prevent crystallisation. Additionally, we have designed a colloidal system that does not crystallise, and instead forms a liquid network with a distribution of ring sizes in an effort to establish a colloidal model of supercooled water. We have identified that the liquid-liquid phase transition in tetrahedral liquids is mediated by the formation/destruction of knots and links, which are entangled ring structures. Finally, we have shown that the patch shape and disposition provides a handle by which it is possible to control the size of rings formed by the particles, allowing for a range of diverse structures to be self-assembled, including chiral photonic crystals.

Looking beyond the work presented in this thesis, there are a number of avenues of enquiry which are of interest and should be pursued in the future. In Chapter 3 we have shown that, while the relative fraction of cubic and hexagonal diamond in a crystal has some influence over the width of the photonic band gap, what is truly important is the relative distribution of the hexagonal layers. By limiting the number of consecutive hexagonal layers we have seen that it is possible to generate a structure that is only 50% cubic diamond but has a near-champion photonic band gap. Additionally in Chapter 4 we have found that the width of the patches on tetrahedral patchy particles influences the

relative stability of the cubic and hexagonal polytypes, as well the fraction of particles in cubic or hexagonal environments in self-assembled structures. Therefore, it will be of interest to see whether the width of the patches can also be used as a handle for the elongated patchy particles to design a system that can reliably assemble into random stacking diamond structures with near-champion photonic band gaps.

Continuing with this line of enquiry, while we have shown that the patch width influences the relative fraction of cubic and hexagonal environments in self-assembled colloidal diamond structures, it is unclear at what point during the assembly process this bias comes into effect. We know that crystallisation of the two-component system of tetrahedral patchy particles proceeds *via* a nucleation and growth mechanism. It will be of interest to see whether the biasing occurs during the nucleation stage or during the growth. This is relevant as it is thought that during ice crystallisation the initial crystal nucleus is predominantly cubic in nature; however, as the nucleus grows so does the fraction of molecules in a hexagonal ice environment until the resulting crystal is 100% hexagonal ice.[221] Understanding how regions of cubic and hexagonal diamond grow in a crystallite of tetrahedral patchy particles as a function of the patch width may therefore provide valuable insight into the fundamental physics governing ice crystallisation, as well as potentially provide insight to related atomic systems such as silicon and carbon.

In Chapter 5 we have shown that two liquid networks of supecooled water are topologically distinct, with the high-density liquid containing an ensemble of topologically complex motifs such as Hopf links, trefoil knots and theta-curves. While we have established this key distinction exists, it is still unclear how this transformation takes place. The helicity has previously been used to study knotted vortices in classical fluids[284] and superfluids[285], where these knots were found to untie *via* a universal topological mechanism. It will be of interest to use the metrics for the degree of entanglement introduced in this thesis to

follow the nucleation of the low-density liquid out of the high-density liquid, and vice versa, and to investigate whether this universal topological mechanism is also relevant in the context of the liquid-liquid phase transition. Additionally, while we have shown that the colloidal water model displays a discontinuous liquid-liquid phase transition and liquid-liquid critical point, it is still unclear why this transition from a low-density liquid to a high-density liquid does not proceed *via* a continuous phase transition. We do show in Chapter 5 that the liquid networks formed by the colloidal water model possessing a density in-between that of the low- and high-density liquids also have a large number of broken bonds (as compared to the low- and high-density liquids). Therefore, it will be of interest to probe the origin of these broken bonds and their relation to the topological motifs in the high-density liquid to see whether that offers further insight into the physical origin of the liquid-liquid phase transition.

We have identified in Chapter 6 that for particular realisations of the rectangular patchy particles it is possible to assemble structures that do not possess long-ranged crystalline order but do possess medium-ranged order in the form of polyhedral cages with tetrahedral and octahedral symmetry. It will be of interest to probe the assembly of these structures in more detail, as well as to better understand their global features. It is well established that hard tetrahedral particles are able to self-assemble into quasi-crystals,[286] however, the assembly of three-dimensional quasi-crystals using patchy particles has only been reported for a multi-component system of chromatic patchy particles with multiple different symmetries.[287] The rectangular patchy particles presented in this thesis may provide an avenue to the assembly of quasi-crystals using a one-component system that is also experimentally realisable. Additionally, we have shown that the chirality of the rectangular patchy particles influences the relative populations of right- and left-handed knotted structures in the entangled liquid networks they form. It will be of interest to

see whether it is possible to use these particles to form a chiral entangled liquid which possesses knotted structures of a single chirality.

Appendices

APPENDIX A

UNIT CELL INFORMATION FOR CRYSTALS

A.1 BRAVAIS LATTICES

We follow the convention laid out in Ref. [194], where we list the conventional and primitive lattice vectors ($\mathbf{a}_1$,$\mathbf{a}_2$,$\mathbf{a}_3$) for each lattice and in the scenario where the primitive and conventional lattices are the same we simply list the "lattice" vectors. Additionally, we provide the high-symmetry points along the irreducible Brillouin zone (IBZ) of the reciprocal lattice where the coordinates are given as fractions of the reciprocal lattice vectors ($\mathbf{b}_1$,$\mathbf{b}_2$,$\mathbf{b}_3$).

A.1.1 SIMPLE CUBIC

Lattice:
$$\mathbf{a}_1 = (a,0,0)$$
$$\mathbf{a}_2 = (0,a,0)$$
$$\mathbf{a}_3 = (0,0,a)$$

	$\times\mathbf{b}_1$	$\times\mathbf{b}_2$	$\times\mathbf{b}_3$
Γ	0	0	0
M	$1/2$	$1/2$	0
R	$1/2$	$1/2$	$1/2$
X	0	$1/2$	0

Table A.1: High-symmetry points of the IBZ for the simple cubic lattice.

A.1.2 FACE-CENTRED CUBIC

Conventional Lattice:	Primitive Lattice
$\mathbf{a}_1 = (a,0,0)$	$\mathbf{a}_1 = (0,a/2,a/2)$
$\mathbf{a}_2 = (0,a,0)$	$\mathbf{a}_2 = (a/2,0,a/2)$
$\mathbf{a}_3 = (0,0,a)$	$\mathbf{a}_3 = (a/2,a/2,0)$

	$\times\mathbf{b}_1$	$\times\mathbf{b}_2$	$\times\mathbf{b}_3$
Γ	0	0	0
K	$3/8$	$3/8$	$3/4$
L	$1/2$	$1/2$	$1/2$
U	$5/8$	$1/4$	$5/8$
W	$1/2$	$1/4$	$3/4$
X	$1/2$	0	$1/2$

Table A.2: High-symmetry points of the IBZ for the face-centred cubic lattice.

A.1.3 HEXAGONAL

Lattice:
$\mathbf{a}_1 = (a/2,-(a\sqrt{3})/2,0)$
$\mathbf{a}_2 = (a/2,(a\sqrt{3})/2,0)$
$\mathbf{a}_3 = (0,0,c)$

	$\times\mathbf{b}_1$	$\times\mathbf{b}_2$	$\times\mathbf{b}_3$
Γ	0	0	0
A	0	0	$1/2$
H	$1/3$	$1/3$	$1/2$
K	$1/3$	$1/3$	0
L	$1/2$	0	$1/2$
M	$1/2$	0	0

Table A.3: High-symmetry points of the IBZ for the orthorhombic lattice.

A.1.4 ORTHORHOMBIC

Lattice:
$\mathbf{a}_1 = (a,0,0)$
$\mathbf{a}_2 = (0,b,0)$
$\mathbf{a}_3 = (0,0,c)$
$a < b < c$

	$\times\mathbf{b}_1$	$\times\mathbf{b}_2$	$\times\mathbf{b}_3$
Γ	0	0	0
R	1/2	1/2	1/2
S	1/2	1/2	0
T	0	1/2	1/2
U	1/2	0	1/2
X	1/2	0	0
Y	0	1/2	0
Z	0	0	1/2

Table A.4: High-symmetry points of the IBZ for the orthorhombic lattice.

A.1.5 BODY-CENTRED CUBIC

Conventional Lattice:	Primitive Lattice
$\mathbf{a}_1 = (a,0,0)$	$\mathbf{a}_1 = (-a/2, a/2, a/2)$
$\mathbf{a}_2 = (0,a,0)$	$\mathbf{a}_2 = (a/2, -a/2, a/2)$
$\mathbf{a}_3 = (0,0,a)$	$\mathbf{a}_3 = (a/2, a/2, -a/2)$

	$\times\mathbf{b}_1$	$\times\mathbf{b}_2$	$\times\mathbf{b}_3$
Γ	0	0	0
H	1/2	-1/2	1/2
P	1/4	1/4	1/4
N	0	0	1/2

Table A.5: High-symmetry points of the IBZ for the body-centred cubic lattice.

A.2 | BASIS FOR CRYSTAL STRUCTURES

A.2.1 CUBIC TETRASTACK / ROD-CONECTED DIAMOND

The primitive unit cell of cubic tetrastack has a four particle basis and an fcc lattice. The fractional coordinates of the particles is:

	$\times\mathbf{a}_1$	$\times\mathbf{a}_2$	$\times\mathbf{a}_3$
$\mathbf{z}_0$	$5/8$	$1/8$	$1/8$
$\mathbf{z}_1$	$1/8$	$1/8$	$5/8$
$\mathbf{z}_2$	$1/8$	$1/8$	$1/8$
$\mathbf{z}_3$	$1/8$	$5/8$	$1/8$

Table A.6: Crystal basis for primitive unit cell of cubic tetrastack/rod-connected diamond.

The conventional unit cell of cubic tetrastack has a sixteen particle basis and a simple-cubic lattice. The fractional coordinates of the particles is:

	$\times\mathbf{a}_1$	$\times\mathbf{a}_2$	$\times\mathbf{a}_3$
$\mathbf{z}_0$	$1/8$	$7/8$	$7/8$
$\mathbf{z}_1$	$3/8$	$7/8$	$5/8$
$\mathbf{z}_2$	$5/8$	$1/8$	$5/8$
$\mathbf{z}_3$	$7/8$	$1/8$	$7/8$
$\mathbf{z}_4$	$1/8$	$3/8$	$3/8$
$\mathbf{z}_5$	$3/8$	$3/8$	$1/8$
$\mathbf{z}_6$	$5/8$	$5/8$	$1/8$
$\mathbf{z}_7$	$7/8$	$5/8$	$3/8$
$\mathbf{z}_8$	$5/8$	$7/8$	$3/8$
$\mathbf{z}_9$	$7/8$	$7/8$	$1/8$
$\mathbf{z}_{10}$	$1/8$	$1/8$	$1/8$
$\mathbf{z}_{11}$	$3/8$	$1/8$	$3/8$
$\mathbf{z}_{12}$	$5/8$	$3/8$	$7/8$
$\mathbf{z}_{13}$	$7/8$	$3/8$	$5/8$
$\mathbf{z}_{14}$	$1/8$	$5/8$	$5/8$
$\mathbf{z}_{15}$	$3/8$	$5/8$	$7/8$

Table A.7: Crystal basis for primitive unit cell of cubic tetrastack/rod-connected diamond.

A.2.2 HEXAGONAL TETRASTACK / ROD-CONECTED DIAMOND

The unit cell of hexagonal tetrastack has an eight particle basis and a hexagonal lattice.

The fractional coordinates of the particles is:

	$\times\mathbf{a}_1$	$\times\mathbf{a}_2$	$\times\mathbf{a}_3$
$\mathbf{z}_0$	$1/2$	$1/2$	0
$\mathbf{z}_1$	$1/2$	0	0
$\mathbf{z}_2$	0	$1/2$	0
$\mathbf{z}_3$	$2/3$	$1/3$	$1/4$
$\mathbf{z}_4$	$1/2$	$1/2$	$1/2$
$\mathbf{z}_5$	0	$1/2$	$1/2$
$\mathbf{z}_6$	$1/2$	0	$1/2$
$\mathbf{z}_7$	$1/3$	$2/3$	$3/4$

Table A.8: Crystal basis for unit cell of hexagonal tetrastack/rod-connected diamond.

A.2.3 DOUBLE HEXAGONAL TETRASTACK / ROD-CONECTED DIAMOND

The unit cell of double hexagonal tetrastack has a sixteen particle basis and a hexagonal lattice. The fractional coordinates of the particles is:

	$\times\mathbf{a}_1$	$\times\mathbf{a}_2$	$\times\mathbf{a}_3$
$\mathbf{z}_0$	$5/6$	$1/6$	$7/8$
$\mathbf{z}_1$	$1/6$	$5/6$	$1/8$
$\mathbf{z}_2$	$5/6$	$2/3$	$7/8$
$\mathbf{z}_3$	$1/6$	$1/3$	$1/8$
$\mathbf{z}_4$	$1/3$	$1/6$	$7/8$
$\mathbf{z}_5$	$1/3$	$2/3$	$1/4$
$\mathbf{z}_6$	$5/6$	$2/3$	$5/8$
$\mathbf{z}_7$	$1/3$	$1/6$	$5/8$
$\mathbf{z}_8$	$2/3$	$5/6$	$3/8$
$\mathbf{z}_9$	$1/6$	$1/3$	$3/8$
$\mathbf{z}_{10}$	$2/3$	$1/3$	$3/4$
$\mathbf{z}_{11}$	$2/3$	$5/6$	$1/8$
$\mathbf{z}_{12}$	0	0	0
$\mathbf{z}_{13}$	0	0	$1/2$
$\mathbf{z}_{14}$	$1/6$	$5/6$	$3/8$
$\mathbf{z}_{15}$	$5/6$	$1/6$	$5/8$

Table A.9: Crystal basis for unit cell of double hexagonal tetrastack/rod-connected diamond.

A.2.4 GYROID

The primitive unit cell of gyroid has a six particle basis and a bcc lattice. The fractional coordinates of the particles is:

	$\times\mathbf{a}_1$	$\times\mathbf{a}_2$	$\times\mathbf{a}_3$
$\mathbf{z}_0$	$1/8$	$3/8$	$3/4$
$\mathbf{z}_1$	$3/4$	$1/4$	$3/8$
$\mathbf{z}_2$	$3/8$	$1/4$	$1/4$
$\mathbf{z}_3$	$1/4$	$3/8$	$1/8$
$\mathbf{z}_4$	$1/8$	$1/4$	$3/8$
$\mathbf{z}_5$	$3/8$	$3/4$	$1/8$

Table A.10: Crystal basis for the primitive unit cell of gyroid.

The conventional unit cell of gyroid has a twelve particle basis and a simle cubic lattice. The fractional coordinates of the particles is:

	$\times\mathbf{a}_1$	$\times\mathbf{a}_2$	$\times\mathbf{a}_3$
$\mathbf{z}_0$	0	$3/4$	$3/8$
$\mathbf{z}_1$	$7/8$	$1/2$	$1/4$
$\mathbf{z}_2$	0	$1/4$	$1/8$
$\mathbf{z}_3$	$5/8$	$1/2$	$3/4$
$\mathbf{z}_4$	$3/4$	$5/8$	$1/2$
$\mathbf{z}_5$	$3/4$	$3/8$	0
$\mathbf{z}_6$	$1/2$	$1/4$	$7/8$
$\mathbf{z}_7$	$3/8$	0	$3/4$
$\mathbf{z}_8$	$1/2$	$3/4$	$5/8$
$\mathbf{z}_9$	$1/8$	0	$1/4$
$\mathbf{z}_{10}$	$1/4$	$1/8$	0
$\mathbf{z}_{11}$	$1/4$	$7/8$	$1/2$

Table A.11: Crystal basis for the conventional unit cell of gyroid.

BIBLIOGRAPHY

1. Whitesides, G. M. & Grzybowski, B. Self-assembly at all scales. *Science* **295,** 2418 (2002).

2. Manoharan, V. N. Colloidal matter: Packing, geometry, and entropy. *Science* **349,** 1253751 (2015).

3. Silverberg, J. L., Bierbaum, M., Sethna, J. P. & Cohen, I. Collective motion of humans in mosh and circle pits at heavy metal concerts. *Phys. Rev. Lett.* **110,** 228701 (2013).

4. Bricard, A. *et al.* Emergent vortices in populations of colloidal rollers. *Nat. Commun.* **6,** 7470 (2015).

5. Lavergne, F. A., Wendehenne, H., Bäuerle, T. & Bechinger, C. Group formation and cohesion of active particles with visual perception–dependent motility. *Science* **364,** 70–74 (2019).

6. Behera, S., Dogra, D. P., Bandyopadhyay, M. K. & Roy, P. P. Understanding crowd flow patterns using active-Langevin model. *Pattern Recognit.* **119,** 108037 (2021).

7. Van Blaaderen, A. From the de Broglie to visible wavelengths: Manipulating electrons and photons with colloids. *MRS Bull.* **23,** 39–43 (1998).

8. Jones, R. A. L. *Soft condensed matter* (Oxford University Press, 2002).

9. Brown, R. On the particles contained in the pollen of plants; and on the general existence of active molecules in organic and inorganic bodies. *Philos. Mag. Lett.* **4,** 161–173 (1828).

10. Einstein, A. Über die von der molekularkinetischen Theorie der Wärme geforderte Bewegung von in ruhenden Flüssigkeiten suspendierten Teilchen. *Ann. Phys.* **322,** 549–560 (1905).

11. Wood, W. W. & Jacobson, J. D. Preliminary results from a recalculation of the Monte Carlo equation of state of hard spheres. *J. Chem. Phys.* **27,** 1207–1208 (1957).

12. Alder, B. J. & Wainwright, T. E. Phase transition for a hard sphere system. *J. Chem. Phys.* **27,** 1208–1209 (1957).

13. Pusey, P. N. & Van Megen, W. Phase behaviour of concentrated suspensions of nearly hard colloidal spheres. *Nature* **320,** 340–342 (1986).

14. Colvin, V. L. From opals to optics: Colloidal photonic crystals. *MRS Bull.* **26,** 637–641 (2001).

15. Biswas, R., Sigalas, M. M., Subramania, G., Soukoulis, C. M. & Ho, K.-M. Photonic band gaps of porous solids. *Phys. Rev. B* **61,** 4549 (2000).

16. Woodcock, L. V. Entropy difference between the face-centred cubic and hexagonal close-packed crystal structures. *Nature* **385,** 141–143 (1997).

17. Bolhuis, P. G., Frenkel, D., Mau, S.-C. & Huse, D. A. Entropy difference between crystal phases. *Nature* **388,** 235–236 (1997).

18. Bruce, A., Wilding, N. & Ackland, G. Free energy of crystalline solids: a lattice-switch Monte Carlo method. *Phys. Rev. Lett.* **79,** 3002 (1997).

19. Sanders, J. V. Diffraction of light by opals. *Acta Crystallogr. A* **24,** 427–434 (1968).

20. Yablonovitch, E. & Gmitter, T. J. Photonic band structure: The face-centered-cubic case. *Phys. Rev. Lett.* **63,** 1950–1953 (1989).

21. Leung, K. M. & Liu, Y. F. Full vector wave calculation of photonic band structures in face-centered-cubic dielectric media. *Phys. Rev. Lett.* **65,** 2646–2649 (1990).

22. Zhang, Z. & Satpathy, S. Electromagnetic wave propagation in periodic structures: Bloch wave solution of Maxwell's equations. *Phys. Rev. Lett.* **65,** 2650–2653 (1990).

23. Pusey, P. N., Zaccarelli, E., Valeriani, C., Sanz, E., Poon, W. C. K. & Cates, M. E. Hard spheres: crystallization and glass formation. *Philos. T. R. Soc. A.* **367,** 4993–5011 (2009).

24. Subramanian, G., Manoharan, V. N., Thorne, J. D. & Pine, D. J. Ordered macroporous materials by colloidal assembly: a possible route to photonic bandgap materials. *Adv. Mater.* **11,** 1261–1265 (1999).

25. He, M. *et al.* Colloidal diamond. *Nature* **585,** 524 (2020).

26. Meade, R. D. V., Johnson, S. G. & Winn, J. N. *Photonic crystals: Molding the flow of light* 2008.

27. Zhang, Z., Keys, A. S., Chen, T. & Glotzer, S. C. Self-assembly of patchy particles into diamond structures through molecular mimicry. *Langmuir* **21,** 11547–11551 (2005).

28. Romano, F., Sanz, E. & Sciortino, F. Crystallization of tetrahedral patchy particles in silico. *J. Chem. Phys* **134,** 174502 (2011).

29. Mahynski, N. A., Rovigatti, L., Likos, C. N. & Panagiotopoulos, A. Z. Bottom-Up Colloidal Crystal Assembly with a Twist. *ACS Nano* **10,** 5459–5467 (2016).

30. Romano, F. & Sciortino, F. Patterning symmetry in the rational design of colloidal crystals. *Nat. Commun.* **3,** 975 (2012).

31. Rao, A. B. *et al.* Leveraging hierarchical self-assembly pathways for realizing colloidal photonic crystals. *ACS Nano* **14,** 5348–5349 (2020).

32. Magkiriadou, S., Park, J.-G., Kim, Y.-S. & Manoharan, V. N. Absence of red structural color in photonic glasses, bird feathers, and certain beetles. *Phys. Rev. E* **90,** 062302 (2014).

33. Kim, J. B., Lee, S. Y., Lee, J. M. & Kim, S.-H. Designing structural-color patterns composed of colloidal arrays. *ACS Appl. Mater. Interfaces* **11,** 14485–14509 (2019).

34. Hwang, V. *et al.* Designing angle-independent structural colors using Monte Carlo simulations of multiple scattering. *Proc. Natl. Acad. Sci. U.S.A.* **118,** e2015551118 (2021).

35. Xiao, M., Stephenson, A. B., Neophytou, A., Hwang, V., Chakrabarti, D. & Manoharan, V. N. Investigating the trade-off between color saturation and angle-independence in photonic glasses. *Opt. Express* **29,** 21212–21224 (2021).

36. Vynck, K. *et al.* Light in correlated disordered media. *arXiv preprint arXiv:2106.13892* (2021).

37. Kim, J. B., Chae, C., Han, S. H., Lee, S. Y. & Kim, S.-H. Direct writing of customized structural-color graphics with colloidal photonic inks. *Sci. Adv.* **7,** eabj8780 (2021).

38. Forster, J. D. *et al.* Biomimetic isotropic nanostructures for structural coloration. *Advanced Materials* **22,** 2939–2944 (2010).

39. Frenkel, D. & Ladd, A. J. New Monte Carlo method to compute the free energy of arbitrary solids. Application to the fcc and hcp phases of hard spheres. *J. Chem. Phys.* **81,** 3188–3193 (1984).

40. Cheng, Z., Russel, W. B. & Chaikin, P. Controlled growth of hard-sphere colloidal crystals. *Nature* **401,** 893–895 (1999).

41. Auer, S. & Frenkel, D. Numerical prediction of absolute crystallization rates in hard-sphere colloids. *J. Chem. Phys.* **120,** 3015–3029 (2004).

42. Schöpe, H. J., Bryant, G. & Van Megen, W. Two-step crystallization kinetics in colloidal hard-sphere systems. *Phys. Rev. Lett.* **96,** 175701 (2006).

43. Zaccarelli, E., Valeriani, C., Sanz, E., Poon, W., Cates, M. & Pusey, P. Crystallization of hard-sphere glasses. *Phys. Rev. Lett.* **103,** 135704 (2009).

44. Mirkin, C. A., Letsinger, R. L., Mucic, R. C. & Storhoff, J. J. A DNA-based method for rationally assembling nanoparticles into macroscopic materials. *Nature* **382,** 607 (1996).

45. Alivisatos, A. P. *et al.* Organization of 'nanocrystal molecules' using DNA. *Nature* **382,** 609 (1996).

46. Park, S. Y. & Stroud, D. Structure formation, melting, and optical properties of gold/DNA nanocomposites: effects of relaxation time. *Phys. Rev. B* **68,** 224201 (2003).

47. Park, S.-J., Lazarides, A. A., Storhoff, J. J., Pesce, L. & Mirkin, C. A. The structural characterization of oligonucleotide-modified gold nanoparticle networks formed by DNA hybridization. *J. Phys. Chem. B* **108,** 12375–12380 (2004).

48. Park, S. Y., Lee, J.-S., Georganopoulou, D., Mirkin, C. A. & Schatz, G. C. Structures of DNA-linked nanoparticle aggregates. *J. Phys. Chem. B* **110,** 12673–12681 (2006).

49. Maye, M. M., Nykypanchuk, D., Van Der Lelie, D. & Gang, O. DNA-regulated micro-and nanoparticle assembly. *Small* **3,** 1678–1682 (2007).

50. Di Michele, L., Varrato, F., Kotar, J., Nathan, S. H., Foffi, G. & Eiser, E. Multistep kinetic self-assembly of DNA-coated colloids. *Nat. Commun.* **4,** 2007 (2013).

51. Angioletti-Uberti, S., Mognetti, B. M. & Frenkel, D. Re-entrant melting as a design principle for DNA-coated colloids. *Nat. Mater.* **11,** 518 (2012).

52. Biancaniello, P. L., Kim, A. J. & Crocker, J. C. Colloidal interactions and self-assembly using DNA hybridization. *Phys. Rev. Lett.* **94,** 058302 (2005).

53. Rogers, W. B., Shih, W. M. & Manoharan, V. N. Using DNA to program the self-assembly of colloidal nanoparticles and microparticles. *Nature Reviews Materials* **1,** 1–14 (2016).

54. Laramy, C. R., O'Brien, M. N. & Mirkin, C. A. Crystal engineering with DNA. *Nat. Rev. Mater.,* 201–224 (2019).

55. Ho, K. M., Chan, C. T. & Soukoulis, C. M. Existence of a photonic gap in periodic dielectric structures. *Phys. Rev. Lett.* **65,** 3152–3155 (1990).

56. Sözüer, H. S., Haus, J. W. & Inguva, R. Photonic bands: Convergence problems with the plane-wave method. *Phys. Rev. B* **45,** 13962 (1992).

57. Maldovan, M. & Thomas, E. L. Diamond-structured photonic crystals. *Nat. Mater.* **3,** 593 (2004).

58. Men, H., Lee, K. Y. K., Freund, R. M., Peraire, J. & Johnson, S. G. Robust topology optimization of three-dimensional photonic-crystal band-gap structures. *Opt. Express* **22,** 22632–22648 (2014).

59. Bianchi, E., Blaak, R. & Likos, C. N. Patchy colloids: state of the art and perspectives. *Phys. Chem. Chem. Phys.* **13,** 6397–6410 (2011).

60. Sacanna, S., Pine, D. J. & Yi, G.-R. Engineering shape: the novel geometries of colloidal self-assembly. *Soft Matter* **9,** 8096–8106 (2013).

61. Whitesides, G. M. & Boncheva, M. Beyond molecules: Self-assembly of mesoscopic and macroscopic components. *Proc. Natl. Acad. Sci. USA* **99,** 4769 (2002).

62. Glotzer, S. C. & Solomon, M. J. Anisotropy of building blocks and their assembly into complex structures. *Nat. Mater.* **6,** 557–562 (2007).

63. Cademartiri, L. & Bishop, K. J. M. Programmable self-assembly. *Nat. Mater.* **14,** 2–9 (2015).

64. Ravaine, S. & Duguet, E. Synthesis and assembly of patchy particles: Recent progress and future prospects. *Curr. Opin. Colloid Interface Sci.* **30,** 45–53 (2017).

65. Romano, F., Sanz, E. & Sciortino, F. Phase diagram of a tetrahedral patchy particle model for different interaction ranges. *J. Chem. Phys.* **132,** 184501 (2010).

66. Noya, E. G., Vega, C., Doye, J. P. K. & Louis, A. A. The stability of a crystal with diamond structure for patchy particles with tetrahedral symmetry. *J. Chem. Phys* **132,** 234511 (2010).

67. Chen, Q., Bae, S. C. & Granick, S. Directed self-assembly of a colloidal kagome lattice. *Nature* **469,** 381–384 (2011).

68. Mao, X., Chen, Q. & Granick, S. Entropy favours open colloidal lattices. *Nat. Mater.* **12,** 217–222 (2013).

69. Romano, F., Russo, J. & Tanaka, H. Influence of patch-size variability on the crystallization of tetrahedral patchy particles. *Phys. Rev. Lett.* **113,** 138303 (2014).

70. Rocklin, D. Z. & Mao, X. Self-assembly of three-dimensional open structures using patchy colloidal particles. *Soft Matter* **10,** 7569–7576 (2014).

71. Fejer, S. N. & Wales, D. J. Design of a Kagome lattice from soft anisotropic particles. *Soft Matter* **11,** 6663–6668 (2015).

72. Reinhart, W. F. & Panagiotopoulos, A. Z. Equilibrium crystal phases of triblock Janus colloids. *J. Chem. Phys.* **145** (2016).

73. Wang, Y. *et al.* Colloids with valence and specific directional bonding. *Nature* **491,** 51–55 (2012).

74. Chen, Q., Diesel, E., Whitmer, J. K., Bae, S. C., Luijten, E. & Granick, S. Triblock colloids for directed self-assembly. *J. Am. Chem. Soc.* **133,** 7725–7727 (2011).

75. Chen, Q., Yan, J., Zhang, J., Bae, S. C. & Granick, S. Janus and multiblock colloidal particles. *Langmuir* **28,** 13555–13561 (2012).

76. Swinkels, P. *et al.* Revealing pseudorotation and ring-opening reactions in colloidal organic molecules. *Nat. Commun.* **12,** 2810 (2021).

77. Hynninen, A.-P., Thijssen, J. H. J., Vermolen, E. C. M., Dijkstra, M. & Van Blaaderen, A. Self-assembly route for photonic crystals with a bandgap in the visible region. *Nat. Mater.* **6,** 202 (2007).

78. Von Freymann, G., Kitaev, V., Lotsch, B. V. & Ozin, G. A. Bottom-up assembly of photonic crystals. *Chem. Soc. Rev.* **42,** 2528–2554 (2013).

79. Romano, F., Russo, J., Kroc, L. & Šulc, P. Designing patchy interactions to self-assemble arbitrary structures. *Phys. Rev. Lett.* **125,** 118003 (2020).

80. Saika-Voivod, I., Romano, F. & Sciortino, F. Nucleation barriers in tetrahedral liquids spanning glassy and crystallizing regimes. *J. Chem. Phys.* **135,** 124506 (2011).

81. Smallenburg, F. & Sciortino, F. Liquids more stable than crystals in particles with limited valence and flexible bonds. *Nat. Phys.* **9,** 554–558 (2013).

82. Noya, E. G., Zubieta, I., Pine, D. J. & Sciortino, F. Assembly of clathrates from tetrahedral patchy colloids with narrow patches. *J. Chem. Phys.* **151,** 094502 (2019).

83. King, S. V. Ring configurations in a random network model of vitreous silica. *Nature* **213,** 1112–1113 (1967).

84. Saika-Voivod, I., Smallenburg, F. & Sciortino, F. Understanding tetrahedral liquids through patchy colloids. *J. Chem. Phys.* **139,** 234901 (2013).

85. Doye, J. P. *et al.* Controlling crystallization and its absence: proteins, colloids and patchy models. *Phys. Chem. Chem. Phys.* **9,** 2197–2205 (2007).

86. Pawar, A. B. & Kretzschmar, I. Patchy particles by glancing angle deposition. *Langmuir* **24,** 355–358 (2008).

87. Romano, F. & Sciortino, F. Two dimensional assembly of triblock Janus particles into crystal phases in the two bond per patch limit. *Soft Matter* **7,** 5799 (2011).

88. Mao, X. Entropic effects in the self-assembly of open lattices from patchy particles. *Phys. Rev. E* **8732,** 062319 (2013).

89. Ngo, T. T., Liddell, C. M., Ghebrebrhan, M. & Joannopoulos, J. D. Tetrastack: colloidal diamond-inspired structure with omnidirectional photonic band gap for low refractive index contrast. *Appl. Phys. Lett.* **88,** 241920 (2006).

90. Jacobs, W. M. & Frenkel, D. Self-assembly of structures with addressable complexity. *J. Am. Chem. Soc.* **138,** 2457–2467 (2016).

91. Chen, Q., Bae, S. C. & Granick, S. Staged self-assembly of colloidal metastructures. *J. Am. Chem. Soc.* **134,** 11080–11083 (2012).

92. Morphew, D., Shaw, J., Avins, C. & Chakrabarti, D. Programming hierarchical self-assembly of patchy particles into colloidal crystals via colloidal molecules. *ACS Nano,* 2355–2364 (2018).

93. Bianchi, E., Largo, J., Tartaglia, P., Zaccarelli, E. & Sciortino, F. Phase diagram of patchy colloids: Towards empty liquids. *Phys. Rev. Lett.* **97,** 168301 (2006).

94. Ruzicka, B. *et al.* Observation of empty liquids and equilibrium gels in a colloidal clay. *Nat. Mater.* **10,** 56–60 (2011).

95. Russo, J., Leoni, F., Martelli, F. & Sciortino, F. The physics of empty liquids: from patchy particles to water. *Rep. Progr. Phys.* **85,** 016601 (2022).

96. Speedy, R. & Angell, C. Isothermal compressibility of supercooled water and evidence for a thermodynamic singularity at -45 °C. *J. Chem. Phys.* **65,** 851–858 (1976).

97. Angell, C., Sichina, W. & Oguni, M. Heat capacity of water at extremes of supercooling and superheating. *J. Phys. Chem.* **86,** 998–1002 (1982).

98. Angell, C. A. Supercooled water. *Annu. Rev. Phys. Chem.* **34,** 593–630 (1983).

99. Debenedetti, P. G. Supercooled and Glassy Water. *J. Condens. Matter Phys.* **15,** R1669 (2003).

100. Russo, J., Akahane, K. & Tanaka, H. Water-like anomalies as a function of tetrahedrality. *Proc. Natl. Acad. Sci. U.S.A.* **115,** E3333–E3341 (2018).

101. Gallo, P. *et al.* Water: A tale of two liquids. *Chem. Rev.* **116,** 7463–7500 (2016).

102. Poole, P. H., Sciortino, F., Essmann, U. & Stanley, H. E. Phase behaviour of metastable water. *Nature* **360,** 324–328 (1992).

103. Palmer, J. C., Martelli, F., Liu, Y., Car, R., Panagiotopoulos, A. Z. & Debenedetti, P. G. Metastable liquid–liquid transition in a molecular model of water. *Nature* **510,** 385–388 (2014).

104. Debenedetti, P. G., Sciortino, F. & Zerze, G. H. Second critical point in two realistic models of water. *Science* **369,** 289–292 (2020).

105. Limmer, D. T. & Chandler, D. The putative liquid-liquid transition is a liquid-solid transition in atomistic models of water. *J. Chem. Phys.* **135,** 134503 (2011).

106. Limmer, D. T. & Chandler, D. The putative liquid-liquid transition is a liquid-solid transition in atomistic models of water. II. *J. Chem. Phys.* **138,** 214504 (2013).

107. Jedrecy, A., Saitta, A. M. & Pietrucci, F. Free energy calculations and unbiased molecular dynamics targeting the liquid–liquid transition in water no man's land. *J. Chem. Phys.* **158,** 014502 (2023).

108. Kim, K. H. *et al.* Experimental observation of the liquid-liquid transition in bulk supercooled water under pressure. *Science* **370,** 978–982 (2020).

109. Smallenburg, F., Filion, L. & Sciortino, F. Erasing no-man's land by thermodynamically stabilizing the liquid–liquid transition in tetrahedral particles. *Nat. Phys.* **10,** 653–657 (2014).

110. Zaccarelli, E. Colloidal gels: equilibrium and non-equilibrium routes. *J. Condens. Matter Phys.* **19,** 323101 (2007).

111. Onsager, L. Crystal statistics. I. A two-dimensional model with an order-disorder transition. *Physical Review* **65,** 117 (1944).

112. Frenkel, D. & Smit, B. *Understanding molecular simulation: from algorithms to applications* (Elsevier, 2001).

113. Allen, M. P. & Tildesley, D. J. *Computer simulation of liquids* (Oxford university press, 2017).

114. Nocedal, J. & Wright, S. J. *Numerical optimization* (Springer, 2006).

115. Wales, D. *Energy landscapes: Applications to clusters, biomolecules and glasses* (Cambridge University Press, 2003).

116. Wales, D. J. & Doye, J. P. K. Global Optimization by Basin-Hopping and the Lowest Energy Structures of Lennard-Jones Clusters Containing up to 110 Atoms (1997).

117. Wales, D. J. Decoding the energy landscape: extracting structure, dynamics and thermodynamics. *Philos. Trans. Royal Soc. A PHILOS T R SOC A* **370,** 2877–2899 (2012).

118. Metropolis, N., Rosenbluth, A. W., Rosenbluth, M. N., Teller, A. H. & Teller, E. Equation of state calculations by fast computing machines. *The journal of chemical physics* **21,** 1087–1092 (1953).

119. Klein, E. D., Perry, R. W. & Manoharan, V. N. Physical interpretation of the partition function for colloidal clusters. *Phys. Rev. E* **98,** 032608 (2018).

120. Cook, J. Rational formulae for the production of a spherically symmetric probability distribution. *Mathematics of Computation* **11,** 81–82 (1957).

121. Marsaglia, G. Choosing a point from the surface of a sphere. *The Annals of Mathematical Statistics* **43,** 645–646 (1972).

122. Sanz, E. & Marenduzzo, D. Dynamic Monte Carlo versus Brownian dynamics: A comparison for self-diffusion and crystallization in colloidal fluids. *The Journal of chemical physics* **132** (2010).

123. Romano, F., De Michele, C., Marenduzzo, D. & Sanz, E. Monte Carlo and event-driven dynamics of Brownian particles with orientational degrees of freedom. *The Journal of chemical physics* **135** (2011).

124. Kikuchi, K., Yoshida, M., Maekawa, T. & Watanabe, H. Metropolis Monte Carlo method as a numerical technique to solve the Fokker—Planck equation. *Chemical Physics Letters* **185,** 335–338 (1991).

125. Malevanets, A. & Kapral, R. Mesoscopic model for solvent dynamics. *The Journal of chemical physics* **110,** 8605–8613 (1999).

126. Huitema, H. & Van der Eerden, J. Can Monte Carlo simulation describe dynamics? A test on Lennard-Jones systems. *The Journal of chemical physics* **110,** 3267–3274 (1999).

127. Eppenga, R. & Frenkel, D. Monte Carlo study of the isotropic and nematic phases of infinitely thin hard platelets. *Molecular physics* **52,** 1303–1334 (1984).

128. Whitelam, S. & Geissler, P. L. Avoiding unphysical kinetic traps in Monte Carlo simulations of strongly attractive particles. *J. Chem. Phys* **127,** 154101 (2007).

129. Růžička, Š. & Allen, M. P. Collective translational and rotational Monte Carlo moves for attractive particles. *Phys. Rev. E* **89,** 033307 (2014).

130. Villar, G. *et al.* Self-assembly and evolution of homomeric protein complexes. *Physical review letters* **102,** 118106 (2009).

131. Madge, J. & Miller, M. A. Design strategies for self-assembly of discrete targets. *The Journal of chemical physics* **143** (2015).

132. Whitelam, S., Feng, E. H., Hagan, M. F. & Geissler, P. L. The role of collective motion in examples of coarsening and self-assembly. *Soft Matter* **5,** 1251–1262 (2009).

133. Matek, C., Ouldridge, T. E., Levy, A., Doye, J. P. & Louis, A. A. DNA cruciform arms nucleate through a correlated but asynchronous cooperative mechanism. *The Journal of Physical Chemistry B* **116,** 11616–11625 (2012).

134. Ržička, Š. & Allen, M. P. Monte Carlo simulation of kinetically slowed down phase separation. *The European Physical Journal E* **38,** 1–12 (2015).

135. Jacobs, W. M., Reinhardt, A. & Frenkel, D. Rational design of self-assembly pathways for complex multicomponent structures. *Proceedings of the National Academy of Sciences* **112,** 6313–6318 (2015).

136. Morphew, D. & Chakrabarti, D. Programming hierarchical self-assembly of colloids: matching stability and accessibility. *Nanoscale* **10,** 13875–13882 (2018).

137. Almarza, N. G. A cluster algorithm for Monte Carlo simulation at constant pressure. *J. Chem. Phys.* **130,** 184106 (2009).

138. Noya, E. G., Conde, M. & Vega, C. Computing the free energy of molecular solids by the Einstein molecule approach: Ices XIII and XIV, hard-dumbbells and a patchy model of proteins. *J. Chem. Phys.* **129,** 104704 (2008).

139. Kirkwood, J. G. Statistical mechanics of fluid mixtures. *The Journal of chemical physics* **3,** 300–313 (1935).

140. Frenkel, D. & Mulder, B. The hard ellipsoid-of-revolution fluid: I. Monte Carlo simulations. *Molecular physics* **55,** 1171–1192 (1985).

141. Bolhuis, P. & Frenkel, D. Tracing the phase boundaries of hard spherocylinders. *The Journal of chemical physics* **106,** 666–687 (1997).

142. Vega, C. & Monson, P. A. Plastic crystal phases of hard dumbbells and hard spherocylinders. *The Journal of chemical physics* **107,** 2696–2697 (1997).

143. Vega, C. & Monson, P. Solid–fluid equilibrium for a molecular model with short ranged directional forces. *The Journal of chemical physics* **109,** 9938–9949 (1998).

144. Vega, C., Abascal, J., Sanz, E., MacDowell, L. & McBride, C. Can simple models describe the phase diagram of water? *Journal of Physics: Condensed Matter* **17,** S3283 (2005).

145. Noya, E., Vega, C., Doye, J. & Louis, A. Phase diagram of model anisotropic particles with octahedral symmetry. *The Journal of chemical physics* **127** (2007).

146. Vega, C., Sanz, E., Abascal, J. L. F. & Noya, E. G. Determination of phase diagrams via computer simulation: methodology and applications to water, electrolytes and proteins. *J. Condens. Matter Phys.* **20,** 153101 (2008).

147. Vissers, T., Preisler, Z., Smallenburg, F., Dijkstra, M. & Sciortino, F. Predicting crystals of Janus colloids. *J. Chem. Phys.* **138,** 164505 (2013).

148. Lepage, G. P. A new algorithm for adaptive multidimensional integration. *J. Comput. Phys.* **27,** 192–203 (1978).

149. Schilling, T. & Schmid, F. Computing absolute free energies of disordered structures by molecular simulation. *J. Chem. Phys.* **131,** 231102 (2009).

150. Romano, F., Sanz, E., Tartaglia, P. & Sciortino, F. Phase diagram of trivalent and pentavalent patchy particles. *J. Condens. Matter Phys.* **24,** 064113 (2012).

151. Preisler, Z. *Self-assembly of attractive one-patch colloids* PhD thesis (Università di Roma Sapienza, 2013). `https://opac.bncf.firenze.sbn.it:443/bncf-prod/resource?uri=TD17047274`.

152. Chau, P.-L. & Hardwick, A. A new order parameter for tetrahedral configurations. *Molecular Physics* **93,** 511–518 (1998).

153. Steinhardt, P. J., Nelson, D. R. & Ronchetti, M. Bond-orientational order in liquids and glasses. *Phys. Rev. B* **28,** 784–805 (1983).

154. Lechner, W. & Dellago, C. Accurate determination of crystal structures based on averaged local bond order parameters. *J. Chem. Phys* **129,** 114707 (2008).

155. Sharma, A. K. & Escobedo, F. A. Nucleus-size pinning for determination of nucleation free-energy barriers and nucleus geometry. *J. Chem. Phys.* **148,** 184104 (2018).

156. Kittel, C. *Introduction to Solid State Physics* 7th (John Wiley & Sons, Inc., New York, 1996).

157. Ashcroft, N. W. & Mermin, N. D. *Solid State Physics* (Saunders College, Philadelphia, 1976).

158. Sukhoivanov, I. A. & Guryev, I. V. *Photonic crystals: physics and practical modeling* (Springer, 2009).

159. Johnson, S. G. & Joannopoulos, J. D. Block-iterative frequency-domain methods for Maxwell's equations in a planewave basis. *Opt. Express* **8,** 173–190 (2001).

160. Meade, R. D., Rappe, A. M., Brommer, K. D. & Joannopoulos, J. D. Nature of the photonic band gap: some insights from a field analysis. *J. Opt. Soc. Am. B* **10,** 328–332 (1993).

161. Johnson, S. G. & Joannopoulos, J. D. *Introduction to photonic crystals: Bloch's theorem, band diagrams, and gaps (but no defects)* Feb. 2003. `http://ab-initio.mit.edu/photons/tutorial/photonic-intro.pdf`.

162. Economou, E. N. *The Physics of Solids: Essentials and Beyond* (Springer Science & Business Media, 2010).

163. Mie, G. Articles on the optical characteristics of turbid tubes, especially colloidal metal solutions. *Ann. Phys.* **25,** 377–445 (1908).

164. Bohren, C. & Huffman, D. R. *Absorption and scattering of light by small particles* (Wiley Science Paperback Series, 1998).

165. Kuznetsov, A. I., Miroshnichenko, A. E., Brongersma, M. L., Kivshar, Y. S. & Luk'yanchuk, B. Optically resonant dielectric nanostructures. *Science* **354,** aag2472 (2016).

166. Inoue, K. & Ohtaka, K. *Photonic crystals: physics, fabrication and applications* (Springer Science & Business Media, 2004).

167. Lidorikis, E., Sigalas, M. M., Economou, E. N. & Soukoulis, C. M. Tight-binding parametrization for photonic band gap materials. *Phys. Rev. Lett.* **81,** 1405–1408 (1998).

168. Vandenbem, C. & Vigneron, J. P. Mie resonances of dielectric spheres in face-centered cubic photonic crystals. *J. Opt. Soc. Am. A* **22,** 1042–1047 (2005).

169. Shi, L., Jiang, X. & Li, C. Effects induced by Mie resonance in two-dimensional photonic crystals. *J. Phys. Condens. Matter* **19,** 176214 (2007).

170. Chern, R.-L. & Chao, S. D. Optimal higher-lying band gaps for photonic crystals with large dielectric contrast. *Opt. Express* **16,** 16600–16608 (2008).

171. Soukoulis, C. M. *Photonic band gaps and localization* (Springer Science & Business Media, 2013).

172. Florescu, M., Torquato, S. & Steinhardt, P. J. Complete band gaps in two-dimensional photonic quasicrystals. *Phys. Rev. B* **80,** 155112 (2009).

173. Sellers, S. R., Man, W., Sahba, S. & Florescu, M. Local self-uniformity in photonic networks. *Nat. Commun.* **8,** 14439 (2017).

174. John, S. & Wang, J. Quantum optics of localized light in a photonic band gap. *Phys. Rev. B* **43,** 12772 (1991).

175. Ducrot, É., He, M., Yi, G.-R. & Pine, D. J. Colloidal alloys with preassembled clusters and spheres. *Nat. Mater.* **16,** 652 (2017).

176. Gong, Z., Hueckel, T., Yi, G.-R. & Sacanna, S. Patchy particles made by colloidal fusion. *Nature* **550,** 234 (2017).

177. Chan, C. T., Ho, K. M. & Soukoulis, C. M. Photonic band gaps in experimentally realizable periodic dielectric structures. *EPL* **16,** 563 (1991).

178. Chaudhary, K., Chen, Q., Juárez, J. J., Granick, S. & Lewis, J. A. Janus Colloidal Matchsticks. *J. Am. Chem. Soc.* **134,** 12901–12903 (2012).

179. Liu, M., Dong, F., Jackson, N. S., Ward, M. D. & Weck, M. Customized Chiral Colloids. *J. Am. Chem. Soc.* **142,** 16528–16532 (2020).

180. Earl, D. J., Ilnytskyi, J. & Wilson, M. R. Computer simulations of soft repulsive spherocylinders. *Mol. Phys.* **99,** 1719–1726 (2001).

181. Cuetos, A., Martínez-Haya, B., Rull, L. F. & Lago, S. Monte Carlo study of liquid crystal phases of hard and soft spherocylinders. *J. Chem. Phys* **117,** 2934–2946 (2002).

182. Cuetos, A. & Martínez-Haya, B. Liquid crystal phase diagram of soft repulsive rods and its mapping on the hard repulsive reference fluid. *Mol. Phys.* **113,** 1137–1144 (2015).

183. Vega, C. & Lago, S. A fast algorithm to evaluate the shortest distance between rods. *Computers & Chemistry* **18,** 55–59 (1994).

184. Morgan, J. W. R., Chakrabarti, D., Dorsaz, N. & Wales, D. J. Designing a Bernal spiral from patchy colloids. *ACS Nano* **7,** 1246–1256 (2013).

185. Haxton, T. K. & Whitelam, S. Do hierarchical structures assemble best *via* hierarchical pathways? *Soft Matter* **9,** 6851–6861 (2013).

186. Gibson, K. D. & Scheraga, H. A. Crystal Packing without Symmetry Constraints. 1. Tests of a New Algorithm for Determining Crystal Structures by Energy Minimization. *J. Phys. Chem.* **99,** 3752–3764 (1995).

187. Stillinger, F. H. Lattice sums and their phase diagram implications for the classical Lennard-Jones model. *J. Chem. Phys* **115,** 5208–5212 (2001).

188. Checoury, X., Enoch, S., López, C. & Blanco, A. Stacking patterns in self-assembly opal photonic crystals. *Appl. Phys. Lett.* **90,** 161131 (2007).

189. Oh, J. S., Lee, S., Glotzer, S. C., Yi, G.-R. & Pine, D. J. Colloidal fibers and rings by cooperative assembly. *Nat. Commun.* **10,** 3936 (2019).

190. Vekilov, P. G. The two-step mechanism of nucleation of crystals in solution. *Nanoscale* **2,** 2346–2357 (2010).

191. Savage, J. R. & Dinsmore, A. D. Experimental evidence for two-step nucleation in colloidal crystallization. *Phys. Rev. Lett.* **102,** 198302 (2009).

192. Russo, J. & Tanaka, H. Nonclassical pathways of crystallization in colloidal systems. *MRS Bull.* **41,** 369–374 (2016).

193. Lee, S., Teich, E. G., Engel, M. & Glotzer, S. C. Entropic colloidal crystallization pathways via fluid–fluid transitions and multidimensional prenucleation motifs. *Proc. Natl. Acad. Sci. USA* **116,** 14843–14851 (2019).

194. Setyawan, W. & Curtarolo, S. High-throughput electronic band structure calculations: Challenges and tools. *Comput. Mater. Sci.* **49,** 299–312 (2010).

195. Edagawa, K., Kanoko, S. & Notomi, M. Photonic Amorphous Diamond Structure with a 3D Photonic Band Gap. *Phys. Rev. Lett.* **100,** 013901 (2008).

196. Edagawa, K. Photonic crystals, amorphous materials, and quasicrystals. *Sci. Technol. Adv. Mater.* **15,** 034805 (2014).

197. Ducrot, É., Gales, J., Yi, G.-R. & Pine, D. J. Pyrochlore lattice, self-assembly and photonic band gap optimizations. *Opt. Express* **26,** 30052–30060 (2018).

198. Haimi, E., Lipsonen, H., Larismaa, J., Kapulainen, M., Krzak-Ros, J. & Hannula, S. P. Optical and structural properties of nanocrystalline anatase (TiO_2) thin films prepared by non-aqueous sol-gel dip-coating. *Thin Solid Films* **519,** 5882–5886 (2011).

199. Dolan J, A., Wilts, B. D., Vignolini, S., Baumberg, J. J., Steiner, U. & Wilkinson, T. D. Optical properties of gyroid structured materials: from photonic crystals to metamaterials. *Adv. Opt. Mater.* **3,** 12–32 (2015).

200. Maldovan, M., Carter, W. C. & Thomas, E. L. Three-dimensional dielectric network structures with large photonic band gaps. *Appl. Phys. Lett.* **83,** 5172–5174 (2003).

201. Neophytou, A., Manoharan, V. N. & Chakrabarti, D. Self-assembly of patchy colloidal rods into photonic crystals robust to stacking faults. *ACS Nano* **15,** 2668–2678 (2021).

202. Rogers, W. B., Shih, W. M. & Manoharan, V. N. Using DNA to program the self-assembly of colloidal nanoparticles and microparticles. *Nat. Rev. Mater.* **1,** 364–368 (2016).

203. Diaz, J. A., Oh, J. S., Yi, G.-R. & Pine, D. J. Photo-printing of faceted DNA patchy particles. *Proc. Natl. Acad. Sci. USA* **117,** 10645–10653 (2020).

204. Kern, N. & Frenkel, D. Fluid-fluid coexistence in colloidal systems with short-ranged strongly directional attraction. *J. Chem. Phys.* **118,** 9882–9889 (2003).

205. Matsumoto, M., Yagasaki, T. & Tanaka, H. GenIce: hydrogen-disordered ice generator. *J. Comput. Chem.* **39,** 61–64 (2017).

206. De Las Heras, D., Tavares, J. M. & Telo da Gama, M. M. Phase diagrams of binary mixtures of patchy colloids with distinct numbers of patches: the network fluid regime. *Soft Matter* **7,** 5615–5626 (2011).

207. De Las Heras, D., Tavares, J. M. & Telo da Gama, M. M. Phase diagrams of binary mixtures of patchy colloids with distinct numbers and types of patches: The empty fluid regime. *J. Chem. Phys.* **134,** 104904 (2011).

208. Wertheim, M. Fluids with highly directional attractive forces. I. Statistical thermodynamics. *J. Stat. Phys.* **35,** 19–34 (1984).

209. Wertheim, M. Fluids with highly directional attractive forces. II. Thermodynamic perturbation theory and integral equations. *J. Stat. Phys.* **35,** 35–47 (1984).

210. Wertheim, M. Fluids with highly directional attractive forces. III. Multiple attraction sites. *J. Stat. Phys.* **42,** 459–476 (1986).

211. Wertheim, M. Fluids with highly directional attractive forces. IV. Equilibrium polymerization. *J. Stat. Phys.* **42,** 477–492 (1986).

212. Stopper, D., Hirschmann, F., Oettel, M. & Roth, R. Bulk structural information from density functionals for patchy particles. *J. Chem. Phys.* **149,** 224503 (2018).

213. Foffi, G. & Sciortino, F. On the possibility of extending the Noro-Frenkel generalized law of correspondent states to non-isotropic patchy interactions. *J. Phys. Chem. B* **111,** 9702–9705 (2007).

214. Dorsaz, N., Filion, L., Smallenburg, F. & Frenkel, D. Spiers Memorial Lecture: Effect of interaction specificity on the phase behaviour of patchy particles. *Faraday Discuss.* **159,** 9–21 (2012).

215. Patra, N. & Tkachenko, A. V. Programmable self-assembly of diamond polymorphs from chromatic patchy particles. *Phys. Rev. E* **98,** 032611 (2018).

216. Spear, K. E., Phelps, A. W. & White, W. B. Diamond polytypes and their vibrational spectra. *J. Mater. Res.* **5,** 2277–2285 (1990).

217. Phelps, A., Howard, W. & Smith, D. Space groups of the diamond polytypes. *J. Mater. Res.* **8,** 2835–2839 (1993).

218. Pronk, S. & Frenkel, D. Can stacking faults in hard-sphere crystals anneal out spontaneously? *J. Chem. Phys.* **110,** 4589–4592 (1999).

219. Bruce, A., Jackson, A., Ackland, G. & Wilding, N. Lattice-switch Monte Carlo method. *Phys. Rev. E* **61,** 906 (2000).

220. Hudait, A., Qiu, S., Lupi, L. & Molinero, V. Free energy contributions and structural characterization of stacking disordered ices. *Phys. Chem. Chem. Phys.* **18,** 9544–9553 (2016).

221. Lupi, L. *et al.* Role of stacking disorder in ice nucleation. *Nature* **551,** 218–222 (2017).

222. Kim, K. H. *et al.* Maxima in the thermodynamic response and correlation functions of deeply supercooled water. *Science* **358,** 1589–1593 (Dec. 2017).

223. Perakis, F. *et al.* Diffusive dynamics during the high-to-low density transition in amorphous ice. *Proc. Natl. Acad. Sci. U.S.A.* **114,** 8193–8198. ISSN: 0027-8424 (31 2017).

224. Chandler, D. Metastability and no criticality. *Nature* **531,** E1–E2 (2016).

225. Hsu, C. W., Largo, J., Sciortino, F. & Starr, F. W. Hierarchies of networked phases induced by multiple liquid-liquid critical points. *Proc. Natl. Acad. Sci. U.S.A.* **105,** 13711–13715 (2008).

226. Smallenburg, F. & Sciortino, F. Tuning the liquid-liquid transition by modulating the hydrogen-bond angular flexibility in a model for water. *Physical review letters* **115,** 015701 (2015).

227. Hueckel, T., Hocky, G. M. & Sacanna, S. Total synthesis of colloidal matter. *Nat. Rev. Mater.* **6,** 1053–1069 (2021).

228. Bianco, V. & Franzese, G. Critical behavior of a water monolayer under hydrophobic confinement. *Sci. Rep.* **4,** 4440 (2014).

229. Wilding, N. & Bruce, A. Density fluctuations and field mixing in the critical fluid. *J. Condens. Matter Phys.* **4,** 3087 (1992).

230. Shiratani, E. & Sasai, M. Molecular scale precursor of the liquid–liquid phase transition of water. *J. Chem. Phys.* **108,** 3264–3276 (1998).

231. Cuthbertson, M. J. & Poole, P. H. Mixturelike behavior near a liquid-liquid phase transition in simulations of supercooled water. *Phys. Rev. Lett.* **106,** 115706 (2011).

232. De Oca, J. M. M., Sciortino, F. & Appignanesi, G. A. A structural indicator for water built upon potential energy considerations. *J. Chem. Phys.* **152,** 244503 (2020).

233. Tanaka, H., Tong, H., Shi, R. & Russo, J. Revealing key structural features hidden in liquids and glasses. *Nat. Rev. Phys.* **1,** 333–348 (2019).

234. Tanaka, H. Liquid-liquid transition and polyamorphism. *J. Chem. Phys.* **153,** 130901 (2020).

235. Steinberg, L., Russo, J. & Frey, J. A new topological descriptor for water network structure. *J. Cheminformatics* **11,** 48 (2019).

236. Foffi, R., Russo, J. & Sciortino, F. Structural and topological changes across the liquid-liquid transition in water. *J. Chem. Phys.* **154,** 184506 (May 2021).

237. Faccio, C., Benzi, M., Zanetti-Polzi, L. & Daidone, I. Low- and high-density forms of liquid water revealed by a new medium-range order descriptor. *J. Mol. Liq.* **355,** 118922 (2022).

238. Russo, J. & Tanaka, H. Understanding water's anomalies with locally favoured structures. *Nat. Commun.* **5,** 3556 (2014).

239. Kell, G. S. Completely hydrogen-bonded interpenetrating networks in low-temperature liquid water: Their geometrical possibility and stability. *Chem. Phys. Lett.* **30,** 223–226 (1975).

240. Hsu, C. W. & Starr, F. W. Interpenetration as a mechanism for liquid-liquid phase transitions. *Phys. Rev. E* **79,** 041502 (2009).

241. Ciarella, S., Gang, O. & Sciortino, F. Toward the observation of a liquid-liquid phase transition in patchy origami tetrahedra: a numerical study. *Eur. Phys. J. E* **39,** 131 (2016).

242. Horner, K. E., Miller, M. A., Steed, J. W. & Sutcliffe, P. M. Knot theory in modern chemistry. *Chem. Soc. Rev.* **45,** 6432–6448 (2016).

243. Liu, Y., Dehmamy, N. & Barabási, A.-L. Isotopy and energy of physical networks. *Nat. Phys.* **17,** 216–222 (2021).

244. Orlandini, E. & Micheletti, C. Topological and physical links in soft matter systems. *J. Condens. Matter Phys.* **34,** 013002 (2021).

245. Patil, K. R. & Nielsen, J. Uncovering transcriptional regulation of metabolism by using metabolic network topology. *Proc. Natl. Acad. Sci. U.S.A.* **102,** 2685–2689 (2005).

246. Gross, T., D'Lima, C. J. D. & Blasius, B. Epidemic dynamics on an adaptive network. *Phys. Rev. Lett.* **96,** 208701 (2006).

247. Centola, D. The spread of behavior in an online social network experiment. *Science* **329,** 1194–1197 (2010).

248. Bonanno, G., Caldarelli, G., Lillo, F. & Mantegna, R. N. Topology of correlation-based minimal spanning trees in real and model markets. *Phys. Rev. E* **68,** 046130 (2003).

249. Diebold, F. X. & Yilmaz, K. On the network topology of variance decompositions: Measuring the connectedness of financial firms. *J. Econom.* **182,** 119–134 (2014).

250. Rolfsen, D. *Knots and Links* (American Mathematical Soc., 2003).

251. Wolcott, K. *The knotting of theta curves and other graphs in* S^3 325–346 (Marcel Dekker, 1987).

252. Kauffman, L. H. Invariants of graphs in three-space. *Trans. Am. Math. Soc.* **311,** 697–710 (1989).

253. Berger, M. A. Introduction to magnetic helicity. *Plasma Phys. Control. Fusion* **41,** B167 (1999).

254. Moffatt, H. K. The degree of knottedness of tangled vortex lines. *J. Fluid Mech.* **35,** 117–129 (1969).

255. Conway, J. H. & McA. Gordon, C. Knots and links in spatial graphs. *J. Graph Theory* **7,** 445–453 (1983).

256. Qu, A. & James, D. L. Fast linking numbers for topology verification of loopy structures. *ACM Trans. Graph.* **40,** 106 (2021).

257. Levitt, M. Protein folding by restrained energy minimization and molecular dynamics. *J. Mol. Biol.* **170,** 723–764 (1983).

258. Klenin, K. & Langowski, J. Computation of writhe in modeling of supercoiled DNA. *Biopolymers* **54,** 307–317 (2000).

259. Taylor, A. J. & other SPOCK contributors. *pyknotid knot identification toolkit* `https://github.com/SPOCKnots/pyknotid`. Accessed 2021-09-04. 2017.

260. Cerf, C. & Stasiak, A. A topological invariant to predict the three-dimensional writhe of ideal configurations of knots and links. *Proc. Natl. Acad. Sci. U.S.A.* **97,** 3795–3798 (2000).

261. Katritch, V., Bednar, J., Michoud, D., Scharein, R. G., Dubochet, J. & Stasiak, A. Geometry and physics of knots. *Nature* **384,** 142–145 (1996).

262. Abascal, J., Sanz, E., Garcıa Fernández, R. & Vega, C. A potential model for the study of ices and amorphous water: TIP4P/Ice. *J. Chem. Phys.* **122,** 234511 (2005).

263. Abascal, J. L. & Vega, C. A general purpose model for the condensed phases of water: TIP4P/2005. *J. Chem. Phys.* **123,** 234505 (2005).

264. Hyde, S. T., O'Keeffe, M. & Proserpio, D. M. A short history of an elusive yet ubiquitous structure in chemistry, materials, and mathematics. *Angew. Chem. Int. Ed.* **47,** 7996–8000 (2008).

265. Hyde, S. T. & Schröder-Turk, G. E. Geometry of interfaces: topological complexity in biology and materials. *Interface Focus* **2,** 529–538 (2012).

266. Lu, L., Fu, L., Joannopoulos, J. D. & Soljačić, M. Weyl points and line nodes in gyroid photonic crystals. *Nat. Photonics* **7,** 294–299 (2013).

267. Lu, L., Joannopoulos, J. D. & Soljačić, M. Topological states in photonic systems. *Nat. Phys.* **12,** 626–629 (2016).

268. Fruchart, M., Jeon, S.-Y., Hur, K., Cheianov, V., Wiesner, U. & Vitelli, V. Soft self-assembly of weyl materials for light and sound. *Proc. Natl. Acad. Sci. USA* **115,** E3655–3664 (2018).

269. Wang, H. *et al.* The emergence of valency in colloidal crystals through electron equivalents. *Nat. Mater.* **21,** 580–587 (2022).

270. Scriven, L. E. Equilibrium bicontinuous structure. *Nature* **263,** 123–125 (1976).

271. Fontell, K. Cubic phases in surfactant and surfactant-like lipid systems. *Colloid Polym. Sci.* **268,** 264–285 (1990).

272. Bates, F. S. & Fredrickson, G. H. Block Copolymers — Designer soft materials. *Phys. Today* **52,** 32–38 (1999).

273. Kutsumizu, S. Recent progress in the synthesis and structural clarification of thermotropic cubic phases. *Isr. J. Chem.* **52,** 844–853 (2012).

274. Feng, X. *et al.* Seeing mesoatomic distortions in soft-matter crystals of a double-gyroid block copolymer. *Nature* **575,** 175–179 (2019).

275. Itoh, M., Kotani, M., Naito, H., Sunada, T., Kawazoe, Y. & Adschiri, T. New metallic carbon crystal. *Phys. Rev. Lett.* **102,** 055703 (2009).

276. Dai, J., Li, Z. & Yang, J. Boron K_4 crystal: a stable chiral three-dimensional sp^2 network. *Phys. Chem. Chem. Phys.* **12,** 12420–12422 (2010).

277. Liu, J., Zhang, S., Guo, Y. & Wang, Q. Phosphorus K_4 crystal: a new stable allotrope. *Sci. Rep.* **6,** 1–9 (2016).

278. Schoen, A. H. *Infinite periodic minimal surfaces without self-intersections* tech. rep. NASA TN D-5541 (National Aeronautics and Space Administration, 1970).

279. Oskooi, A. F., Roundy, D., Ibanescu, M., Bermel, P., Joannopoulos, J. D. & Johnson, S. G. MEEP: A flexible free-software package for electromagnetic simulations by the FDTD method. *Comput. Phys. Commun.* **181,** 687–702 (2010).

280. Lee, J. C. W. & Chan, C. Polarization Gaps in Spiral Photonic Crystals. *Opt. Express* **13,** 8083–8088 (2005).

281. Saba, M. *et al.* Circular dichroism in biological photonic crystals and cubic chiral nets. *Phys. Rev. Lett.* **106,** 103902 (2011).

282. Saba, M., Wilts, B. D., Hielscher, J. & Schröder-Turk, G. E. Absence of circular polarisation in reflections of butterfly wing scales with chiral gyroid structure. *Mater. Today Proc.* **1,** 193–208 (2014).

283. Pawar, A. B. & Kretzschmar, I. Multifunctional patchy particles by glancing angle deposition. *Langmuir* **25,** 9057–9063 (2009).

284. Kleckner, D. & Irvine, W. T. Creation and dynamics of knotted vortices. *Nat. Phys.* **9,** 253–258 (2013).

285. Kleckner, D., Kauffman, L. H. & Irvine, W. T. How superfluid vortex knots untie. *Nat. Phys.* **12,** 650–655 (2016).

286. Haji-Akbari, A. *et al.* Disordered, quasicrystalline and crystalline phases of densely packed tetrahedra. *Nature* **462,** 773–777 (2009).

287. Noya, E. G., Wong, C. K., Llombart, P. & Doye, J. P. How to design an icosahedral quasicrystal through directional bonding. *Nature* **596,** 367–371 (2021).